

Elmar Lohmüller



# **Transfer of the Metal Wrap Through Solar Cell Concept to n-Type Silicon**

# Transfer of the Metal Wrap Through Solar Cell Concept to n-Type Silicon

Dissertation  
zur Erlangung des Doktorgrades  
der Technischen Fakultät  
der Albert-Ludwigs-Universität Freiburg im Breisgau

vorgelegt von

Elmar Lohmüller

Fraunhofer Institut für Solare Energiesysteme (ISE)  
Freiburg im Breisgau

2015

Dekan:  
Prof. Dr. Georg Lausen

Erstgutachter:  
Prof. Dr. Holger Reinecke  
Zweitgutachter:  
Prof. Dr. Gerhard Willeke

Vorsitzender der Prüfungskommission:  
Prof. Dr. Moritz Diehl  
Beisitzer:  
Prof. Dr. Roland Zengerle

Datum der Prüfung: 18.12.2015

Institut für Mikrosystemtechnik  
Technische Fakultät der Albert-Ludwigs-Universität Freiburg

Schriftenreihe der Reiner Lemoine-Stiftung

**Elmar Lohmüller**

**Transfer of the Metal Wrap Through  
Solar Cell Concept to n-Type Silicon**

Shaker Verlag  
Aachen 2015

**Bibliographic information published by the Deutsche Nationalbibliothek**

The Deutsche Nationalbibliothek lists this publication in the Deutsche Nationalbibliografie; detailed bibliographic data are available in the Internet at <http://dnb.d-nb.de>.

Zugl.: Freiburg, Univ., Diss., 2015

Copyright Shaker Verlag 2015

All rights reserved. No part of this publication may be reproduced, stored in a retrieval system, or transmitted, in any form or by any means, electronic, mechanical, photocopying, recording or otherwise, without the prior permission of the publishers.

Printed in Germany.

ISBN 978-3-8440-4196-5

ISSN 2193-7575

Shaker Verlag GmbH • P.O. BOX 101818 • D-52018 Aachen

Phone: 0049/2407/9596-0 • Telefax: 0049/2407/9596-9

Internet: [www.shaker.de](http://www.shaker.de) • e-mail: [info@shaker.de](mailto:info@shaker.de)

*"Twenty years from now you will be more disappointed by the things you didn't do than by the ones you did do. So throw off the bowlines. Sail away from the safe harbor. Catch the trade winds in your sails.  
Explore. Dream. Discover."*

Mark Twain (1835 – 1910)



## Abstract

This thesis presents the transfer of the metal wrap through (MWT) solar cell concept from *p*-type to *n*-type crystalline Czochralski-grown silicon (Cz-Si) wafers with 156 mm edge length. An industrially-feasible MWT solar cell structure with screen-printed metallization is developed, which combines the advantages of *n*-doped silicon with those of a rear contact cell structure. The conversion efficiency of the fabricated solar cells increases continuously within various development cycles. The studies focus on reverse bias stability, emitter diffusion, and electrical contacting of highly boron-doped surfaces. Specific characterization of the reverse bias behavior of the solar cells point out the major challenge to be overcome for a reliable operation after module encapsulation. The vias and the rear *p*-type contacts represent the most important MWT specific structures. Detailed investigations result in optimizations and process simplifications with respect to the rear contact configuration. The maximum energy conversion efficiency achieved for large-area *n*-type Cz-Si MWT solar cells within this work is 20.4%. Analytical calculations yield a potential energy conversion efficiency of almost 22% for *n*-type Cz-Si MWT solar cells by integration of technological improvements.

New tube furnace diffusion processes are developed to form deep driven-in boron dopings with low surface concentration in a single process step. The emitters formed therewith feature low dark saturation current density of  $(30 \pm 3) \text{ fA/cm}^2$  for passivated and textured surface with a sheet resistance of about  $120 \Omega/\text{sq}$ . Despite low maximum dopant concentration of only  $(1.8 \pm 0.2) \cdot 10^{19} \text{ cm}^{-3}$ , low specific contact resistance of less than  $4 \text{ m}\Omega\text{cm}^2$  is obtained for screen-printed and fired metal contacts. It is experimentally shown for the first time that the depth-dependent course of the dopant concentration contributes to a low-ohmic contact formation. This correlation is also demonstrated by means of an analytical model which is based on metal crystallites. Furthermore, it is shown that charge carrier recombination underneath the metal contacts correlates with both the metal crystallites and the junction depths of the boron dopings.

The progress in emitter formation and the improved understanding of metallization related issues are also of high interest for other solar cell types. Furthermore, findings from this thesis also contributed fundamentally to the ongoing development in *p*-type MWT solar cell technology.



## Kurzfassung

Diese Arbeit beschäftigt sich damit, das „Metal Wrap Through“ (MWT) Solarzellenkonzept von *p*-dotierten auf *n*-dotierte Substrate zu übertragen, die aus kristallinem Czochralski-Silicium (Cz-Si) mit einer Kantenlänge von 156 mm bestehen. Es wird eine industriell umsetzbare MWT-Solarzellenstruktur mit siebgedruckter Metallisierung entwickelt, welche die Vorteile von *n*-dotiertem Silicium mit den Vorteilen einer rückseitig kontaktierten Zellstruktur vereint. Die Effizienz der hergestellten Solarzellen steigt über mehrere Entwicklungszyklen hinweg kontinuierlich an. Die Untersuchungen beschäftigen sich vor allem mit der Rückwärtsstabilität, der Emitterdiffusion und der elektrischen Kontaktierung stark Bor-dotierter Oberflächen. Die Herausforderungen, die für einen zuverlässigen Betrieb nach Moduleinkapselung überwunden werden müssen, werden durch spezifische Untersuchungen des Verhaltens der Solarzellen unter Rückwärtsspannung aufgezeigt. Die Durchkontakte (Vias) und die rückseitigen *p*-Kontakte bilden die wichtigsten MWT-spezifischen Strukturen. Die rückseitige Kontaktanordnung konnte im Zuge detaillierter Untersuchungen optimiert und deren Herstellung vereinfacht werden. Der erreichte Wirkungsgrad für großflächige MWT-Solarzellen aus *n*-dotiertem Cz-Si beträgt 20,4%. Analytische Berechnungen zeigen ein Effizienzpotenzial von nahezu 22% für MWT-Solarzellen aus *n*-dotiertem Cz-Si bei Integration technologischer Verbesserungen auf.

Neue Rohrofen-Diffusionsprozesse werden entwickelt, um tief eingetriebene Bordotierungen mit geringer Oberflächenkonzentration in einem einzigen Prozessschritt auszubilden. Die damit hergestellten Emittoren weisen eine geringe Dunkelsättigungsstromdichte von  $(30 \pm 3) \text{ fA/cm}^2$  für eine passivierte und texturierte Oberfläche und einen Schichtwiderstand von ungefähr  $120 \Omega/\text{sq}$  auf. Trotz geringer maximaler Dotierkonzentration von nur  $(1,8 \pm 0,2) \cdot 10^{19} \text{ cm}^{-3}$  ergeben sich geringe spezifische Kontaktwiderstände kleiner  $4 \text{ m}\Omega\text{cm}^2$  für siebgedruckte und gefeuerte Metallkontakte. Erstmals wird experimentell gezeigt, dass der tiefenabhängige Verlauf der Dotierung zu einer niederohmigen Kontaktausbildung beiträgt. Diese Korrelation wird auch anhand eines analytischen Modells, welches auf Metallkristalliten beruht, demonstriert. Des Weiteren wird gezeigt, dass die Ladungsträgerrekombination unterhalb der Metallkontakte sowohl mit den Metallkristalliten als auch mit der Tiefe der Bor-Dotierprofile korreliert.

Die Fortschritte in der Emitterausbildung und das verbesserte Verständnis metallisierungsbedingter Fragestellungen sind auch für andere Solarzellentypen von besonderem Interesse. Erkenntnisse aus dieser Arbeit trugen auch grundlegend zur Weiterentwicklung der MWT-Solarzellentechnologie auf *p*-dotierten Substraten bei.



# Table of Contents

<b>1</b>	<b>Introduction</b>	<b>1</b>
1.1	Motivation and objectives .....	1
1.2	Thesis outline.....	3
<b>2</b>	<b>Fundamentals of Silicon Solar Cell Technology</b>	<b>5</b>
2.1	Introduction .....	5
2.2	Solar cell characteristics.....	5
2.2.1	Two-diode model and dark saturation current densities .....	6
2.2.2	Determination of dark saturation current densities of passivated surfaces.....	8
2.2.3	Current-voltage characteristics and cell parameters.....	13
2.3	Fundamentals of diffusion and dopant properties in crystalline silicon	16
2.3.1	Fick's law .....	17
2.3.2	Properties and diffusion of boron atoms in silicon .....	19
2.3.3	Properties and diffusion of phosphorus atoms in silicon.....	23
2.4	Metal-semiconductor contact .....	25
2.4.1	Schottky contact.....	26
2.4.2	Current transport mechanisms.....	28
<b>3</b>	<b>MWT Solar Cells: State of the Art and Transfer to n-Type Silicon</b>	<b>29</b>
3.1	Introduction .....	29
3.2	State of the art solar cell structures with front side emitter.....	29
3.2.1	H-pattern concept and others.....	30
3.2.2	Metal wrap through (MWT) concept .....	35
3.3	Ongoing development of p-type MWT technology.....	38
3.4	Processes for fabrication of n-type H-pattern solar cells .....	42
3.4.1	Basic process sequence .....	43
3.4.2	Challenges in the fabrication process and approaches .....	45
3.5	Transfer of the MWT concept to n-type silicon .....	50
3.6	Chapter summary .....	53

## Table of Contents

---

<b>4 Boron Emitter Formation and Passivation</b>	<b>55</b>
4.1 Introduction .....	55
4.2 Boron diffusion with liquid $\text{BBr}_3$ as dopant precursor .....	55
4.2.1 Principle, process sequence, and objectives .....	56
4.2.2 Samples for processes characterization .....	58
4.3 Characterization of basic diffusion processes .....	61
4.3.1 Process description and approach .....	61
4.3.2 Emitter sheet resistances .....	62
4.3.3 Doping profiles.....	65
4.3.4 Emitter dark saturation current densities .....	67
4.3.5 Impact of varied drive-in temperatures .....	69
4.4 Formation of custom-made doping profiles .....	70
4.4.1 Doping profiles with deeper junction .....	70
4.4.2 Doping profiles with lower surface dopant concentration.....	71
4.4.3 Doping profiles without surface depletion by wet-chemical etching .....	75
4.5 Identification of suitable diffusion barrier layers .....	77
4.5.1 Sample preparation.....	78
4.5.2 Results.....	79
4.6 Chapter summary .....	83
<b>5 Contacting of Boron Emitters Using Ag-Al Screen-Printing Pastes</b>	<b>85</b>
5.1 Introduction .....	85
5.2 Review on electrical contacting of boron-doped surfaces .....	85
5.3 Impact of junction depth on the specific contact resistance .....	87
5.3.1 Sample preparation.....	88
5.3.2 Specific contact resistance.....	90
5.3.3 Microstructure analysis.....	91
5.4 Analytical model for calculation of specific contact resistances .....	94
5.4.1 Approach .....	95
5.4.2 Calculation of specific contact resistances.....	97
5.4.3 Impact of the doping profile shape on the specific contact resistance .....	101
5.4.4 Discussion .....	102
5.5 Doping profiles with decreased maximum dopant concentration....	104
5.5.1 Sample preparation.....	104
5.5.2 Specific contact resistance.....	106
5.6 Charge carrier recombination at metal crystallites.....	107
5.7 Chapter summary .....	112

---

<b>6 Electrical Properties of the Backside Contacts of MWT Solar Cells</b>	<b>115</b>
6.1 Introduction .....	115
6.2 Challenges for the MWT backside contact structure.....	115
6.3 Methodology for characterization of the electrical contact behavior.118	
6.3.1 Approach and test structure fabrication .....	118
6.3.2 Procedure for current-voltage measurements .....	121
6.3.3 Leakage currents and their impact on forward current-voltage characteristics.....	121
6.3.4 Thermal power dissipation under reverse bias load.....	122
6.4 Results of the test structures for various MWT cell concepts .....	123
6.5 Study of impact factors on leakage current after reverse biasing....	130
6.6 Detailed investigation of leakage current after reverse biasing .....	133
6.7 Chapter summary .....	136
<b>7 Solar Cell Results and Loss Mechanisms</b>	<b>139</b>
7.1 Introduction .....	139
7.2 Development of the energy conversion efficiency.....	139
7.3 Impact of reverse bias load on cell characteristics.....	143
7.3.1 Cell fabrication and measurement methods .....	144
7.3.2 Current-voltage characteristics .....	147
7.3.3 Dark reverse current-voltage characteristics and dark lock-in thermography measurements I.....	149
7.3.4 Dark lock-in thermography measurements II .....	152
7.3.5 Section summary .....	155
7.4 Decrease of metallization-losses and discussion of MWT-specific issues.....	156
7.4.1 Cell fabrication and basic process characterization .....	157
7.4.2 Current-voltage characteristics .....	160
7.4.3 Implied open-circuit voltages and metallization-related voltage losses .....	163
7.4.4 Series resistance contributions and MWT-specific losses.....	166
7.4.5 Section summary .....	171
7.5 Solar cells utilizing the latest BBr <sub>3</sub> diffusion processes .....	172
7.5.1 Cell fabrication and process characterization .....	173
7.5.2 Current-voltage characteristics .....	175
7.5.3 Metallization-related voltage losses .....	180
7.5.4 Section summary .....	183
7.6 Simplified fabrication process for n-type MWT solar cells .....	185
7.6.1 Cell fabrication and process characterization .....	186

## Table of Contents

---

7.6.2 Current-voltage characteristics .....	188
7.6.3 Section summary and conclusion .....	192
7.7 Estimation of conversion efficiency potential .....	193
7.8 Chapter summary .....	195
<b>8 Summary</b>	<b>199</b>
<b>9 Outlook</b>	<b>202</b>
<b>10 Deutsche Zusammenfassung</b>	<b>203</b>
<b>Appendix</b>	<b>207</b>
A Current transport models and specific contact resistance.....	207
B Measurement and characterization methods .....	211
B.1 Current-voltage measurements of bifacial n-type solar cells....	211
B.2 Electrochemical capacitance-voltage measurement.....	214
B.3 Inductive sheet resistance measurement.....	215
B.4 Transmission line model .....	217
C Structuring methods for the rear phosphorus doping .....	218
C.1 Inkjet-assisted structuring of diffusion barrier layers .....	219
C.2 Redistribution of phosphorus doping by laser irradiation.....	220
D Parameters for calculation of series resistance contributions .....	222
<b>Bibliography</b>	<b>223</b>
<b>List of Symbols</b>	<b>249</b>
<b>List of Abbreviations</b>	<b>257</b>
<b>List of Publications</b>	<b>261</b>
<b>Danksagung</b>	<b>267</b>

# 1 Introduction

## 1.1 Motivation and objectives

Our society is more than ever confronted with the urgent need for a sustainable and ecologically-oriented power supply. In addition to limited resources of fossil fuels [1], the necessity to develop, establish, and optimize more climate-friendly energy systems is apparent. In the long term, there is no other opportunity than to transform the global energy production to sustainable raw materials and to keep on improving the energy efficiency of future high-tech products. Harvesting solar energy, which is available in virtually unlimited extent [2, p. 2], takes on a key role. Photovoltaics (PV), i.e. the direct conversion of solar energy into electrical energy, prove to be an especially indispensable technology [3]. Most of the PV module production worldwide is based on crystalline silicon solar cells (about 90% market share in 2014 [4]). A rapidly growing market is predicted [5] and technological progress is necessary to further reduce costs.

The driving force in industrial production in the past and still in the present is the *p*-type silicon solar cell with full-area aluminum back surface field [4]. After years of intensive research and development, *p*-type silicon solar cells with dielectric passivated rear side took their way into mass production within the last two years, and their market share is forecasted to gradually increase [4]. Monocrystalline *n*-type Czochralski-grown silicon (Cz-Si) [6] solar cells are also already being manufactured industrially, though only on a small scale, but a growing market share is also predicted [4]. The main advantage of *n*-type Cz-Si over *p*-type Cz-Si is that it is less sensitive to common impurities, such as e.g. iron [7], and hence allows for higher minority charge carrier diffusion lengths compared to *p*-type substrates with a similar impurity concentration. On the other hand, *p*-type Cz-Si solar cells suffer from boron-oxygen related light-induced degradation (LID). Although there are quite novel approaches to suppress this LID utilizing processes with cycle times that might be even suitable for mass

production [8,9], *n*-type Cz-Si solar cells do not suffer at all from this degradation mechanism.

Another field of intensive research activity is dedicated to solar cells in which the external contacts are located solely on the backside. The metal wrap through (MWT) concept is a member of this back contact solar cell species. It still features a metal grid on the front side, but the external front contacts are relocated to the backside by metallized vias [10]. This allows for a decrease in shaded front side area of up to 50%. The MWT concept has been studied for a long time only on *p*-type silicon, what resulted in highly efficient and very promising *p*-type MWT cell structures for industrial implementation [11–14]. In 2010, the first *n*-type Cz-Si MWT solar cells were presented [15]. To the beginning of this work in 2011, their reported maximum energy conversion efficiency was 19.7% on wafers with an industry-typical edge length of 156 mm [16]. However, until today, no comprehensive details about the specific structure of these *n*-type MWT cells or the corresponding fabrication processes have been released.

This thesis looks into these topics. It aims at obtaining in-depth knowledge regarding *n*-type MWT solar cells with front side *p-n*-junction and examines the challenges resulting from the transfer of the MWT cell concept from *p*-type to *n*-type Cz-Si. The results obtained are meant to support the PV community in their quest for further progress. This includes the development and optimization of processes and process sequences needed for fabrication of large-area passivated and high-efficient *n*-type Cz-Si MWT solar cells with screen-printed and fired contacts on pilot-line level. Main topics are the formation of the different highly doped surfaces, their simultaneous passivation, their electrical contacting, and also the MWT-specific contact separation on the backside. Furthermore, analytical calculations and numerical simulations are utilized for the interpretation of experimental data.

The chosen approach to form the boron-doped emitter and the phosphorus-doped back surface field (BSF) is based on sequential tube furnace diffusion processes with, first, boron tribromide ( $\text{BBr}_3$ ) and, second, phosphorus oxychloride as liquid dopant precursors. One focus of the process development is the optimization of  $\text{BBr}_3$  diffusion processes in terms of lowering recombination at the passivated boron-doped emitter surfaces. Furthermore, the formation of tailor-made boron doping profiles is an important topic in order to investigate metallization-related questions in more detail. Apart from investigating the interaction between metal contacts and the

junction depth of the boron doping profiles regarding contact resistivity, also charge carrier recombination below the metal contacts is examined on the basis of these tailor-made doping profiles. The results are not only relevant to *n*-type MWT solar cells, but also for solar cells in general with highly boron-doped areas. The overall currents and their spatial distributions in reverse operation with respect to module integration of solar cells are important parameters. Also the impact of reverse biasing onto the forward characteristics of the solar cells needs to be quantified.

## 1.2 Thesis outline

*Chapter 2* deals with the basics of the silicon solar cell technology. Following the description of solar cells by the two-diode model, relevant parameters describing the solar cells' performance are introduced. The properties and the diffusion of boron and phosphorus atoms in crystalline silicon are discussed, and the theory of metal-semiconductor contacts is reviewed.

*Chapter 3* first gives a detailed overview of the state of the art for relevant solar cell concepts at the beginning of this work in 2011, including the MWT concept. Then, the ongoing development in *p*-type MWT technology is discussed, as this significantly influenced the design of the *n*-type MWT solar cell structures that are introduced. Basic process sequences are elaborated for fabrication of conventional and MWT solar cells utilizing *n*-type Cz-Si as base material. This includes a detailed discussion regarding challenges that have to be overcome in general for fabrication of *n*-type Cz-Si solar cells and those in particular important for the implementation of the MWT concept.

The formation of boron emitters using liquid  $\text{BBr}_3$  as dopant precursor in high-temperature tube furnace diffusion processes is presented in *Chapter 4*. After detailed characterization of three basic diffusion processes, diverse process variations are examined. These aim at decreasing the recombination activity of the highly doped surfaces by lowering the surface doping concentration and to form boron doping profiles tailor-made for the study of certain issues. The qualification of diffusion barrier layers for the usage in sequential diffusion processes concludes the chapter.

*Chapter 5* is dedicated to the screen-printing metallization of the highly boron-doped surfaces. After reviewing existing knowledge in terms of con-

tact formation between boron-doped surfaces and fired metal pastes, the impact of the doping profile curve on specific contact resistance is examined experimentally for various scenarios. Based on microstructural analysis of the contact interface, calculations based on an analytical model support the understanding of the experimentally obtained results. Finally, charge carrier recombination below the metallized areas is modelled by numerical simulations which allow an in-depth insight into the processes prevailing at the metal-silicon interface.

The electrical properties of the external rear contact structure of MWT solar cells in the area of the vias are examined in detail in *Chapter 6* utilizing special test structures with *n*-type and *p*-type silicon bulk. The interaction between screen-printed silver paste, surface doping, surface topography, and dielectric insulation layer is examined in terms of current flow both under forward and reverse bias operation.

*Chapter 7* deals with the results obtained for fabricated *n*-type Cz-Si solar cells within the thesis period. The current flow under reverse bias load and its impact on energy conversion efficiency is examined on cell level, both for *n*-type H-pattern and for *n*-type MWT solar cells. Several process optimizations, including results from the previous chapters, and simplifications for fabrication of *n*-type MWT solar cells are dealt with. Also, MWT-specific loss mechanisms are discussed. Finally, an estimate for the energy conversion efficiency potential of *n*-type MWT solar cells is performed, which might be achieved by integration of further technological progresses.

The work concludes with the *Chapters 8* and *9*, which summarize the work at hand and give an outlook on further optimization potentials.

The *Appendix* contains further information on the current transport models for metal-silicon contacts, measuring and characterization methods for processes used for solar cell fabrication, techniques for structuring highly doped regions, and parameters for calculation of series resistance contributions on the cell level.

## **2 Fundamentals of Silicon Solar Cell Technology**

### **2.1 Introduction**

This chapter deals with the basics of silicon solar cell technology. Following the description of solar cells by the two-diode model, relevant parameters describing the solar cells' performance under forward operation are introduced. As the highly doped surface layers in this work are formed by high-temperature tube furnace diffusion processes, the fundamentals of diffusion are considered both thermodynamically and at the atomic level. This includes a review on the properties of boron and phosphorus atoms in crystalline silicon, as well as the impact of thermal oxidation on the dopant distribution. Thereafter, the theory of metal-semiconductor contacts, also known as Schottky contacts, and their current transport mechanisms are discussed.

### **2.2 Solar cell characteristics**

The most important parameter to describe the ability of a silicon solar cell—like any other solar cell made of different semiconductor material—to convert solar energy into electrical energy, is the energy conversion efficiency  $\eta$ . In principle, two basic tasks have to be met by the solar cell. Namely, first, light absorption for the generation of electrons and holes and, second, the spatial separation and transport of these generated excess charge carriers. The first point describes the optics of the cells, which is not discussed in more detail in the following, whereas in the second point the main electrical characteristics are summarized.

### 2.2.1 Two-diode model and dark saturation current densities

Essentially, the structural composition of a silicon solar cell is very similar to that of a silicon diode. Both have a *p*-type and *n*-type-doped region (also referred to as base and emitter), which are separated by a depletion region (i.e. the space-charge region). The current–voltage (*I*–*V*) characteristic of an ideal diode is based on the theory of *Shockley* [17]. Upon illumination, the following applies for the voltage-dependent current density  $j(V)$ :

$$j(V) = j_0 \left[ \exp\left(\frac{qV}{k_B T}\right) - 1 \right] - j_{ph}, \quad (2.1)$$

with elementary charge  $q$ , Boltzmann constant  $k_B$ , temperature  $T$ , and the collected photo current density  $j_{ph}$ , which is generated by the illumination. The dark saturation current density  $j_0$  of the diode summarizes the contributions of the dark saturation current density of base  $j_{0b}$  and emitter  $j_{0e}$ . Apart from radiative recombination [18,19], also Auger recombination [20], and Shockley-Read-Hall (SRH) [21,22] recombination within the bulk as well as at the surfaces are included in  $j_0$  (in case non-ideal injection dependencies can be neglected). In case of an ideal diode, these recombination losses are described by a diode ideality factor of  $n_1 = 1$ .

In practice, a solar cell does not behave like an ideal diode because of electrical losses, either caused by losses due to series resistance  $R_S$  contributions, or by leakage currents  $j_{leak}$  between the two differently doped regions (considered by shunt resistance  $R_P$ ). In addition, further SRH recombination losses occur within the space-charge region of the *p-n*-junction, and also non-ideal injection dependencies occur. This is taken into account by a more realistic description of the *I*–*V* characteristic of a solar cell by the two-diode model [23], whose equivalent circuit diagram is shown in Fig. 2.1. Apart from  $R_S$  and  $R_P$  (both quantities are used area-decoupled in the unit  $\Omega\text{cm}^2$ ), this model considers the SRH recombination in the space charge region and non-ideal recombination by the introduction of a second diode with a theoretical diode ideality factor of  $n_2 = 2$ ,

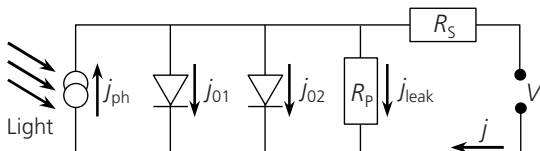


**Fig. 2.1.** Equivalent circuit diagram of the two-diode model according to Eq. (2.2).

$$j(V) = j_{01} \left[ \exp\left(\frac{q(V-jR_S)}{n_1 k_B T}\right) - 1 \right] + j_{02} \left[ \exp\left(\frac{q(V-jR_S)}{n_2 k_B T}\right) - 1 \right] + \frac{V-jR_S}{R_P} - j_{ph}. \quad (2.2)$$

The dark saturation current density  $j_{01}$  of the first diode (theoretical diode ideality factor  $n_1 = 1$ ) is equal to  $j_0$  in Eq. (2.1) under the assumption of low-level injection or uniform injection density. It is given by linear addition of the dark saturation current densities  $j_{0e}$ <sup>1</sup> and  $j_{0b}$  of the emitter and the base, respectively,

$$j_{01} = j_{0e} + j_{0b}. \quad (2.3)$$

When  $n_1 = 1$  is assumed for all injection levels in the two-diode model, all recombination from emitter and base add to  $j_{01}$  in principle, whereas injection dependencies deviating from the ideal behavior contribute to the dark saturation current density of the second diode  $j_{02}$ . This can be, e.g. the SRH recombination in the space-charge region or the injection-dependence of the SRH recombination. In practice, the diode ideality factors  $n_1$  and  $n_2$  depend on the injection level and deviate from their theoretical ideal values [24].

For the evaluation of  $j_{01}$  according to Eq. (2.3),  $j_{0e}$  and  $j_{0b}$  are needed. The experimental determination of  $j_{0e}$  will be introduced in Chapter 2.2.2, whereas the calculation of  $j_{0b}$  is now discussed. The quantity  $j_{0b}$  contains the recombination within the silicon bulk and the recombination at the rear side of the solar cell. According to Ref. [25],  $j_{0b}$  can be expressed for an  $n$ -type bulk in low-level injection as

$$j_{0b} = \frac{q D_p n_{i,eff}^2}{L_{eff} N_{bulk}}, \quad (2.4)$$

with hole diffusion coefficient  $D_p$ , effective intrinsic charge carrier concentration  $n_{i,eff}$ , effective diffusion length of the holes  $L_{eff}$ , and bulk doping concentration  $N_{bulk}$ . The effective diffusion length  $L_{eff}$  takes into account recombination within the silicon bulk and at the surfaces, and is given by [25]

$$L_{eff} = L_p \frac{1 + \frac{S_{rear} L_p}{D_p} \tanh\left(\frac{W}{L_p}\right)}{\frac{S_{rear} L_p}{D_p} + \tanh\left(\frac{W}{L_p}\right)}. \quad (2.5)$$

---

<sup>1</sup>Strictly speaking, this quantity should be referred to as  $j_{01e}$ . For simplicity, however, the 1 is omitted in the following, and  $j_{0e}$  is used instead. This also applies for  $j_{0b}$  and further parameters.

For the calculation of  $L_{\text{eff}}$ , the thickness of the silicon bulk  $W$  is correlated with the bulk diffusion length of the holes  $L_p$ , and the rear surface recombination velocity  $S_{\text{rear}}$  is included.

To obtain  $j_{0b}$  also in high-level injection, *Kimmerle et al.* [26] suggest adapting Eq. (2.4) by replacing  $N_{\text{bulk}}$  with  $(N_{\text{bulk}} + \Delta p)$  and  $D_p$  with the ambipolar diffusion coefficient  $D_{\text{amb}}$  (given in Ref. [27]). Here,  $\Delta p$  is the excess charge carrier density (holes in case of an  $n$ -type silicon bulk). Hence, the approximation to calculate  $j_{0b}$  for any injection level reads

$$j_{0b} = \frac{qD_{\text{amb}}n_{i,\text{eff}}^2}{L_{\text{eff}}(N_{\text{bulk}} + \Delta p)}. \quad (2.6)$$

For the  $n$ -type silicon solar cells investigated in this work—see e.g. the schematic cross section of the cell structure in Fig. 3.2(b)—the rear side recombination of the phosphorus-doped back surface field (BSF) is summarized in the dark saturation current density  $j_{0\text{BSF}}$ . If the value for  $j_{0\text{BSF}}$  is known,  $S_{\text{rear}}$  can be calculated in dependence of  $\Delta p$  at the rear side, and is given by [28]

$$S_{\text{rear}} = j_{0\text{BSF}} \frac{N_{\text{bulk}} + \Delta p}{qn_{i,\text{eff}}^2}. \quad (2.7)$$

As the emitter and the base are partly metallized in a final solar cell, the  $j_{0e}$  and  $j_{0b}$  can be further subdivided into contributions from the metallized and from the non-metallized areas. With the respective metallization fractions  $F_{M,e}$  and  $F_{M,b}$ , the following applies:

$$j_{0e} = j_{0e,\text{pass}} (1 - F_{M,e}) + j_{0e,\text{met}} F_{M,e}, \quad (2.8)$$

$$j_{0b} = j_{0b,\text{pass}} (1 - F_{M,b}) + j_{0b,\text{met}} F_{M,b}. \quad (2.9)$$

Here,  $j_{0e,\text{pass}}$  and  $j_{0b,\text{pass}}$  are the dark saturation current densities of the passivated (non-metallized) areas. Accordingly,  $j_{0e,\text{met}}$  and  $j_{0b,\text{met}}$  are the dark saturation current densities of the metallized areas.

## 2.2.2 Determination of dark saturation current densities of passivated surfaces

The experimental determination of the dark saturation current densities for passivated emitters  $j_{0e}$  and passivated BSFs  $j_{0\text{BSF}}$  is discussed in this section. Their determination is based on the injection-dependent measure-

ment of the effective minority charge carrier lifetimes of symmetrical lifetime samples by quasi-steady-state photoconductance measurements.

### Quasi-steady-state photoconductance measurements

The quasi-steady-state photoconductance (QSSPC) measurement technique is used to determine effective minority charge carrier lifetimes  $\tau_{\text{eff}}$  over a certain injection level range on non-metallized lifetime samples [29]. A schematic cross section of an exemplary lifetime sample is shown in Fig. 4.3(c). The QSSPC measurement principle is briefly described in the following considering an  $n$ -type silicon bulk substrate; more details can be found e.g. in Refs. [29–31].

The starting point is the continuity equation for uniform generation of electrons and holes within the sample, which is given by

$$\frac{d\Delta p(t)}{dt} = G(t) - R(t) = G(t) - \frac{\Delta p(t)}{\tau_{\text{eff}}(\Delta p)}. \quad (2.10)$$

It describes the change of the time-dependent excess charge carrier density  $\Delta p(t)$ , which depends on the generation rate  $G(t)$  and the recombination rate  $R(t)$  of electron-hole pairs. The recombination rate is defined by  $R(t) = \Delta p(t)/\tau_{\text{eff}}$ . After rearrangement of Eq. (2.10), the injection-dependent effective lifetime  $\tau_{\text{eff}}$  reads

$$\tau_{\text{eff}}(\Delta p) = \frac{\Delta p(t)}{G(t) - \frac{d\Delta p(t)}{dt}}. \quad (2.11)$$

In order to calculate  $\tau_{\text{eff}}$  quantitatively,  $G(t)$  and  $\Delta p(t)$  need to be known. The QSSPC technique offers the determination of both quantities. The most widely used QSSPC measurement tool is a system from *Sinton Instruments* (in this work, the WCT-120 [32] is used). The schematic setup of the QSSPC measuring apparatus is shown in Fig. 2.2(a). It consists of a photo-flash lamp, a red filter (not shown), a measurement chuck with an integrated high-frequency resonant circuit (shown in simplified form as coil), and a calibrated reference solar cell. The coil, with a diameter of 40 mm, is mounted directly below the sample in the center of the chuck; see also Fig. 2.2(b).

By a light flash with decreasing intensity, free charge carriers are generated, which results in a time-dependent change in conductivity  $\Delta\sigma$ . Assuming  $\Delta n = \Delta p$ , the depth-averaged excess charge carrier density  $\Delta p(t)$  is given by

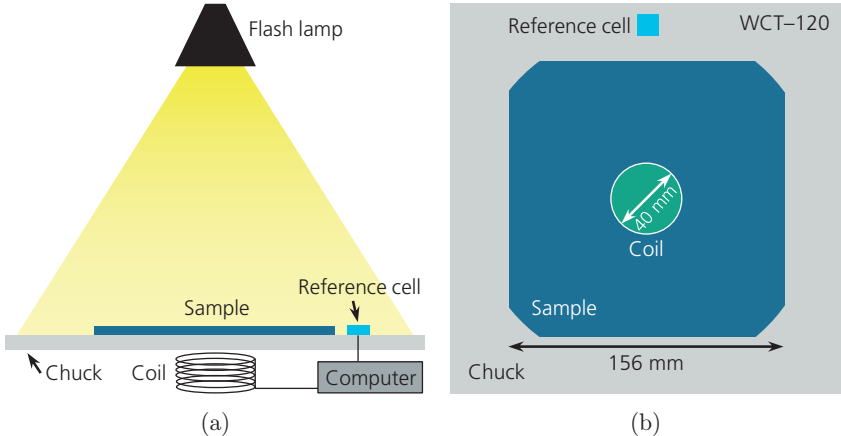


**Fig. 2.2.** (a) Schematic illustration of the QSSPC measurement setup. Due to the generation of excess charge carriers by illumination, the conductance of the sample changes. The change in conductance is measured via inductive coupling. The light intensity for the determination of the generation rate is monitored by a calibrated reference solar cell. (b) Top view on a pseudo-square wafer with 156 mm edge length on the QSSPC measurement chuck with marked coil (ratios drawn to scale).

$$\Delta p(t) = \frac{\Delta\sigma(t)}{qW(\mu_n + \mu_p)}. \quad (2.12)$$

The averaged excess charge carrier density  $\Delta p$  is linked to the change in conductivity  $\Delta\sigma$  via the charge carrier mobilities  $\mu_n$  and  $\mu_p$  of electrons and holes, respectively. The dependency of  $\mu_n$  and  $\mu_p$  on doping density and on injection level is well known from literature [32–36]. The change in conductivity  $\Delta\sigma$  is detected by the resonant circuit, by the fact that the free charge carriers in the sample couple to the electromagnetic field in the vicinity of the coil. The generation rate  $G(t)$  can be determined by using the reference cell, which measures the time-dependent flash intensity.

The determination of the effective lifetime  $\tau_{\text{eff}}$  by using Eq. (2.11) is also called the generalized analysis method, proposed by Nagel *et al.* [37]. An exemplary injection-dependent measurement of  $\tau_{\text{eff}}$  is shown in Fig. 2.3(a). Apart from that, also the quasi-steady-state and the quasi-transient analysis methods exist. Both analysis methods depend on the selection of the boundary conditions, i.e. the relationship between lifetime and decay time of the flash. To measure  $\tau_{\text{eff}}$  in the quasi-steady-state mode,  $\tau_{\text{eff}}$  must be significantly smaller than the decay time of the flash, which leads to  $d\Delta p(t)/dt = 0$ . The measure-

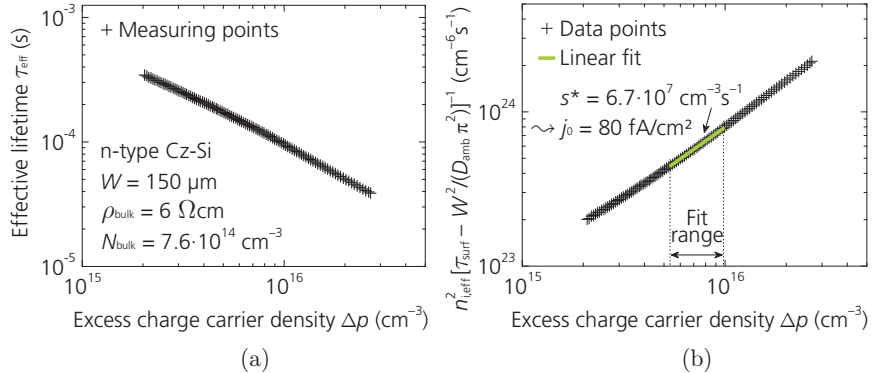


**Fig. 2.3.** (a) Injection-dependent effective minority charge carrier lifetime  $\tau_{\text{eff}}$  measured by QSSPC for a symmetrical and passivated lifetime sample with highly doped surfaces. (b) The slope  $s^*$  to determine  $j_0$  according to Eq. (2.18) is extracted in high-level injection:  $\Delta p \approx 10 \cdot N_{\text{bulk}}$ . Hence, the applied fit range is  $7.6 \cdot 10^{15} \text{ cm}^{-3} \pm 30\%$ .

ment of  $\tau_{\text{eff}}$  in the quasi-transient mode is carried out without further generation. Hence,  $\tau_{\text{eff}}$  must be significantly larger than the decay time of the flash, which leads to  $G(t) = 0$ . Both approximations lead to a simplification of Eq. (2.11). In this work, the generalized mode is used unless otherwise stated.

### Extraction of dark saturation current densities

The dark saturation current density  $j_0$  can be extracted from the injection-dependent effective minority charge carrier lifetime  $\tau_{\text{eff}}$  by quantitative evaluation of recombination losses. The determination of  $j_0$  is performed in high-level injection in this work. High-level injection means that the excess charge carrier concentration  $\Delta p$  is significantly larger than the doping concentration of the silicon bulk  $N_{\text{bulk}}$ :  $\Delta p \geq 10 \cdot N_{\text{bulk}}$ . In high-level injection, the recombination of the highly doped surface layers is dominant [38]. Hence, the bulk material utilized for  $j_0$  measurements in this work are *n*-type Czochralski-grown silicon (Cz-Si) [6] wafers with a specific bulk resistance  $\rho_{\text{bulk}} > 5 \Omega\text{cm}$ , which equals a bulk doping concentration  $N_{\text{bulk}} < 9 \cdot 10^{14} \text{ cm}^{-3}$ .

A standard method for extraction of dark saturation current densities  $j_0$  from QSSPC measurements is the so-called *slope-method* introduced by *Kane and Swanson* [39]. Recently, the corresponding analysis method has been revised and improved [40–42]. In this work, the latest analysis method as published by *Kimmerle et al.* [42] is used, which also takes finite charge

carrier diffusion into account. This method is briefly introduced in the following; refer to Ref. [42] for further details.

The starting point forms Eq. (2.7), which correlates  $j_0$  with the effective surface recombination velocity  $S_{\text{eff}}$  and is given after minor rearrangement by

$$j_0 = S_{\text{eff}} \frac{qn_{\text{ieff}}^2}{N_{\text{bulk}} + \Delta p}. \quad (2.13)$$

One method to extract  $j_0$  from  $S_{\text{eff}}$  of highly doped surface regions on symmetrical lifetime samples is to form the derivation of  $j_0$  with respect to  $\Delta p$ ,

$$j_0 = q \frac{d}{d\Delta p} (n_{\text{ieff}}^2 S_{\text{eff}}). \quad (2.14)$$

To determine  $S_{\text{eff}}$ , the surface minority charge carrier lifetime  $\tau_{\text{surf}}$  is needed, which is defined by [43]

$$\frac{1}{\tau_{\text{surf}}} = \frac{1}{\tau_{\text{eff}}} - \frac{1}{\tau_{\text{bulk}}} \quad (2.15)$$

with bulk minority charge carrier lifetime  $\tau_{\text{bulk}}$ . This corresponds to the addition of the single recombination rates. The contribution from the bulk can be further divided in shares of intrinsic ( $\tau_{\text{intr}}$ ) and SRH recombination ( $\tau_{\text{SRH}}$ ). The former contains radiative and Auger recombination. Eq. (2.15) changes to

$$\frac{1}{\tau_{\text{surf}}} = \frac{1}{\tau_{\text{eff}}} - \frac{1}{\tau_{\text{intr}}} - \frac{1}{\tau_{\text{SRH}}}. \quad (2.16)$$

For symmetrical lifetime samples, the correlation between  $S_{\text{eff}}$  and  $\tau_{\text{surf}}$  is given by the approximation [28]

$$S_{\text{eff}} = \frac{W}{2} \left( \tau_{\text{surf}} - \frac{W^2}{D_{\text{amb}} \pi^2} \right)^{-1}. \quad (2.17)$$

Inserting Eq. (2.17) in Eq. (2.14) yields

$$j_0 = \frac{1}{2} q W \frac{d}{d\Delta p} \underbrace{\left( \frac{n_{\text{ieff}}^2}{\tau_{\text{surf}} - \frac{W^2}{D_{\text{amb}} \pi^2}} \right)}_{s^*} = \frac{1}{2} q W s^*. \quad (2.18)$$

Thereby,  $s^*$  is the slope of the injection dependent part of the equation, which is determined by a linear fit; see Fig. 2.3(b). For the evaluation of  $s^*$ , the effective lifetimes  $\tau_{\text{eff}}$  are measured by QSSPC for the various  $\Delta p$ ; see Eq. (2.11) and Fig. 2.3(a). The injection dependent effective intrinsic charge carrier densities  $n_{i,\text{eff}}$  are taken into account according to the parametrization from *Sproul and Green* [44], which are adapted to *Altermatt et al.* [45] by using a prefactor of 0.9688. Therein, the band gap energy  $E_g$  and the band gap narrowing is considered according to *Green* [46] and *Schenk* [47], respectively. In Eqs. (2.4) and (2.7),  $n_{i,\text{eff}}$  is equally taken into account. Furthermore, the intrinsic lifetime  $\tau_{\text{intr}}$  is determined by the parameterization from *Richter et al.* [20]. The injection-independent contribution of  $\tau_{\text{SRH}}$  is approximated by an iterative procedure. Refer to Ref. [42] for further information on this procedure as well as the calculation of  $D_{\text{amb}}$ .

Throughout this work, the given  $j_0$  represent the dark saturation current densities of one side of the samples, as is defined in Eq. (2.18).

### 2.2.3 Current-voltage characteristics and cell parameters

The forward current-voltage ( $I$ - $V$ ) characteristics of a solar cell in the dark and under illumination are sketched in Fig. 2.4(a). During their measurement, the externally applied voltage is varied stepwise, while the current is determined for each measurement point. In case of illumination, the light absorption shifts the  $I$ - $V$  curve to negative<sup>2</sup> currents—equivalent to the generation of electrical energy. Based on the illuminated  $I$ - $V$  curve, several characteristic parameters can be extracted to describe the performance of solar cells: the short-circuit current density  $j_{\text{SC}}$ , the open-circuit voltage  $V_{\text{OC}}$ , the fill factor  $FF$ , the maximum power point (MPP), and the energy conversion efficiency  $\eta$ . See also Appendix B.1 for further information about the  $I$ - $V$  measurements performed in this work.

For determination of values for the shunt resistance  $R_p$ , the slope of the dark  $I$ - $V$  characteristics is fitted at the voltage zero point (e.g. in this work between  $-50 \text{ mV} \leq V \leq 50 \text{ mV}$ ). The inverse of the fitted slope then gives  $R_p$ .

The dark  $I$ - $V$  characteristic in semi-logarithmic depiction shows Fig. 2.4(b). Depending on the voltage, certain parameters influence the shape of the  $I$ - $V$  curve most [48,49]. Their values can be determined by fitting the two-diode

<sup>2</sup>The signs in the two-diode model (Eq. (2.2)) are chosen such that  $j_{\text{ph}}$  shifts the curve to negative currents. The curve could be represented equally in the first quadrant with positive currents.

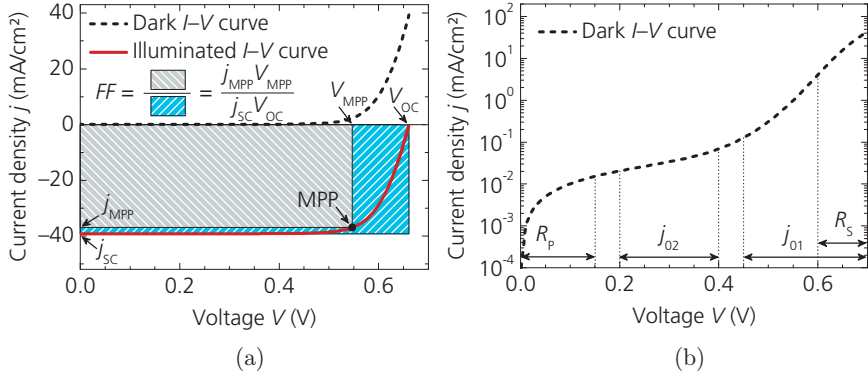


**Fig. 2.4.** (a) Current-voltage characteristics for a silicon solar cell in forward bias under both dark and illuminated condition. (b) Semi-logarithmically scaled dark  $I$ - $V$  curve in forward bias. The arrows indicate the sections from which the stated parameters can be extracted by fitting the curve with the two-diode model.

model to the curve. For instance, the influence of  $j_{01}$  dominates at  $V_{OC}$ , while  $j_{02}$  affects the  $I$ - $V$  curve particularly at lower voltages. On the other hand, the values for  $R_P$  and  $R_S$  can be extracted by a two-diode model fit for low and high voltages, respectively.

Now consider again the illuminated  $I$ - $V$  curve in Fig. 2.4(a). The short-circuit current density  $j_{SC}$  is the maximum current density of a solar cell, when no voltage is applied. Using  $V = 0$  V and by neglecting  $R_S$  ( $R_S = 0 \Omega\text{cm}^2$ ), Eq. (2.2) simplifies to:

$$j_{SC} = -j_{ph}. \quad (2.19)$$

If no current is extracted from the solar cell ( $j = 0 \text{ mA}/\text{cm}^2$ ), it is operated in open-circuit and the applied voltage is maximum. Neglecting both the recombination in the space-charge region ( $j_{02} = 0 \text{ nA}/\text{cm}^2$ ) and the occurrence of leakage currents ( $j_{leak} = 0 \text{ mA}/\text{cm}^2$ , i.e.  $R_P \rightarrow \infty$ ), the open-circuit voltage  $V_{OC}$  is given according to Eq. (2.2) to be

$$V_{OC} = \frac{k_B T}{q} \ln \left( \frac{j_{ph}}{j_{01}} + 1 \right). \quad (2.20)$$

A lower  $j_{01}$  therefore leads to a higher  $V_{OC}$ . Eq. (2.20) has to be understood as an upper limit for  $V_{OC}$  (also referred to as  $V_{OC,\text{limit}}$ ), because of the previously mentioned simplifications used to obtain this equation.

The fill factor  $FF$  describes the "squareness" of the  $I$ - $V$  curve; see Fig. 2.4(a). In other words, the  $FF$  describes the ratio of the solar cell's power at the maximum power point ( $j_{\text{MPP}}$ ,  $V_{\text{MPP}}$ ) to the product of  $j_{\text{SC}}$  and  $V_{\text{OC}}$ ,

$$FF = \frac{j_{\text{MPP}} V_{\text{MPP}}}{j_{\text{SC}} V_{\text{OC}}}. \quad (2.21)$$

The energy conversion efficiency  $\eta$  of a solar cell is defined as the ratio between maximum extractable power density  $p_{\text{MPP}}$  and the power density of the incident light  $p_{\text{STC}}$  under standard test conditions (STC),

$$\eta = \frac{p_{\text{MPP}}}{p_{\text{STC}}} = \frac{j_{\text{MPP}} V_{\text{MPP}}}{p_{\text{STC}}} = \frac{j_{\text{SC}} V_{\text{OC}} FF}{p_{\text{STC}}}. \quad (2.22)$$

The STC are described in IEC 60904-3 [50] and define the  $I$ - $V$  measurements to be performed with a specified spectrum of incident light (AM1.5G) at an irradiance of 1000 W/m<sup>2</sup> (equivalent to 1 sun), and a temperature of 25°C.

According to Green [51] it is possible, to determine the so-called ideal fill factor  $FF_0$ , which is free of losses caused by  $R_{\text{S}}$  and  $R_{\text{P}}$  contributions ( $R_{\text{S}} = 0 \Omega \text{cm}^2$ ,  $R_{\text{P}} \rightarrow \infty$ ), as well as non-ideal recombination ( $j_{02} = 0 \text{nA/cm}^2$ ). With the normalized voltage  $v_{\text{OC}} = V_{\text{OC}}/(k_{\text{B}}T/q)$ ,  $FF_0$  calculates to

$$FF_0 = \frac{v_{\text{OC}} - \ln(v_{\text{OC}} + 0.72)}{v_{\text{OC}} + 1}. \quad (2.23)$$

For example, a value of  $V_{\text{OC}} = 660 \text{ mV}$  results in  $FF_0 = 84\%$  ( $T = 25^\circ\text{C}$ ).

A further important parameter is the so-called pseudo fill factor  $pFF$ , as can be determined by *Suns*- $V_{\text{OC}}$  measurements [52]. The *Suns*- $V_{\text{OC}}$  method offers the possibility, to measure the open-circuit voltage of a solar cell over varying illumination intensity. For this purpose, the voltage of a cell is measured in open-circuit condition between a conductive chuck and contact pins on the front side (currentless measurement method). In doing so, the illumination intensity is varied with a relatively slowly decaying light pulse from a photoflash lamp, monitored by a reference cell. This varying illumination intensity leads to different injection levels within the cell, which correlate to different operating points along a pseudo  $I$ - $V$  characteristic; e.g. no illumination corresponds to the  $j_{\text{SC}}$ , whereas an illumination with 1 sun equals the  $V_{\text{OC}}$ . Is the  $j_{\text{SC}}$  known under 1 sun illumination, the pseudo  $I$ - $V$  curve can be determined from the *Suns*- $V_{\text{OC}}$  data and thus, also the  $pFF$ . This pseudo  $I$ - $V$  curve is unaffected by  $R_{\text{S}}$  losses, as no current is extracted

**Table 2.1.** Summary of some loss quantities, as introduced in this section.

Loss quantity	Loss type
$FF_0 - pFF$	Measure for $FF$ losses due to $j_{02}$ and $j_{\text{leak}}$ contributions
$pFF - FF$	Measure for $FF$ losses due to $R_S$ contributions
$iV_{\text{OC}} - V_{\text{OC}}$	Measure for $V_{\text{OC}}$ losses due to recombination at metal contacts

from the cell during the measurement sequence. Hence, the difference between  $pFF$  and  $FF$  simply corresponds to the fill factor loss due to  $R_S$  contributions [53]. Furthermore, the difference between  $FF_0$  and  $pFF$  are caused by  $j_{02}$  contributions and a finite  $R_P$  (i.e. leakage currents  $j_{\text{leak}}$ ); see also Table 2.1.

Another important parameter is the implied open-circuit voltage  $iV_{\text{OC}}$ , which can be determined by QSSPC measurements (see Chapter 2.2.2) on cell precursors prior to metallization; see e.g. Fig. 7.11 for  $n$ -type cell precursors as investigated in this work. From the excess charge carrier density  $\Delta p$  of a cell precursor with  $n$ -type bulk doping, the  $iV_{\text{OC}}$  calculates to [29]

$$iV_{\text{OC}}(\Delta p) = \frac{k_B T}{q} \ln\left(\frac{(N_{\text{bulk}} + \Delta p)\Delta p}{n_{\text{eff}}^2}\right). \quad (2.24)$$

For each illumination intensity, i.e. injection level  $\Delta p$ , an  $iV_{\text{OC}}$  can be obtained. In the  $iV_{\text{OC}}$ , all recombination effects within the silicon bulk, within the highly doped layers, and at the surfaces are taken into account. By extracting the  $iV_{\text{OC}}$  at an illumination intensity equivalent to 1 sun, the  $iV_{\text{OC}}$  represents an upper limit for the cells'  $V_{\text{OC}}$  after application of metal contacts. Hence, the difference between  $iV_{\text{OC}}$  and  $V_{\text{OC}}$  is a measure of metallization induced recombination losses, assuming that the series resistances are equally distributed across the whole cell area.

## 2.3 Fundamentals of diffusion and dopant properties in crystalline silicon

For the formation of the highly doped surface layers in the  $n$ -type solar cells investigated in this work, high-temperature diffusion processes in a tube furnace are used. As will be discussed in Chapter 3.2 in more detail, these  $n$ -type solar cells need both externally introduced boron and phosphorus dopings. The boron doping forms the emitter on the illuminated front side, while the phosphorus doping represents the phosphorus BSF on the rear side; see also Fig. 3.2(b). Following the description of diffusion as

## 2.3 Fundamentals of diffusion and dopant properties in crystalline silicon

thermodynamic process in general, the properties of boron and phosphorus atoms in crystalline silicon are reviewed. In doing so, diffusion of impurities<sup>3</sup> in silicon is also discussed on the atomic level. In addition, also the impact of thermal oxidation on boron and phosphorus diffusion is addressed.

### 2.3.1 Fick's law

Diffusion occurs if the distribution of particles is not homogenous. In this case, particles from the region with the higher particle density diffuse to the region with the lower particle concentration. This process continues until thermal equilibrium is reached. Diffusion processes can be described by *Fick's* law [54,55]. The first *Fick's* law connects the particle flux  $J$  through a unit area per unit time with the diffusion coefficient  $D$  and the gradient of the particle concentration  $N$  per unit volume,

$$J(t) = -D \frac{\partial N(x,t)}{\partial x}. \quad (2.25)$$

The dopant concentration  $N$  is a function of the location  $x$  and the time  $t$ .

Using the continuity equation (conservation of mass) and Eq. (2.25), the diffusion equation (second *Fick's* law) for spatially constant diffusion coefficients in one dimension is given by

$$\frac{\partial N(x,t)}{\partial t} = D \frac{\partial^2 N(x,t)}{\partial x^2}. \quad (2.26)$$

The diffusion coefficient of one single diffusion mechanism

$$D = D_0 \exp\left(-\frac{E_a}{k_B T}\right). \quad (2.27)$$

depends on temperature  $T$ , the maximum diffusion coefficient  $D_0$  (extrapolated to infinite temperature), and the activation energy  $E_a$ . Each diffusion mechanism has characteristic values for  $D_0$  and  $E_a$ . Furthermore,  $D_0$  and  $E_a$  can also depend on the dopant concentration. In this work, diffusion of dopant atoms (boron and phosphorus), starting from the wafer surface, is of interest for the formation of the boron emitter and the phosphorus BSF. Hence, the variable  $x$  is the distance from the wafer surface.

---

<sup>3</sup>Any foreign atoms that are not silicon atoms are referred to as impurities.

The diffusion profile of the dopant atoms results from initial and boundary conditions. Two important cases are the constant-surface-concentration diffusion and the constant-total-dopant diffusion. For the former, the dopant concentration at the wafer surface  $N_s$  is set to a constant level during the entire diffusion process. This diffusion process is also referred to as diffusion with unlimited dopant source, and the initial and boundary conditions are:

$$N(x,0) = 0, \quad (2.28)$$

$$N(0,t) = N_s, \quad (2.29)$$

$$N(\infty,t) = 0. \quad (2.30)$$

The resulting diffusion profile is then given by the solution of the diffusion equation (Eq. (2.26)), namely by

$$N(x,t) = N_s \operatorname{erfc} \left( \frac{x}{2\sqrt{Dt}} \right), \quad (2.31)$$

where  $\operatorname{erfc}$  is the complementary error function [55, pp. 457–458], and  $\sqrt{Dt}$  is the diffusion length of the impurities. Exemplary diffusion profiles for the constant-surface-concentration condition with different diffusion times, according to Eq. (2.31), are shown in Fig. 2.5(a). Thereby,  $D$  is fixed for a given diffusion temperature. The dopants penetrate the deeper into the silicon the longer the diffusion time.

For the second case, the constant-total-dopant diffusion, a fixed amount of dopant is deposited onto the silicon wafer surface, and the dopant subsequently diffuses into the silicon. This diffusion process is also referred to as diffusion with limited dopant source. The initial condition and one of the boundary conditions are the same as given in Eqs. (2.28) and (2.30), respectively. The other boundary condition is

$$\int_0^{\infty} N(x,t) dx = Q_{\text{tot}}, \quad (2.32)$$

with the total dose of dopant  $Q_{\text{tot}}$  per unit area. In this case, the Gaussian distribution is a solution for the diffusion equation (Eq. (2.26)),

$$N(x,t) = \frac{Q_{\text{tot}}}{\sqrt{\pi Dt}} \exp \left( -\frac{x^2}{4Dt} \right). \quad (2.33)$$

As the dopant diffuses into the silicon, the surface dopant concentration  $N_s$  must decrease, in order to keep the total dopant dose  $Q_{\text{tot}}$  constant; see

## 2.3 Fundamentals of diffusion and dopant properties in crystalline silicon

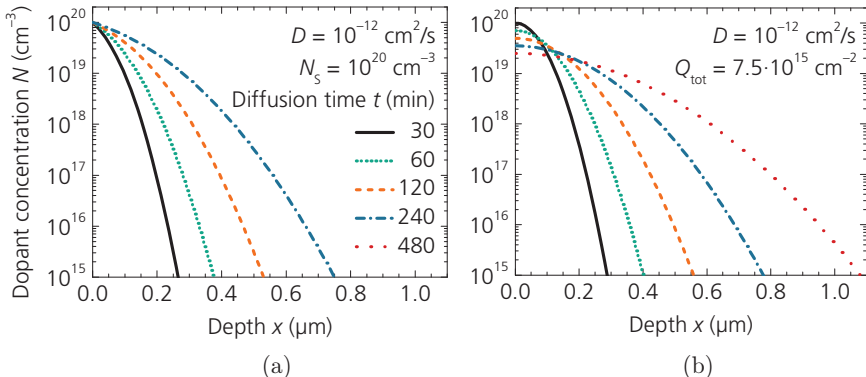


**Fig. 2.5.** Exemplary development of dopant concentration  $N$  as function of depth  $x$  with increasing diffusion time  $t$  for (a) an unlimited dopant source, and (b) a limited dopant source. The curves are calculated according to (a) Eq. (2.31) and (b) Eq. (2.33) using the stated parameters.

Fig. 2.5(b). Once again, the dopants penetrate the deeper into the silicon the longer the diffusion time.

### 2.3.2 Properties and diffusion of boron atoms in silicon

Boron atoms occupy predominantly substitutional sites in the silicon lattice [56,57]. As boron atoms act as acceptors, a hole is introduced into the valence band. The ionization energy of substitutional boron is found to be approximately 0.04 eV [58, p. 337].

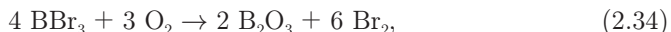
On an atomistic scale, the diffusion of impurity atoms is attributed to a diffusion of the substitutional impurities either interacting with vacancies or with interstitial silicon (also known as self-interstitials<sup>4)</sup> [59–65]. Vacancies can be caused by, e.g. vibrations of the lattice atoms around their equilibrium lattice sites at elevated temperatures. Thereby, the lattice atom can acquire sufficient energy to leave its lattice site and to become an interstitial atom. A nearby substitutional impurity atom may change its lattice site with the vacancy and thus, migrate to the vacancy site. This diffusion mechanism is referred to as vacancy-assisted diffusion. On the other hand, the interstitial diffusion mechanism can be explained as follows: a substitutional impurity and an interstitial silicon atom change their sites

<sup>4</sup>Interstitial sites, which contain only atoms of the same species as those already present in the host lattice, are referred to as self-interstitials.

(also referred to as kick-out mechanism), which results in a substitutional silicon and an interstitial impurity atom. Then, the interstitial impurity atom diffuses until it changes again its lattice site with a substitutional silicon atom by kick-out. Thereby, the impurity atom becomes again substitutional, whereas the silicon atom becomes likewise interstitial. This diffusion mechanism of impurities, which involves self-interstitials and the kick-out mechanism, is referred to as interstitial-assisted diffusion. Also a mixture of both diffusion processes, vacancy and interstitial diffusion, is possible.

The diffusion of boron in silicon was initially attributed to both diffusion via vacancies [59], and diffusion via self-interstitials [60]. However, recent studies state that boron diffusion in crystalline silicon dominantly occurs via self-interstitials, and hence is mediated by the interstitial diffusion mechanism [61,62,65].

In this work, the boron diffusion is performed in a tube furnace with boron tribromide ( $\text{BBr}_3$ ) as liquid dopant precursor; see Chapter 4.2 for further technical information. The  $\text{BBr}_3$  diffusion is a very complex oxidation-diffusion process, in which the deposition of the dopant source onto the silicon surface and the diffusion of the dopants into the silicon bulk proceed simultaneously [66]. In a preliminary chemical reaction,  $\text{BBr}_3$  and oxygen ( $\text{O}_2$ ) form boric oxide ( $\text{B}_2\text{O}_3$ ) and bromine ( $\text{Br}_2$ ),



wherein the  $\text{B}_2\text{O}_3$  condenses on the silicon surface. The reaction of oxygen and silicon leads to both the formation of silicon dioxide ( $\text{SiO}_2$ )<sup>5</sup> at the interface as well as some interstitial silicon atoms,



Both, the  $\text{B}_2\text{O}_3$  and the  $\text{SiO}_2$  mingle and form the borosilicate glass (BSG), which then serves as the dopant source. Elemental boron (B) and  $\text{SiO}_2$  result from the reaction of the  $\text{B}_2\text{O}_3$  within the BSG and the silicon at the interface,



In general, the diffusion of impurity atoms in silicon correlates with their interaction with point defects, as previously discussed. Hence, an increase in point defect concentration will affect the diffusion characteristics of im-

<sup>5</sup>During the thermal oxidation process, silicon is consumed and the  $\text{Si}/\text{SiO}_2$  interface moves into the silicon. Thereby, 44% of the resulting  $\text{SiO}_2$  layer thickness was formerly silicon [55, p. 372].

## 2.3 Fundamentals of diffusion and dopant properties in crystalline silicon

purity atoms. One of the best known examples of this is the so-called oxidation-enhanced diffusion of impurities in silicon [67,68]. As the name suggests, oxidation thereby plays the crucial role. Due to thermal oxidation of the silicon surface, a large number of additional self-interstitials is introduced into the silicon promoting the impurity diffusion. This means that in strongly oxidizing atmosphere, the boron atoms move faster into the silicon, resulting in a deeper doping profile compared with a boron diffusion performed with less oxygen content. Furthermore, it has been shown that boron diffusion coefficients depend apart from temperature also on the boron doping concentration [65,69–71]. The boron diffusion coefficient is reported to be essentially constant for boron dopant concentrations below  $10^{19} \text{ cm}^{-3}$ , while an increase towards larger dopant concentrations is observed.

Additionally, thermal oxidation processes lead to redistribution of boron atoms at the silicon surface; see Fig. 2.6(a). As the segregation coefficient

$$k = \frac{\text{equilibrium concentration of impurity atoms in silicon}}{\text{equilibrium concentration of impurity atoms in } \text{SiO}_2} \quad (2.37)$$

for boron is lower than 1 ( $k \approx 0.3$  [72]), the solubility of boron is higher in  $\text{SiO}_2$  than in silicon. Hence, the boron concentration in the silicon is reduced close to the surface (hereafter referred to as doping depletion zone). Just the opposite is true for phosphorus. Its solubility in  $\text{SiO}_2$  is lower ( $k \approx 10$  [72]), and therefore results in an increase in the phosphorus concentration at the surface; see Fig. 2.6(b). The diffusion rates for both impurities are low in the  $\text{SiO}_2$  layer.

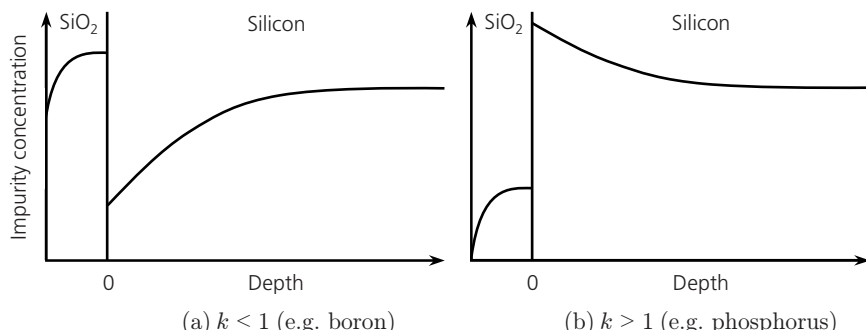


**Fig. 2.6.** Schematic illustration of impurity redistribution in silicon due to thermal oxidation (redrawn from Ref. [72]). For both illustrated cases, the diffusivity of the impurities is low in the  $\text{SiO}_2$  layer.

In order to act as acceptors and thus, to release a hole into the valence band, the boron atoms must be incorporated into the silicon lattice in electrically active state. For this purpose, the solubility of substitutional boron in silicon is the crucial parameter; see Fig. 2.7. The higher the maximum temperature, the more boron can be dissolved in silicon in substitutional form. For boron atoms, a differentiation between active and inactive dopants is not known. However, due to incomplete ionization, not all boron/phosphorus atoms might release a hole/electron even at room temperature and contribute to the charge carrier concentration for the doping concentration interval between  $\approx 10^{17} \text{ cm}^{-3}$  and  $\approx 10^{19} \text{ cm}^{-3}$  [75]. The magnitude of this effect for typical doping profiles in this thesis is similar to the relevant measurement accuracy. Hence, incomplete ionization is of minor importance. In case the boron concentration is higher than the solubility limit, a boron rich boundary layer of silicon boride compounds ( $\text{SiB}_{4-6}$ ) forms particularly at the silicon surface; also known as boron rich layer (BRL) [66,76–79]. Obviously, the solubility of boron in solid silicon is significantly lower than that of phosphorus. This means that for boron diffusion, higher temperatures are necessary in order to obtain comparable doping levels and profile depths, since the diffusion coefficients of boron and phosphorus atoms differ not more than by about a factor of two [80, p. 33].

The determination of doping profiles is the key for process characterization and process development. The total impurity concentration—the dopant can be both electrically active and inactive—can be measured by secondary ion mass spectroscopy (SIMS) [31, pp. 102–103]. Another measurement

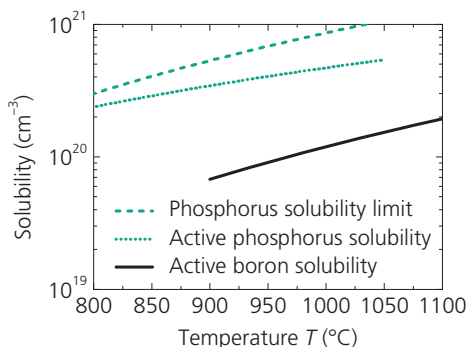


**Fig. 2.7.** Solubility limit for active and inactive phosphorus as well as active boron in crystalline silicon as function of the temperature for thermal diffusion processes (active means that the dopants are incorporated substitutional). The data for the graph are taken from Refs. [73,74].

## 2.3 Fundamentals of diffusion and dopant properties in crystalline silicon

---

method is the electrochemical capacitance-voltage (ECV) technique, which determines the charge carrier density [81]. See Appendix B.2 with respect to the ECV measurement principle. Hence, the dopant concentration of electrically active boron (and phosphorus) can be extracted by the ECV method. If only electrically active dopants are present in the sample to be measured, SIMS and ECV measurements are in very good agreement [81,82].

The presence of a BRL after boron diffusion is very undesirable, as it leads to both a decrease in bulk lifetime of the silicon wafers [79], and to an increase in surface recombination [83,84]. On the other hand, the BRL is proven to be very effective in gettering iron impurities [84]. Additionally, the BRL itself acts as dopant source during the diffusion process [76]. This means when a BRL is present, the boron concentration within the BRL mainly controls the diffusion process. Furthermore, it has been reported that boron diffusion processes with conditions giving rise to the formation of a BRL are more reproducible [76]. Without a BRL, the reproducibility and uniformity depend mainly on the  $\text{BBr}_3$  and  $\text{O}_2$  concentration in the tube; see Eq. (2.34). That is why the formation of a BRL during the diffusion process is initially tolerated very often. In these cases, the BRL is removed after the diffusion process. This is, however, not possible in hydrofluoric acid (HF). The only mean to remove the BRL is oxidation, as e.g. in boiling nitric acid ( $\text{HNO}_3$ ) [76,84], or by thermal oxidation [85,86]. Apart from thermal oxidation of the BRL in a subsequent process step, also the incorporation of the thermal oxidation of the BRL at the end of the diffusion process, while the BSG is still present, is possible. This option is used in this work to avoid the presence of a BRL after the boron diffusion process utilizing  $\text{BBr}_3$ , and is referred to as post-oxidation in the following. However, in case of iron gettering within the BRL, its thermal oxidation leads to a release of the gettered iron atoms back into the silicon bulk. In order to completely prevent the formation of a BRL during the diffusion process, the ratio of the process gases, in particular the  $\text{O}_2/\text{BBr}_3$  ratio, is of utmost importance [87].

### 2.3.3 Properties and diffusion of phosphorus atoms in silicon

Just like boron atoms, also phosphorus atoms occupy predominantly substitutional sites in the silicon lattice up to a certain doping concentration [56]. As phosphorus atoms act as donors, an electron is introduced into the conduction band. The ionization energy of substitutional phosphorus is also found to be approximately 0.04 eV [58, p. 390].

For phosphorus, two solubility limits exist as Fig. 2.7 shows. Below the active solubility limit, all phosphorus atoms are dissolved in substitutional form. If the phosphorus concentration exceeds the active solubility limit, the phosphorus atoms are no longer dissolved substitutional and are thus electrically inactive. For even higher phosphorus concentrations, the solubility limit specifies from which concentrations phosphorus is bonded in silicon-phosphorus precipitates.

The curve progression in Fig. 2.8 is characteristic for a phosphorus doping profile. As the diffusion of phosphorus in silicon depends on two different diffusion mechanisms, two typical sections can be distinguished in the doping profile: the so-called kink and tail. This is because the dominating diffusion mechanism for each section depends on the doping concentration.

For concentrations of up to  $\approx 5 \cdot 10^{19} \text{ cm}^{-3}$ , phosphorus diffuses mainly via the interstitial diffusion mechanism [62,64]. For phosphorus concentrations exceeding  $5 \cdot 10^{19} \text{ cm}^{-3}$ , this diffusion mechanism becomes ineffective due to finite interstitial concentration and the diffusion via double negatively charged vacancies is dominant [64,89]. As their energy level is 0.11 eV below the conduction band energy, a high Fermi level and thus, a high doping concentration are necessary so that the diffusion mechanism via vacancies prevails. This can be the explanation for the onset of vacancy diffusion for a doping concentration of  $5 \cdot 10^{19} \text{ cm}^{-3}$ . The characteristic kink and tail curve progression is explained by Bentzen [64, pp. 51–69] as follows: due to very limited kick-out processes at high doping concentrations, the surface-near and highly doped part of the profile diffuses much slower than the deeper and less doped part. The kink designates the area with the

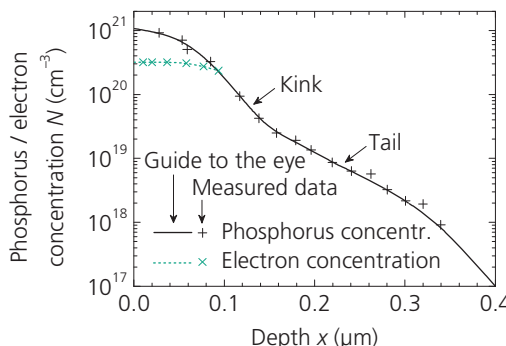


**Fig. 2.8.** Exemplary illustration of a phosphorus doping profile from a  $\text{POCl}_3$  source with both total phosphorus and electron concentration (redrawn from Ref. [88]).

strongest drop in the phosphorus concentration, while the tail describes the deeper section with a shallower gradient.

As the boron diffusion, also the phosphorus diffusion is performed in a tube furnace in this work. As dopant source, liquid phosphorus oxychloride ( $\text{POCl}_3$ ) is used. The process sequence for  $\text{POCl}_3$  diffusion is basically the same as for  $\text{BBr}_3$  diffusion. The latter will be discussed in more detail in Chapter 4.2.1. The  $\text{POCl}_3$  diffusion is likewise a very complex oxidation-diffusion process. In the preliminary chemical reaction,  $\text{POCl}_3$  and  $\text{O}_2$  form phosphorus pentoxide ( $\text{P}_4\text{O}_{10}$ ) on the silicon surface and chlorine ( $\text{Cl}_2$ ) [90, p. 297],



It also forms  $\text{SiO}_2$  on the silicon surface, which mixes with the  $\text{P}_4\text{O}_{10}$ . This mixture represents the phosphosilicate glass (PSG). Subsequently, the chemical reaction between  $\text{P}_4\text{O}_{10}$  within the PSG and silicon at the interface leads to the formation of elemental phosphorus (P) and  $\text{SiO}_2$ ,



As already mentioned in the previous section, thermal oxidation processes lead to an increase in phosphorus concentration at the surface; see Fig. 2.6(b). With a segregation coefficient of  $k \approx 10$  [72], the solubility of phosphorus is higher in silicon than in  $\text{SiO}_2$ . Thus, phosphorus doping profiles do not feature a doping depletion zone at the surface. Oxidation-enhanced diffusion also leads to an increase of the diffusion rate for phosphorus atoms. By incorporation of thermal oxidation into the  $\text{POCl}_3$  diffusion process, it is furthermore possible, to realize phosphorus doping profiles without presence of electrically inactive phosphorus near the surface [91,92].

## 2.4 Metal-semiconductor contact

For the *n*-type solar cells dealt with in this work, the contact resistivity of front and rear side metallization to the underlying highly doped silicon plays an important role. With values in the range of a few  $\text{m}\Omega\text{cm}^2$  per wafer side, the specific contact resistance  $\rho_c$  is not negligible for screen-printed metallization. This section provides a brief overview of metal-semiconductor contacts in general and discusses the different current transport mechanism in a metal-semiconductor contact. The theoretical calculation of  $\rho_c$  is dealt with in Appendix A.

### 2.4.1 Schottky contact

The ideal contacting of solar cells consists of an ohmic contact with negligible  $\rho_C$ , which also does not degrade the cell performance. The ohmic contact is characterized by a linear  $I$ - $V$  characteristic both for positive and negative voltages.

However, *Schottky* discovered in 1938 that metal-semiconductor contacts have a rectifying behavior, as a potential barrier formed in between the two materials [93–95]. This potential barrier is called the Schottky barrier. Since then, a metal-semiconductor contact is also referred to as a Schottky contact. Following *Schottky's* discovery, many works have been devoted to metal-semiconductor contacts in order to further develop their understanding and the underlying theoretical models, as e.g. in Refs [96–104]. A comprehensive review of the models describing metal-semiconductor contacts is given, e.g. by *Schroder* and *Meier* [105] as well as by *Rhoderick* and *Williams* [106]. In the following, the aspects relevant for screen-printed metal contacts and silicon are briefly discussed.

After joining metal and semiconductor, the Fermi energies  $E_F$  of both materials align themselves due to electron flow from the material with the higher  $E_F$  to the material with the lower  $E_F$ . This leads to a bending of the energy band in the semiconductor right on the metal-semiconductor interface, as illustrated for an *n*-type and a *p*-type semiconductor in Fig. 2.9(a) and (b), respectively. Due to the band bending, the Schottky barrier height  $q\phi_b^6$  is present at the contact interface, which is

$$q\phi_b = \begin{cases} q\phi_m - q\chi_s & (\text{n-type doping}) \\ E_g - (q\phi_m - q\chi_s) & (\text{p-type doping}) \end{cases}, \quad (2.40)$$

for an ideal metal-semiconductor contact with energy band gap  $E_g$  of the semiconductor. Note that  $q\phi_b$  is not dependent on doping density, i.e. is not dependent on the position of  $E_F$  within the bandgap. The metal work function  $q\phi_m$  and the semiconductor work function  $q\phi_s$  represent the energy necessary to excite an electron from the Fermi level  $E_F$  to the vacuum level. The electron affinity  $q\chi_s$  equals the energy difference between the conduction band edge  $E_C$  of the semiconductor and the vacuum level.

---

<sup>6</sup>In literature, both  $q\phi_b$  (in eV) and  $\phi_b$  (in V) are referred to as the Schottky barrier height.

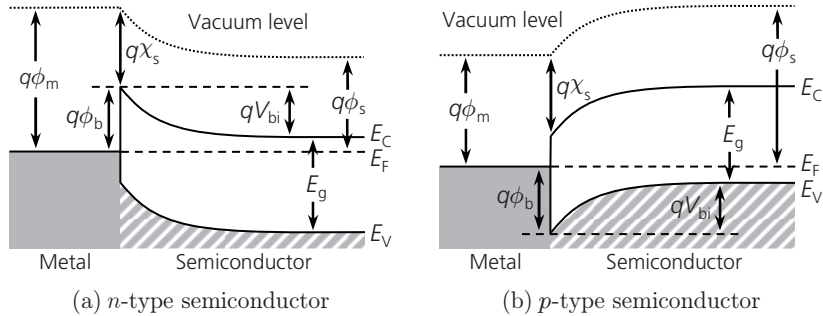


**Fig. 2.9.** Energy band diagrams of metal-semiconductor contacts in thermal equilibrium for an (a) *n*-type and a (b) *p*-type doped semiconductor.

The built-in potential  $V_{bi}$  has to be overcome either by electrons in the conduction band or by holes in the valence band when moving into the metal,

$$qV_{bi} = \begin{cases} q\phi_b - (E_C - E_F) & (\text{\textit{n}-type doping}), \\ q\phi_b - (E_F - E_V) & (\text{\textit{p}-type doping}), \end{cases} \quad (2.41)$$

with the energy of the valence band edge  $E_V$  of the semiconductor.

Fig. 2.10 shows measured  $q\phi_b$  for various metals on *n*-type and *p*-type silicon. As predicted by Eq. (2.40),  $q\phi_b$  increases with increasing  $q\phi_m$  for *n*-type silicon, whereas  $q\phi_b$  decreases with increasing  $q\phi_m$  for *p*-type silicon. However, the dependence of  $q\phi_b$  from  $q\phi_m$  is much less pronounced as expected from Eq. (2.40). This is because surface states at the interface located within the forbidden band gap act as donors or acceptors in practical metal-

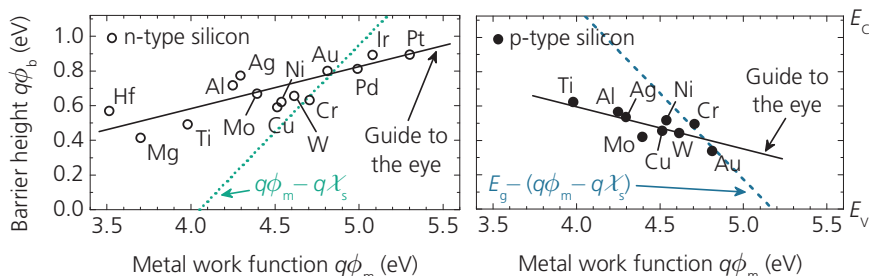


**Fig. 2.10.** Measured Schottky barrier heights  $q\phi_b$  on *n*-type and *p*-type silicon as function of the metal work function  $q\phi_m$  for various evaporated metals (redrawn from Ref. [105]). The dotted lines represent Eq. (2.40) with  $E_g = 1.1242$  eV [107], and  $q\chi_s = 4.05$  eV [108, p. 275].

semiconductor contacts, as first shown by Bardeen [98]. These surface states are not considered in the theory for ideal Schottky contacts, but influence the determination of  $q\phi_b$  quite considerably.

Another effect which occurs in practical metal-semiconductor contacts is the lowering of  $q\phi_b$  due to image forces, when an electrical field is present; see Appendix A.

### **2.4.2 Current transport mechanisms**

Depending on charge carrier concentration  $N$  of the semiconductor and on temperature  $T$ , three different current transport mechanisms via charge carrier (tunneling) flow have been proposed for metal-semiconductor contacts [103–105,109], namely thermionic emission (TE), thermionic field emission (TFE), and field emission (FE). Fig. 2.11 illustrates these current transport mechanisms for an  $n$ -type doped semiconductor, for which electrons are the majority charge carriers. These emission mechanisms also apply to a  $p$ -type doped semiconductor, but then holes represent the majority charge carriers and the Schottky barrier is present in the valence band; see Fig. 2.9(b). For TE in Fig. 2.11(a), the charge carriers are exclusively thermally excited over the potential barrier. In case of TFE for somewhat higher  $N$ , Fig. 2.11(b), the charge carriers can cross the potential barrier by a combination of thermal excitation and quantum mechanical tunneling. For even higher  $N$ , Fig. 2.11(c), FE becomes dominant and the charge carriers can directly tunnel through this case quite thin potential barrier. Refer to Appendix A for further details about the theoretical calculation of specific contact resistances  $\rho_C$  for the different current transport mechanisms.

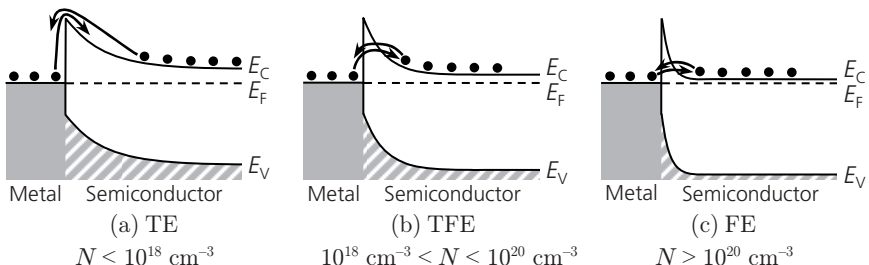


**Fig. 2.11.** Schematic illustration of current transport mechanisms between metal and  $n$ -type semiconductor in dependence on the semiconductor charge carrier concentration  $N$ : (a) thermionic emission (TE), (b) thermionic field emission (TFE), and (c) field emission (FE). The stated values for  $N$  refer to  $T = 300$  K, and serve as a rough reference point. Image force barrier lowering is not taken into account.

## **3 MWT Solar Cells: State of the Art and Transfer to n-Type Silicon**

### **3.1 Introduction**

First, the state of the art in solar cell technology at the beginning of this work (in 2011) is discussed. This review includes large-area monocrystalline *p*-type and *n*-type silicon solar cells with thermally diffused front-side emitter and screen-printed metallization. The benefits and challenges of different cell concepts, such as the H-pattern or the metal wrap through (MWT) approach, are also covered. Subsequently, the ongoing development in *p*-type MWT technology as of 2012 is briefly presented; also results from this work contributed to this significantly. The achieved improvements for *p*-type MWT solar cells influenced the selection of the structural design of the *n*-type MWT solar cells to be developed within this work. The remaining part of the chapter deals with the development of process sequences for fabrication of *n*-type Cz-Si H-pattern and *n*-type Cz-Si MWT solar cells with front-side boron emitter and rear-side phosphorus doping. Starting with the introduction of a basic process sequence for *n*-type H-pattern solar cells, the challenges that have to be overcome in fabrication of such devices are discussed. These challenges are then examined in more detail starting in Chapter 4. Following the presentation of individual processes, the transfer and the implementation of the MWT structure to and on *n*-type Cz-Si is in focus. The cell structures introduced for possible *n*-type MWT solar cells form the fundament of the development of the *n*-type MWT technology in the further course of this work.

### **3.2 State of the art solar cell structures with front side emitter**

The present work deals with the development of monocrystalline *n*-type Cz-Si solar cells featuring a thermally diffused front-side emitter and

screen-printed metallization grids on both sides of the wafer. The following two sections expound the relevant state of the art in science and technology of such or similar solar cell types on *p*-type and *n*-type silicon with a wafer edge length  $\geq 125$  mm, utilized at the beginning of this work in the year 2011—both for research and for industrial production.

### 3.2.1 H-pattern concept and others

The world's most widespread crystalline silicon solar cell concept in industrial production—in 2011 and still to date [4]—is the very mature *p*-type silicon H-pattern structure with aluminum back surface field (Al-BSF) [48]; see Fig. 3.1. Typically, the *p*-type silicon wafer is doped with boron atoms, whereas the *n*-type front side emitter is doped with phosphorus atoms. The latter is mainly realized by a thermal tube furnace diffusion process using phosphorus oxychloride ( $\text{POCl}_3$ ) as liquid dopant precursor. The light trapping on the cell's front side is enhanced by a textured surface and a silicon nitride ( $\text{SiN}_x$ ) layer acting as an antireflection coating, and also serving as a passivation layer. The front- and rear-side contacts are applied by screen printing, what is the most commonly used metallization technology [4]. During a high temperature process in a fast firing oven, the rear aluminum contact alloys into the *p*-type-doped base creating a highly *p*-type-doped layer, the so-called Al-BSF. Simultaneously, the contact formation takes place between emitter and front side metallization—consisting of a screen-printed paste with silver as conductive component [49,110,111]. The basic ingredients of such a screen-printing silver paste, beside the metal powder, are glass frits and organic components such as binders, solvents, and additives. During the firing process, the solvents and binders are burned off at temperatures up to  $550^\circ\text{C}$ . Above this temperature, the glass frits become liquid, etch the  $\text{SiN}_x$  layer, and form a glass layer at the silicon surface by oxidation of the silicon. The silver powder dissolves and sinters into a compact structure. During rapid cooling from the peak firing

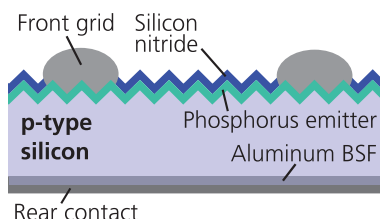


**Fig. 3.1.** Schematic cross section of a *p*-type H-pattern Al-BSF solar cell structure.

temperature in the range of  $800^{\circ}\text{C}$  to room temperature, epitaxial silver crystallite growth into the silicon surface occurs. The sintered silver bulk is separated from the silicon by the thin glass layer with embedded silver particles. The glass layer ensures the mechanical adhesion to the substrate. Especially direct current paths via silver crystallites, which connect the silicon and the silver bulk, are assumed to be responsible for low specific contact resistance [110,112]. The metallization grid consists of contact fingers with a width of  $w_t \leq 90 \mu\text{m}$  [113], and typically 1.5 mm wide straight or tapered external busbar contacts. The thickness of the silicon wafers is  $W \approx 180 \mu\text{m}$  [113]. The name “H-pattern” originates from the fact that the busbars are applied perpendicular to the fingers and thus the grid layout is reminiscent of the letter “H”. The achieved energy conversion efficiencies  $\eta$  for these cells are about between 17% and 19% [113,114].

In 1989, *Blakers et al.* proposed a solar cell structure on *p*-type silicon with dielectric rear side passivation between full-area aluminum contact and silicon base—the so-called passivated emitter and rear cell (PERC) [115]; illustrated in Fig. 3.2(a). The passivation layer—which can be silicon dioxide ( $\text{SiO}_2$ ) [116–118,11] or aluminum oxide ( $\text{Al}_2\text{O}_3$ ) [116,117,119]—has to be protected from the screen-printed aluminum layer during the firing process by an intermediate  $\text{SiN}_x$  layer. The electrical contacting of the base is realized with local contacts. Therefore, either the passivation layer stack is opened prior to metallization [120,121] and local aluminum contacts form during the firing process, or laser-alloying is used to form the local contacts after metallization and firing [122,123]. The rear side passivation of the PERC concept includes two advantages over the Al–BSF structure. On the one hand, the internal re-

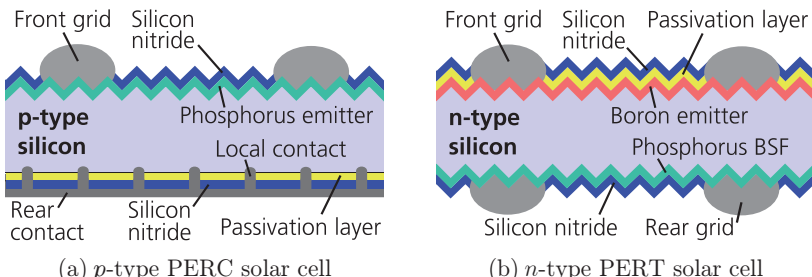


**Fig. 3.2.** Schematic cross sections of H-pattern solar cell structures: (a) *p*-type PERC and (b) *n*-type PERT. The front side of the *p*-type PERC concept resembles that of the front side of the Al–BSF cell, with the only difference being the rear side passivation. Furthermore, the rear side of the *n*-type PERT solar cell has the same structure as the front side of the *p*-type PERC device.

flection is significantly increased compared with alloyed aluminum, on the other hand, the surface recombination velocity is significantly lowered [116]. For those *p*-type PERC cells, pilot-line conversion efficiencies up to 20.2% have been reported in 2011 [124,125]. However, there is no industrial mass production of this cell type at this time. The rear surface passivation results in a conversion efficiency boost of  $\Delta\eta \approx 1\%_{\text{abs}}$  compared with Al–BSF cells [116].

However, one major drawback of boron-doped *p*-type Cz-Si is that it suffers from light-induced degradation (LID), as boron-oxygen complexes are activated upon illumination resulting in a reduction of the minority charge carrier lifetime [126,127]. The presence of oxygen in Cz-Si cannot be avoided due to its manufacturing process [128, pp. 23–32]. The conversion efficiency of solar cells in the degraded state (activated boron-oxygen complexes) can be lower by up to 10%<sub>rel</sub> than in the annealed state (deactivated boron-oxygen complexes) [129]. To overcome, or at least, decrease the detrimental impact of LID in Cz-Si, the number of boron-oxygen complexes needs to be reduced. This can be achieved by using alternative substrate materials. One option is boron-doped Cz-Si grown by the magnetic-field-assisted Cz method [130], in which significantly less oxygen is present [129,131]. However, it is much more expensive and has not yet been produced on a large scale in industrial production. Another option is to replace boron with gallium [129,131]. Unfortunately, gallium has an extremely low segregation coefficient<sup>7</sup> in silicon resulting in a very large resistivity variation along the ingot height and thus, to a low production yield. A third option is to transform the highly recombination active state of the boron-oxygen complexes into a non-recombination active, so-called regenerated state [133]. This regenerated state is stable under illumination. However, the duration of the process needed for a complete transformation is in the range of tens of minutes up to some hours. A fourth option is to replace boron with phosphorus resulting in an *n*-type-doped silicon crystal. This *n*-type Cz-Si is not only insensitive to boron-oxygen related LID [126,129], but is also less sensitive to common metal impurities—such as iron—compared with *p*-type doped Cz-Si due to the asymmetric capture cross sections of their defects for electrons and holes (mostly high hole lifetime and low electron lifetime) [7]. Hence, in principle, solar cells made of *n*-type silicon have a higher energy conversion efficiency potential.

---

<sup>7</sup>The segregation coefficient  $k$  describes the relation between the impurity atom concentration in the growing silicon crystal and in the silicon melt. Typically,  $k$  is lower than 1, as e.g. in silicon:  $k(\text{boron}) = 0.8$ ,  $k(\text{phosphorus}) = 0.35$ , and  $k(\text{gallium}) = 0.008$  [132].

By substituting the *p*-type base material with *n*-type silicon for H-pattern solar cells with front side emitter, the cell structure has to be significantly changed. Fig. 3.2(b) depicts the *n*-type counterpart to the *p*-type PERC cell, namely the *n*-type passivated emitter rear totally diffused (PERT) concept. This *n*-type H-pattern cell concept is often referred to as a bifacial cell, as the rear side metallization has an open structure, allowing light to also penetrate the cell from that side. The phosphorus doping in this case no longer forms the emitter; instead it forms the back surface field (BSF). The emitter is boron-doped and is usually passivated with a  $\text{SiO}_2$  layer [134]. An even improved passivation might be achieved with an  $\text{Al}_2\text{O}_3$  layer [135], however, its use is still not very widespread. The overlying  $\text{SiN}_x$  layer again serves as antireflection coating. One option to realize the two different highly doped surfaces is their simultaneous formation within a single high-temperature step, the so-called “*co-diffusion*” [136]. *Cabal et al.* utilize a borosilicate glass (BSG)—which is applied to only one wafer side—as a solid doping source for boron atoms during a  $\text{POCl}_3$  diffusion, and achieve a peak conversion efficiency of 18.9%<sup>8</sup> [136,137]. Another, rather more common approach is the use of sequential tube furnace diffusion processes utilizing boron tribromide ( $\text{BBr}_3$ ) or boron trichloride ( $\text{BCl}_3$ ) and  $\text{POCl}_3$  as liquid dopant precursors [134,137,138]. For both approaches, however, almost no information is available on the actual implementation of the diffusion processes. That is, the order in which the diffusion processes are performed, and how it is ensured that each dopant type is present on only one side of the wafer, is not very clear. Peak conversion efficiencies up to 19.5% have been published for *n*-type H-pattern solar cells fabricated with sequential diffusion processes [134,138], which have been industrially produced since the end of 2010 by *Yingli Green Energy* under the brand name “*Panda*” [139].

For low-loss electrical contacting the boron-doped emitter in *n*-type solar cells by screen printing, a small percentage of aluminum (Al) must be added to the silver (Ag) paste [140–142]. For aerosol printed seed layers it has been shown that an Ag ink (no Al added) can also provide a low-ohmic electrical contact to boron emitters [143]. Unfortunately, especially the screen-printed Ag-Al pastes trigger enhanced recombination below the metallized areas leading to severe voltage losses [16,138] and hence, conversion efficiency losses. *Edler et al.* propose the deep and homogeneous penetra-

---

<sup>8</sup>The type of measurement for *n*-type cells with open rear side metallization is often not accurately described in literature. Unless specifically indicated, the cited conversion efficiencies for such bifacial cells most likely refer to measurements performed on a reflective and conductive measurement chuck or with double-sided irradiation.

tion of metal into the boron emitter—along the whole contact area—as a possible cause [138]. They suggest further a two-step printing process to reduce the impact of the highly recombination active Ag-Al metallization. By printing only the fingers with Ag-Al paste and the external busbar contacts with a less aggressive silver paste [144], the voltage loss after metallization could be significantly decreased. Furthermore, *Lago et al.* report on metal crystallites perforating the boron emitter with crystallite depths up to a few microns, deep enough to shunt the boron emitter [142].

As partial shading of a photovoltaic module can lead to reverse biasing the shaded cells [145], it is important that those cells are not harmed by the applied negative voltage, and that the reverse behavior is not detrimental to the module. *Cabal et al.* show for *n*-type Cz-Si H-pattern cells that the currents occurring under reverse bias load are significantly higher than those observed for *p*-type Cz-Si H-pattern cells [137]. Other publications devoted to different reverse bias behaviors of *p*-type and *n*-type solar cells, or others which investigate the impact of reverse stress on the conversion efficiency, are not known.

For all H-pattern cell types, the external front busbar contacts cover almost 3%<sup>9</sup> of the active cell surface. The finger contacts contribute about the same percentage to the total metal coverage which thus amounts to just fewer than 6%. Unfortunately, the busbar width cannot be arbitrarily reduced<sup>10</sup>, as the reliable interconnectability of the solar cells must be guaranteed for module manufacturing. Nevertheless, several cell concepts aim at reducing the principal shading on the cell's front side, as e.g. approaches that feature no busbars but only fingers on cell level, which are then interconnected by thin metal wires [146,147]. The back-contact back-junction (BC–BJ) cell concept features no front side metallization at all, however, the emitter is located on the rear side, necessitating the use of silicon material with high bulk lifetime [148]. Superior conversion efficiencies up to 24.2% have been reported by *Sunpower* for their BC–BJ cells on *n*-type Cz-Si wafers with 125 mm edge length and passivated contacts [149]. Since both, emitter and base contacts are located on the rear side, the realization of BC–BJ cells on 156 mm wafers is anything but trivial without new and sophisticated metallization approaches. A state of the art third approach to reduce the front side shading—which can be classified structurally between the H-pat-

<sup>9</sup>This applies to a configuration with three 1.5 mm-wide straight busbars on a 156 mm wafer.

<sup>10</sup>To decrease silver consumption, also busbar widths of 1.2 mm are prevalent. Even if these thinner busbars are realized tapered, typically 1.5 mm-wide cell interconnectors are soldered on them resulting in no decreased shading of the cell's front side after module integration.

tern and the BC–BJ concept and is the focus of the present work—is discussed in the following section.

### 3.2.2 Metal wrap through (MWT) concept

The metal wrap through (MWT) solar cell concept was first introduced in 1998 by *Kerschaver et al.* [10]. In contrast to the H-pattern cell approach (Fig. 3.1 and Fig. 3.2), both externally interconnectable contacts are located on the rear side; see Fig. 3.3. This is achieved by a relocation of the external front contacts to the rear side using metallized vias. This means that interconnectable busbar contacts are no longer required on the solar cell front side, leading to reduced shading up to 50%. Focus was initially only set on the use of *p*-type silicon as base material for this back-contacted cell technology. Several different *p*-type MWT cell structures have been developed, mainly differing in the structural configuration of the wafer's rear side (with or without passivation layer) and of the emitter.

The MWT–BSF concept (Fig. 3.3(a)) is the simplest *p*-type MWT structure published up to 2011 [150–152]. Besides the front emitter, the MWT–BSF solar cell also features an emitter inside the vias and on the rear side. Compared with H-pattern cells with Al–BSF (Fig. 3.1), only laser-drilling the vias and a contact separation on the rear side are additionally needed. This leads to an efficiency advantage of  $\Delta\eta \approx 0.5\%_{\text{abs}}$  for MWT–BSF cells [151], and peak conversion efficiencies up to 19.4% have been reported [152].

In 2006, *Dross et al.* presented the first *p*-type MWT solar cell with a passivation layer below the back metal contacts [153]. The introduction of such

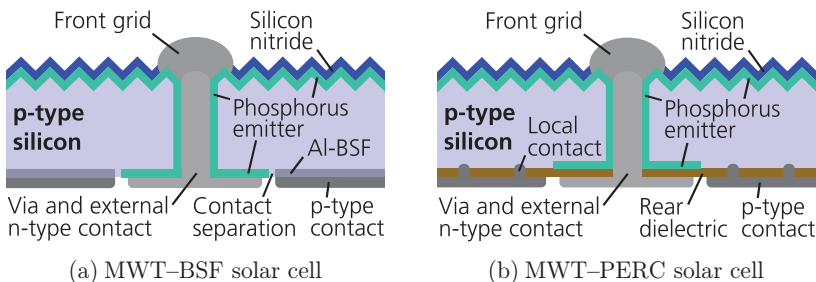


**Fig. 3.3.** Schematic cross sections of *p*-type MWT solar cell structures with different rear side configuration: (a) Al–BSF and (b) PERC. The phosphorus-doped emitter permeates the vias reaching the back. The rear dielectric layer in (b) is a stack consisting of the passivation layer and the  $\text{SiN}_x$  capping layer.

a passivation layer lead to an efficiency gain of  $\Delta\eta \approx 1\%_{\text{abs}}$  in comparison with non-passivated MWT–BSF cells [154]. In 2010, the term “MWT–PERC” was introduced by *Thaidigsmann et al.* for these cells combining the MWT structure and the PERC approach [155], as depicted in Fig. 3.3(b). Again, the emitter extends from the front side through the vias up to the rear side. In 2011, the maximum conversion efficiency for such *p*-type MWT–PERC solar cells reached 19.4% utilizing Cz-Si and screen-printed metallization [11]. Using high-quality float-zone silicon (FZ-Si), the conversion efficiency has been increased to 20.1% for the otherwise identically fabricated cells. In the same experiment, also extruded front contacts [156] have been used in combination with FZ-Si, resulting in a peak conversion efficiency of 20.6% [11]. At the time of publication in 2011, this value represented the world record for large-area *p*-type silicon solar cells (125 mm edge length).

Typically, the external rear contacts (both *n*-type and *p*-type polarity) and the vias are metallized simultaneously with a non-fire-through silver screen-printing paste, called “via paste”. The term “non-fire-through” refers to the property of the paste not to penetrate<sup>11</sup>  $\text{SiN}_x$  layers. One of the main challenges in the fabrication of MWT solar cells is the use of such suitable via pastes. A reliable and continuous via metallization is essential in terms of achieving a low series resistance contribution [151]. For the previously discussed *p*-type MWT–BSF (Fig. 3.3(a)) and MWT–PERC cells (Fig. 3.3(b)), the presence of an emitter both inside the vias and on the rear side ensures electrical contact separation between via paste (*n*-type contact) and *p*-type silicon base. For this application, via pastes have been designed so that they do not shunt the emitter [153,157–159].

In 2011, it became apparent that the rear emitter of passivated MWT solar cells is not necessarily needed if adapted passivation layer stacks and appropriate via pastes are used—this was the launch of the high-performance MWT (HIP–MWT) architecture [118,160], as shown in Fig. 3.4. This significant simplification of the MWT–PERC structure—the complex structuring of the rear emitter is no longer necessary (compare with Fig. 3.3(b))—shows no drawbacks under forward bias conditions as, e.g. for the conversion efficiency. Hence, the HIP–MWT concept offers the use of significantly more cost-effective fabrication process sequences. Under reverse bias conditions

---

<sup>11</sup>This does not mean that the via paste does not attack the  $\text{SiN}_x$  layer at all, which probably would lead to mechanical adhesion problems. Rather, it means that the via paste does not completely penetrate the  $\text{SiN}_x$  layer up to the silicon.

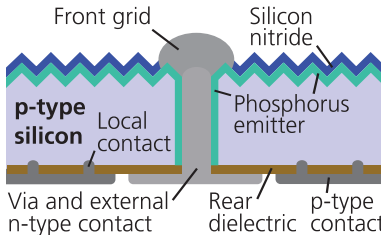


**Fig. 3.4.** Schematic cross section of the *p*-type HIP–MWT solar cell structure without a rear-side emitter. The dielectric layer stack on the backside must ensure both surface passivation and electrical contact separation between external *n*-type contact and *p*-type base.

performed up to  $-12$  V, the external *n*-type contacts initially showed increased current flow for the HIP–MWT cells compared with the MWT–PERC cells [160]. The investigation of further dielectric layers revealed that the current flow under reverse bias load can be manipulated by the choice of the dielectric layer [161], and that comparable low current flows as for MWT–PERC cells can be achieved with HIP–MWT cells [162]. However, in case of low breakdown voltages and an adequate spatial distribution of the current flow, the early breakdown behavior can be potentially used on cell level as an integrated bypass diode approach [161,163].

In 2010, *Guillevin et al.* presented first MWT solar cells using *n*-type Cz-Si as base material [15]. They reported a peak conversion efficiency of  $18.7\%^{12}$  for cells with a wafer edge length of 156 mm. The rear side grid of these *n*-type MWT cells has an open structure and consists of curved finger contacts and external contact pads for both polarities. With use of a specific unit cell design, (pseudo-) busbar contacts are neither needed on the front nor on the rear side. In the following year, they increased the conversion efficiency by  $\Delta\eta = 1\%_{\text{abs}}$ , now achieving  $19.7\%$  with straight finger contacts and perpendicular (pseudo-) busbar contacts both on the front and rear side; see Fig. 3.5 [16]. The MWT cells show about  $0.3\%_{\text{abs}}$  higher conversion efficiencies than H-pattern cells processed in parallel due to higher voltage and current values.

However, further information about these *n*-type MWT cells—especially concerning the structural configuration of the via contacts and the rear side of

<sup>12</sup>As for bifacial *n*-type H-pattern cells, the type of measurement is often not accurately described in literature. Unless specifically indicated, the cited conversion efficiencies for *n*-type MWT cells most likely refer to measurements performed on a reflective and non-conductive chuck.

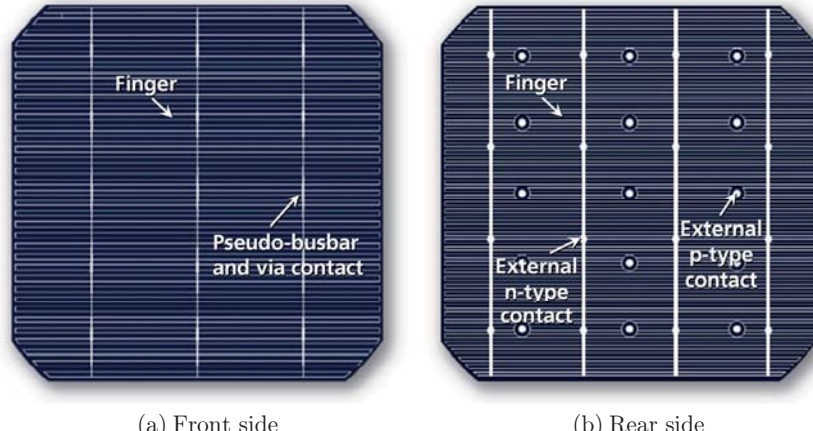


**Fig. 3.5.** Image of (a) front side and (b) rear side of an *n*-type MWT solar cell with 156 mm edge length, as published by *Guillevin et al.* in 2011 [16] (the labeling is added). Narrow pseudo-busbars on the front side conduct the current from the fingers to the vias. Wider busbars on the rear side collect the finger current and conduct it to the round-shaped external *n*-type contacts. The also round-shaped external *p*-type contacts are not in contact with the rest of the rear metallization.

the cells—has not been published by these authors. Furthermore, there are no known publications regarding the reverse bias behavior as well as the impact of reverse bias load on the forward behavior of such *n*-type MWT solar cells. In September 2011, *Yingli Green Energy* announced research collaboration with the *Energy Research Center of the Netherlands (ECN)* and *Amtech Systems* on the development of *n*-type MWT solar cells [164].

### 3.3 Ongoing development of *p*-type MWT technology

The development of *n*-type MWT solar cells within this work has been strongly influenced by the concurrent ongoing development of *p*-type MWT solar cells. Results from this work also contributed significantly to this development in *p*-type MWT technology. In particular, the use of further optimized via pastes to metallize the vias and the external contacts on the rear side allow for significant simplifications in *p*-type MWT cell structures. Building upon the status of *p*-type MWT solar cells at the beginning of this work in 2011 (as discussed in the previous section 3.2.2), this section deals with the ongoing development in *p*-type MWT technology as of 2012.

### Simplification of the p-type HIP–MWT cell concept

The idea to further simplify the *p*-type HIP–MWT concept is based on the target to enable the use of conventional and passivated *p*-type PERC cell precursors<sup>13</sup> for fabrication of MWT cells. This means that laser-drilling the vias may take place only after application of the passivation layers. So far, for HIP–MWT cells, laser-drilling the vias is performed prior to  $\text{POCl}_3$  diffusion in order to form an emitter also at the inside of the vias [118]; see Fig. 3.4. By performing the laser-drilling process after passivation and hence, just before the metallization process, it is clear that an emitter within the vias can no longer be present. The MWT cell structure resulting from this idea is shown in Fig. 3.6(a). This simplified MWT structure has been introduced as the *p*-type HIP–MWT+ cell concept [14,165]. The difference to the HIP–MWT cell in Fig. 3.4 is the no longer existing emitter within the via, since the emitter is present on the front side only. For both, the HIP–MWT and the HIP–MWT+ cell concept, the laser-drilling of the vias is the only additional process step needed to fabricate passivated MWT cells instead of H-pattern PERC cells. But only the HIP–MWT+ approach enables the use of passivated PERC cell precursors, as the via-drilling is performed directly before the metallization process. This makes the HIP–MWT+ cell concept very attractive for industrial implementation.

On the other hand, the via paste is in direct contact to the *p*-type silicon base within the vias for the HIP–MWT+ cell structure. Note that the cross sections, as e.g. in Fig. 3.6(a), are not drawn to scale. The actual dimensions for an exemplary *p*-type MWT solar cell are summarized in Table 3.1. The proportion of the metallized surface of the external *n*-type contact compo-

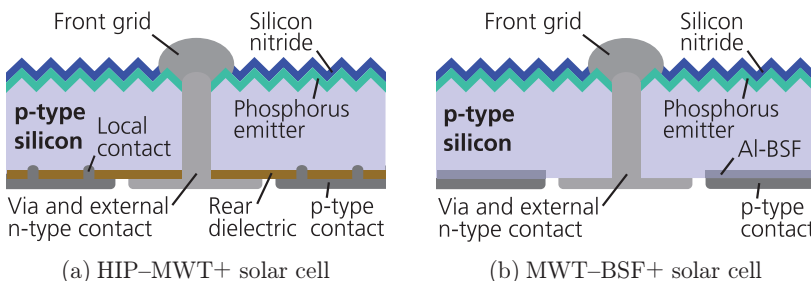


**Fig. 3.6.** Schematic cross sections of *p*-type MWT solar cell structures without emitter neither inside the via nor at the rear side: (a) HIP–MWT+ and (b) MWT–BSF+.

<sup>13</sup>Here, the term precursor refers to a *p*-type PERC solar cell which is passivated but not yet metallized. The precursor has so far gone through all fabrication steps up to metallization.

**Table 3.1.** Actual dimensions of the external  $n$ -type contact structure for an exemplary  $p$ -type MWT solar cell on pseudo-square silicon wafers with 156 mm edge length and a thickness of  $W = 175 \mu\text{m}$ . The values are given for a metallization geometry with 24 round  $n$ -type contact pads with a diameter of 2.5 mm and two via contacts per contact pad. The via diameters are 70  $\mu\text{m}$  and 140  $\mu\text{m}$  on front and rear side, respectively.

Total wafer surface $A_{\text{wafer}}$ (mm $^2$ )	Area $n$ -type contact pads $A_{\text{pads}}$ (mm $^2$ )	Area inside the vias $A_{\text{vias}}$ (mm $^2$ )	$\frac{A_{\text{pads}}}{A_{\text{wafer}}}$ (%)	$\frac{A_{\text{vias}}}{A_{\text{wafer}}}$ (%)	$\frac{A_{\text{vias}}}{A_{\text{pads}} + A_{\text{vias}}}$ (%)
23895	117.8	2.8	0.5	0.01	2.3

nents in relation to the total wafer surface is 0.5% and 0.01% for the contact pads and the vias, respectively. The proportion of the vias at the total external  $n$ -type contact area amounts to only 2.3%. However, for the successful realization of the HIP–MWT+ cell concept, a via paste is needed, which—in the ideal case—does not form any type of electrically conductive contact to the directly adjacent  $p$ -type silicon within the vias.

In order to evaluate the availability of such a via paste, a first study utilizing six different via pastes concerning their electrical contact behavior—both to  $p$ -type and to  $n$ -type silicon—has been performed within this work at the beginning of 2012. The performed experiments and the obtained results are published in Ref. [165]. The investigations reveal significant differences between the examined via pastes concerning their electrical contact behavior, both in forward and reverse bias condition. This study reveals one via paste which shows by far the lowest leakage currents of all examined via pastes when applied on  $p$ -type silicon, either with or without an intermediate dielectric layer. Furthermore, for the first time, this study showed a potential impact of reverse bias load on the occurring leakage currents in forward direction. Therefore, it forms the basis for the comprehensive studies carried out in Chapter 6 utilizing even further optimized via pastes.

However, the identified via paste has been used to fabricate  $p$ -type HIP–MWT and HIP–MWT+ solar cells using FZ-Si wafers with 125 mm edge length. The obtained peak conversion efficiencies are 20.2% and 20.3% for the best HIP–MWT and HIP–MWT+ cells, respectively. At the time of publication of the  $I$ – $V$  data in 2012 [165], this HIP–MWT+ solar cell was the best performing MWT cell fabricated at *Fraunhofer ISE* using screen-printed contacts only. Furthermore, this HIP–MWT+ cell features comparable low current flow under reverse bias load as the parallel fabricated HIP–MWT cell. Later,

*Thaidigsmann* [166, p. 46] also showed that recombination losses at the inner surface of the via contacts are negligible for these HIP–MWT+ solar cells.

#### Simplification of the p-type MWT–BSF cell concept

In the above mentioned first via paste evaluation [165], also a MWT–BSF cell without rear-side emitter is introduced (an emitter within the vias is still present). This means that in comparison with the MWT–BSF structure in Fig. 3.3(a), the via paste is in direct contact with the subjacent bare *p*-type silicon in the area of the external *n*-type contact pads. According to Table 3.1, the area proportion of the silicon wafer in direct contact with the via paste is 0.5% in this case. Hence, the requirements on the via paste concerning its electrical insulation property for its application in such MWT–BSF cells is significantly higher than for its use in HIP–MWT+ cells. None of the examined via pastes is found to be suitable for the realization of this cell concept. The fabricated MWT–BSF devices show shunting issues with respect to low shunt resistances (i.e. low pseudo fill factors) and high currents under reverse bias load.

In 2013, *Yin et al.* [13] published a further adjusted MWT structure with Al–BSF in which the via paste is also applied directly onto the subjacent bare *p*-type silicon base. Their published MWT structure has no emitter in the vias nor at the rear side, see Fig. 3.6(b), and is referred to as MWT–BSF+ in the following. *Yin et al.* report a peak conversion efficiency of 19.6% on full-square *p*-type cast-mono silicon wafers with 156 mm edge length [13]. The published results for this cell configuration, in which the via paste is directly applied onto the *p*-type silicon wafer, imply that no significant leakage currents occur between the two components. In other words, this means that the used via paste is optimized such that it does not form an electrically conductive contact to the underlying bare silicon. The availability of such optimized via pastes will be also shown in the studies in Chapter 6. The MWT–BSF+ concept offers a significant simplification of the fabrication process for MWT solar cells with Al–BSF, as the contact separation step on the rear side is no longer necessary.

#### Need for electrically non-contacting via pastes

As the preceding discussion of the different *p*-type MWT cell structures shows, solely the non-fire-through property of the via pastes is no longer sufficient. In addition, the via pastes themselves have to prevent electrical

contact formation not only when printed on top of an intermediate dielectric layer, but also when applied directly onto the bare *p*-type silicon base. To meet both requirements, the glass components of the newer via paste generations probably form a thin tunneling barrier, i.e. insulating glass layer, during the contact firing process, resulting in an electrically non-conducting contact system [163,167]. Furthermore, the actual requirements on the via pastes depend on the cell structure of choice. In accordance to the results from *Yin et al.* [13] with the via paste being directly applied on bare *p*-type silicon, some of the via pastes investigated in Chapter 6 also show no significant electrical contact to directly adjacent *p*-type silicon.

#### Conclusion

The fabrication of *p*-type HIP–MWT+ solar cells can be simply performed by using *p*-type PERC cell precursors. This is possible because of the significant simplification of the *p*-type MWT cell structure compared with the initial MWT–PERC concept. The MWT–BSF+ approach also provides a more cost-efficient fabrication of MWT cells with Al–BSF. However, these *p*-type HIP–MWT+ or MWT–BSF+ solar cells suffer from boron-oxygen related light-induced degradation (LID), resulting in lower performance under illumination. To overcome this LID, one option is to replace the *p*-type silicon base with *n*-type silicon material. The aim now is to transfer the MWT concept to *n*-type silicon and likewise to use *n*-type PERT cell precursors, if possible. In order to do that, the “parent” cell—the *n*-type PERT cell with H-pattern metallization grid—and all processes for their fabrication are needed. Hence, the fabrication process for *n*-type H-pattern PERT cells is discussed first in the next section, before the realization of *n*-type MWT solar cells is in focus of Chapter 3.5.

#### 3.4 Processes for fabrication of *n*-type H-pattern solar cells

In order to start the development of *n*-type MWT solar cells, a basic fabrication process for *n*-type H-pattern PERT solar cells is mandatory. However, at the beginning of this work in 2011, such a basic fabrication process was not yet available in the PV–TEC pilot-line [168] at *Fraunhofer ISE*. Aside from the non-availability of a proven process flow, the development of  $\text{BBr}_3$  diffusion processes for forming the boron-doped emitter for wafers with 156 mm edge length was only established during the end of 2012, as the tube furnace for this purpose was only then available.

As discussed in Chapter 3.2.1, co-diffusion [136] or sequential diffusion processes [134,137,138] can be used to form the different highly doped surfaces necessary in *n*-type silicon solar cells; see e.g. Fig. 3.2(b). The co-diffusion approach, as introduced by *Cabal et al.* [136], utilizes a solid dopant source on one wafer side during a high-temperature gas phase diffusion of the other dopant atoms on the other wafer side. This approach has been also investigated at *Fraunhofer ISE* by *Rothhardt* in a parallel PhD thesis [169]. Refer to this thesis or recent results from *Cabal et al.* [170] for further information concerning the co-diffusion approach. The process route utilized in this work is based on a sequential diffusion approach, which is now being introduced.

### 3.4.1 Basic process sequence

The persecuted process sequence for fabrication of *n*-type Cz-Si H-pattern PERT solar cells within this work, utilizing sequential diffusion processes, is illustrated in Fig. 3.7(a). The schematic cross section of the resulting cell structure is given in Fig. 3.2(b). A final *n*-type H-pattern solar cell, fabricated according to this process sequence, is shown in Fig. 3.7(b).

Following wet-chemical alkaline texture, which is performed in a bath with potassium hydroxide (KOH) and additives to form random pyramids on either wafer side, the rear side is covered by a diffusion barrier layer applied by plasma-enhanced chemical vapor deposition (PECVD). During BBr<sub>3</sub> dif-

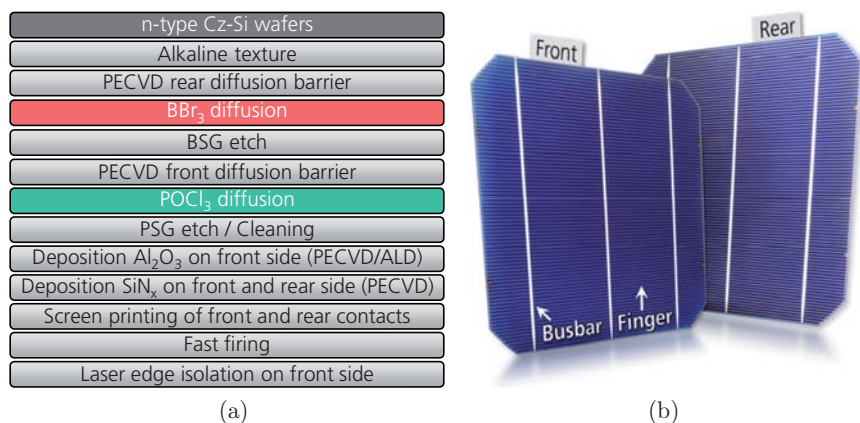


**Fig. 3.7.** (a) Schematic process sequence for fabrication of *n*-type Cz-Si H-pattern PERT solar cells with sequential diffusion approach; see Fig. 3.2(b) for the resulting cell cross section. (b) Photographs of front and rear sides of a bifacial *n*-type H-pattern cell with three external busbar contacts, fabricated according to the sequence in (a).

fusion, this barrier layer has to prevent boron atoms to enter the silicon on the covered rear side and thus, has to ensure the presence of boron doping after the diffusion process on the uncovered front side only. Both the BSG and the barrier layer are then removed in 10% HF solution, which is referred to as BSG etch. Prior to  $\text{POCl}_3$  diffusion, a further barrier layer is applied by PECVD on the previously boron-doped front side. The phosphorus BSF on the rear side is formed during the subsequently performed  $\text{POCl}_3$  diffusion. The PSG and the barrier layer are again removed in 10% HF solution, which is referred to as PSG etch.

A wet-chemical cleaning step precedes the deposition of an  $\text{Al}_2\text{O}_3$  layer with a thickness of up to 10 nm on the boron-doped emitter on the front side. The  $\text{Al}_2\text{O}_3$  passivation layer can either be applied by PECVD [171–174] or by atomic layer deposition (ALD) [135,172,174,175]. Subsequently, a  $\text{SiN}_x$  layer is applied by PECVD on both wafer sides. On the front side, this  $\text{SiN}_x$  layer acts as an antireflection coating, whereas on the rear side, it acts in addition as a passivation layer. The  $\text{SiN}_x$  layer thickness on the rear side is typically 75 nm, whereas its thickness on the front side is reduced according to the already present  $\text{Al}_2\text{O}_3$  layer (the total layer thickness is again about 75 nm). This is also reflected in a similar color of the front and rear sides in Fig. 3.7(b).

In order to be able to extract generated current from the so far passivated cell precursors, metal contacts in the shape of finger and busbar structures are applied on either wafer surface by screen printing technology; see Fig. 3.7(b). For this purpose, different screen-printing pastes are employed. As discussed in Chapter 3.2.1, an Ag-Al paste is necessary for the metallization of the front-side boron emitter, in order to achieve low specific contact resistance. The rear-side phosphorus BSF is metallized with an Ag paste. After each printing step, the pastes are dried in a drying furnace at about 200°C to evaporate the solvents. Upon completion of the screen printing process, contact formation takes place during fast firing in a conveyor belt furnace at significantly higher temperatures (wafer temperature between 700°C and 800°C). Moreover, the firing step activates the chemical passivation property of the passivation layers. This is correlated with the diffusion of e.g. hydrogen from the  $\text{Al}_2\text{O}_3$  or  $\text{SiN}_x$  layer (which is more likely) to the silicon interface, where it effectively saturates dangling bonds [175–177]. In order to electrically separate front and rear side, laser edge isolation on the front side terminates the fabrication process.

### 3.4.2 Challenges in the fabrication process and approaches

Like any fabrication process, also this process sequence entails challenges not only regarding single processes, but also in terms of their mutual interaction. In the following subsections, these challenges are examined more closely. Ways to address these challenges are presented in part directly, or are referenced to the following chapters, in which the corresponding approaches are discussed in detail.

#### Quality of n-type Cz-Si wafer material

As the *n*-type Cz-Si wafers are exposed to several high temperature steps, their bulk lifetimes must not significantly degrade. A prominent example for very significant lifetime degradation after a high temperature step is the presence of so-called “swirl” structures. These swirl defects are correlated to oxygen precipitates [178–180], resulting in bulk lifetimes of up to only a few tens of microseconds [180]; see also Fig. 3.8(b) and (c). To ensure no degradation of the bulk lifetime during the applied fabrication process, *n*-type Cz-Si wafers from different material suppliers have been evaluated prior to their usage within this work. For that purpose, some of the wafers from each supplier have undergone a process sequence similar to that in Fig. 3.7(a) up to the PSG etch. Following the PSG etch, the highly doped surface layers and the random pyramids on either wafer side are wet-chemically etched. Subsequently, the surfaces are passivated and the bulk lifetimes are measured after firing by means of QSSPC. An exemplary result

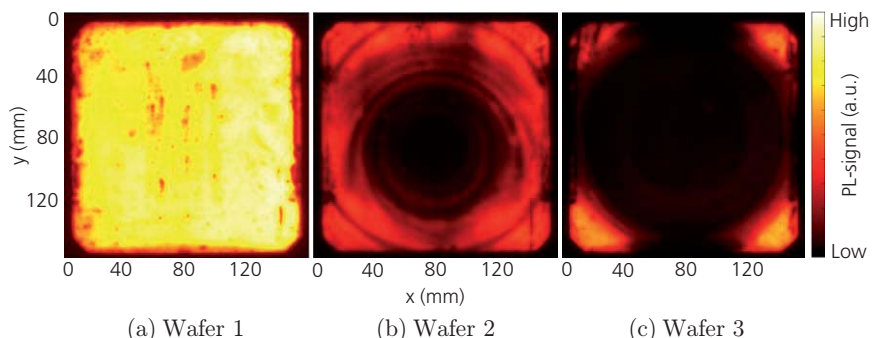


**Fig. 3.8.** Photoluminescence (PL) images of three *n*-type Cz-Si wafers after they have undergone the material evaluation process sequence. The wafers in (b) and (c) feature swirl defects, resulting in bulk lifetimes in the wafer center of only 70  $\mu$ s and 240  $\mu$ s, respectively. The wafer in (a) features no ring structures and has a bulk lifetime of 2.6 ms in the center.

of this material screening is depicted in Fig. 3.8. Clearly visible are the swirl defects in Fig. 3.8(b) and (c), resulting in bulk lifetimes of only 70  $\mu$ s and 240  $\mu$ s in the wafer center, respectively. Thus, this material is not suitable for the applied process sequence, whereas the material in Fig. 3.8(a) is highly suitable with a bulk lifetime of 2.6 ms in the wafer center.

### Diffusion barrier layers

For the selected process route with sequential diffusions, suitable diffusion barrier layers are mandatory to ensure the doping on only one wafer side during  $\text{BBr}_3$  and  $\text{POCl}_3$  diffusion. Hence, single-sided application methods for the barrier layers are imperative. Because for the  $\text{POCl}_3$  diffusion the already boron-doped silicon surface has to be protected by a diffusion barrier layer, the interaction of this layer with the boron atoms has to be known. As also oxygen is present in the gas atmosphere during the  $\text{POCl}_3$  diffusion, the barrier effect of the applied layers against oxygen is also of high interest. Especially since, as discussed in Chapter 2.3.2, oxidation of the boron-doped surface would lead to oxidation-enhanced diffusion of boron atoms and to a depletion of boron atoms at the surface. Following the diffusion processes, the used sacrificial barrier layer should also be removable in 10% HF solution. An excerpt of the experiments performed concerning the evaluation of different diffusion barrier layers is discussed in Chapter 4.5. These investigations resulted in the selection of a suitable diffusion barrier layer which is used for fabrication of *n*-type solar cells within this work.

### Formation of the boron emitter by $\text{BBr}_3$ diffusion

The newly acquired quartz tube furnace from *Tempress Systems* for boron diffusion using liquid  $\text{BBr}_3$  as dopant precursor—see Chapter 4.2 for further technical information—has been ready for processing from the end of 2012. The then performed development of  $\text{BBr}_3$  diffusion processes<sup>14</sup>, in order to form suitable boron emitters on alkaline textured surfaces, includes several challenges. First, the doping with boron atoms should be as homogeneous as possible across the whole wafer surface. This is equivalent to the need for a sufficiently homogeneous sheet resistance. As for the following points, it is also important that the diffusion processes also yield similar results for the different process boat positions. Second, the dark saturation current densities  $j_{0e}$  after passivation and firing of the formed boron emitters should be as

<sup>14</sup>As will be discussed in Chapter 4, some basic diffusion processes and corresponding parameters have been provided by *Tempress Systems*.

low as possible on alkaline textured surfaces. This implies that no boron-rich layer may be present at the silicon surface after  $\text{BBr}_3$  diffusion, as discussed in Chapter 2.3.2. Third, the formed boron emitters should be electrically contactable with low resistance by using screen-printed and fired metal pastes. In order to evaluate and to better understand the performed  $\text{BBr}_3$  diffusion processes with respect to these challenges, for each performed diffusion several test specimens are either prepared separately or along with solar cells. Further challenges concerning, e.g. the electrical contacting of the boron-doped emitters are the interplay between the formed boron doping profiles and the recombination activity of charge carriers below the metallized areas. Also shunting issues in correlation to the boron doping profile play a decisive role in developing promising  $\text{BBr}_3$  diffusion processes.

The development of the  $\text{BBr}_3$  diffusion processes, and the ability to customize the resulting doping profiles with respect to the aforementioned challenges, will be discussed in detail in Chapter 4.

#### **Formation of the phosphorus back surface field (BSF) by $\text{POCl}_3$ diffusion**

The phosphorus diffusion using liquid  $\text{POCl}_3$  as dopant precursor are performed in a quartz tube furnace from *centrotherm photovoltaics*. The industrial system used is the “Centronic E2000 HT 410–4” with four horizontal quartz tubes. The challenges for the formation of the phosphorus-doped BSF by  $\text{POCl}_3$  diffusion are almost equivalent to those mentioned above for the formation of the boron-doped emitter by  $\text{BBr}_3$  diffusion. Hence, e.g. the homogeneity in sheet resistance across the whole wafer surface, low dark saturation current densities  $j_{0\text{BSF}}$ , and the ability to contact the phosphorus-doped surface with low specific contact resistance utilizing screen-printed and fired metal contacts are issues that are linked to the  $\text{POCl}_3$  diffusion process.

The idea with respect to the order of the diffusion processes is that both the  $\text{BBr}_3$  and the  $\text{POCl}_3$  diffusion processes might be optimized separately, in case the already present boron doping profile does not alter during  $\text{POCl}_3$  diffusion. This makes the process sequence with  $\text{BBr}_3$  diffusion first very attractive, as the independent developments in boron emitter and phosphorus BSF formation can be directly implemented in the cell fabrication process. The feasibility of this approach depends on the applied diffusion barrier layer, as discussed before, and the effect of the thermal budget of the  $\text{POCl}_3$  diffusion process on the rearrangement of the boron dopants. As the solubility of phosphorus atoms in silicon is significantly higher than that of

boron atoms, see Fig. 2.7,  $\text{POCl}_3$  diffusion is performed at clearly lower temperatures than  $\text{BBr}_3$  diffusion processes. The studies, which are devoted to the topic with respect to the diffusion barrier layers, will be dealt with in Chapter 4.5. Another advantage of the diffusion order with  $\text{BBr}_3$  diffusion first is that the diffusion process with the higher getter efficiency—which is the  $\text{POCl}_3$  diffusion [181,182]—comes last. In principle, also the inverted order of the diffusion processes, i.e. the  $\text{BBr}_3$  diffusion follows the  $\text{POCl}_3$  diffusion, is an option for a sequential diffusion approach. In this case, the higher thermal budget of the  $\text{BBr}_3$  diffusion process would inevitably lead to a significant redistribution of phosphorus dopants. Hence, an independent optimization of the two diffusion processes is no longer easily possible.

With regard to  $\text{POCl}_3$  diffusion itself, no comprehensive process developments and optimizations are carried out within this work. The processes used to form the phosphorus BSF have been developed as part of other works, as e.g. published in Refs. [91,92], and are not more than slightly modified for their implementation in *n*-type cell fabrication. Particularly the publication from Werner *et al.* [92] provides an overview on current  $\text{POCl}_3$  diffusion processes developed at *Fraunhofer ISE*. In order to evaluate the used  $\text{POCl}_3$  diffusion processes, several test specimens are prepared along with the solar cells.

#### **Wet-chemical cleaning and passivation layers**

Prior to the application of dielectric passivation layers, contaminants on the wafer surface need to be reduced in order to achieve maximum surface passivation quality. The surface passivation is crucial, as the silicon crystal abruptly terminates at the wafer surfaces and thus, many defects are present. Two different passivation mechanisms are distinguished [183], namely the saturation of dangling bonds at the silicon surface, and keeping out of charge carriers of either type from the surface. Both mechanisms are also known as chemical and field effect passivation, wherein the second mechanism is based on fixed charges within the passivation layer. Hence, layer types have to be used which can effectively passivate the highly boron- and the highly phosphorus-doped surfaces.

Within this work, the wet-chemical cleaning prior to the deposition of the passivation layer is performed either in HF solution<sup>15</sup>, or in a SC1/SC2

<sup>15</sup>The immersion in HF solution is strictly speaking no real cleaning, as the HF etches only the native  $\text{SiO}_2$  layer and thus has no real purifying effect.

cleaning<sup>16</sup>, or in nitric acid ( $\text{HNO}_3$ ) preceded and followed by a dip in 1% HF solution. The latter is referred to as HNF cleaning in the following.  $\text{HNO}_3$  is often used to wet-chemically oxidize silicon surfaces [185,186].

A  $\text{SiN}_x$  layer can effectively passivate phosphorus-doped surfaces [187], whereas it cannot provide an effective passivation of boron-doped surfaces [188]. Hence, the boron-doped surfaces are passivated with a thin  $\text{Al}_2\text{O}_3$  layer, either applied by PECVD or ALD with layer thicknesses of approximately 10 nm or 5 nm, respectively. The PECVD depositions of the  $\text{SiN}_x$  layers on either wafer side are performed as described previously.

#### Screen printing and fast firing process

In order to extract the generated current out of the solar cell, electrical conductive metal contacts to the highly doped surfaces are needed. The most common method to form metal contacts in solar cell fabrication offers the screen printing technology. The requirements on the metallization are, e.g. minimum shading, especially at the cell front side, high line conductivity, low specific contact resistances, low recombination at the metal contacts, and no shunting of the emitter layer.

The low-loss electrical contacting of the phosphorus doping on the rear side of the *n*-type solar cells is possible with Ag pastes, as they are commonly used for contacting phosphorus emitters in *p*-type cells. However, these Ag pastes are not suitable to contact boron-doped surfaces with low specific contact resistance [140,142]. Instead, Ag-Al pastes have to be used to realize the electrical contacting of boron emitters with low series resistance contribution [140,142], as described also in Chapter 3.2.1. Unfortunately, these Ag-Al pastes trigger enhanced recombination below the metallized areas leading to severe voltage losses [16,138]. The conductivity of Ag-Al pastes is also somewhat lower than that of Ag pastes [140,142]. The selection of a suitable fast firing process is also important, during which the contact formation takes place between the applied metal contacts and the doped surfaces.

All in all, the metallization of the front boron emitter is one of the crucial challenges in the fabrication of such *n*-type solar cells. Concerning this issue, especially the studies in Chapter 5 target the generation of knowledge and

---

<sup>16</sup>The terms SC1 and SC2 stand for standard clean 1 and 2, respectively. The SC1/SC2 cleaning is a shortened version of the RCA cleaning [184] used in microelectronics.

deeper understanding of the mechanisms that are prevailing at the contact interface between Ag-Al metallization and the boron-doped silicon surface.

An obvious approach to reduce the impact of the highly recombination active Ag-Al metallization is the reduction of the therewith metallized areas. For this purpose, the screen printing of the finger structures and the external busbar contacts can be carried out with two different pastes: the finger contacts are printed with an Ag-Al paste, whereas the external busbar contacts are formed with a non-fire-through and electrically non-contacting silver paste [138]. This method is known as the dual printing approach [189], wherein the busbar contacts are also referred to as floating busbars. Another promising approach to reduce the Ag-Al covered area on the cell's front side of *n*-type solar cells represents the MWT approach, which is now being dealt with in more detail.

### 3.5 Transfer of the MWT concept to *n*-type silicon

As discussed in Chapter 3.2.2, *Yingli Green Energy*, *ECN*, and *Amtech Systems* started their collaboration on the development of *n*-type MWT solar cells in 2011. However, no scientifically reliable cross sections or detailed fabrication process sequences for *n*-type MWT solar cells have been published by them to date. Hence, at the beginning of this work, one of the first tasks regarding the development of *n*-type MWT solar cells has been to evaluate and assess possible cell structures and their associated fabrication processes.

The first realization of *n*-type MWT solar cells within this work resulted in fully functional devices with a peak conversion efficiency of 17.7% on

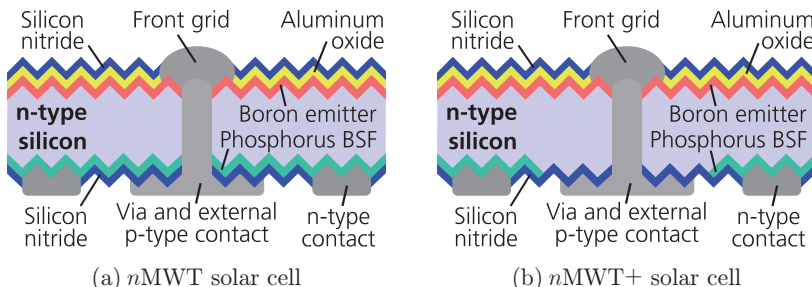


**Fig. 3.9.** Schematic cross sections of *n*-type MWT solar cell structures with emitter on the front side only. The rear-side configurations are different: (a) *n*MWT with full-area phosphorus BSF and (b) *n*MWT+ with structured phosphorus BSF.

### 3.5 Transfer of the MWT concept to n-type silicon

pseudo-square Cz-Si wafers with 125 mm edge length. More information about these first *n*-type MWT solar cells can be found in Ref. [190].

In the present work, the cell structures shown in Fig. 3.9 form the basis for the development of the *n*-type MWT cell technology. Both *n*-type MWT cell structures exhibit the boron emitter on the front side only and hence, resemble the *p*-type HIP–MWT+ structure in Fig. 3.6(a). The naming *n*MWT is used in the following for the cell with full-area phosphorus BSF, as depicted in Fig. 3.9(a), whereas the term *n*MWT+ denotes the cell without phosphorus doping below the external *p*-type contacts, as apparent in Fig. 3.9(b). The “+” symbolizes that the phosphorus BSF is (additionally) structured. The fact that no emitter is present within the vias offers the possibility to drill the vias directly before metallization, as this has been already discussed with respect to the *p*-type HIP–MWT+ solar cells in Chapter 3.2. A possible fabrication process for the *n*MWT and *n*MWT+ solar cells as well as for H-pattern reference cells is illustrated in Fig. 3.10.

One option to ensure that no phosphorus doping is present below the external *p*-type contacts for the *n*MWT+ cell is the use of structured diffusion barrier layers during  $\text{POCl}_3$  diffusion. Another possibility is to structure the phosphorus-doped surfaces subsequent to the diffusion process. For both approaches, the use of an inkjet-printed masking resist and wet-chemical etching is an option [191–193]. Laser processes also allow for structuring dielectric layers serving as diffusion barriers or for the direct struc-

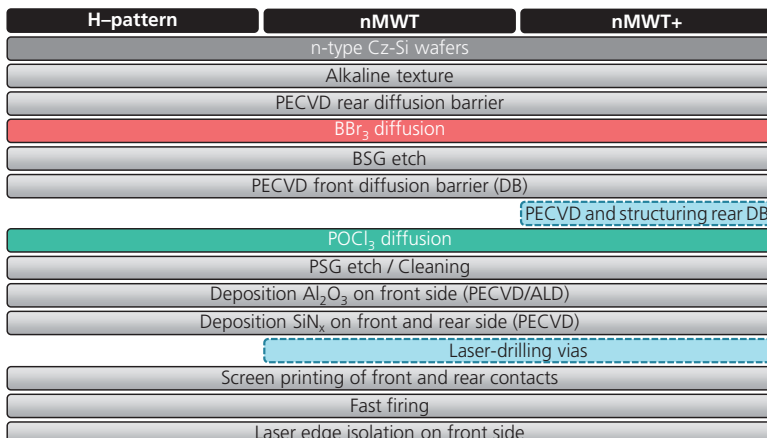


**Fig. 3.10.** Schematic process sequence for fabrication of *n*-type Cz-Si H-pattern as well as *n*MWT and *n*MWT+ solar cells as depicted in Fig. 3.9.

turing of highly doped silicon surfaces [194]. The application of local diffusion barrier layers by inkjet printing or screen printing prior to  $\text{POCl}_3$  diffusion is in principle also possible, in case the material used can withstand the high temperatures and is easily removable afterwards [195]. Another option is the use of a screen-printed etching paste to locally remove the phosphorus-doped surface layer [195,196].

For most of the  $n\text{MWT}^+$  cells fabricated and investigated in this work, the diffusion barrier layers are structured prior to  $\text{POCl}_3$  diffusion using inkjet-printed masking resist and wet-chemical etching in buffered HF; see Appendix C.1 for further details. This process sequence to structure dielectric layers is robust and already well-proven. Furthermore, this method allows realizing the  $n\text{MWT}^+$  cell structure, as depicted in Fig. 3.9(b), by the use of diffusion barrier layers whose properties are known.

This allows for the investigation and comparison of the two different  $n$ -type MWT cell concepts  $n\text{MWT}$  and  $n\text{MWT}^+$ , as this will be done in the Chapters 6 and 7. However, in case a structured phosphorus BSF is found to be necessary to prevent shunting on the rear side, this inkjet-based structuring method is not suitable on industrial scale. In order to evaluate if laser processes are an opportunity to structure the phosphorus BSF subsequent to  $\text{POCl}_3$  diffusion, a proof-of-concept on cell level is performed and discussed in section 7.6. The principle of the laser processes that are used is described in Appendix C.2.

The first realized  $n\text{MWT}$  and  $n\text{MWT}^+$  solar cells with an edge length of 156 mm feature a front-side metallization pattern with three (pseudo-) busbar contacts; see Fig. 3.11(a). Accordingly, three contact rows are located on the rear side with the external contact pads for each polarity. Then, the switch was made to a metallization layout with four (pseudo-) busbar contacts on the front side; see Fig. 3.11(b). On the rear side, four contact rows are present for each polarity. The increase in contact rows leads to a shortening of the effective finger length on front and rear side. This results in a reduction of the series resistance contribution of the finger contacts and allows for an increase in fill factor [197,198]. The change in metallization geometry, i.e. the position of the external contact pads, is connected with considerable effort, as for each geometry, a suitable measurement chuck must be available. Hence, the arrangement of the external contact pads is as shown in Fig. 3.11 throughout this work.

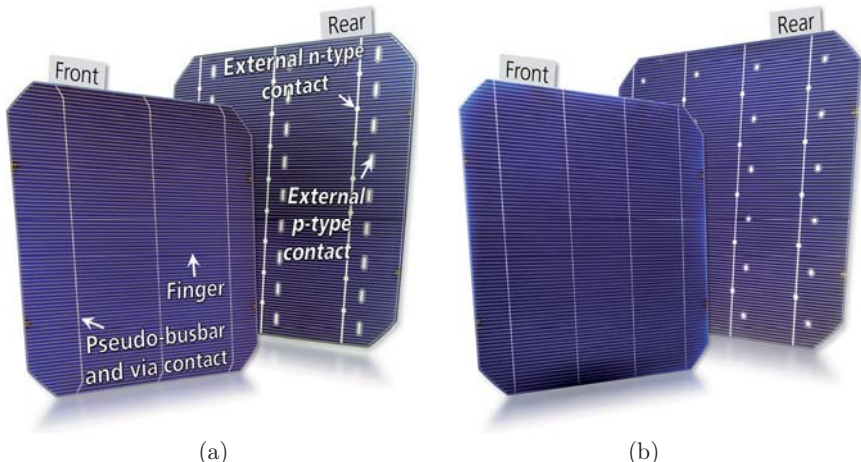


**Fig. 3.11.** Photographs of front and rear sides of *n*-type MWT cells with 156 mm edge length and a different number of contact rows per polarity: (a) three and (b) four.

By comparing the *n*MWT structure in Fig. 3.9(a) with the *n*-type H-pattern structure in Fig. 3.2(b), it is clear that the *n*MWT approach represents the structurally simplest realization opportunity of an MWT cell using *n*-type silicon. However, the significantly higher risk of shunting and unwanted leakage currents in the area of the external *p*-type contacts still remains for the *n*MWT concept in comparison with the *n*MWT+ approach. This topic is content of the Chapters 6 and 7, where it is examined and discussed very detailed.

## 3.6 Chapter summary

Following a comprehensive review about the state-of-the-art for relevant *p*-type and *n*-type silicon solar cells at the beginning of the work in 2011, it is elaborated that the development of *n*-type MWT solar cell structures has been strongly influenced by concurrent ongoing improvements in *p*-type MWT cell technology. Also based on results that have arisen in the context of this work, the *p*-type MWT structures were considerably simplified.

One key for the successful fabrication of MWT cells in general—either using *p*-type or *n*-type silicon wafers—is the silver-based via paste, which is used to metallize the via contacts as well as the external contacts on the rear side. For the *p*-type HIP-MWT solar cell with passivated rear surface

and the *p*-type MWT–BSF cell structure, the requirements on the via paste are originally that it should not fire-through dielectric layers, that it ensures reliable and continuous via metallization with low series resistance, and that it does not shunt an adjacent emitter layer. The availability of further optimized via pastes then resulted in the development of simplified *p*-type MWT cell concepts, namely the *p*-type HIP–MWT+ and the *p*-type MWT–BSF+ solar cell. These both MWT cell structures have in common that the emitter is present on the front side only and thus, no emitter is present neither within the vias nor at the rear side. These simplifications are only possible as the new via paste generation utilized is able to prevent or at least to significantly suppress electrical contact formation to the directly underlying (bare) *p*-type silicon surface and thus, is able to prevent shunting in the critical areas. These higher requirements on the via paste also apply accordingly to the transfer of the MWT technology to *n*-type silicon bulk material.

The challenges with respect to individual processes or process clusters to fabricate *n*-type Cz-Si solar cells with a boron-doped emitter on the front side, a phosphorus doping on the rear side, and screen-printed metallization are discussed in detail. The approach chosen to realize the boron- and phosphorus-doped surfaces within this work is based on utilizing sequential diffusion processes, which are performed in quartz tube furnaces with liquid  $\text{BBr}_3$  and  $\text{POCl}_3$  as dopant precursors, respectively. The process sequence with  $\text{BBr}_3$  diffusion first is assessed as very attractive, as the independent developments in  $\text{BBr}_3$  and  $\text{POCl}_3$  diffusion most likely can be directly implemented in the cell fabrication process.

The first realization of *n*-type Cz-Si MWT solar cells results in a maximum conversion efficiency of 17.7%, demonstrating the overall basic functionality of the fabricated devices. Based on the *p*-type HIP–MWT+ cell concept, two *n*-type MWT structures are introduced. The characteristic feature of those *n*-type MWT cells is that the emitter is present on the front side only and hence, no emitter within the vias and at the rear side exists. These *n*-type MWT cell structures, either with full-area phosphorus doping on the rear side (designated as *n*MWT) or a doping recess in the area of the external *p*-type contacts (designated as *n*MWT+), form the basis for the experiments performed and discussed in the Chapters 6 and 7. However, the former configuration of the *n*MWT structure might represent a major challenge for achieving high pseudo fill factors due to possibly increased risk of leakage currents under forward operation in the area of the external *p*-type contact pads.

## **4      Boron Emitter Formation and Passivation**

### **4.1     Introduction**

This chapter summarizes the performed characterizations and optimizations regarding boron diffusion in a quartz tube furnace using liquid boron tribromide ( $\text{BBr}_3$ ) as dopant precursor. For the *n*-type silicon solar cells investigated in this work, the  $\text{BBr}_3$  diffusion is necessary to form the *p-n*-junction on the front side. Different objectives with respect to optimization of  $\text{BBr}_3$  diffusion processes are discussed, assuming the electrical contactability to be potentially realized by screen-printed and fired metal contacts. A set of test specimens is introduced that allows for determination of characteristic parameters to analyze the various examined  $\text{BBr}_3$  diffusion processes. This set includes samples to extract the homogeneity in sheet resistance across single wafers and from wafer to wafer along the process boat, the boron doping profile, and the recombination of the highly boron-doped surface layers. Of course, apart from these parameters, also metallization-related issues are of high interest, which will be dealt with in Chapter 5. Following the characterization of three basic  $\text{BBr}_3$  diffusion processes, which have been provided by *Tempress Systems*, some of the performed process variations are presented. As sequential diffusion processes with first  $\text{BBr}_3$  and second  $\text{POCl}_3$  diffusion are used for cell fabrication within this work, the diffusion must be restricted to one wafer side. For this purpose, also the qualification of diffusion barrier layers as well as the impact of  $\text{POCl}_3$  diffusion on the boron doping profile is examined.

### **4.2     Boron diffusion with liquid $\text{BBr}_3$ as dopant precursor**

The *p*-type-doped emitter in *n*-type silicon solar cells is frequently formed by using high-temperature atmospheric pressure tube furnace diffusion pro-

cesses with  $\text{BBr}_3$  as a liquid dopant precursor. The industrial system used is the “TS81255” from *Tempress Systems* with five horizontal quartz tubes.

#### 4.2.1 Principle, process sequence, and objectives

A sketch of the quartz tube, in which the  $\text{BBr}_3$  diffusion processes take place, is shown in Fig. 4.1. The quartz boat has 262 slots and can take up wafers with edge lengths up to 156 mm. During diffusion, the wafers are oriented in the so-called diamond position, where one of a wafer’s corners faces the upper side of the tube. An inert carrier gas (nitrogen,  $\text{N}_2$ ) is bubbled through the reservoir with liquid  $\text{BBr}_3$ . Subsequently, the rather small quantity of  $\text{N}_2\text{-BBr}_3$  vapor is mixed with  $\text{N}_2$  and oxygen ( $\text{O}_2$ ) before the gas mixture enters the quartz tube. The temperatures used for boron diffusion usually range from  $\approx 850^\circ\text{C}$  to  $\approx 1000^\circ\text{C}$ . Refer to Chapter 2.3.2 for details about the properties and the diffusion mechanism of boron atoms in silicon, as well as the chemical reactions taking place at the silicon surface.

A typical boron diffusion process with one temperature plateau utilizing  $\text{BBr}_3$  is shown in Fig. 4.2(a). After inserting the quartz boat with the silicon wafers in the quartz tube, the temperature is raised to the processing temperature. This step is performed in inert gas atmosphere with  $\text{N}_2$  only. The second step is the deposition phase, during which  $\text{N}_2\text{-BBr}_3$  is introduced into the tube along with  $\text{O}_2$  and  $\text{N}_2$ . The chemical reaction between  $\text{O}_2$  and  $\text{BBr}_3$  as well as  $\text{O}_2$  and silicon leads to the formation of a borosilicate glass (BSG) on the wafer surfaces; see Chapter 2.3.2. For the following drive-in step, the  $\text{N}_2\text{-BBr}_3$  supply is switched off and the grown BSG layer acts as dopant source. This step can be performed either with  $\text{N}_2 + \text{O}_2$  or just with  $\text{N}_2$ . The last step consists of cooling down with an integrated post-oxidation featuring a significantly higher share of  $\text{O}_2$ . The post-oxida-

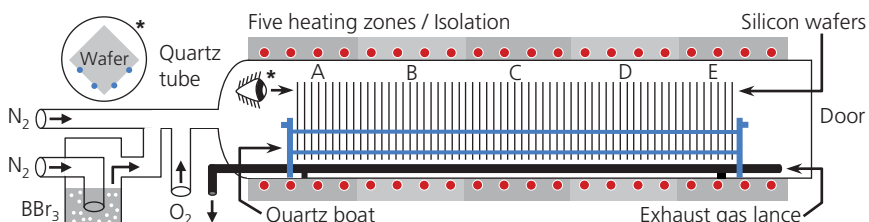


**Fig. 4.1.** Schematic cross section of the quartz tube with resistance heating used for the  $\text{BBr}_3$  diffusion processes (\*the wafers are oriented in the so-called diamond position). The wafer positions in the quartz boat are indicated by the letters A–E.

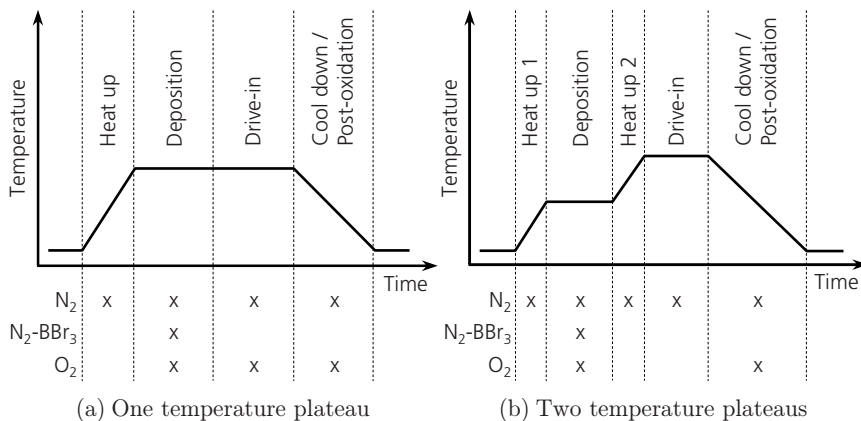


**Fig. 4.2.** Schematic illustration of process sequences with (a) one and (b) two temperature plateaus for boron diffusion utilizing  $\text{BBr}_3$  as liquid dopant precursor. The gases marked with “x” are introduced into the tube at different steps.

tion is performed throughout this work to avoid the presence of a highly recombination-active boron-rich layer (BRL) at the boron-doped silicon surface after  $\text{BBr}_3$  diffusion. A more sophisticated process sequence with two temperature plateaus is depicted in Fig. 4.2(b). The deposition step is performed at lower temperature  $T_{\text{dep}}$  than the drive-in step with  $T_{\text{DrIn}}$ . Both fundamental process sequences are utilized in the following.

The characterization and the development of  $\text{BBr}_3$  diffusion processes are based on different objectives. These include e.g.

- A homogeneous boron doping across wafers with an edge length of 156 mm (synonymous with a homogeneous sheet resistance  $R_{\text{sh}}$ )
- Similar  $R_{\text{sh}}$  for different boat positions A–E (see Fig. 4.1)
- Determination of boron doping profiles in order to understand the relationship between diffusion process and shape of the resulting boron doping
- Low recombination of the highly boron-doped surfaces after passivation and firing (i.e. low dark saturation current densities)
- Electrical contact formation by screen-printed and fired metal contacts to the highly boron-doped silicon surfaces with low specific contact resistance
- Custom-made boron doping profiles in order to investigate their interaction with screen-printed metallization

### 4.2.2 Samples for processes characterization

To characterize  $\text{BBr}_3$  diffusion processes and to determine their quality, various sample types are examined to extract characteristic quantities, such as

- The sheet resistance  $R_{\text{sh}}$  of the boron-doped surface layers
- The  $R_{\text{sh}}$  standard deviation  $\sigma$  as measure for the uniformity of the doping
- The boron doping profile  $N(d)$
- The dark saturation current density  $j_{0e}$  of the highly doped and passivated surfaces
- The specific contact resistance  $\rho_c$  between metal contact and boron-doped silicon

For this purpose, the set of test specimens typically includes the sample types with both-sided boron doping shown in Fig. 4.3. Their following designation is based on the extracted quantities. The corresponding fabrication processes, including the performed measurements to extract the characteristic properties, are illustrated in Fig. 4.4. Initially, all sample types undergo the same process flow (apart from the surface formation) up to the determination of the emitter sheet resistances  $R_{\text{sh}}$  after  $\text{BBr}_3$  diffusion. The different sample types will now be briefly introduced.

#### Samples for determining emitter sheet resistances $R_{\text{sh}}$

The emitter sheet resistances  $R_{\text{sh}}$  after diffusion are determined using the  $R_{\text{sh}}$  samples illustrated in Fig. 4.3(a) and (b). The surfaces can be either alkaline saw-damage etched or alkaline textured, depending on which surface is to be examined. One method to measure  $R_{\text{sh}}$  is based on inductive coupling [199], which is a non-destructive measurement method. The bulk doping type is irrelevant for this measurement method as only differences in  $R_{\text{sh}}$  are considered (no  $p$ - $n$ -junction is required). More specifically,  $R_{\text{sh}}$  is calculated from the bulk resistance<sup>17</sup> (measured before diffusion) and the total sheet resistance of the both sides diffused wafer (measured after diffusion). In doing so, a parallel connection of the differently doped layers is assumed.  $R_{\text{sh}}$  is the mean value for the various measurement locations; i.e. multiple measurements are performed along the wafer length on three parallel straight lines (see Appendix B.3). This method can be used to determine  $R_{\text{sh}}$  on wafers with BSG layer directly after boron diffusion (see Fig. 4.3(a)), or af-

<sup>17</sup>Any existing thermal donors [200] have been previously dissolved during a high-temperature step.

ter removal of the BSG (see Fig. 4.3(b)). It is found that the  $R_{\text{sh}}$  obtained on the same sample once with and once without BSG layer are equal to each other. Furthermore, the standard deviation  $\sigma$  of the measured data points is determined for each sample representing a measure for the homogeneity in  $R_{\text{sh}}$  across the measurement range.

Another method to determine  $R_{\text{sh}}$  represents the 4-point-probe (4pp) technique [31,199], which permits direct  $R_{\text{sh},4\text{pp}}$  measurements on the boron-doped surfaces after BSG etch (Fig. 4.3(b)), in case n-type silicon wafers are used. With the 4pp method, spatially resolved  $R_{\text{sh},4\text{pp}}$  mappings with 20 x 20 measuring points (distance 7.7 mm) across almost the whole wafer

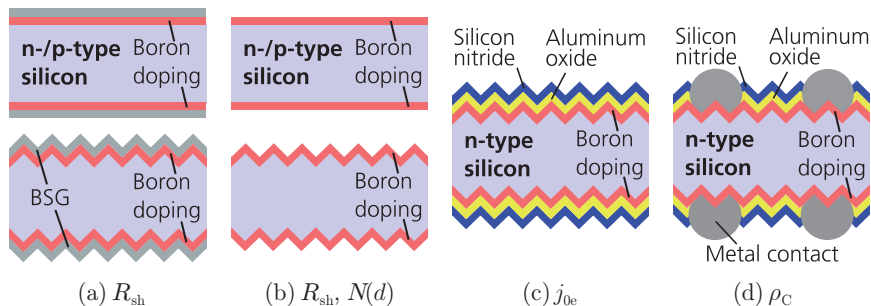


**Fig. 4.3.** Schematic cross sections of different symmetric sample types used to characterize BBr<sub>3</sub> diffusion processes with regard to different parameters: (a,b) sheet resistance  $R_{\text{sh}}$ , (b) boron doping profile  $N(d)$ , (c) dark saturation current density  $j_{0e}$ , and (d) specific contact resistance  $\rho_c$ .

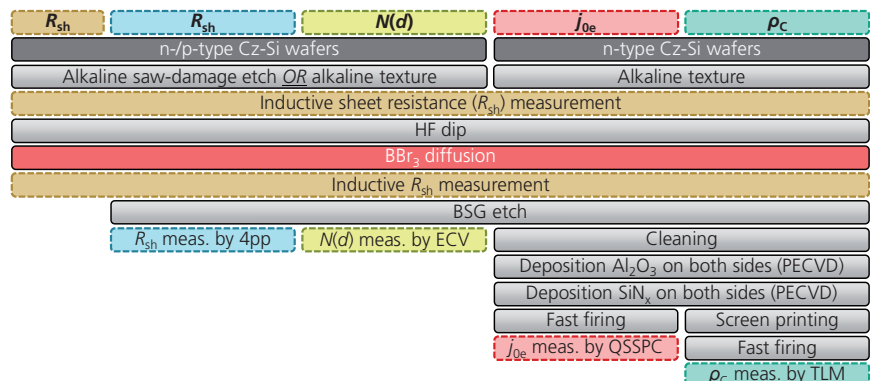


**Fig. 4.4.** Schematic process sequences for fabrication of the characterization samples shown in Fig. 4.3. The utilized characterization techniques are marked by colored boxes with dashed borders.

surface are made. Again, the standard deviation  $\sigma_{4\text{pp}}$  of the measured data points is a measure for the homogeneity of the formed boron-doped layers.

Note that data relating to 4pp measurements are indicated by the subscript “4pp” in this work. Data relating to inductive  $R_{\text{sh}}$  measurements are shown without additional index.

### Samples for determining boron doping profiles $N(d)$

Using the samples just discussed (Fig. 4.3(b)), boron doping profiles  $N(d)$  can be extracted from electrochemical capacitance-voltage (ECV) measurements. With the ECV method, the amount of charge carriers is determined [81]. Although the surfaces of the solar cells are alkaline textured, the doping profiles within this chapter are always determined on alkaline saw-damage etched surfaces, as ECV measurements on flat surfaces are more reliable than on textured ones. Refer to Appendix B.2 with respect to the ECV measurement principle and measurement uncertainties.

### Samples for determining emitter dark saturation current densities $j_{0e}$

Dark saturation current densities  $j_{0e}$  of the alkaline textured, boron-doped, and passivated surfaces are determined by quasi-steady-state photoconductance (QSSPC) measurements; see Fig. 4.3(c) for the cross section of the  $j_{0e}$  samples. Refer to Chapter 2.2.2 for more information about the method for extracting  $j_{0e}$ . Within this chapter, all  $j_{0e}$  samples are passivated by a layer stack consisting of  $\text{Al}_2\text{O}_3$  and  $\text{SiN}_x$ , both applied by PECVD. The passivation mechanism of the passivation layers is activated by a fast firing process in a conveyer belt furnace at temperatures representative for  $n$ -type solar cells. The  $j_{0e}$  samples resemble the front side of the  $n$ -type solar cells to be developed.

### Samples for determining specific contact resistances $\rho_c$

The  $\rho_c$  samples in Fig. 4.3(d) enable the determination of specific contact resistances  $\rho_c$  to evaluate the electrical contact between metal contacts and the boron-doped surfaces. Subsequent to the BSG etch, cleaning, and the both-sided deposition of the passivation layer stack, the metal contacts on either side are formed by screen printing. Subsequently, contact formation takes place during fast firing in a conveyer belt furnace. Apart from the possibility to examine two different pastes on each  $\rho_c$  sample, the both-sided metallization equals the final solar cell metallization and hence,

wafer temperatures are comparable in both cases. The  $\rho_C$  measurement is performed according to the transmission line model (TLM) [201,202], which is described in more detail in Appendix B.4. Within the course of this work, the  $\rho_C$  samples have been used extensively for process development concerning  $BBr_3$  diffusion and for evaluation of screen-printing pastes. However, all  $\rho_C$  dealt with starting in Chapter 5 are determined using complete solar cell structures.

## 4.3 Characterization of basic diffusion processes

In the course of this work, the process parameters for three generations of  $BBr_3$  diffusion processes have been provided by *Tempress Systems*. These basic diffusion processes are referred to as Gen1–Gen3 in the following<sup>18</sup>.

### 4.3.1 Process description and approach

The processes Gen1 and Gen2 are based on process sequences with one temperature plateau, as shown in Fig. 4.2(a). In contrast, the Gen3 process is based on a process sequence with two temperature plateaus, see Fig. 4.2(b). For Gen3,  $T_{dep}$  is lower as for Gen1/Gen2, while  $T_{DrIn}$  is higher. Two characteristic gas flux ratios during the deposition step of the diffusion processes relative to process Gen1 are stated in Table 4.1. From Gen1 to Gen2, the ratio between  $N_2-BBr_3$  and  $O_2$  is kept constant, while the ratio of  $N_2-BBr_3+O_2$  to  $N_2$  is reduced by 67%. This means that process Gen2 is performed with significantly less  $N_2-BBr_3$  flux. Process Gen3 features a slightly larger ratio between  $N_2-BBr_3$  and  $O_2$  as process Gen1, but the  $N_2-BBr_3$  share is also significantly reduced. In this case, the ratio between  $N_2-BBr_3+O_2$  and  $N_2$  is reduced by 51%. For all three process generations, the sum of deposition time and drive-in time is virtually identical, only the ratios of the two times with each other vary significantly. For diffusion process Gen3, an additional variation is performed. Diffusion process Gen3\* features identical process parameters as process Gen3, but no post-oxidation after the drive-in step.

**Table 4.1.** Changes in gas fluxes  $\Delta g_f$  during the deposition step for the  $BBr_3$  diffusion processes Gen2 and Gen3 with respect to process Gen1.

Changes relative to Gen1	Gen1	Gen2	Gen3
$\Delta g_f (N_2-BBr_3/O_2)$ (%)	–	0	+2.2
$\Delta g_f ([N_2-BBr_3+O_2]/N_2)$ (%)	–	-67	-51

<sup>18</sup>Date of availability: Gen1 (November 2012), Gen2 (November 2013), and Gen3 (January 2014).

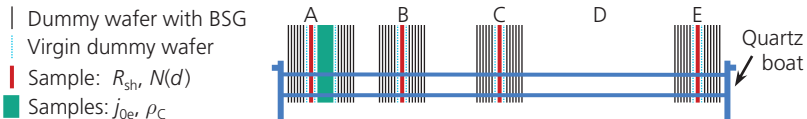


**Fig. 4.5.** Schematic illustration of the wafer arrangement in the quartz boat for the characterization of  $\text{BBr}_3$  diffusion processes (not so scale, 50 wafers fit at each position). The boat positions are indicated by A–E (see also Fig. 4.1). Position A is located at the gas inlet, position E by the furnace door. The neighboring wafers to the samples of either type are virgin wafers to prevent any influence of a BSG covered surface.

A typical arrangement of the wafers in the quartz boat is depicted in Fig. 4.5, as it is used for the characterization of the  $\text{BBr}_3$  diffusion processes within this chapter. The gas inlet is located on the left, the door on the right hand side; see Fig. 4.1. At each position under study (A–C, E), the test samples are surrounded by one virgin dummy wafer on each side. One  $R_{\text{sh}}/N(d)$  sample is located at positions B, C, and E, whereas at position A, also several  $j_{\text{oe}}$  and  $\rho_C$  samples are present apart from the  $R_{\text{sh}}/N(d)$  sample. Each sample package is surrounded by six BSG-coated dummy wafers on either side. Unless otherwise stated, the results presented in the following refer to samples located at position A.

### 4.3.2 Emitter sheet resistances

The  $R_{\text{sh},4\text{pp}}$  distributions determined by 4pp measurements across wafers with 156 mm edge length for the different process generations shows Fig. 4.6. The lower left wafer corner showed towards the upper part of the tube furnace during the  $\text{BBr}_3$  diffusion processes; see also Fig. 4.1. The highest  $R_{\text{sh},4\text{pp}}$  are obtained for the upper right corner (bottom of the boat), whereas the lowest  $R_{\text{sh},4\text{pp}}$  are apparent for the lower left corner (top of the boat). This diagonal trend is very strongly pronounced especially for diffusion process Gen1. It is also apparent that  $R_{\text{sh},4\text{pp}}$  varies most across the wafer for process Gen1. Looking at the wafers directly after the respective diffusion processes (not shown), the discoloration of the surface, which is related to the BSG layer thickness, is significantly more inhomogeneous for process Gen1 than for the others.

Some characteristic  $R_{\text{sh}}$  parameters are summarized in Table 4.2, both for the 4pp measurements (top) as well as the conducted inductive measurements (bottom). The obtained mean  $R_{\text{sh}}$  between 60  $\Omega/\text{sq}$  and 70  $\Omega/\text{sq}$  are quite similar for both measuring methods for the respective  $\text{BBr}_3$  diffusion, and  $R_{\text{sh}}$  decreases across the different generations. In terms of percentaged

### 4.3 Characterization of basic diffusion processes

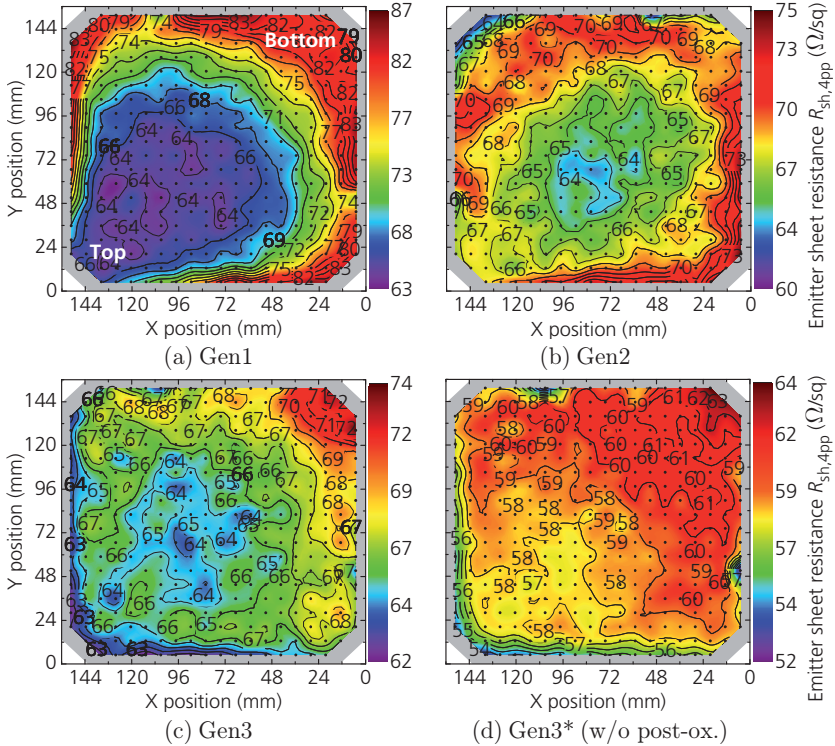


**Fig. 4.6.** Mapping of emitter sheet resistances  $R_{sh,4pp}$  obtained by 4pp measurements on alkaline saw-damage etched  $n$ -type Cz-Si wafers for  $BB_3$  diffusion processes (a) Gen1, (b) Gen2, (c) Gen3, and (d) Gen3\*. As indicated in (a), the lower left corner showed towards the upper part of the tube; see also Fig. 4.1. The black dots illustrate the  $20 \times 20$  measurement pattern on the sample, which is indicated by the grey shaded wafer in the background. Note that the scaling is different for all four  $R_{sh}$  plots.

**Table 4.2.** Characteristic  $R_{sh}$  parameters for the samples shown in Fig. 4.6 with alkaline saw-damage etched surface, determined by 4pp measurements (top) and inductive inline measurements (bottom). The mean, minimum, and maximum values in  $R_{sh}$  as well as the percentage standard deviation  $\sigma$  (equal to standard deviation divided by  $R_{sh}$ ) are stated for Gen1 to Gen3.

	$BB_3$ diffusion process		Gen1	Gen2	Gen3	Gen3*
4pp meas.	$R_{sh,4pp}$ mean	( $\Omega/sq$ )	72	68	66	59
	$R_{sh,4pp}$ std.-dev. $\sigma_{4pp}$	(%)	8.8	3.4	2.7	2.7
	$R_{sh,4pp}$ min./max.	( $\Omega/sq$ )	63/87	61/75	62/74	52/64
Induc- tive meas.	$R_{sh}$ mean	( $\Omega/sq$ )	71	69	69	60
	$R_{sh}$ std.-dev. $\sigma$	(%)	7.6	1.7	2.0	2.1
	$R_{sh}$ min./max.	( $\Omega/sq$ )	65/84	66/71	67/73	58/63

standard deviation  $\sigma$  (equal to standard deviation divided by  $R_{\text{sh}}$ ), the 4pp measurements yield higher values compared with the inductive measurements, since the measuring points for the 4pp measurement are equally distributed across almost the entire wafer surface, while the inductive measurement is only performed over three lines in vertical direction; see Fig. B.2 in Appendix B.3. Hence, the 4pp method is more sensitive to  $R_{\text{sh}}$  inhomogeneities occurring particularly in the wafer edge regions which the inductive measurement tool does not completely capture. Hence, the spatial resolution of the 4pp method is much higher. However, the inductive measurements, which are carried out by default prior and after  $\text{BBr}_3$  diffusion also point out the important trends and are thus a meaningful way to simply measure  $R_{\text{sh}}$  and  $\sigma$  for a large number of wafers. Inductive and 4pp measurements performed on samples with alkaline textured surface (not shown) yield nearly the same  $R_{\text{sh}}$  as the ones performed on samples with alkaline saw-damage etched surface.

The improvement in the single wafer's  $R_{\text{sh}}$  homogeneity over the process generations is clearly evident. The standard deviation  $\sigma_{\text{4pp}}$  across the wafers decreases for the 4pp measurements from 8.8% for Gen1, to 3.4% for Gen2, and finally to only 2.7% for Gen3. Despite reduced  $\text{N}_2\text{-BBr}_3$  flux for process Gen2, see Table 4.1,  $\sigma_{\text{4pp}}$  is significantly reduced compared with process Gen1. The two plateau process Gen3—the deposition step is carried out at lower  $T_{\text{dep}}$  than the drive-in step with  $T_{\text{Dri}}$ —with also less  $\text{N}_2\text{-BBr}_3$  flux than in process Gen1 improves uniformity further. For all three generations, the minimum  $R_{\text{sh},\text{4pp}}$  are about  $60 \Omega/\text{sq}$ , while the maximum  $R_{\text{sh},\text{4pp}}$  is much higher for Gen1. The comparison between Gen3 and Gen3\* (without post-oxidation) reveals that the post-oxidation leads to an increase in  $R_{\text{sh},\text{4pp}}$ . Expressed in numbers this means an increase from  $R_{\text{sh},\text{4pp}} = (59 \pm 3) \Omega/\text{sq}$  for Gen3\* to  $R_{\text{sh},\text{4pp}} = (66 \pm 3) \Omega/\text{sq}$  for Gen3, which is equivalent to about 10%. On the other hand, no impact on  $\sigma_{\text{4pp}}$  is observed when post-oxidation is incorporated into the diffusion process. Corresponding trends yield the inductive inline measurements. Further details on this topic are discussed in section 4.3.3. Note that the values for  $R_{\text{sh}}$  and  $\sigma$  stated in the following sections refer to the inductive inline measurements.

For a homogeneous performance of solar cells over their full area, the homogeneity in  $R_{\text{sh}}$  over each wafer is of major importance. Furthermore, the homogeneity in  $R_{\text{sh}}$  from wafer to wafer along the process boat is crucial for the performance of a whole cell bath. According to the wafer arrangement introduced in Fig. 4.5, the homogeneity of the four  $\text{BBr}_3$  diffusion processes is examined at different boat positions (A–C, E). The results are summarized

**Table 4.3.** Mean emitter sheet resistances  $R_{\text{sh}}$  and standard deviations  $\sigma$  determined by inductive measurements on alkaline saw-damage etched  $R_{\text{sh}}$  samples processed with the four  $\text{BBr}_3$  diffusions at the different boat positions A–C, and E (see Fig. 4.5).

Boat position → $\text{BBr}_3$ diffusion	A		B		C		E	
	$R_{\text{sh}}$ ( $\Omega/\text{sq}$ )	$\sigma$ (%)						
Gen1	71	7.6	70	5.9	70	6.3	—	—
Gen2	69	1.7	68	3.9	72	2.3	—	—
Gen3	69	2.0	69	2.0	70	1.5	70	1.4
Gen3*	60	2.1	61	1.9	63	1.3	—	—

in Table 4.3. Note that position E is examined only for Gen3. For each diffusion process, the mean  $R_{\text{sh}}$  are quite similar for the different boat positions. The remaining differences in  $R_{\text{sh}}$  can be reduced by adjusting the temperatures of the five individually controlled heating zones; see Fig. 4.1. However, this was not carried out in this thesis. Regarding the standard deviation  $\sigma$ , the different boat positions result in partially different values within each diffusion processes, particularly for Gen1 and Gen2. On the other hand, processes Gen3 and Gen3\* show  $\sigma \leq 2.1\%$  for each examined boat position. Even at position E, the position farthest from the gas inlet,  $\sigma$  is not increased for Gen3. This shows that fairly low  $\sigma$  across the wafers and hence, a high homogeneity in  $R_{\text{sh}}$  might be achieved along the whole process boat in case of full load for process generation Gen3.

### 4.3.3 Doping profiles

The resulting doping profiles  $N(d)$  are determined by ECV measurements on samples with alkaline saw-damage etched surfaces. The profiles extracted at the wafer center are shown in Fig. 4.7(a). As introduced based on Fig. 4.2, diffusion processes Gen1–Gen3 feature a post-oxidation step at the end of the diffusion process, which leads to the pronounced boron depletion at the wafer surface due to segregation of boron into the growing  $\text{SiO}_2$  layer at the silicon interface; see Chapter 2.3.2. For Gen3\*, in which no post-oxidation is incorporated, the depletion at the surface is much less pronounced, leading to  $\approx 10\%$  lower  $R_{\text{sh}}$ . The  $R_{\text{sh}}$  measured by means of inductive coupling as well as the maximum dopant concentrations  $N_{\text{max}}$  are depicted in the graph.

It is striking that the doping profiles show a steeper drop in  $N(d)$  for boron concentrations  $N(d) \lesssim 10^{19} \text{ cm}^{-3}$ . From literature [69,70] it is known that diffusion profiles with concentrations  $N(d) > 10^{19} \text{ cm}^{-3}$  cannot be correctly described by simple complementary error functions, Eq. (2.31), or Gaussian

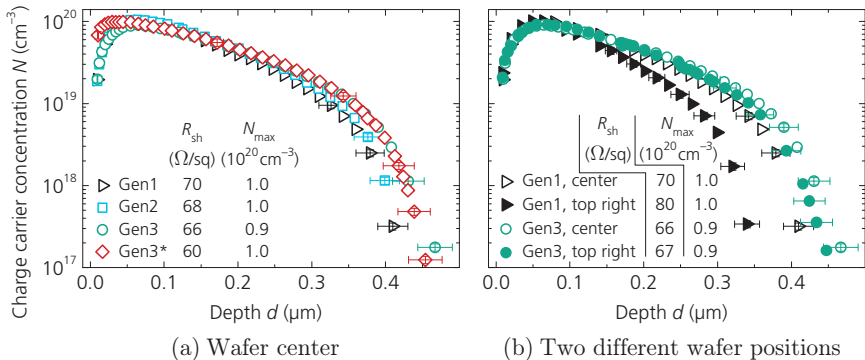


**Fig. 4.7.** Boron doping profiles  $N(d)$ , determined by ECV measurements on alkaline saw-damage etched surfaces for the different  $\text{BBr}_3$  diffusion process generations. The measurements are performed at (a) the wafer center for the four processes and at (b) the wafer center as well as the top right wafer corner (labeled with “bottom” in Fig. 4.6) for processes Gen1 and Gen3. Exemplary error bars are shown. The given  $R_{\text{sh}}$  correspond to inductive measurements performed at the respective spots.

functions, Eq. (2.33). This is due to the fact that the effective boron diffusion coefficient  $D_{B,\text{eff}}$  is not constant with boron concentration. In fact,  $D_{B,\text{eff}}$  is reported to be essentially constant for  $N(d) < 10^{19} \text{ cm}^{-3}$ , while it increases towards larger doping concentrations [65,69–71]. This deviation from Fick’s law (Eq. (2.26)) is not astonishing, as the flux of migrating boron atoms is not purely determined by the local gradient in the substitutional boron concentration (i.e. the boron atom flux is mediated by the interstitial diffusion mechanism; see Chapter 2.3.2).

The  $N_{\max}$  given in Fig. 4.7(a) are in agreement with the solubility limit of boron in silicon; see Fig. 2.7. Processes Gen1 and Gen2 show very similar profile progressions with similar  $N_{\max} = (1.0 \pm 0.1) \cdot 10^{20} \text{ cm}^{-3}$  and profile depth  $d = (420 \pm 42) \text{ nm}$  (determined at  $N = 10^{17} \text{ cm}^{-3}$ ), resulting in a similar  $R_{\text{sh}} \approx 70 \Omega/\text{sq}$ . Gen3 shows a slightly lower  $N_{\max} = (0.91 \pm 0.09) \cdot 10^{20} \text{ cm}^{-3}$ , and a slightly deeper profile with  $d = (460 \pm 46) \text{ nm}$ , resulting in  $R_{\text{sh}} \approx 66 \Omega/\text{sq}$ . Due to the not performed post-oxidation for Gen3\*,  $N_{\max} = (1.0 \pm 0.1) \cdot 10^{20} \text{ cm}^{-3}$  is somewhat higher for process Gen3\* than for process Gen3.

The total amount of boron atoms  $Q_{\text{tot}}$  present in the silicon is  $Q_{\text{tot}} = (1.7 \pm 0.2) \cdot 10^{15} \text{ cm}^{-2}$  for Gen1 and Gen3,  $Q_{\text{tot}} = (1.8 \pm 0.2) \cdot 10^{15} \text{ cm}^{-2}$  for Gen2, and  $Q_{\text{tot}} = (1.9 \pm 0.2) \cdot 10^{15} \text{ cm}^{-2}$  for Gen3\*. The difference in  $Q_{\text{tot}}$  between Gen3\* and Gen3 yields  $\Delta Q_{\text{tot}} = (0.2 \pm 0.3) \cdot 10^{15} \text{ cm}^{-2}$ . It seems that due to post-oxidation, less boron atoms remain in the silicon for diffusion process Gen3.

Comparing ECV measurements in Fig. 4.7(b) performed at two wafer locations with different  $R_{\text{sh}}$  values (wafer center and top right corner in Fig. 4.6) reveals that for Gen1, the distribution in  $R_{\text{sh}}$  over the wafer surface correlates with a variation in profile depth  $d$  and rather not in  $N_{\text{max}}$ . The doping profiles on those two locations have nearly identical  $N_{\text{max}}$ , but significantly different depths  $d$ . As already mentioned, the discoloration of the BSG covered surface and thus, the BSG layer thickness, is least homogenous on the wafers processed with diffusion Gen1. Hence, the different depths  $d$  might be explained by local differences in the effective boron diffusion coefficient  $D_{\text{B,eff}}$  for  $N(d) > 10^{19} \text{ cm}^{-3}$  across the wafer. This means that  $D_{\text{B,eff}}$  is lower for the top right corner compared with  $D_{\text{B,eff}}$  in the wafer center. In contrast, Gen3 yields nearly identical measurements of both  $N_{\text{max}}$  and  $d$  at the different wafer locations, as this process features a very homogeneous BSG layer and thus, boron diffusion. The same findings hold for the processes Gen2 and Gen3\* (not shown).

#### 4.3.4 Emitter dark saturation current densities

The emitter dark saturation current densities  $j_{0e}$  of the alkaline textured  $j_{0e}$  samples are determined from QSSPC measurements according to Eq. (2.18), as described in Chapter 2.2.2. On each  $j_{0e}$  sample, five QSSPC measurements are performed at the positions indicated in Fig. 4.8. The error on the extracted  $j_{0e}$  is assumed to be  $\pm 10\%$ . However, the error bars shown for  $j_{0e}$  in the following represent the standard deviation of the measurement data reflect-

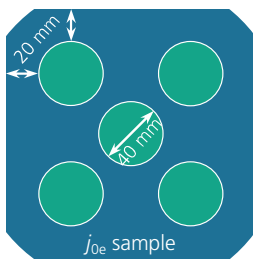


**Fig. 4.8.** Pseudo-square wafer with 156 mm edge length and marked positions for QSSPC measurements to determine  $j_{0e}$  at different positions (ratios are to scale; see also Fig. 2.2(b)).

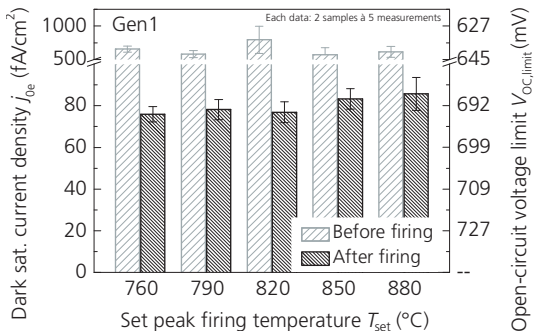


**Fig. 4.9.** Dark saturation current densities  $j_{0e}$  of alkaline textured  $j_{0e}$  samples processed with  $\text{BBr}_3$  diffusion Gen1 before and after firing at different set peak firing temperatures. The passivation consists of PECVD  $\text{Al}_2\text{O}_3$  and  $\text{SiN}_x$  layers. The  $V_{\text{OC,limit}}$  is calculated according to Eq. (2.20) utilizing  $j_{\text{ph}} = 39 \text{ mA/cm}^2$ .

ing the uniformity in  $j_{0e}$  over the wafer surface for more than one wafer.

The need for activation of the passivation property of the passivation layer stack, consisting of  $\text{Al}_2\text{O}_3$  and  $\text{SiN}_x$  layers both applied by PECVD, is clear by studying the  $j_{0e}$  results for  $\text{BBr}_3$  diffusion Gen1, shown in Fig. 4.9. Before firing, the obtained  $j_{0e}$  clearly exceed  $500 \text{ fA/cm}^2$ . After firing with set peak firing temperatures in the range between  $760^\circ\text{C} \leq T_{\text{set}} \leq 880^\circ\text{C}$ , the chemical passivation property is activated resulting in significantly lower  $j_{0e} = (80 \pm 5) \text{ fA/cm}^2$ . This activation is correlated with the diffusion of e.g. hydrogen from the  $\text{Al}_2\text{O}_3$  or  $\text{SiN}_x$  layer (which is more likely) to the silicon interface, where it effectively saturates dangling bonds [175–177]. Up to a temperature of  $820^\circ\text{C}$ , the  $j_{0e} = (77 \pm 5) \text{ fA/cm}^2$  are not influenced by increased firing temperature. For higher temperatures, the measured  $j_{0e}$  slightly increase to  $j_{0e} = (85 \pm 6) \text{ fA/cm}^2$ . This increase might be correlated with the onset of blistering [203]. Hence, the set peak temperature used for firing the  $j_{0e}$  samples is always  $790^\circ\text{C}$  in the following. According to Eq. (2.20), a limit in open open-circuit voltage  $V_{\text{OC},\text{limit}}$  can be calculated based on the measured  $j_{0e}$ , using a photo current density  $j_{\text{ph}} = 39 \text{ mA/cm}^2$ , and temperature  $T = 25^\circ\text{C}$ . A  $j_{0e} = 77 \text{ fA/cm}^2$  is equal to  $V_{\text{OC},\text{limit}} = 692 \text{ mV}$ .

A comparison of  $j_{0e}$  values for all four  $\text{BBr}_3$  diffusion processes is illustrated in Fig. 4.10(a). Processes Gen1 and Gen2 are at the same level with  $j_{0e} = (77 \pm 5) \text{ fA/cm}^2$  and  $j_{0e} = (76 \pm 5) \text{ fA/cm}^2$ , respectively, as expected since the doping profiles shown in Fig. 4.7 are almost identical. Process

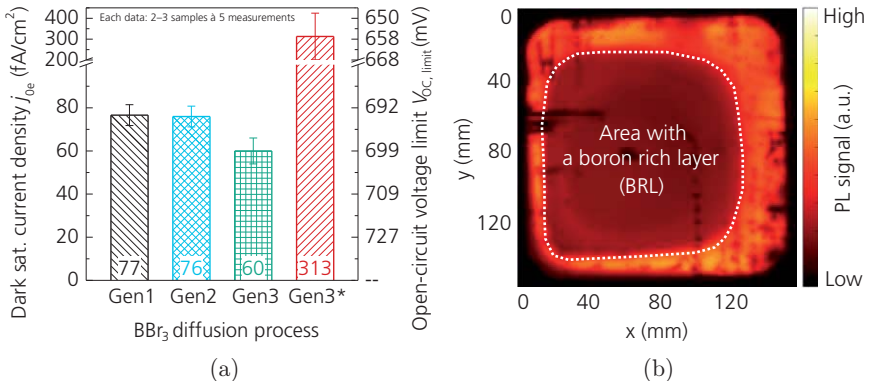


**Fig. 4.10.** (a) Dark saturation current densities  $j_{0e}$  of alkaline textured  $j_{0e}$  samples (PECVD  $\text{Al}_2\text{O}_3/\text{SiN}_x$ ) after firing processed with the indicated  $\text{BBr}_3$  diffusion processes. The  $V_{\text{OC},\text{limit}}$  is calculated according to Eq. (2.20) utilizing  $j_{\text{ph}} = 39 \text{ mA/cm}^2$ . (b) PL image of a  $j_{0e}$  sample with boron emitter Gen3\*.

Gen3 yields lower  $j_{0e} = (60 \pm 6) \text{ fA/cm}^2$  due to reduced  $N_{\max}$  (i.e. less Auger recombination), whereas process Gen3\* without post-oxidation shows significant higher  $j_{0e} = (313 \pm 112) \text{ fA/cm}^2$ . This high  $j_{0e}$  suggests that a boron rich layer (BRL) is present at the surface and is the reason for the higher recombination. This assumption is confirmed by the photoluminescence (PL) image shown in Fig. 4.10(b). The region with a BRL is clearly visible. This part of the wafer surface also stayed hydrophilic after removal of the BSG layer in HF solution, which is a hint for a potential presence of a BRL. In case no BRL is present, the surfaces are perfectly hydrophobic directly after removal of the BSG layer, as this has been observed for the diffusion processes Gen1–Gen3. While the surface depletion is reduced utilizing diffusion process Gen3\*, see Fig. 4.7(a), a BRL remains at the wafer surfaces<sup>19</sup> due to the omitted post-oxidation, which makes this diffusion process unfavorable for implementation in solar cells.

#### 4.3.5 Impact of varied drive-in temperatures

The impact of different drive-in temperatures  $T_{\text{DrIn}}$  for the three process generations Gen1–Gen3 on emitter sheet resistance  $R_{\text{sh}}$ , maximum dopant concentration  $N_{\max}$ , and profile depth  $d$  is also studied; see Fig. 4.11. The results for different  $T_{\text{DrIn}}$  are plotted against the normalized drive-in temperatures  $T_{\text{DrIn,norm}}$  with respect to the diffusion processes Gen1/Gen2. It is

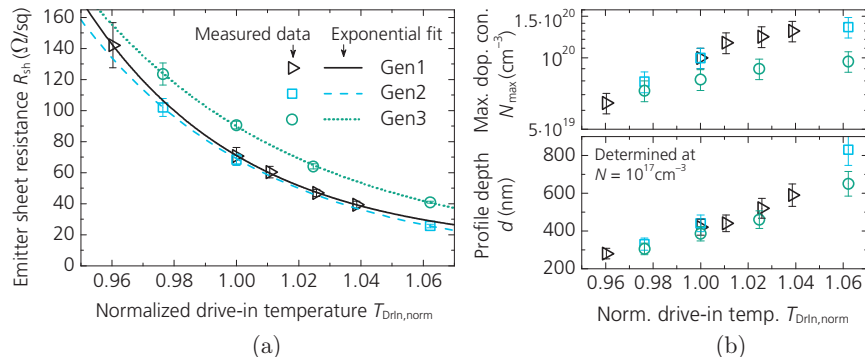


**Fig. 4.11.** (a) Emitter sheet resistances  $R_{\text{sh}}$  plotted against normalized drive-in temperatures  $T_{\text{DrIn,norm}} = T_{\text{DrIn}} / T_{\text{DrIn(Gen1,Gen2)}}$  for  $\text{BBr}_3$  diffusion processes which are based on Gen1–Gen3. (b) Maximum dopant concentration  $N_{\max}$  (top) and profile depths  $d$  (bottom) determined at  $N = 10^{17} \text{ cm}^{-3}$  plotted against  $T_{\text{DrIn,norm}}$ . For both quantities, the error of each measuring point is assumed to be  $\pm 10\%$ .

<sup>19</sup>As the ECV technique only measures charge carriers, the electrically inactive  $\text{SiB}_{4-6}$  compounds, which are characteristic for a BRL, are not detectable by ECV.

found that the correlation between  $T_{\text{DrIn,norm}}$  and  $R_{\text{sh}}$  is very similar for processes based on the generations Gen1 and Gen2, which can be empirically described by almost the same exponential function; see Fig. 4.11(a). For diffusion processes based on generation Gen3, the exponential fit is shifted by  $\approx 20 \Omega/\text{sq}$  towards higher  $R_{\text{sh}}$  compared to Gen1 and Gen2. The reason therefore is that both  $N_{\text{max}}$  and  $d$  are lower for Gen3-based processes for the same  $T_{\text{DrIn,norm}}$ ; see Fig. 4.11(b).

## 4.4 Formation of custom-made doping profiles

In order to obtain custom-made doping profiles for different purposes, a variety of  $\text{BBr}_3$  diffusion processes have been examined. In the following, some of the performed variations based on diffusion process Gen3 are discussed. Apart from lowering  $j_{0e}$ , also obtaining a better understanding of the decrease of  $N_{\text{max}}$  or the increase of the profile depth  $d$  is in focus. The resulting profiles enable e.g. the investigation of the interaction between profile shape of the boron doping and the specific contact resistance  $\rho_C$  of metal contacts, as this will be examined in Chapter 5. Finally, whether or not the doping depletion zone increases recombination—and hence  $j_{0e}$ —at the boron-doped surfaces is examined.

### 4.4.1 Doping profiles with deeper junction

One possible approach to increase the junction depth  $d$  while maintaining  $N_{\text{max}}$  for process Gen3 is to extend the drive-in time  $t_{\text{DrIn}}$  while keeping all other parameters the same. Fig. 4.12(a) shows a variation in  $t_{\text{DrIn}}$ . Thereby, diffusion process Gen3 forms the reference profile with  $t_{\text{DrIn}} = t_1$ . For diffusion processes Gen3-DrIn1 and Gen3-DrIn2,  $t_{\text{DrIn}}$  is extended to  $3t_1$  and  $6t_1$ , respectively. It is evident that the profile depths  $d$  increase significantly when  $t_{\text{DrIn}}$  is increased ( $d$  increases by a factor of approximately 2 for six times longer  $t_{\text{DrIn}}$ ). On the other hand,  $N_{\text{max}} \approx 9 \cdot 10^{19} \text{ cm}^{-3}$  is found to be in the same range for all three profiles, and the curve progressions are identical up to  $d \approx 60 \text{ nm}$ . For  $t_{\text{DrIn}}$  under study, the BSG layers represent an unlimited dopant source. As discussed before, the profile shapes cannot be correctly described by the complementary error function, as given in Eq. (2.31), for one constant effective boron diffusion coefficient  $D_{\text{B,eff}}$ . Nevertheless, the impact of longer  $t_{\text{DrIn}}$  can be evaluated qualitatively by the complementary error function by considering two different  $D_{\text{B,eff}}$ , once for  $N(d) > 10^{19} \text{ cm}^{-3}$  and once for  $N(d) \leq 10^{19} \text{ cm}^{-3}$ . This rough estimate (not

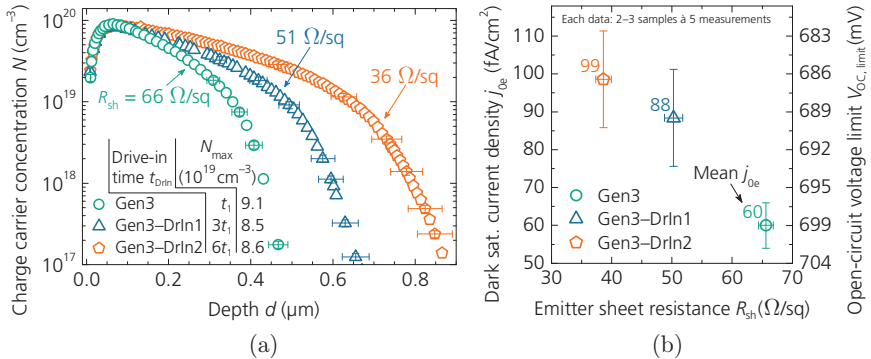


**Fig. 4.12.** (a) Boron doping profiles  $N(d)$ , determined by ECV measurements on alkaline saw-damage etched surfaces for the indicated  $\text{BBr}_3$  diffusion processes. Exemplary error bars are shown. (b) Dark saturation current densities  $j_{0e}$  of alkaline textured  $j_{0e}$  samples (PECVD  $\text{Al}_2\text{O}_3/\text{SiN}_x$ ) after firing depending on  $R_{sh}$ . The  $V_{OC,limit}$  is calculated according to Eq. (2.20) utilizing  $j_{ph} = 39 \text{ mA}/\text{cm}^2$ . Note that the given  $R_{sh}$  in (a) relate only to the area where the ECV measurements are performed and thus, their values might be somewhat different to the  $R_{sh}$  given in (b).

shown) qualitatively yields the same relationship between  $d$  and  $t_{DrIn}$  as mentioned above. When  $t_{DrIn}$  is increased as specified,  $R_{sh}$  decreases from initially  $66 \Omega/\text{sq}$  for Gen3 to  $36 \Omega/\text{sq}$  for Gen3-DrIn2. The standard deviations  $\sigma$  over the wafers remain at very low levels with  $\sigma = 1.2\%$  for Gen3-DrIn1 and  $\sigma = 2.8\%$  for Gen3-DrIn2.

The  $j_{0e}$  determined on  $j_{0e}$  samples with alkaline texture for the three diffusion processes are summarized in Fig. 4.12(b). A linear relationship arises for the  $j_{0e}$  with respect to  $R_{sh}$ : the higher  $R_{sh}$ , the lower  $j_{0e}$ . The diffusion processes Gen3-DrIn1 and Gen3-DrIn2 result in  $j_{0e} = (88 \pm 13) \text{ fA}/\text{cm}^2$  and  $j_{0e} = (99 \pm 13) \text{ fA}/\text{cm}^2$ , respectively, which are higher as for process Gen3 with  $j_{0e} = (60 \pm 6) \text{ fA}/\text{cm}^2$ . These higher  $j_{0e}$  are because Auger recombination increases for increasing  $d$ , while the surface recombination velocity is identical for all three doping profiles (profile progressions are identical near the surface).

#### 4.4.2 Doping profiles with lower surface dopant concentration

In order to lower the maximum dopant concentration  $N_{max}$ , one approach is to vary the post-oxidation (PO) step which follows the drive-in phase. Starting from diffusion process Gen3 with standard (Std) post-oxidation, five further diffusion processes with different post-oxidations are examined for this purpose while all other parameters are kept the same; see Fig. 4.13(a). For

process Gen3–PO1, the post-oxidation step takes place during the whole cool-down (CD) phase starting from the drive-in temperature  $T_{\text{DrIn}}$ . For processes Gen3–PO2 to Gen3–PO5, the post-oxidation also starts at  $T_{\text{DrIn}}$ , but the temperature is first kept constant for a certain time  $t_{\text{PO}}$  before the cool-down phase begins. Thereby,  $t_{\text{PO}}$  is stepwise increased between  $t_{\text{PO}} = t_2$  and  $t_{\text{PO}} = 6t_2$ . The impact of the varied post-oxidation times is clearly visible in Fig. 4.13(a). On the one hand,  $N_{\text{max}}$  decreases stepwise with increased  $t_{\text{PO}}$ , while on the other hand, the profiles become deeper. The reasons, therefore, are segregation of boron into the growing  $\text{SiO}_2$  layer at the silicon interface (see Chapter 2.3.2), longer diffusion times, and oxidation-enhanced diffusion of boron; see also the following more detailed discussion.

When comparing every pair of successive diffusion processes, as listed in Fig. 4.13(a), the strongest decrease in  $N_{\text{max}}$  is apparent from  $(9.1 \pm 0.9) \cdot 10^{19} \text{ cm}^{-3}$  for Gen3 to  $(5.2 \pm 0.5) \cdot 10^{19} \text{ cm}^{-3}$  for Gen3–PO1. With further extended post-oxidation, the reduction in  $N_{\text{max}}$  takes place at a slower rate, as the gradient in the dopant concentration decreases (which is always the driving force in a diffusion process). For process Gen3–PO5 with the longest post-oxidation,  $N_{\text{max}}$  is decreased to  $(1.8 \pm 0.2) \cdot 10^{19} \text{ cm}^{-3}$ , while  $d$  is increased to  $(830 \pm 83) \text{ nm}$ . This results in an increased  $R_{\text{sh}} \approx 104 \Omega/\text{sq}$ . The standard deviation  $\sigma$  over the wafers only slightly increases to 3.3%–4.2% for all five diffusion processes with varied post-oxidations, which still corresponds to sufficiently low values.

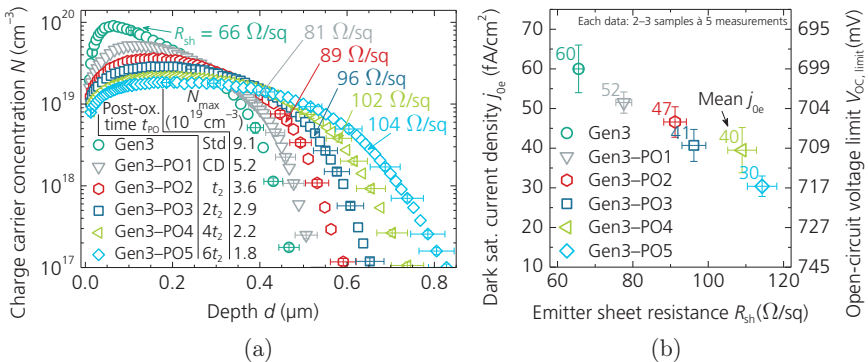


**Fig. 4.13.** (a) Boron doping profiles  $N(d)$ , determined by ECV measurements on alkaline saw-damage etched surfaces for the indicated  $\text{BBr}_3$  diffusion processes (Std: standard, CD: cool-down). Exemplary error bars are shown. (b) Dark saturation current densities  $j_{\text{oe}}$  of alkaline textured  $j_{\text{oe}}$  samples (PECVD  $\text{Al}_2\text{O}_3/\text{SiN}_x$ ) after firing depending on  $R_{\text{sh}}$ . The  $V_{\text{OC,limit}}$  is calculated according to Eq. (2.20) utilizing  $j_{\text{ph}} = 39 \text{ mA}/\text{cm}^2$ . Note that the given  $R_{\text{sh}}$  in (a) relate only to the area where the ECV measurements are performed and thus, their values might be somewhat different to the  $R_{\text{sh}}$  given in (b).

During the initial phase of post-oxidation, the growth of an  $\text{SiO}_2$  layer at the interface between BSG and silicon is fast, and the gradient in the boron concentration between  $\text{SiO}_2$  and silicon is very strongly pronounced. The oxidation of boron-doped silicon, the segregation of boron atoms into the growing  $\text{SiO}_2$  layer, and the diffusion of boron atoms into the  $\text{SiO}_2$  layer—which is much faster than the diffusion of boron atoms into the bulk silicon—lead to the distinctive depletion zone for process Gen3, as apparent in Fig. 4.13(a). For the diffusion processes with extended post-oxidation, the growth of the  $\text{SiO}_2$  layer slows down as its thickness increases, and a concentration gradient of boron atoms towards the silicon surface is also present. Furthermore, boron atoms originating from the BSG layer are also present in the growing  $\text{SiO}_2$  layer. Thus, diffusion of boron atoms towards the silicon surface and diffusion of boron atoms into the  $\text{SiO}_2$  layer approach each other. This results in a significantly less pronounced doping depletion zone, the longer the post-oxidation takes place; see Fig. 4.13(a).

However, a large amount of boron atoms initially present in the silicon—with respect to profile Gen3—segregate or diffuse into the growing  $\text{SiO}_2$  layer during the extended post-oxidation times. The total amount of boron  $Q_{\text{tot}}$  and its percentage change  $\Delta Q_{\text{tot}}$  with respect to profile Gen3 are summarized in Table 4.4. For process Gen3–PO5 with the longest post-oxidation, up to 50% less boron atoms are present in the silicon compared with Gen3. Hence, the extension of the post-oxidation is an effective approach to achieve deep doping profiles with lower  $N_{\text{max}}$  and less pronounced doping depletion zones.

The  $j_{0e}$  determined on  $j_{0e}$  samples with alkaline texture for the six diffusion processes are summarized in Fig. 4.13(b). It arises again a linear relationship between  $j_{0e}$  and  $R_{\text{sh}}$ : the higher  $R_{\text{sh}}$ , the lower  $j_{0e}$ . Decreased surface recombination velocity and lower Auger recombination lead to lower  $j_{0e}$  for the stepwise extended post-oxidations. From initially  $j_{0e} = (60 \pm 6) \text{ fA/cm}^2$  for diffusion process Gen3,  $j_{0e}$  is significantly reduced to  $j_{0e} = (30 \pm 3) \text{ fA/cm}^2$  for process Gen3–PO5. Expressed in terms of  $V_{\text{OC,limit}}$ , this results in a remark-

**Table 4.4.** Total amount of boron  $Q_{\text{tot}}$  and its change  $\Delta Q_{\text{tot}}$  for  $\text{BBr}_3$  diffusion processes with extended post-oxidations with respect to process Gen3.

$\text{BBr}_3$ diffusion	Gen3	Gen3–PO1	Gen3–PO2	Gen3–PO3	Gen3–PO4	Gen3–PO5
Total boron	1.7	1.4	1.2	1.1	0.92	0.88
doping $Q_{\text{tot}}$ ( $10^{15} \text{ cm}^{-2}$ )	$\pm 0.2$	$\pm 0.1$	$\pm 0.1$	$\pm 0.1$	$\pm 0.09$	$\pm 0.09$
Change $\Delta Q_{\text{tot}}$ (%)	–	$21 \pm 13$	$34 \pm 12$	$39 \pm 12$	$47 \pm 11$	$49 \pm 11$

able gain in  $\Delta V_{\text{OC,limit}} = (18 \pm 4) \text{ mV}$  from initially  $V_{\text{OC,limit}} = (699 \pm 3) \text{ mV}$  to  $V_{\text{OC,limit}} = (717 \pm 2) \text{ mV}$ .

To obtain doping profiles with low  $N_{\text{max}}$  but further increased depth  $d$ , the combination of prolonged drive-in time and adapted post-oxidation is promising. An exemplary result of this approach is shown in Fig. 4.14(a). Based on diffusion process Gen3–DrIn1, post-oxidation with  $t_{\text{PO}} = 1.5t_{\text{D}}$  is integrated into this diffusion process, which is referred to as Gen3–DrIn1–PO6. It becomes evident that the adapted post-oxidation step significantly reduces  $N_{\text{max}}$  to  $N_{\text{max}} = (4.1 \pm 0.4) \cdot 10^{19} \text{ cm}^{-3}$  and further deepens the profile to  $d = (780 \pm 78) \text{ nm}$ . Again, this correlates with increased segregation and diffusion of boron atoms into the growing  $\text{SiO}_2$  layer, longer diffusion time for boron atoms into the bulk silicon as well as oxidation-enhanced diffusion of boron. The  $j_{0e}$  is determined to be  $j_{0e} = (54 \pm 2) \text{ fA/cm}^2$  for this process and hence, is lower as for the other two with  $j_{0e} = (60 \pm 6) \text{ fA/cm}^2$  and  $j_{0e} = (88 \pm 13) \text{ fA/cm}^2$  for Gen3 and Gen3–DrIn1, respectively.

In case  $N_{\text{max}}$  is to be decreased without increasing  $d$ , an option is to perform the drive-in step at a lower temperature; see Fig. 4.14(b). Based on  $\text{BBr}_3$  diffusion Gen3–PO2, both  $T_{\text{DrIn}}$  and the post-oxidation temperature are decreased by 25 K. This adapted diffusion process with lower  $T_{\text{DrIn}}$  is referred to as Gen3–PO2–LT. As it is clear from Fig. 4.14(b),  $N_{\text{max}}$  is decreased to  $N_{\text{max}} = (3.9 \pm 0.4) \cdot 10^{19} \text{ cm}^{-3}$ , while  $d$  is almost the same as that of Gen3. This result can be explained by the following considerations: after the drive-in

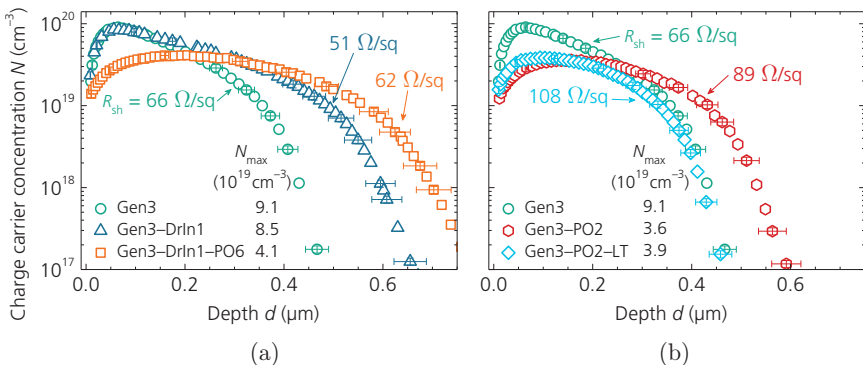


**Fig. 4.14.** Boron doping profiles  $N(d)$ , determined by ECV measurements on alkaline saw-damage etched surfaces for the different  $\text{BBr}_3$  diffusion processes in (a) and (b) as discussed in the text. Exemplary error bars are shown. The given  $R_{\text{sh}}$  correspond to inductive measurements performed in the area of the ECV measurements.

step and hence, prior to post-oxidation, the doping profile for process Gen3–PO2–LT would show lower  $N_{\max}$  and  $d$  than the profile for process Gen3, as  $T_{\text{DrIn}}$  is lower. The lower  $N_{\max}$  results from the lower solubility of boron in silicon for lower  $T_{\text{DrIn}}$ ; see Fig. 2.7. The lower  $d$  correlates with lower effective boron diffusion coefficients at lower  $T_{\text{DrIn}}$  [69,71]. Performing the post-oxidation then leads to further lowering of  $N_{\max}$  and increasing  $d$ , as already discussed. By suitable combination of adjusted  $T_{\text{DrIn}}$  and post-oxidation, as performed for process Gen3–PO2–LT,  $N_{\max}$  can be lowered compared with process Gen3, while almost the same  $d$  results. Thus, the lower  $N_{\max}$  for diffusion process Gen3–PO2–LT leads to both an increase in  $R_{\text{sh}}$  of about  $40 \Omega/\text{sq}$  and significantly lower  $j_{0e} = (37 \pm 4) \text{ fA}/\text{cm}^2$  in comparison with process Gen3 with  $j_{0e} = (60 \pm 6) \text{ fA}/\text{cm}^2$ .

#### 4.4.3 Doping profiles without surface depletion by wet-chemical etching

For the used  $\text{BBr}_3$  diffusion processes with incorporated post-oxidation, a characteristic doping depletion zone at the surface is always present. In some publications [204,205], this doping depletion zone is suspected to trigger increased recombination at the passivated surfaces. Rothhardt [169, p. 58–61] simulated the difference in  $j_{0e}$  for boron doping profiles with and without a doping depletion zone (the further course of the profiles and the depth are identical). He concluded that the profile with a doping depletion zone yields slightly lower recombination in the passivated area, which is equivalent to lower  $j_{0e}$ . In the following, the influence of the doping depletion zone on  $j_{0e}$  will be studied experimentally. For this purpose, in addition to doping profiles with doping depletion zone, doping profiles without one are mandatory.

The dopant depletion at the surface can be reduced, if the post-oxidation is omitted as in diffusion process Gen3\*, but on the other hand, a BRL remains at the surface leading to high  $j_{0e}$ ; see Fig. 4.7(a) and Fig. 4.10(b). Hence, alternatives are necessary in order to realize boron doping profiles without dopant depletion towards the surface and without BRL.

Apart from fine-tuning the  $\text{BBr}_3$  diffusion process without post-oxidation, another approach is the removal of the doping depletion zone of the boron-doped silicon surface after  $\text{BBr}_3$  diffusion by wet-chemical etching; see Fig. 4.15(a). The as-diffused and the resulting doping profiles after etching of the doping depletion zones are shown. The wet-chemical etching has been performed in a solution containing ozone, HF, and hydrochloric acid

(HCl) [206] for both  $N(d)$  as well as  $j_{0e}$  samples processed with  $\text{BBr}_3$  diffusions Gen3–DrIn1, Gen3–PO2, and Gen3–PO4. The different surface topographies, i.e. alkaline saw-damage etched surfaces for the  $N(d)$  samples and alkaline textured surfaces for the  $j_{0e}$  samples, result in different etching rates. As also found in Ref. [206], the etching rate for the textured surface is lower. Accordingly, the etching time for the textured  $j_{0e}$  samples is prolonged in such a manner that the same change in  $R_{sh}$  is achieved as for the alkaline saw-damage etched  $N(d)$  samples. The thicknesses of the removed silicon layers range between  $(85 \pm 9)$  nm and  $(225 \pm 23)$  nm. The depth of the doping profiles is reduced accordingly, which leads to an increase in  $R_{sh}$  between  $10 \Omega/\text{sq}$  and  $76 \Omega/\text{sq}$  compared to the non-etched profiles.

The  $j_{0e}$  results are depicted in Fig. 4.15(b). It is found that no significant differences in  $j_{0e}$  between initial (as diffused) and etched doping profiles are apparent, despite significantly increased  $R_{sh}$  for the latter. It seems that the increased recombination directly at the surface due to a higher dopant concentration for the etched profiles is compensated by reduced Auger recombination within the doped volume, which extent is decreased. Transferred to a profile pair without and with doping depletion zone but identical profile depth, this means that  $j_{0e}$  must be higher for the doping profile

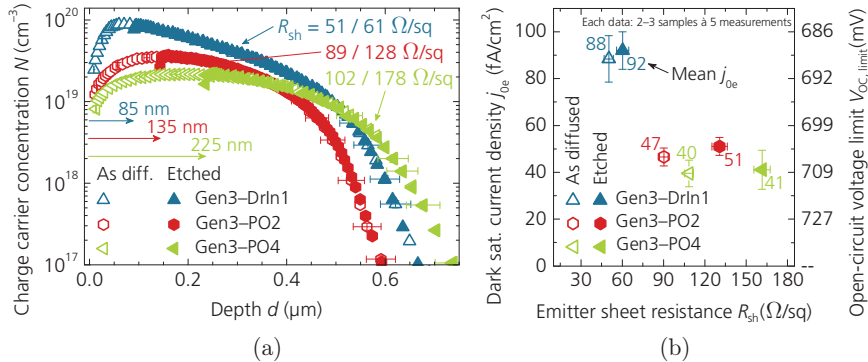


**Fig. 4.15.** (a) Boron doping profiles  $N(d)$ , determined by ECV measurements on alkaline saw-damage etched surfaces for different  $\text{BBr}_3$  diffusion processes (as diffused) and after wet-chemical etching of their doping depletion zones (etched). The etched profiles are shifted to the right by the stated silicon surface removal ( $R_{sh}$ : as diffused/etched). Exemplary error bars are shown. (b) Dark saturation current densities  $j_{0e}$  of alkaline textured  $j_{0e}$  samples ( $\text{PECVD Al}_2\text{O}_3/\text{SiN}_x$ ) after firing depending on  $R_{sh}$ . The  $V_{OC,\text{limit}}$  is calculated according to Eq. (2.20) utilizing  $j_{ph} = 39 \text{ mA}/\text{cm}^2$ . Note that the given  $R_{sh}$  in (a) relate only to the area where the ECV measurements are performed and thus, their values might be somewhat different to the  $R_{sh}$  given in (b).

without doping depletion zone. Hence, these results suggest that the presence of a doping depletion zone does lead to reduced recombination and lower  $j_{0e}$  at boron-doped and passivated areas and thus, the doping depletion zone is found to be beneficial in terms of low emitter recombination. This is in accordance with the results from Rothhardt [169, p. 58–61].

## 4.5 Identification of suitable diffusion barrier layers

For the fabrication of  $n$ -type solar cells within this work, the differently doped surfaces are realized by a sequential diffusion approach with first  $\text{BBr}_3$  and second  $\text{POCl}_3$  diffusion; see Chapters 3.4 and 3.5. The main requirement on the diffusion barrier layers used during both diffusion processes is to prevent boron or phosphorus diffusion into the masked silicon surface. Additionally, for  $\text{POCl}_3$  diffusion, the interaction between the already present boron-doped surface, the applied barrier layer, and the gas atmosphere has to be known.

As discussed in Chapter 3.4.2, the idea with respect to the order of the diffusion processes is that both the  $\text{BBr}_3$  and the  $\text{POCl}_3$  diffusion processes are supposed to be independently optimized and characterized, and that the respective processes then can be directly implemented into cell fabrication. Allowing for this scenario it means that the boron doping profile must not significantly change during  $\text{POCl}_3$  diffusion. The feasibility of this approach depends on the applied diffusion barrier layer and the effect of the thermal budget of the  $\text{POCl}_3$  diffusion process on the rearrangement of boron dopants. The advantage in this approach is the fact that  $\text{POCl}_3$  diffusions are performed at clearly lower temperatures than  $\text{BBr}_3$  diffusion processes, because the solubility of phosphorus atoms in silicon is significantly higher than that of boron atoms; see Fig. 2.7. For the selection of diffusion barrier layers this means that such barrier layers should be considered which are able to prevent further substantial boron depletion at the silicon surface. Furthermore, it is also important that the used diffusion barrier layers are easily removable in HF solution after the high-temperature processes.

The most obvious choice for a diffusion barrier layer is thermally grown  $\text{SiO}_2$  because it is commonly used in  $\text{POCl}_3$  processes [11], and it can be easily removed in HF solution [207]. Unfortunately, a thermally grown  $\text{SiO}_2$  layer is known to lead to a pronounced surface depletion of boron due to the segregation of boron into the  $\text{SiO}_2$  layer; see Fig. 2.6. As thermal oxidation oc-

curls on both wafer sides, the unilateral removal of the  $\text{SiO}_2$  layer would be also necessary. Hence, alternatives to thermal oxidation are required. This can be, e.g.  $\text{SiO}_x$ <sup>20</sup> or  $\text{SiN}_x$  layers deposited by PECVD or sputtering, as both methods allow for a single-sided layer deposition. As  $\text{SiN}_x$  features lower etching rates in HF solution than  $\text{SiO}_x$  [207,208], only thin  $\text{SiN}_x$  layers are preferred.

In order to identify suitable barrier layers, comprehensive studies have been carried out utilizing various  $\text{SiO}_x$  and  $\text{SiN}_x$  layers applied by PECVD or sputtering. A large part of the performed experiments and the obtained results regarding  $\text{POCl}_3$  diffusion is published in Ref. [209]. Hereinafter, selected experiments and important results concerning  $\text{POCl}_3$  diffusion are discussed for the PECVD barrier layers summarized in Fig. 4.16. The results concerning diffusion barrier layers in  $\text{BBr}_3$  diffusion are not discussed separately, but they are considered in the final selection of a suitable diffusion barrier layer.

#### 4.5.1 Sample preparation

The process sequence depicted in Fig. 4.16 enables the investigation of whether or not the thermal budget of the applied  $\text{POCl}_3$  diffusion process affects the masked boron-doped surfaces with respect to a redistribution of boron atoms. Note that all diffusion barrier layers, listed in Fig. 4.16, have been previously examined on alkaline saw-damage etched and alkaline textured surfaces with respect to their masking properties against phosphorus in-diffusion during  $\text{POCl}_3$  diffusion. All layers are found to effectively mask the silicon surface against phosphorus from the  $\text{POCl}_3/\text{O}_2$  gas atmosphere at  $T = 835^\circ\text{C}$ . In addition, these extended investigations target the barrier effect of the layers against oxygen from the  $\text{POCl}_3/\text{O}_2$  gas atmosphere.

Following the alkaline saw-damage etch of the *p*-type Cz-Si wafers,  $\text{BBr}_3$  diffusion process Gen1, including post-oxidation, is performed. After etching off the BSG layer in 10% HF solution, the reference doping profile of the applied  $\text{BBr}_3$  diffusion is determined by ECV on sample RefProf. Note that the ECV measurement on each sample is carried out at the same spot in the lower left corner of the wafer, as this region features sufficient homogeneous sheet resistances for the applied  $\text{BBr}_3$  diffusion process Gen1; see Fig. 4.6(a).  $\text{SiN}_x$  and  $\text{SiO}_x$  layers are then applied by PECVD on either wafer side for samples DB1–DB6, according to Fig. 4.16. The subsequently performed  $\text{POCl}_3$  diffusion process Phos1 takes place at  $T = 822^\circ\text{C}$  (it is

<sup>20</sup>The term “ $\text{SiO}_x$ ” is used for silicon oxide layers applied by either PECVD or sputtering. In contrast, thermally-grown silicon oxide is referred to as “ $\text{SiO}_2$ ”.

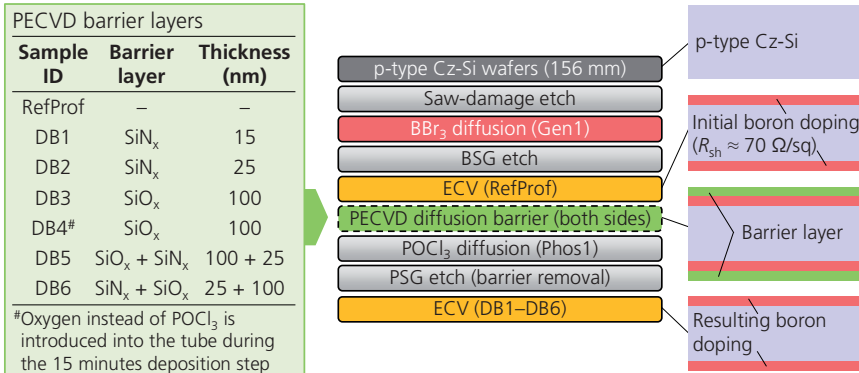


**Fig. 4.16.** Left: Overview of the investigated PECVD layers on the both-sides coated samples DB1–DB6. Sample RefProf serves as reference for the initial charge carrier concentration profile of the boron-doped surface. Right: Schematic process sequence for fabrication of the test samples with selected schematic cross sections.

assumed that the barrier layers also mask the silicon surface during this process as  $T$  is lower as in the  $\text{POCl}_3$  diffusion mentioned above). To test the influence of higher oxygen content, pure oxygen at increased flow rates instead of  $\text{POCl}_3$  is introduced into the tube during the 15 minutes deposition phase for sample DB4, while leaving the rest of the process parameters unchanged. Following the barrier layer removal in 10% HF solution, the resulting boron doping profiles of samples DB1–DB6 are also determined by ECV. In the following, the naming DB1–DB6 is used both for the samples as well as for the measured boron doping profiles.

## 4.5.2 Results

### $\text{SiN}_x$ diffusion barrier layers

The boron doping profiles for reference sample RefProf and samples DB1 and DB2 are shown in Fig. 4.17(a). Obviously, the boron doping profiles DB1 and DB2 hardly differ from the reference profile RefProf. No significant differences are visible neither for the surface doping concentrations nor for the course in the depth. Hence, the temperature loading of the  $\text{POCl}_3$  diffusion, which is much lower than for  $\text{BBr}_3$  diffusion, shows no significant redistribution of the boron atoms.

It also follows that the 15 nm-thick  $\text{SiN}_x$  layer can sufficiently protect the boron-doped surface against oxidation, as neither a decrease in the maxi-

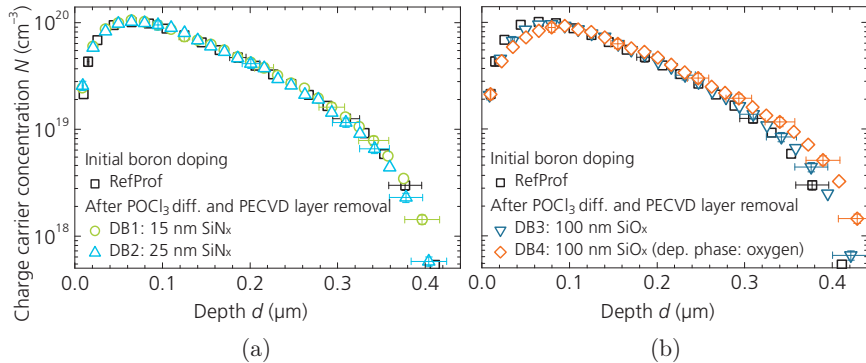


**Fig. 4.17.** Boron doping profiles  $N(d)$ , determined by ECV measurements for reference sample RefProf and samples (a) DB1–DB2 and (b) DB3–DB4. Exemplary error bars are shown.

imum dopant concentration nor a deepening of the profile is observed for sample DB1. This is due to the following reason: if oxygen would reach the interface between barrier layer and silicon, this would cause an oxidation leading to surface depletion and oxidation-enhanced diffusion of boron atoms, as discussed in Chapter 2.3.2. Also from literature,  $\text{SiN}_x$  layers are known to efficiently mask silicon against oxygen [208].

### **$\text{SiO}_x$ diffusion barrier layers**

The boron doping profiles for reference sample RefProf and samples DB3 and DB4 are shown in Fig. 4.17(b). It is clear that both profiles differ from the reference profile RefProf. For profile DB3, the dopant concentration close to the surface is somewhat lower and the profile is slightly deeper. Profile DB4 shows further lowering of the surface dopant concentration and a further profile deepening. Remember that for sample DB4, a high oxygen flow instead of  $\text{POCl}_3$  has been used during the deposition phase of the diffusion process. It is obvious that the larger the surface depletion, the deeper the resulting profile. Both resulting profiles are characteristic for the oxidation of boron-doped surfaces and also for oxidation-enhanced diffusion of boron. Since oxygen has a higher diffusion coefficient in  $\text{SiO}_x$  than phosphorus [208,210], oxygen originating from the  $\text{POCl}_3/\text{O}_2$  gas atmosphere during the deposition phase is suspected to reach the interface between barrier layer and silicon, which then leads to oxidation of the boron-doped silicon surface.

### **SiO<sub>x</sub> and SiN<sub>x</sub> diffusion barrier layer stacks**

The doping profiles for samples DB5 and DB6 are shown in Fig. 4.18. With an additional 25 nm-thick SiN<sub>x</sub> layer, neither surface depletion nor profile deepening is observed for samples DB5 and DB6, irrespective of whether the SiO<sub>x</sub> or the SiN<sub>x</sub> layer is deposited first.

As mentioned above, oxygen originating from the POCl<sub>3</sub>/O<sub>2</sub> gas atmosphere is suspected to reach the silicon interface and to trigger oxidation in case of the SiO<sub>x</sub> barrier layers shown in Fig. 4.17(b). However, also other sources of oxygen could in principle be possible, as the SiO<sub>x</sub> layers or the silicon wafers.

By comparing profiles DB5 and DB6, a contribution of oxygen from the SiO<sub>x</sub> layers themselves is very unlikely, as both profiles equal the reference profile RefProf. The segregation of boron into the barrier layers is most probably insignificant, as the profiles DB5 and DB6 are equal whether the silicon surface is in direct contact with the SiN<sub>x</sub> layer or with the SiO<sub>x</sub> layer. Hence, no significant segregation of boron into the PECVD SiO<sub>x</sub> layer is observed, which is in contrast to strongly pronounced boron segregation in case of thermally grown SiO<sub>2</sub>; see Fig. 2.6(a). Also, oxygen present in the Cz-Si wafer (due to the fabrication process) can be excluded as oxygen source; otherwise also wafers with a SiN<sub>x</sub> layer should show altered doping profiles.

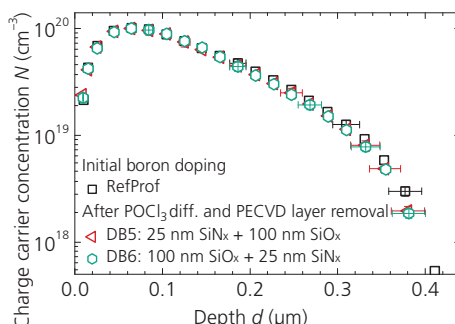


**Fig. 4.18.** Boron doping profiles  $N(d)$ , determined by ECV measurements for reference sample RefProf and samples DB5–DB6. Exemplary error bars are shown.

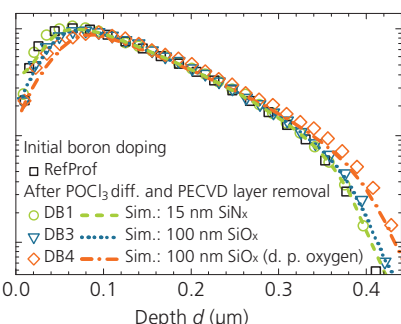


**Fig. 4.19.** Boron doping profiles  $N(d)$ , determined by ECV measurements (symbols, no error bars shown) for samples DB1, DB3, and DB4 as well as the corresponding simulated profiles (lines).

### Numerical simulations

The findings are supported by numerical simulations of the redistribution of boron atoms during  $\text{POCl}_3$  diffusion, which have been performed by *Schön* with *Sentaurus Process* [211]. To be more sensitive to the differences in the boron doping profiles evolving during  $\text{POCl}_3$  diffusion, the reference profile RefProf, measured directly after  $\text{BBr}_3$  diffusion, is used as input.

In addition to sample DB1 coated with 15 nm-thick  $\text{SiN}_x$  layers, also samples DB3 and DB4 with 100 nm-thick  $\text{SiO}_x$  layers are considered. The process conditions, i.e. temperature profiles and gas fluxes, are taken as in the corresponding experiments. *Schön* used the models and the diffusion parameters as he published them in Ref. [212]. Only the diffusivity of oxygen in the  $\text{SiO}_x$  layer is fitted. The diffusion of oxygen to the reacting  $\text{Si}/\text{SiO}_2$  interface determines the oxidizing velocity and thus, the depletion and the oxidation-enhanced diffusion of boron atoms.

The simulation results, shown as lines in Fig. 4.19, are in very good agreement with the ECV measurements. The simulation of profile DB1 confirms that the temperature loading in the  $\text{POCl}_3$  process has no significant effect on the resulting boron profile, and that no oxidation at the interface occurs. It is found that the simulated profiles DB3 and DB4 match the measured ones for an oxygen diffusion coefficient in the PECVD  $\text{SiO}_x$  layer which is about 10 times higher than in thermally grown  $\text{SiO}_2$  [209]. Furthermore, the simulations prove that the 15 nm-thick  $\text{SiN}_x$  layer completely masks the boron-doped silicon surface against oxygen, whereas the 100 nm-thick  $\text{SiO}_x$  layer is permeable to oxygen.

### Selected diffusion barrier layer for cell fabrication

Based on the discussed results and further not shown examinations, the PECVD diffusion barrier layer for fabrication of *n*-type solar cells is chosen to be a layer stack consisting of 50 nm  $\text{SiO}_x$  and 30 nm  $\text{SiN}_x$ . This layer stack masks against boron in  $\text{BBr}_3$  diffusion, and against phosphorus and oxygen in  $\text{POCl}_3$  diffusion. In Chapter 7, the  $\text{POCl}_3$  diffusion processes Phos2 [92] and Phos3 utilized for fabrication of solar cells feature an incorporated in-situ oxidation at temperatures of up to 880°C. Even for these elevated temperatures, no significant redistribution of boron atoms is found for the boron-doped surfaces masked with the above mentioned barrier layer stack. The total barrier layer stack thickness of 80 nm results in a

dark blue color of the masked surfaces, enabling simple process control after both PECVD deposition and PSG etch.

The fact that the boron doping profiles are not significantly changed during  $\text{POCl}_3$  diffusions Phos1–Phos3 enables the usage of  $j_{0e}$  samples to characterize the  $\text{BBr}_3$  diffusion processes without the need to undergo  $\text{POCl}_3$  diffusion with both sides' masked surfaces. Thus,  $j_{0e}$  samples, as already introduced, are representative to examine the emitter properties in connection with the entire cell fabrication process.

## 4.6 Chapter summary

The characterization and optimization of diffusion processes to form the boron-doped emitter are essential tasks for the development and steady improvement of  $n$ -type silicon solar cells. Using boron tribromide ( $\text{BBr}_3$ ) as liquid dopant precursor, various diffusion processes in an industrial quartz tube furnace are examined with respect to achieve low emitter dark saturation current densities  $j_{0e}$ , and to create knowledge how to control the shape of the doping profiles for further studies (performed in the following chapters). All investigations are performed on wafers with 156 mm edge length.

Three basic  $\text{BBr}_3$  diffusion process generations Gen1–Gen3, whose parameters have been provided by *Tempress Systems*, are comprehensively examined. Each process is equipped with an integrated post-oxidation to avoid the presence of a highly recombination-active boron-rich layer after diffusion. All three diffusion processes yield emitter sheet resistances  $R_{\text{sh}} \approx 70 \Omega/\text{sq}$ , while  $j_{0e}$  is found to be  $j_{0e} = (76 \pm 5) \text{ fA}/\text{cm}^2$  for diffusion processes Gen1/Gen2, and  $j_{0e} = (60 \pm 6) \text{ fA}/\text{cm}^2$  for process Gen3 on alkaline textured surface with PECVD  $\text{Al}_2\text{O}_3/\text{SiN}_x$  passivation layers after firing. Basically, the profile shapes are very similar, with small differences in maximum dopant concentrations  $N_{\text{max}}$  (in the range of  $10^{20} \text{ cm}^{-3}$ ) and in profile depths  $d$  (close to 500 nm). More pronounced is the difference of the homogeneity in  $R_{\text{sh}}$  across the wafers for the three process generations. The percentage standard deviation  $\sigma_{4\text{pp}}$  in  $R_{\text{sh},4\text{pp}}$  across single wafers, determined by 4-point-probe (4pp) measurements, decreases from 8.8% for Gen1, to 3.4% for Gen2, and finally to only 2.7% for Gen3. This decrease in  $\sigma_{4\text{pp}}$  originates from the fact that the variation of the profile depths across the wafer is significantly reduced, which correlates with a more homogeneous formation of the BSG layer for  $\text{BBr}_3$  diffusion processes Gen2 and Gen3. The found homogeneity in  $R_{\text{sh}}$

with  $\sigma < 3\%$  on single wafers at different positions in the process boat, which has in total 262 slots, is also excellent for diffusion process Gen3.

Based on diffusion process Gen3, deeper doping profiles with similar  $N_{\max}$  are realized by extending the drive-in time, which offer the opportunity to investigate the correlation of profile depth and specific contact resistance to screen-printed and fired metal contacts, as this is performed in Chapter 5.

In order to decrease  $j_{0e}$ ,  $N_{\max}$  needs to be reduced to lower both surface and Auger recombination. For this purpose, the extension of the post-oxidation is found to be a very promising method to change the boron doping profiles accordingly. With this approach, fairly low  $j_{0e} = (30 \pm 3) \text{ fA/cm}^2$  at  $R_{sh} \approx 120 \Omega/\text{q}$  is achieved on alkaline textured surface passivated by PECVD  $\text{Al}_2\text{O}_3/\text{SiN}_x$  layers. The respective doping profile depth is just over 800 nm, while  $N_{\max}$  is decreased to  $N_{\max} = (1.8 \pm 0.2) \cdot 10^{19} \text{ cm}^{-3}$ . The measured  $j_{0e}$  equals an open-circuit voltage limit of  $V_{OC,\text{limit}} = (717 \pm 2) \text{ mV}$ , which is higher by remarkable  $(18 \pm 4) \text{ mV}$  as that of the original process Gen3. With the knowledge gained concerning the  $\text{BBr}_3$  diffusion processes, it is possible to adjust  $N_{\max}$  and profile depth more or less independently from each other, and to realize custom-made doping profiles.

The incorporated post-oxidation leads to depletion of boron atoms at the silicon surface. By comparing doping profiles as diffused and after wet-chemically etching of the doping depletion zone, it is concluded that the surface depletion is beneficial in terms of low recombination at boron-doped and passivated areas (assuming the same junction depth). The possible impact of the near-surface doping depletion zone with respect to screen-printed and fired metal contacts will be dealt with in Chapter 5.

For fabrication of  $n$ -type solar cells, each of the two wafer surfaces has to be doped with different dopants. An approach to realize this is to use sequential diffusion processes with first  $\text{BBr}_3$  and second phosphorus diffusion using phosphorus oxychloride ( $\text{POCl}_3$ ). In doing so, suitable diffusion barrier layers have to be applied on the surface not to be doped during the respective diffusion processes. A therefor suitable diffusion barrier layer stack is found to consist of 50 nm  $\text{SiO}_x$  and 30 nm  $\text{SiN}_x$ , both applied by PECVD. The fact that the boron doping profile is not significantly changed during  $\text{POCl}_3$  diffusion, independently pre-optimized boron and phosphorus dopings can be implemented into the  $n$ -type silicon solar cell fabrication process by using sequential  $\text{BBr}_3$  and  $\text{POCl}_3$  diffusions.

## **5 Contacting of Boron Emitters Using Ag-Al Screen-Printing Pastes**

### **5.1 Introduction**

For the contacting of boron-doped emitters with screen-printed and fired metallization in *n*-type silicon solar cells, usually a small amount of aluminum is added to the silver-based pastes. The reasons and some associated consequences are briefly discussed on the basis of recent publications. Subsequently, the possible impact of boron doping profiles with deeper junctions on specific contact resistance  $\rho_C$ , measured between Ag-Al contacts and alkaline textured, boron-doped, and passivated surfaces, is investigated both experimentally as well as with an analytical model. The properties of formerly metallized areas are examined by microstructural investigations. As all boron emitters applied in this work feature dopant depletion towards the surface, the potential impact of this doping depletion zone on  $\rho_C$  is also addressed. Furthermore, some emitter profiles developed in the previous chapter with decreased maximum dopant concentrations are tested for their low-ohmic electrical contactability. Finally, charge carrier recombination underneath the metal contacts is examined in-depth on the basis of numerical simulations.

### **5.2 Review on electrical contacting of boron-doped surfaces**

The electrical contacting of boron-doped emitter surfaces in *n*-type silicon solar cells is one major challenge for further increasing their energy conversion efficiency. Using screen-printed metal pastes, the pastes' task is to fire-through the passivation layer during a short contact firing process and to form a highly conductive connection to the boron-doped silicon surface. To date, to achieve low specific contact resistances  $\rho_C$  in the range of a few  $m\Omega cm^2$  after firing, a small percentage of aluminum (Al) needs to be added

to the screen-printing silver (Ag) pastes [140–142,213,214]. For aerosol printed seed layers it has been shown that an Ag ink (no Al added) can also provide a low-ohmic electrical contact to boron emitters after firing with  $\rho_C$  also in the range of a few  $\text{m}\Omega\text{cm}^2$  [143].

However, especially the screen-printed and fired Ag-Al contacts trigger enhanced charge carrier recombination below the metallized areas leading to severe open-circuit voltage losses [16,213–216] and hence, energy conversion efficiency losses. The reasons, therefore, are currently being discussed within the photovoltaic community, as e.g. in Refs. [142,213,215,216]. For instance, *Edler et al.* propose that the deep and homogeneous layer-like penetration of metal—across the whole contact area—into the boron emitter might be a possible cause [215]. By assuming that the metal penetrates the emitter along the whole width of the contacts, they found agreement between simulation and experimental data. On the other hand, several authors report on the observation of large and deep metal crystallites at the interface between the bulk of the Ag-Al contact and the boron-doped surface [142,213,217]. These metal crystallites reach depths up to a few microns, deep enough to even shunt the boron emitter.

Up to now, only a few studies have addressed the underlying mechanism in contact formation of such Ag-Al pastes to boron emitters [217–219]. During the contact firing process, the Al most likely catalyzes the formation of much larger and deeper crystallites [217] than in case of pure Ag pastes used to contact phosphorus-doped surfaces [220,221]. According to the current state of knowledge, Al is needed to create crystallites by means of an Ag-Al-Si alloy phase [217,219]; however, the formed crystallites themselves consist mainly of Ag (reported Al contents of the crystallites vary between 1% [213,219] and 3%–10% [217]). No highly doped regions are observed underneath the crystallites [213,217], which would imply presence of an Al alloy. Several authors have shown that a higher Al share in the Ag paste leads to lower  $\rho_C$  [141,142,213,214,222]. The lower  $\rho_C$  is attributed to a higher density and a larger size of crystallites observed on the silicon surface for Ag-Al pastes with higher Al content [141,213,222]. At the same time, a higher Al content in the paste leads to increased charge carrier recombination in the metallized areas and thus, to larger metallization-induced voltage losses [213]. The voltage loss increases with increasing contact firing temperature, as the amount and size of crystallites is found to increase [223]. Furthermore, also the glass components in the Ag-Al paste are identified to play an important role for contact formation [224].

*Heinz et al.* [213] propose that the formation of only small crystallites of sufficient number is favorable to ensure low  $\rho_C$  without pronounced recombination losses at the Ag-Al contacts, because deep crystallites are found to be highly recombination active. Furthermore, it has been shown that the recombination rate below the Ag-Al contacts can be decreased by utilizing boron emitters with larger junction depth [215,216]. According to the theory of ideal planar contacts, see Fig. A.2, high dopant concentration at the surface is necessary to achieve reasonable low  $\rho_C$ . *Fritz et al.* [225] report that apart from the maximum dopant concentration  $N_{\max}$  of the boron emitter, also other emitter properties—like their doping profile shapes or the defect concentration at the emitter surface—possibly play a decisive role for achieving low  $\rho_C$ . From two different boron emitters investigated in their studies, surprisingly, the emitter with the lower  $N_{\max}$  yields the lower  $\rho_C$ , contradicting the theory of ideal planar contacts. The reason for this observation could not be found within the performed investigations.

In conclusion, the contact behavior is influenced by a lot of parameters and necessitates further research. Therefore, some specific issues concerning the relationship between metal contacts and doping profiles are studied in detail in the following sections. For this purpose, use is made of  $\text{BBr}_3$  diffusion processes from Chapter 4, some of which were developed to meet special requirements needed with respect to the doping profile properties. The examinations aim, on the one hand, at clarifying whether or not the junction depth of the boron dopings has an impact on  $\rho_C$ . This includes the issue whether the dopant depletion of the boron profiles towards the surface affect the electrical contact. On the other hand is to be found, whether doping profiles with quite low  $N_{\max}$  of just above  $10^{19} \text{ cm}^{-3}$  can be contacted with reasonable  $\rho_C$  in the range of a few  $\text{m}\Omega\text{cm}^2$ . Finally, numerical simulations are utilized to clarify if the reported increased charge carrier recombination below Ag-Al contacts can be indeed correlated with the presence of (partly) deep penetrating metal crystallites.

## 5.3 Impact of junction depth on the specific contact resistance

In this section, the impact of an increase in junction depth of the boron emitter on  $\rho_C$  is experimentally investigated utilizing two different, commercially available Ag-Al screen-printing pastes from two different paste manufacturers, referred to as “Ag-Al1” and “Ag-Al2”. For this purpose, three

boron doping profiles with different junction depths, but nearly equal curve progressions in the near-surface region are utilized. The  $\rho_c$  are measured after contact firing according to the transmission line model (TLM); see Appendix B.4. Scanning electron microscopy (SEM) [226] images of the sample surfaces taken following wet-chemical etching of metal contacts, glass layers, and dielectric passivation layer stacks, reveal the microscopic structure of the formerly metallized areas. The results of this section and the following section 5.4 are also published in Ref. [227].

### 5.3.1 Sample preparation

The samples used for determining  $\rho_c$  equal final solar cells. The applied fabrication process is very similar to that shown in Fig. 3.7(a) and is briefly described now.

Following alkaline texture of the *n*-type Cz-Si wafers with an edge length of 156 mm, the boron-doped front sides and the phosphorus-doped rear sides are formed by tube furnace diffusion processes with, first, a  $\text{BBr}_3$ , and second, a  $\text{POCl}_3$  liquid dopant precursor. The necessary diffusion barrier layers consist of a layer stack with 50 nm  $\text{SiO}_x$  and 30 nm  $\text{SiN}_x$  both applied by PECVD. For  $\text{BBr}_3$  diffusion, three different processes are used, namely diffusion process Gen3, Gen3–DrIn1, and Gen3–DrIn2 from Chapter 4.4.1. All samples receive the same  $\text{POCl}_3$  diffusion Phos2, during which their boron doping profiles do not alter significantly, as shown in Chapter 4.5. This is an important fact for the investigations to be performed.

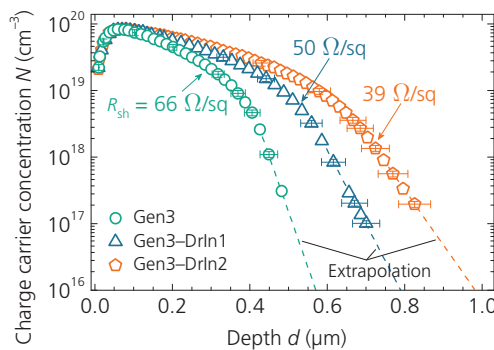


**Fig. 5.1.** Boron doping profiles  $N(d)$ , determined by ECV measurements at the center of alkaline textured wafers for the  $\text{BBr}_3$  diffusion processes Gen3, Gen3–DrIn1, and Gen3–DrIn2. The given sheet resistances  $R_{sh}$  correspond to inductive measurements performed in the area of the ECV measurements. Exemplary error bars are shown.

After the three different  $\text{BBr}_3$  diffusions and subsequent wet-chemical etching of the borosilicate glass (BSG), the boron doping profiles are determined by electrochemical capacitance-voltage (ECV) measurements (see Appendix B.2) on the alkaline textured surfaces. The doping profiles are shown in Fig. 5.1. They are in close agreement with profiles measured on reference wafers with alkaline saw-damage etched surfaces; see Fig. 4.12(a). The three boron dopings feature almost identical curve progressions up to a depth  $d \approx 60$  nm with maximum dopant concentration  $N_{\max} \approx 8 \cdot 10^{19} \text{ cm}^{-3}$ , but different junction depths, determined by extrapolation at a dopant concentration  $N = 10^{16} \text{ cm}^{-3}$  ( $d_{\text{Gen3}} \approx 570$  nm,  $d_{\text{Gen3-DrIn1}} \approx 790$  nm, and  $d_{\text{Gen3-DrIn2}} \approx 980$  nm). The depletion of the boron concentration close to the surface (hereafter referred to as doping depletion zone) originates from the post-oxidation performed at the end of the  $\text{BBr}_3$  diffusion process; see Chapter 4.3.3.

Prior to metallization, both wafer sides are coated with dielectric layers applied by PECVD. A layer stack of 10 nm-thick  $\text{Al}_2\text{O}_3$  and 65 nm-thick  $\text{SiN}_x$  is deposited on the front boron emitter, whereas a 75 nm-thick  $\text{SiN}_x$  layer is applied on the rear phosphorus doping. Subsequently, each of the two Ag-Al pastes is screen printed in the form of an H-pattern grid with a nominal screen opening of 75  $\mu\text{m}$  onto the boron-doped and coated surfaces. The rear side H-pattern grid is screen printed with a silver paste. For the following evaluation, the rear side of the samples is not of interest, and is therefore no longer discussed. After contact firing in an industrial conveyor belt furnace (peak wafer temperature about  $720^\circ\text{C}$ <sup>21</sup> for < 1 s), all samples are cut into 10 mm-wide strips and  $\rho_c$  is measured by the TLM method. Measurements with a light microscope reveal the finger widths to be  $w_f \approx 80 \mu\text{m}$  for both Ag-Al pastes.

### Sheet resistance distribution and TLM measurement points

The homogeneity of the boron emitter sheet resistance  $R_{\text{sh},4\text{pp}}$  over almost the entire wafer is determined by four-point-probe (4pp) measurements with a resolution of 20 x 20 data points. The  $R_{\text{sh},4\text{pp}}$  distribution measured for one textured wafer after each boron diffusion and BSG etching is illustrated in Fig. 5.2. Emitter Gen3 shows a low percentage standard deviation  $\sigma_{4\text{pp}}$  of only 3.1% in  $R_{\text{sh},4\text{pp}}$ . For emitters Gen3-DrIn1 and Gen3-DrIn2,  $\sigma_{4\text{pp}}$  is somewhat higher with 4.7% and 6.1%, respectively. However, the ar-

---

<sup>21</sup>This peak wafer temperature belongs to the optimal contact firing process identified for cell fabrication within this thesis.

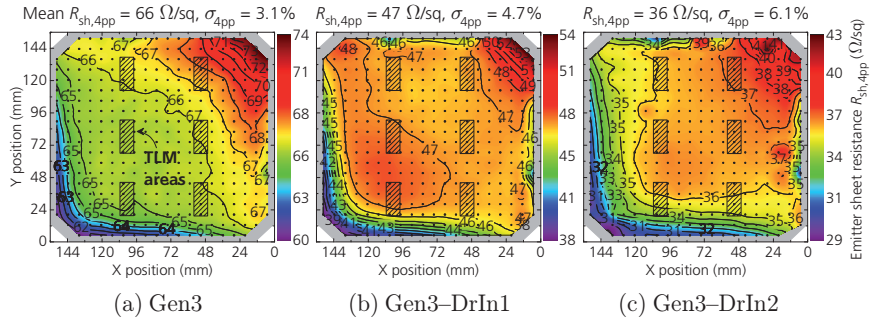


**Fig. 5.2.** Emitter sheet resistances  $R_{sh,4pp}$  obtained by 4pp measurements on alkaline textured  $n$ -type Cz-Si wafers after the specified  $\text{BBr}_3$  diffusions and etching of the BSG layer. The mean  $R_{sh,4pp}$  and the percentage standard deviation  $\sigma_{4pp}$  are stated above the figures. The slightly lower  $R_{sh,4pp}$  in the wafer center compared with the  $R_{sh}$  obtained by the inductive measurements, Fig. 5.1, originate from the 4pp technique applied on textured surfaces. The black dots illustrate the  $20 \times 20$  measurement pattern on the sample, which is indicated by the grey shaded wafer in the background. The black dashed rectangles indicate the areas utilized for the TLM measurements. Note that the scaling is different for all three  $R_{sh,4pp}$  plots.

eas with significantly different  $R_{sh,4pp}$  are located particularly in the lower left and in the upper right corner. This is due to the fact that during  $BBr_3$  diffusion, the wafers are oriented in the so-called diamond position—the lower left wafer corner showed up in the tube; see Fig. 4.1. Hence, a large area in the wafer center, where the TLM measurements are performed, shows nearly identical  $R_{sh,4pp}$ . The same  $R_{sh,4pp}$  indicate the same junction depths at the investigated spots. This fact is very important for the task to investigate the correlation between junction depth and  $\rho_C$ .

### 5.3.2 Specific contact resistance

Fig. 5.3 shows the  $\rho_C$  measured at the six TLM positions marked in Fig. 5.2. For each boron doping with each Ag-Al paste, two wafers are examined. As the doping profiles feature an initial doping depletion zone (extending to a profile depth  $d \approx 60$  nm, see Fig. 5.1), the low doping concentration of  $2 \cdot 10^{19} \text{ cm}^{-3}$  at the surface could cause a high  $\rho_C$ . But nevertheless, the obtained  $\rho_C$  are overall very low with  $\rho_C \lesssim 5 \text{ m}\Omega\text{cm}^2$ . A clear trend is visible for both Ag-Al pastes and the three boron doping profiles: lower  $\rho_C$  is measured for increasing junction depth  $d$ . For example,  $\rho_C$  determined for paste Ag-Al1 decreases from  $\rho_C = (3.7 \pm 0.8) \text{ m}\Omega\text{cm}^2$  for profile Gen3 ( $d \approx 570$  nm) to  $\rho_C = (2.0 \pm 0.4) \text{ m}\Omega\text{cm}^2$  for profile Gen3–DrIn2 ( $d \approx 980$  nm). Paste Ag-Al2 con-

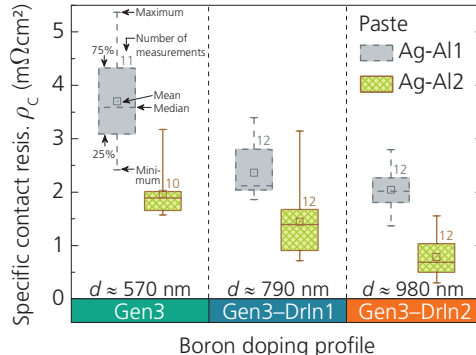


**Fig. 5.3.** Specific contact resistances  $\rho_C$  for the two Ag-Al pastes obtained by TLM measurements on the alkaline-textured and boron-doped surfaces Gen3, Gen3-DrIn1, and Gen3-DrIn2 after contact firing. The surfaces are coated with a layer stack of  $\text{Al}_2\text{O}_3$  and  $\text{SiN}_x$  both applied by PECVD. The junction depths  $d$  are also stated. The meaning of the box plots is exemplary explained for the first data set.

sistently shows about half the  $\rho_C$  as paste Ag-Al1 for each doping profile with the same trend regarding the junction depths.

This result clearly demonstrates that the doping profile progression after the doping depletion zone for deeper profiles with dopant concentrations  $N$  well below  $N_{\max}$  significantly affects the measured  $\rho_C$ . Thus,  $N_{\max}$  is not the only parameter of the doping profile which impacts the low-ohmic electrical contactability of boron-doped surfaces utilizing Ag-Al contacts, but also the junction depth. On the other hand, it is also clear that the Ag-Al paste itself has a major influence on the electrical contact formation.

### 5.3.3 Microstructure analysis

In order to investigate the silicon surface below the screen-printed and fired Ag-Al contacts, SEM images are taken after wet-chemical etching<sup>22</sup> of the TLM measurement strips. The wet-chemical etching process is performed such that the bulk Ag-Al contacts, the glass layer, the passivation layer stack, and all metal crystallites penetrating the boron-doped silicon (emitter)—either in direct contact with the bulk metal or separated from it by an intermediate thin glass layer [228]—are removed. Two exemplary SEM images

<sup>22</sup>Performed wet-chemical etching sequence (in each case at room temperature): (a) 35%  $\text{HNO}_3$  for 2 min, (b)  $\text{H}_2\text{O}/\text{HCl}/\text{H}_2\text{O}_2$  (mix ratio 1.5 : 1 : 0.2) for 5 min, (c) buffered HF for 45 min, (d) 35%  $\text{HNO}_3$  for 2 min, and (e)  $\text{H}_2\text{O}/\text{HCl}/\text{H}_2\text{O}_2$  (mix ratio 1.5 : 1 : 0.2) for 5 min.

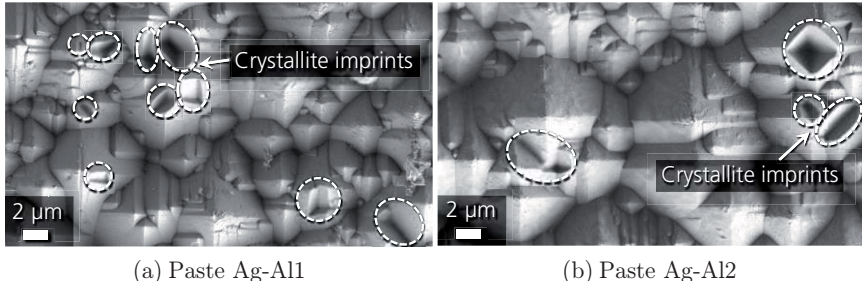


**Fig. 5.4.** Scanning electron microscopy images of alkaline textured Cz-Si surfaces with boron doping Gen3-DrIn1 after wet-chemical etching of (a) paste Ag-Al1, (b) paste Ag-Al2, the glass layer, the passivation layer stack, and the crystallites after contact firing. Each imprint was occupied by a crystallite before wet-chemical etching.

for both Ag-Al pastes and boron emitter Gen3-DrIn1 are shown in Fig. 5.4. The marked crystallite imprints imply a former metal crystallite presence at these locations [220]. The crystallites were either in direct contact to the bulk metal or separated from it by an intermediate thin glass layer. Different sizes of crystallite imprints can be observed, and also very large and thus deep imprints are apparent. This finding is in line with the findings from other authors, as already discussed in section 5.2. The imprints are significantly larger in size than those observed for silver pastes on phosphorus-doped surfaces [220,221]. This significant difference in size can also be seen by comparing the SEM images shown in Fig. 7.13(b) and (d).

To determine a rough estimation of both the crystallite coverage fraction  $A_{\text{cryst}}$  and their distribution in penetration depth  $d_{\text{cryst}}$ , for both Ag-Al pastes and each of the three boron emitters, 30 of such SEM images as in Fig. 5.4 are taken at different spots across the TLM measurement strips. For each combination of Ag-Al paste and boron emitter, the areas of clearly recognizable crystallite imprints are manually measured in the first step. To determine the respective crystallite coverage fraction  $A_{\text{cryst}}$ , the sum of all measured imprint areas is divided by the total area of all taken images per group. For estimating the depth distribution of the crystallites, each measured imprint area is assumed as a square area of the same size. This square area is taken as the quadratic base of an inverted pyramid representing the crystallite. Thereby, the crystallites are assumed to be represented by perfect, i.e. fully-formed, inverted pyramids. Based on the side lengths of the quadratic base, the depths of the crystallites  $d_{\text{cryst}}$  are calculated and the relative frequency of their occurrence is determined. The re-

### 5.3 Impact of junction depth on the specific contact resistance

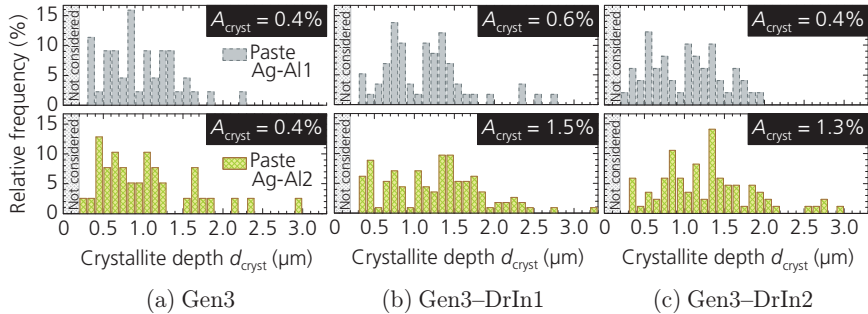


**Fig. 5.5.** Relative frequency of crystallite imprints with certain depths for boron emitters (a) Gen3, (b) Gen3–DrIn1, and (c) Gen3–DrIn2. The depths are estimated for both Ag-Al pastes according to the discussion in the text. The estimated total crystallite coverage fractions  $A_{\text{crys}}$  are also stated. Crystallite imprints with depths less than 0.2  $\mu\text{m}$  are not considered.

sults are shown in Fig. 5.5, summarized in groups with a difference of 0.1  $\mu\text{m}$  in  $d_{\text{cryst}}$ . The crystallites penetrate some 100 nm up to several microns deep into the boron-doped emitter surfaces. No clear differences in  $d_{\text{cryst}}$  are obvious for both Ag-Al pastes and the three boron emitters. Due to the large cutout of the SEM images and the fact that only clearly recognizable crystallite imprints are considered for this evaluation, the minimal resolvable depth of the crystallite imprints amounts to 0.2  $\mu\text{m}$ . However, smaller and thus not very deep crystallite imprints have been observed as well. The procedure yields crystallite coverage fractions  $A_{\text{cryst}}$  between 0.4% and 1.5%. It seems that paste Ag-Al2 features a somewhat higher  $A_{\text{cryst}}$  at least for the samples with boron emitters Gen3-DrIn1 and Gen3-DrIn2. However, the absolute numbers for  $A_{\text{cryst}}$  should only be understood as a rough estimate.

According to the theory for ideal planar metal contacts, see Fig. A.2, no significant difference in  $\rho_C$  is expected for the three different boron-doped surfaces, as the boron dopant concentrations in Fig. 5.1 are basically equal directly at the surface. Hence, the decrease in  $\rho_C$  with increasing junction depth  $d$  of the boron emitters seems to be correlated with the presence of the observed deep penetrating metal crystallites. It has to be noted again that Fig. 5.5 refers to all crystallites whether they have been in direct contact with the contact bulk or separated from it by an intermediate thin glass layer. Hence, a direct correlation between the obtained microstructure results and the measured absolute  $\rho_C$  in Fig. 5.3 is not possible. This is because the estimated coverage fractions  $A_{\text{crys}}$  only represent an upper limit for all occurring crystallites. However, the estimated  $A_{\text{crys}}$  are yet to become helpful in section 5.4.2.

## 5.4 Analytical model for calculation of specific contact resistances

The potential relationship between  $\rho_C$ , junction depth  $d$ , and deep penetrating crystallites is examined with the aid of an analytical model. Therewith, the causes for the observed differences in the measured  $\rho_C$  for the three boron doping profiles with different junction depths are supposed to be identified. Also, the impact on  $\rho_C$  of the doping depletion zone of the boron profiles close to the surface is addressed.

### Preliminary considerations

Various theories for current transport mechanisms exist and have been extensively studied within the last decade in terms of their applicability to silicon solar cells mainly featuring screen-printed and fired silver contacts on phosphorus-doped emitters, as e.g. in Refs. [111,229,230]. Apart from current transport via direct silicon-silver contacts (including silver crystallites penetrating the phosphorus emitter), electron tunneling through a thin interfacial glass layer is discussed. However, the latter is not further considered in the following sections, as recent results from *Hoenig* [230] emphasize that current transport via direct Si-Ag contacts is more likely for phosphorus emitters and silver contacts, which is supported by results of *Cabrera et al.* [221]. Additionally, *Fritz et al.* [225] propose the direct current conduction between Ag-Al contacts and boron-doped silicon as also being more likely to occur than other current transport mechanisms. Furthermore, results published by, e.g. *Heinz et al.* [213] reveal that the crystallites formed below fired Ag-Al contacts on textured and boron-doped surface consist almost solely of silver (the Al content is in the range of 1%).

Hence, for the analytical calculations to be performed, it is assumed that current transport occurs exclusively via metal crystallites in direct contact both with the bulk of the Ag-Al contact and with the boron-doped emitter. The Schottky barrier height  $q\phi_b$  for silver and aluminum is only slightly different (see Table 5.1); however, the small difference has a distinct effect on the performed calculations. As  $q\phi_b$  is one of the input parameters with unknown exact value for the investigated contact system, as is discussed in Chapter 5.4.2, the real composition of the metal crystallites is therefore rather of minor importance. The author is aware that metal-silicon contacts are much more complex than considered in the used analytical model. Despite its simplicity, however, not only can the experimentally deter-

mined  $\rho_C$  be matched qualitatively, but also quantitatively by choice of appropriate and physically reasonable input parameters.

### 5.4.1 Approach

The procedure introduced in Refs. [111,230] for silver contacts on phosphorus-doped surfaces forms the starting point to calculate  $\rho_C$ . The analytical model applied in these works considers the three current transport mechanisms between metal and highly doped silicon as introduced in Chapter 2.4 and summarized in Table A.1 in Appendix A, namely thermionic emission (TE), thermionic field emission (TFE), and field emission (FE). Of course, for using the analytical model for boron-doped surfaces, the dopant-type-dependent variables concerning the applied current transport mechanisms have to be adapted to the *p*-type boron doping. Exemplarily calculated  $\rho_C$  for *p*-doped silicon as function of dopant concentration  $N$  shows Fig. A.2 for the three different current transport models. The unified model for  $\rho_C$  from *Varahramyan and Verret*, labeled with TFE/FE in Fig. A.2, describes the TFE and FE very well for  $N > 10^{18} \text{ cm}^{-3}$ . On the other hand, for  $N \leq 10^{18} \text{ cm}^{-3}$ , this unified model does not consider TE, which is becoming more and more important towards lower  $N$ .

As the depth-dependent progression of the dopant concentration also for  $N \leq 10^{18} \text{ cm}^{-3}$  has to be considered for the examinations to be performed due to the deep penetrating crystallites, the unified TFE/FE model is not suitable for calculating  $\rho_C$  for dopant concentrations in the range of  $10^{16} \text{ cm}^{-3} \leq N \leq 10^{20} \text{ cm}^{-3}$ . Since the dopant concentrations of the three boron emitters under investigation are less than  $10^{20} \text{ cm}^{-3}$ , FE processes do not have to be taken into account. Hence, the combination of TE and TFE for calculation of  $\rho_C$  is clearly more appropriate and is given by

$$\rho_C(\text{TE/TFE}) = \left( \frac{1}{\rho_C(\text{TE})} + \frac{1}{\rho_C(\text{TFE})} \right)^{-1}. \quad (5.1)$$

The resulting curve for  $\rho_C$  from Eq. (5.1) is plotted in Fig. 5.6 as solid line along with the curves for TE and TFE. The formulae to calculate  $\rho_C(\text{TE})$  and  $\rho_C(\text{TFE})$  are given in Eqs. (A.6) and (A.7), respectively.

The approach pursued now allows for calculating  $\rho_C$  depending on e.g. doping profile, crystallite penetration depth, and crystallite coverage fraction. For the calculations, the following assumptions are made:

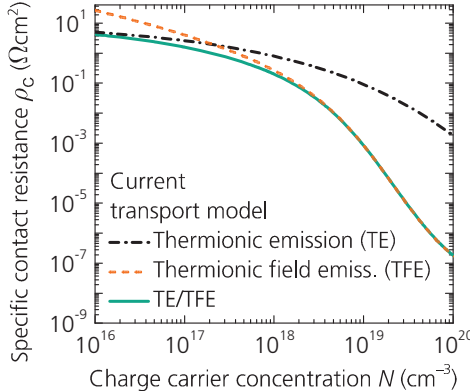


**Fig. 5.6.** Specific contact resistances  $\rho_C$  on  $p$ -doped silicon as function of charge carrier concentration  $N$  for the different current transport models (used parameters: see Table 5.2). Image force barrier lowering is taken into account. Note that the maximum  $N = 10^{20} \text{ cm}^{-3}$  on the  $x$ -axis is different from that in Fig. A.2.

- The considered wafer surface is smooth and parallel to the (100) crystal plane of silicon.
- The crystallites are represented by fully-formed inverted pyramids with a quadratic base grown into the boron-doped silicon surface with an angle of  $54.7^\circ$  [108, p. 495] to the (100) plane.

As the dopant concentrations of the boron emitters vary with increasing (crystallite penetration) depth, this fact has to be considered for the calculation of the total contact resistance  $R_{C,\text{cryst}}$  of a single crystallite. For this purpose, the sidewall surface of the crystallite in contact to the boron-doped silicon is divided in arbitrary small area elements  $\Delta A_i$ , as sketched in Fig. 5.7. For each area element  $\Delta A_i$ , the average contact resistance  $R_{C,\text{cryst},i}$  is calculated by considering the depth-dependent dopant concentration. This is implemented by the calculation of the specific contact resistance  $\rho_{C,\text{cryst},i}$  according to Eq. (5.1). Assuming a parallel connection of all single contact resistances  $R_{C,\text{cryst},i}$ , the total contact resistance of a single crystallite  $R_{C,\text{cryst}}$  is given by

$$R_{C,\text{cryst}} = \left( \sum_i \frac{1}{R_{C,\text{cryst},i}} \right)^{-1} = \left( \sum_i \frac{1}{\rho_{C,\text{cryst},i}} \right)^{-1} \cdot \frac{1}{\Delta A_i}. \quad (5.2)$$

In order to compare calculated and experimentally measured  $\rho_C$ , it is helpful to define the specific contact resistance of a single crystallite  $\rho_{C,\text{cryst}}$  as the

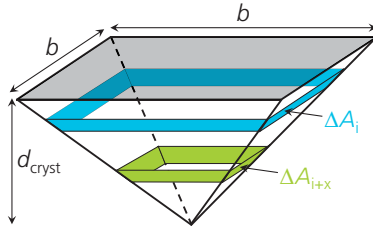


**Fig. 5.7.** Sketch of an inverted pyramid representing a metal crystallite with depth  $d_{\text{cryst}}$  and side length  $b$  of the quadratic base. For calculation of the doping-profile-dependent contact resistance, the pyramid's sidewall area is divided in arbitrary small area elements  $\Delta A_i$ .

total contact resistance  $R_{C,\text{cryst}}$  in relation to the base area of the crystallite with side length  $b$ ,

$$\rho_{C,\text{cryst}} = R_{C,\text{cryst}} b^2. \quad (5.3)$$

To finally calculate the theoretically expected macroscopic specific contact resistance  $\rho_C$  between an ideal Ag-Al contact (all crystallites are in direct contact with the Ag-Al bulk) and the boron-doped silicon, the specific contact resistance of a single crystallite  $\rho_{C,\text{cryst}}$  has to be divided by the crystallite coverage fraction  $A_{\text{cryst}}$  below the Ag-Al contact:

$$\rho_C = \frac{\rho_{C,\text{cryst}}}{A_{\text{cryst}}}. \quad (5.4)$$

#### 5.4.2 Calculation of specific contact resistances

For calculation of the specific contact resistances  $\rho_C$  between the Ag-Al contacts and the boron-doped silicon emitters, according to Eqs. (5.1) and (5.4), several input parameters are necessary. Different values can be found in literature for the various parameters needed for the considered TE and TFE processes. Table 5.1 gives an overview of these parameters for both *p*-type as well as *n*-type silicon at room temperature (i.e.  $T = 300$  K). It is clear that different parameter sets have to be used depending on the doping type. It has to be noted that the effective charge carrier tunneling mass  $m_t^*$ —which is, e.g. dependent on doping density and crystal orientation [231]—is least precisely known especially for holes [232]. Thus, the given values for  $m_t^*$  have to be taken as rough estimation. Furthermore, the Schottky barrier height  $q\phi_b$  on practical silicon surfaces can differ quite significantly, as exemplarily shown by *Turner* and *Rhoderick* [233], depending on the structure of the interface and in particular on the structure of

**Table 5.1.** Overview of several doping-type-dependent parameters at  $T = 300$  K as found in the literature. The constant  $\bar{c}$  for the unified TFE/FE model, Eq. (A.11), is also specified.

Parameter (Unit)	$q\phi_b$ (Ag) (eV)	$q\phi_b$ (Al) (eV)	$A^*$ ( $\text{A}\cdot\text{cm}^{-2}\cdot\text{K}^{-2}$ )	$m_t^*/m_0$ (1)	$\bar{c}$ (1)
<i>p</i> -type Si	0.54 [108]	0.58 [108]	32 [237]	0.35–0.5 [231]	0.355
	0.53–0.55 [236]	0.57–0.58 [236]			[238]
<i>n</i> -type Si	0.78 [108]	0.72 [108]	112 [237]	0.25–0.4 [239]	0.425
	0.68–0.83 [106]	0.61–0.77 [106]			[238]

**Table 5.2.** Overview of the parameters used within this chapter for the calculations of  $\rho_C$  unless otherwise stated.

Parameter (Unit)	$T$ (K)	$q\phi_b$ (eV)	$A^*$ ( $\text{A}\cdot\text{cm}^{-2}\cdot\text{K}^{-2}$ )	$m_t^*/m_0$ (1)	$\varepsilon_r$ (1)	$N_V$ ( $\text{cm}^{-3}$ )
<i>p</i> -type Si	300	0.54	32	0.5	11.7	$2.503 \cdot 10^{19}$

the interfacial layer. Also other parameters, like the surface orientation, play an important role for  $q\phi_b$ , as shown by *Tung* [234] and by *Butler* and *Harding* [235]. A summary of different  $q\phi_b$  on *n*-type silicon is found in Ref. [106, p. 52]. However, for all performed calculations of  $\rho_C$  on *p*-doped silicon within this chapter, the parameters given in Table 5.2 are used unless otherwise stated.

### Dependence on crystallite coverage fraction and crystallite depth

The calculated macroscopic  $\rho_C$  for the doping profile of boron emitter Gen3 is exemplified in Fig. 5.8(a). Apart from varying the crystallite coverage fraction  $A_{\text{cryst}}$  ( $0.005\% \leq A_{\text{cryst}} \leq 20\%$ ), also the crystallite penetration depth  $d_{\text{cryst}}$  is varied ( $7.5 \text{ nm} \leq d_{\text{cryst}} \leq 480 \text{ nm}$ ). The maximum considered  $d_{\text{cryst}}$  are chosen such that the crystallites stay within the emitter. The measured data points of doping profile Gen3 are interpolated with the software “OriginPro 8.5” to have more data points available for the calculations (1000 data points in total). The results demonstrate the clear dependence of  $\rho_C$  both on  $A_{\text{cryst}}$  and  $d_{\text{cryst}}$  for the assumption that current transport exclusively occurs via metal crystallites in direct contact with both the highly boron-doped silicon and the Ag-Al contact bulk. It is clear that the higher  $A_{\text{cryst}}$ , the lower  $\rho_C$  will be because more crystallites contribute to the conductivity. For crystallites, which penetrate the boron emitter only up to the depth of the doping depletion zone ( $d_{\text{cryst}} \leq 60 \text{ nm}$ ), initially a significant reduction of  $\rho_C$  is apparent for increasing crystallite depth  $d_{\text{cryst}}$ . After

reaching a minimum,  $\rho_C$  gradually increases for crystallites deeper than 120 nm. This is even more obvious in Fig. 5.9(a), in which the course of  $\rho_C$  is demonstrated in dependence of  $d_{\text{cryst}}$  for constant  $A_{\text{cryst}} = 0.2\%$ . This increase has two reasons: first, more and more of the crystallite's flank surface is in touch with lower doping densities for increasing  $d_{\text{cryst}}$ . So, the more the specific contact resistance of each crystallite  $\rho_{C,\text{cryst}}$  increases, the deeper the crystallites are. Second, the quadratic base area of every crystallite increases for increasing  $d_{\text{cryst}}$  and therefore, the number of crystallites decreases for increasing  $d_{\text{cryst}}$  for a given  $A_{\text{cryst}}$ .

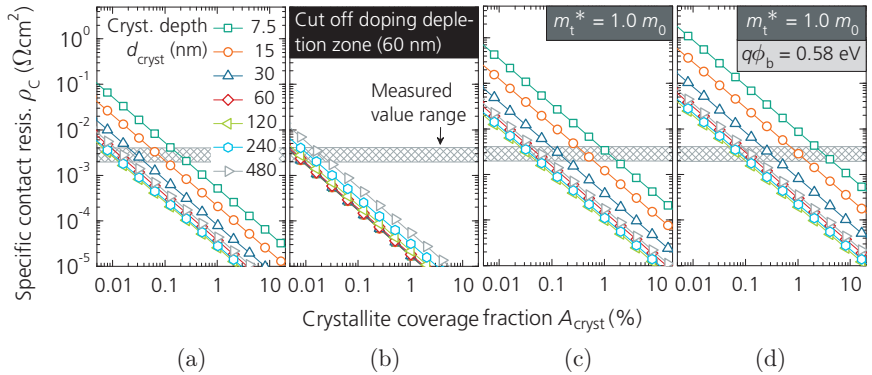


**Fig. 5.8.** Calculated specific contact resistance  $\rho_C$  for boron profile Gen3 (Fig. 5.1) according to Eqs. (5.1) and (5.4) as function of crystallite coverage fraction  $A_{\text{cryst}}$  and crystallite penetration depth  $d_{\text{cryst}}$  (used input parameters: see Table 5.2). The experimentally measured value range of  $\rho_C$  ( $2 \text{ m}\Omega\text{cm}^2 \lesssim \rho_C \lesssim 4 \text{ m}\Omega\text{cm}^2$ ; Fig. 5.3) is also plotted. In (b), the doping depletion zone of profile Gen3 (i.e. the first 60 nm) is cut off to account for a possible etching of the boron emitter during contact firing. In (c) and (d), the stated input parameters are changed compared to (a).

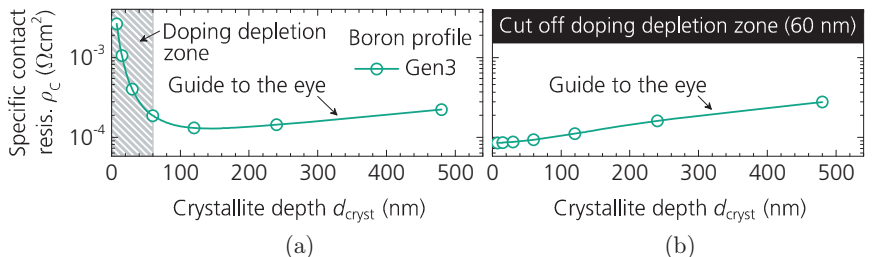


**Fig. 5.9.** Calculated  $\rho_C$  for a crystallite coverage fraction  $A_{\text{cryst}} = 0.2\%$  according to Eqs. (5.1) and (5.4) as function of the crystallite penetration depth  $d_{\text{cryst}}$  (used input parameters: see Table 5.2). (a) Doping profile Gen3 with doping depletion zone (Fig. 5.1), (b) the depletion zone (the first 60 nm) of profile Gen3 is cut off.

The experimentally measured  $\rho_C$ -range for the Ag-Al contacts, as shown in Fig. 5.3, is also indicated in Fig. 5.8. The calculated  $\rho_C$  are in agreement with the measured ones for crystallite coverage fraction  $A_{\text{cryst}}$ , determined to be lower than about 0.3%. Compared with the experimentally extracted total coverage fractions between  $0.4\% \leq A_{\text{cryst}} \leq 1.5\%$  from section 5.3.3 (Fig. 5.5), the coverage fractions that need to be considered in the calculations to explain the measured  $\rho_C$  rather seem a bit too low (especially for the deeper crystallites for which  $A_{\text{cryst}}$  must be even lower). However, they are within the bounds of possibility. It should be kept in mind that section 5.3.3 deals with the total crystallite coverage fraction  $A_{\text{cryst}}$ , whereas the estimate of  $A_{\text{cryst}} \leq 0.3\%$  from the calculation refers to the area of crystallites being in direct contact both with the boron-doped silicon and the Ag-Al contact bulk, which is a subset of the former.

### **Impact of the doping depletion zone**

The impact of the doping depletion zone on  $\rho_C$  can be characterized by comparison of calculations of  $\rho_C$  for profile Gen3 either with or without the doping depletion zone. For this purpose, the doping depletion zone (i.e. the first 60 nm) of profile Gen3 is cut off, which simulates a possible layer-like etching of the emitter by paste ingredients during contact firing. The comparison may be carried out based on Fig. 5.8(a) and (b), or based on Fig. 5.9(a) and (b). Using the latter graphs the course in  $\rho_C$  is easier to see. For the scenario with cut off doping depletion zone, no initial strong decrease in  $\rho_C$  occurs; instead,  $\rho_C$  continuously increases for increasing  $d_{\text{cryst}}$ . The calculations yield comparable  $\rho_C$  values for profile Gen3 whether with or without the doping depletion zone for sufficiently deep crystallites (i.e.  $d_{\text{cryst}} \gtrsim 120$  nm). Only for very small crystallites with  $d_{\text{cryst}} \leq 60$  nm,  $\rho_C$  is one order of magnitude larger for the profile with depletion zone than for the one without. In other words, the doping depletion zone has no significant negative impact on  $\rho_C$  given that the crystallites are somewhat deeper than the extent of the depletion zone. As discussed in section 5.3.3 (Fig. 5.5), this is the case for the examined Ag-Al contacts. On the other hand, considering Fig. 5.8(a), even for the scenario in which only very small crystallites are formed, reasonable low  $\rho_C$  can be achieved for doping profiles with depletion zone in case a sufficient number of crystallites is present.

## Variation of input parameters

As already discussed, especially the effective tunneling mass  $m_t^*$  and the Schottky barrier height  $q\phi_b$  are input parameters whose exact values are not known for the investigated contact system. The influence of a higher  $m_t^*$  on  $\rho_C$  is depicted in Fig. 5.8(c), whereas in Fig. 5.8(d)  $q\phi_b$  is increased further to the value of aluminum. Comparing both graphs with Fig. 5.8(a), it is clear that both parameters affect the calculated  $\rho_C$  considerably. On the other hand, the crystallite coverage fractions  $A_{\text{cryst}}$ , for which the calculated  $\rho_C$  are in line with the measured ones, are closer to the values as experimentally determined in section 5.3.3. This shows that the macroscopically measured  $\rho_C$  can be described by the proposed model using the assumption that current transport occurs exclusively via metal crystallites, which are in direct contact both with the boron-doped emitter and the Ag-Al contact bulk.

### 5.4.3 Impact of the doping profile shape on the specific contact resistance

The previously discussed analytical model is now used to find an explanation for the observed decreasing  $\rho_C$  with increasing junction depth, as shown for the boron emitters under investigation in Fig. 5.3. For this purpose,  $\rho_C$  is calculated for all three boron doping profiles under variation of the crystallite penetration depth  $d_{\text{cryst}}$  between  $0 \text{ nm} < d_{\text{cryst}} \leq 980 \text{ nm}$ .

As already discussed, the measured doping profiles are interpolated with “OriginPro 8.5” to have more data points for the calculations, which are performed with 1000 data points in total. Between  $0 \text{ nm} < d_{\text{cryst}} \leq 60 \text{ nm}$ —the section corresponding to the doping depletion zone of the profiles—the same data points are used for all three doping profiles to only investigate the influence of the different curve progressions for  $N < N_{\text{max}}$  after the depletion zone.

Similar to Fig. 5.9(a), Fig. 5.10(a) depicts exemplarily calculated  $\rho_C$  values for a crystallite coverage fraction  $A_{\text{cryst}} = 0.2\%$  as a function of the crystallite penetration depth  $d_{\text{cryst}}$ , but now for all three boron emitters and the two sets of input parameters. The maximum considered  $d_{\text{cryst}}$  equal the junction depths for each profile. As already seen, the used input parameters have a significant influence on the absolute value of the calculated  $\rho_C$  which is apparent by a shift of  $\rho_C$  by one order of magnitude. For crystallites with  $d_{\text{cryst}} \leq 60 \text{ nm}$ , no difference is visible for the calculated  $\rho_C$  of the three profiles.

This is because identical data points are used for the three boron doping profiles up to the profile depth of 60 nm. Starting at  $d_{\text{cryst}} = 60$  nm, the  $\rho_C$ -curves deviate from each other:  $\rho_C$  decreases relative to profile Gen3 for the deeper profiles Gen3–DrIn1 and Gen3–DrIn2 in dependence of  $d_{\text{cryst}}$ . The lowest  $\rho_C$  are obtained for profile Gen3–DrIn2. Fig. 5.11(a) depicts the respective relative differences for the calculated  $\rho_C$  in relation to the  $\rho_C$  obtained for boron profile Gen3. The relative differences in  $\rho_C$ , which are independent of  $A_{\text{cryst}}$ , between profile Gen3 and Gen3–DrIn1 amount up to  $-20\%$ , whereas the relative differences in  $\rho_C$  between profile Gen3 and Gen3–DrIn2 are found to be up to  $-40\%$ . These values are in the range of the experimentally determined differences; see Fig. 5.3. The calculated relative differences are more or less independent of the used input parameters. The most significant relative reduction in  $\rho_C$  results for  $d_{\text{cryst}} \lesssim 500$  nm.

Similar results are obtained with respect to the three doping profiles for which the first 60 nm are cut off. The absolute values of  $\rho_C$  in dependence on  $d_{\text{cryst}}$  are depicted in Fig. 5.10(b) for  $A_{\text{cryst}} = 0.2\%$  and the corresponding ones relative to Gen3 are shown in Fig. 5.11(b). The same trends are seen as discussed above, however, larger relative differences in  $\rho_C$  result from these calculations: up to  $-30\%$  for profile Gen3–DrIn1, and up to  $-60\%$  for profile Gen3–DrIn2. Although the  $\rho_C$ -curves slightly differ for the two sets of input parameters, the clear relative differences for profile Gen3–DrIn1 and Gen3–DrIn2 in comparison with profile Gen3 further remain. Hence, the actual selection of the input parameters has no significant effect on the relative  $\rho_C$ -differences between the three boron doping profiles. On the contrary, the analytical calculations clearly show the influence of deeper doping profiles in terms of lower  $\rho_C$ .

#### 5.4.4 Discussion

The proposed analytical model for calculating  $\rho_C$  with direct current conduction between metal crystallites and the boron-doped emitter—considering thermionic emission and thermionic field emission processes—can be brought into agreement with the  $\rho_C$  measured experimentally. Therefore, physical reasonable input parameters are used. However, it has to be emphasized that the exact values of the input parameters are not known, as e.g.  $m_t^*$ ,  $q\phi_b$ , and  $A_{\text{cryst}}$ . Hence, a predictive calculation of  $\rho_C$  based only on given doping profiles is rather speculation. On the other hand, the exact knowledge of the input parameters is not necessary when comparing only relative differences between different doping profiles (assuming that the

same values are valid for all profiles). The results from the analytical calculations indicate that the experimentally observed lower  $\rho_C$  for boron emitter profiles Gen3-DrIn1 and Gen3-DrIn2, compared with those of profile Gen3, can be explained by their higher dopant concentrations  $N$  for profile depths larger than 60 nm and metal crystallite depths  $d_{\text{cryst}}$  of several 100 nm. Apart from the maximum boron dopant concentration  $N_{\max}$ , also the junction depth affects the specific contact resistance obtained for screen-printed and fired Ag-Al contacts: the deeper the profile, the lower  $\rho_C$  is.

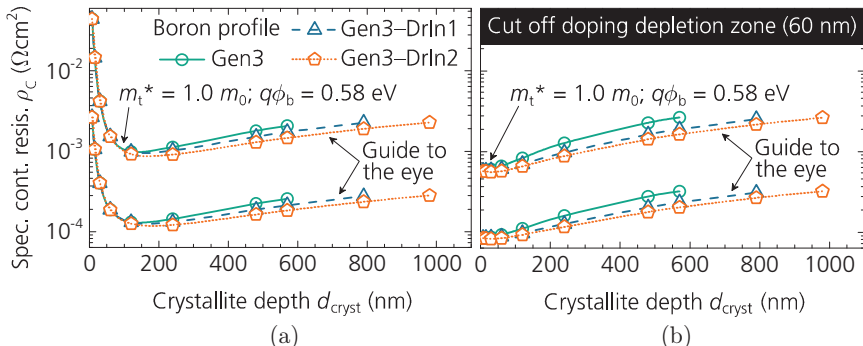


**Fig. 5.10.** Calculated  $\rho_C$  for a crystallite coverage fraction  $A_{\text{cryst}} = 0.2\%$  as a function of the crystallite penetration depth  $d_{\text{cryst}}$  (used input parameters: see Table 5.2; other values for  $m_t^*$  and  $q\phi_b$  are used as indicated). (a) Doping profiles with doping depletion zones (Fig. 5.1), (b) the depletion zones (the first 60 nm) of the profiles are cut off.

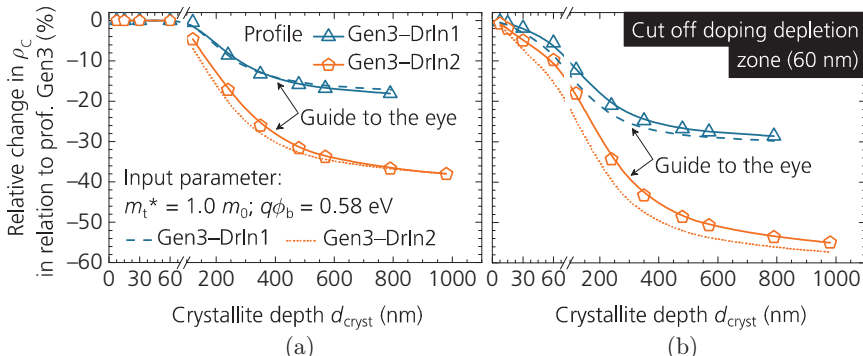


**Fig. 5.11.** Calculated relative changes in  $\rho_C$  independent of  $A_{\text{cryst}}$  for the profiles Gen3-DrIn1 and Gen3-DrIn2 in relation to  $\rho_C$  for profile Gen3 (used input parameters: see Table 5.2; other values for  $m_t^*$  and  $q\phi_b$  are used as indicated). (a) Doping profiles with doping depletion zone (Fig. 5.1), (b) the depletion zone (the first 60 nm) of the profiles is cut off. For profile Gen3,  $N$  is set to  $10^{16} \text{ cm}^{-3}$  for larger depths than the junction depth in order to be able to calculate relative differences for  $d_{\text{cryst}} > 570 \text{ nm}$ .

This is because the decrease in doping density occurs later, when the junction is deeper. Hence, for a given crystallite penetration depth, a larger proportion of the crystallite's flank surface is in contact with higher doping densities for deeper junctions. Furthermore, the doping depletion zone turns out to be negligible with respect to  $\rho_c$  for crystallite penetration depths somewhat larger than the depth of the depletion zone.

### 5.5 Doping profiles with decreased maximum dopant concentration

As shown in Chapter 4.4.2, lowering maximum dopant concentration  $N_{\max}$  of the boron doping profiles leads to a significant decrease in dark saturation current density  $j_{0e}$ . However, the question arises if boron-doped silicon emitters featuring those doping profiles can form a low-ohmic contact to screen-printed and fired Ag-Al contacts. To answer this question, four selected boron doping profiles with stepwise decreased  $N_{\max}$  are examined utilizing screen-printing paste Ag-Al1. Paste Ag-Al1 is selected as it is supposed to be more sensitive with respect to doping profile changes. The results discussed below have been obtained based on finished *n*-type MWT solar cells, as they will be dealt with in detail in Chapter 7.5.

#### 5.5.1 Sample preparation

The main differences to the fabrication process as used in section 5.3 will now be discussed, otherwise refer to Fig. 7.15 for the complete fabrication process of the utilized *n*-type MWT solar cell samples.

Four Gen3-based  $\text{BBr}_3$  diffusion processes, introduced in Chapter 4, are employed. They are referred to as Gen3, Gen3–A, Gen3–B, and Gen3–C within this chapter. Their original designation from Chapter 4 is given in Table 5.3. The doping profiles, measured by ECV on alkaline saw-damage etched surfaces, are illustrated in Fig. 5.12. The associated characteristic parameters like sheet resistance  $R_{\text{sh}}$ , maximum dopant concentration  $N_{\max}$ , and junction depth  $d$  are summarized in Table 5.3. The  $\text{BBr}_3$  diffusion processes are selected such that the resulting doping profiles exhibit pairwise either the same  $N_{\max}$  or the same  $d$ . Doping profile Gen3–A has the same  $d$  but lower  $N_{\max}$  compared with Gen3. The  $N_{\max}$  of profile Gen3–A is almost equal to that of Gen3–B, but the latter has a significant deeper junction.

Profile Gen3–C shows a further decreased  $N_{\max}$  while having more or less the same  $d$  as Gen3–B.

A 6 nm-thick ALD  $\text{Al}_2\text{O}_3$  and a 70 nm-thick PECVD  $\text{SiN}_x$  layer stack passivates the alkaline textured and boron-doped emitter surfaces<sup>23</sup>. Paste Ag-Al1 is used for the screen-printed metallization of the boron-doped surfaces, yielding finger widths of  $w_f \approx 70 \mu\text{m}$  after contact firing, which is performed

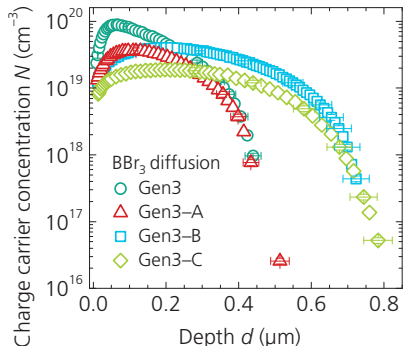


**Fig. 5.12.** Boron doping profiles, determined by ECV measurements on alkaline saw-damage etched surfaces for the specified Gen3-based  $\text{BBr}_3$  diffusion processes. Exemplary error bars are shown. Further data on the boron profiles are summarized in Table 5.3.

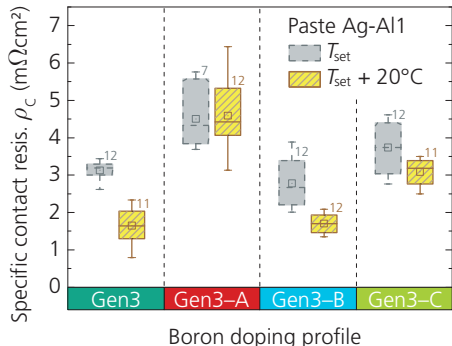


**Fig. 5.13.** Specific contact resistances  $\rho_C$  for paste Ag-Al1 obtained by TLM measurements on the alkaline textured and boron-doped surfaces after contact firing with two different set temperatures  $T_{\text{set}}$ . The boron-doped surfaces are coated with an ALD  $\text{Al}_2\text{O}_3$  and PECVD  $\text{SiN}_x$  layer stack.

**Table 5.3.** Summary of characteristic parameters for the different Gen3-based  $\text{BBr}_3$  diffusion processes obtained from alkaline saw-damage etched ECV samples ( $R_{\text{sh}}$ ,  $N_{\max}$ ,  $d$ ). Profile depth  $d$  is estimated at a dopant concentration  $N = 1.3 \cdot 10^{15} \text{ cm}^{-3}$ , which corresponds to the bulk doping concentration of the wafers utilized for  $\rho_C$  determination.

Designation	BBr <sub>3</sub> diffusion processes	$R_{\text{sh}}$ ( $\Omega/\text{sq}$ )	$N_{\max}$ ( $10^{19} \text{ cm}^{-3}$ )	$d$ ( $\mu\text{m}$ )
This chapter	Chapter 4			
Gen3	Gen3	$\approx 65$	$8.9 \pm 0.9$	$580 \pm 58$
Gen3–A	Gen3–PO2–LT	$\approx 111$	$3.6 \pm 0.4$	$570 \pm 57$
Gen3–B	Gen3–DrIn1–PO6	$\approx 62$	$4.1 \pm 0.4$	$820 \pm 82$
Gen3–C	Gen3–PO5	$\approx 108$	$1.8 \pm 0.2$	$840 \pm 84$

<sup>23</sup> $R_{\text{sh}}$  for the textured samples:  $R_{\text{sh}} = (70 \pm 2) \Omega/\text{sq}$  (Gen3),  $R_{\text{sh}} = (131 \pm 7) \Omega/\text{sq}$  (Gen3–A),  $R_{\text{sh}} = (68 \pm 2) \Omega/\text{sq}$  (Gen3–B), and  $R_{\text{sh}} = (125 \pm 4) \Omega/\text{sq}$  (Gen3–C).

with two different set peak temperatures  $T_{\text{set}}$  and  $T_{\text{set}} + 20^\circ\text{C}$ .  $T_{\text{set}}$  is equal to that used in the previous section. Again, all samples are cut into 10 mm-wide strips and  $\rho_{\text{C}}$  is measured by the TLM method.

### 5.5.2 Specific contact resistance

Fig. 5.13 summarizes the measured  $\rho_{\text{C}}$ . It is striking that all measured  $\rho_{\text{C}}$  are fairly low with mean  $\rho_{\text{C}} < 5 \text{ m}\Omega\text{cm}^2$  even for profile Gen3-C with  $N_{\text{max}}$  of only about  $2 \cdot 10^{19} \text{ cm}^{-3}$ . The slightly higher firing temperature leads to somewhat lower  $\rho_{\text{C}}$ , but the trend in  $\rho_{\text{C}}$  between the different boron doping profiles is identical for both contact-firing processes. Hence, only the results obtained for  $T_{\text{set}}$  are considered in the following discussion.

Comparing the results between Gen3 and Gen3-A shows an increase in  $\rho_{\text{C}}$  from  $\rho_{\text{C}} = (3.1 \pm 0.2) \text{ m}\Omega\text{cm}^2$  to  $\rho_{\text{C}} = (4.5 \pm 0.8) \text{ m}\Omega\text{cm}^2$ . Since the profile depths  $d$  are almost equal for both emitters, the somewhat higher  $\rho_{\text{C}}$  for Gen3-A most likely originates from the lower  $N_{\text{max}} = (3.6 \pm 0.4) \text{ cm}^{-3}$ . Note that the crystallite coverage fractions  $A_{\text{cryst}}$  and/or the crystallite depths  $d_{\text{cryst}}$  might vary for the emitters under investigation. So the conclusions drawn here are based on the assumption that all four emitters have the same  $A_{\text{cryst}}$  and  $d_{\text{cryst}}$ . The benefit of a deeper doping profile in terms of lower  $\rho_{\text{C}}$  is seen for emitter Gen3-B, which almost has the same  $N_{\text{max}}$  as emitter Gen3-A. The  $\rho_{\text{C}} = (2.8 \pm 0.6) \text{ m}\Omega\text{cm}^2$  determined for profile Gen3-B is  $\approx 40\%$  less than that of Gen3-A and thus, even below  $\rho_{\text{C}} = (3.1 \pm 0.2) \text{ m}\Omega\text{cm}^2$ , obtained for profile Gen3. This finding demonstrates that a deeper junction can compensate the increase in  $\rho_{\text{C}}$  due to lower  $N_{\text{max}}$ . However, the extent to which  $d$  must be increased to compensate a certain decrease in  $N_{\text{max}}$  cannot be quantified. Starting from profile Gen3-B, further lowering  $N_{\text{max}}$  to  $N_{\text{max}} = (1.8 \pm 0.2) \text{ cm}^{-3}$  yields only slightly increased  $\rho_{\text{C}} = (3.7 \pm 0.7) \text{ m}\Omega\text{cm}^2$  for profile Gen3-C.

Furthermore, it can be concluded that the electrical contacting behavior of paste Ag-Al1 does not differ significantly for the different passivation layer stacks applied in this section (6 nm-thick ALD  $\text{Al}_2\text{O}_3$  + 70 nm-thick PECVD  $\text{SiN}_x$ ) and in section 5.3 (10 nm-thick  $\text{Al}_2\text{O}_3$  + 65 nm-thick  $\text{SiN}_x$  both applied by PECVD). In both experiments, the measured  $\rho_{\text{C}}$  for emitter Gen3 for the same  $T_{\text{set}}$  are found to be nearly equal with  $\rho_{\text{C}} \approx 3.5 \text{ m}\Omega\text{cm}^2$ .

In summary, lowering  $N_{\text{max}}$  from initially  $N_{\text{max}} = (8.9 \pm 0.9) \text{ cm}^{-3}$  to  $N_{\text{max}} = (1.8 \pm 0.2) \text{ cm}^{-3}$ , while increasing  $d$ , leads to the finding that both boron

emitters Gen3 and Gen3–C can be electrically contacted by screen-printed and fired Ag-Al contacts with similar low  $\rho_c$  of about  $4 \text{ m}\Omega\text{cm}^2$ . All four examined doping profiles are found to be suitable for use in the fabrication of  $n$ -type solar cells in terms of their electrical contactability.

## 5.6 Charge carrier recombination at metal crystallites

As the preceding sections show, metal crystallites penetrating the boron-doped silicon emitter ensure low specific contact resistance  $\rho_c$  between emitter and applied metal contacts. On the other hand, deep penetrating metal crystallites are suspected to be the origin of significantly increased dark saturation current densities of the metallized areas for Ag-Al contacts on boron-doped emitters, as discussed in section 5.2. The latter issue will now be dealt with in more detail.

In an ongoing PhD thesis at *Fraunhofer ISE*, *Nico Wöhrle* developed a numerical three-dimensional (3D) simulation model of charge carrier recombination at metal crystallites penetrating into highly boron-doped silicon surfaces. The simulation is performed with *Sentaurus Device* [240] and is based on the QSSPC technique. Therein, the metal layer covering the surface is defined as optically transparent and the crystallites are considered as inverted pyramids. The basic equations for determining the dark saturation current density  $j_0$  by means of the QSSPC approach are identical to those discussed in Chapter 2.2.2. Depending on the boron doping profile, the dark saturation current densities  $j_{0,\text{met}}$  underneath the metal contacts can thus be simulated for varying  $d_{\text{cryst}}$  and  $A_{\text{cryst}}$ . The 3D QSSPC simulation has been applied for the four boron doping profiles from the previous section. The obtained results are also published in Ref. [241], where also further information on the simulation approach can be found. The following discussion covers the most important findings.

Fig. 5.14 depicts two exemplary two-dimensional (2D) cross-sections of the 3D QSSPC simulation results for boron doping profile Gen3 with reference to two crystallites of different depths but same coverage fraction. Visible is the electron current density under illumination at the metal-silicon interface, triggered by recombination at the metal contact. For the deeper crystallite, the current density at its tip is strongly increased compared with the shallower crystallite, which leads to a doubling from  $j_{0,\text{met}} \approx 900 \text{ fA/cm}^2$  to  $j_{0,\text{met}} \approx 1800 \text{ fA/cm}^2$  for this exemplified case. It is also apparent that the tip

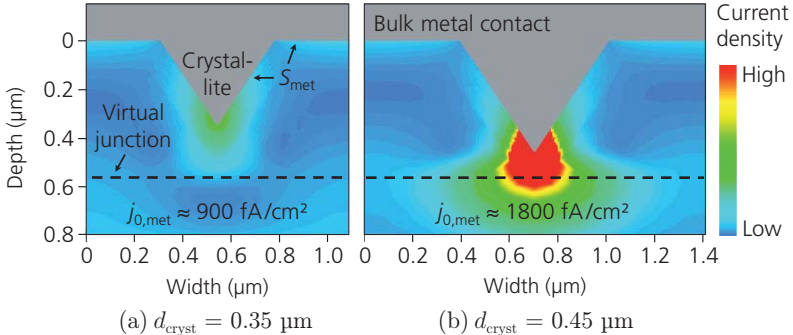


**Fig. 5.14.** 2D cross sections through the crystallite's tip plane of the 3D QSSPC symmetry element for two crystallites with different depths  $d_{\text{cryst}}$  but same coverage fraction  $A_{\text{cryst}} = 20\%$ . The images show the electron current density (minority charge carriers) below the metal contact under illumination during the QSSPC flash. The surface recombination velocity  $S_{\text{met}}$  for the entire metal-silicon interface is  $S_{\text{met}} = 10^7 \text{ cm/s}$ . Profile Gen3 is used for this example, the simulated  $j_{0,\text{met}}$  are given by (a)  $j_{0,\text{met}} \approx 900 \text{ fA/cm}^2$  and (b)  $j_{0,\text{met}} \approx 1800 \text{ fA/cm}^2$ . As the bulk region is considered being boron-doped, the dashed line represents the virtual junction of the doping profile.

of the deeper crystallite even draws charge carriers from the bulk region over the virtual junction. For both crystallites, the current density is highest at the tips, wherein the flanks contribute only a minor part.

Fig. 5.15(a) exemplifies the trend in  $j_{0,\text{met}}$  based on boron doping profile Gen3 for varied  $d_{\text{cryst}}$  and  $A_{\text{cryst}}$ . Consider first the result for  $d_{\text{cryst}} = 0 \mu\text{m}$ . This scenario, in which no crystallite formation occurs, represents the simple loss of the whole passivated area below the metal contact during contact firing (no metal penetrates the boron emitter). The simulated  $j_{0,\text{met,min}} \approx 750 \text{ fA/cm}^2$  equals the minimal achievable value for a non-passivated contact. Modeling of crystallites with depths exceeding the virtual junction is not recommended with the currently available physical models for metal-silicon interfaces in *Sentaurus Device*.<sup>24</sup> Thus, the curves stop shortly before the crystallites' tips reach the virtual junction. From Fig. 5.15(a), it is clear that when the crystallites penetrate deeper,  $j_{0,\text{met}}$  increases. This is because more and more charge carriers recombine at the metal-silicon interface closer to the virtual junction. The beginning and the characteristics of the increase in  $j_{0,\text{met}}$  depends obviously on  $A_{\text{cryst}}$ : the higher  $A_{\text{cryst}}$ , the sooner and steeper the increase occurs. At some point, the (electron) recombination at the crys-

<sup>24</sup>The metal-silicon interface would have to be considered for a very large interval of doping densities along the crystallite's flank, which is too large for the currently available physical models.

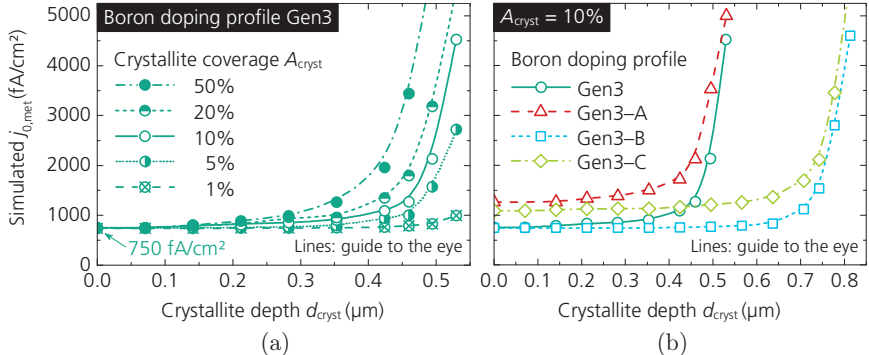


**Fig. 5.15.** 3D QSSPC simulation results for dark saturation current densities  $j_{0,\text{met}}$  underneath the metal contacts in dependence on crystallite depth  $d_{\text{cryt}}$ . (a) Variation in crystallite coverage fraction  $A_{\text{cryt}}$  based on boron doping profile Gen3. (b) Comparison between the four specified boron doping profiles at a constant  $A_{\text{cryt}} = 10\%$ .

tallites' tips increases so rapidly that  $j_{0,\text{met}}$  rises in an over-exponential manner. On the other hand,  $j_{0,\text{met}}$  stays almost constant on a low level up to a certain crystallite depth, which is roughly 250 nm before reaching the virtual junction.

In principle, the observed  $j_{0,\text{met}}$  characteristics in Fig. 5.15(b) for the other three boron doping profiles Gen3–A, Gen3–B, and Gen3–C are quite similar. However, the minimal  $j_{0,\text{met},\min}$  (for  $d_{\text{cryt}} = 0 \mu\text{m}$ ) and the point for steep  $j_{0,\text{met}}$  increase are different. The illustrated data refer to  $A_{\text{cryt}} = 10\%$ , wherein the same trends between the emitters also hold for other  $A_{\text{cryt}}$  (not shown). Table 5.4 summarizes the simulated  $j_{0,\text{met},\min}$ . For doping profiles Gen3 and Gen3–B,  $j_{0,\text{met},\min} \approx 750 \text{ fA/cm}^2$  is almost equal. Higher  $j_{0,\text{met},\min}$  are simulated for doping profiles Gen3–A and Gen3–C, which are about 1260 fA/cm<sup>2</sup> and 1090 fA/cm<sup>2</sup>, respectively. The observed differences in  $j_{0,\text{met},\min}$  between the four doping profiles without presence of any crystallites can be explained by the shielding effect of the doping against charge carri-

**Table 5.4.** Summary of simulated  $j_{0,\text{met},\min}$  for the four doping profiles, their maximum dopant concentrations  $N_{\max}$  and profile depths  $d$ , and the respective total amount of boron  $Q_{\text{tot}}$ . For ease of readability, the uncertainties for  $N_{\max}$  and  $d$  are not specified.

Boron doping profile →	Gen3	Gen3–A	Gen3–B	Gen3–C
Sim. $j_{0,\text{met},\min}$ for $d_{\text{cryt}} = 0 \mu\text{m}$ (fA/cm <sup>2</sup> )	750	1260	740	1090
Max. dopant concentr. $N_{\max}$ ( $10^{19} \text{ cm}^{-3}$ )	8.9	3.6	4.1	1.8
Profile depth $d$ (nm)	580	570	820	840
Total boron doping $Q_{\text{tot}}$ ( $10^{15} \text{ cm}^{-2}$ )	$1.7 \pm 0.2$	$0.9 \pm 0.1$	$1.5 \pm 0.1$	$0.8 \pm 0.1$

ers from the bulk region. Therein, the depth-dependent dopant concentrations  $N(d)$ , represented by the maximum dopant concentration  $N_{\max}$  as well as the profile depths  $d$ , affect this shielding effect, which is now discussed in more detail.

The effect of doping density on shielding can be initially evaluated by comparing doping profile pairs with either similar doping near the surface or similar depth. Considering first the profile pairs with same depth, namely profile pairs Gen3/Gen3–A and Gen3–B/Gen3–C (the respective first-mentioned profile is more highly doped), the simulations yield lower  $j_{0,\text{met,min}}$  for the profiles with the higher  $N_{\max}$ . The total dopant concentration  $Q_{\text{tot}}$ , which results from the integration of  $N(d)$  and is specified in Table 5.4, is thus a measure for the charge carrier shielding effect. The profile with lower  $j_{0,\text{met,min}}$  has the higher  $Q_{\text{tot}}$  for the considered profile pairs. Second, in case of similar dopant concentrations near the surface (or similar  $N_{\max}$ ), which is given for profile pair Gen3–A/Gen3–B, the higher depth of profile Gen3–B—which is equivalent to higher  $Q_{\text{tot}}$ —results also in lower  $j_{0,\text{met,min}}$ .

When comparing profiles which differ in both dopant concentration near the surface and depth, as e.g. profile pair Gen3–A/Gen3–C, caution is advised. Here,  $j_{0,\text{met,min}}$  is higher for profile Gen3–A despite its higher  $Q_{\text{tot}}$ . In this case,  $Q_{\text{tot}}$  is no appropriate quantity to account for differences in charge carrier shielding. This means that, in general, it is not so easy to quantify whether the charge carrier shielding is more determined by the higher dopant concentration near the surface or by the higher profile depth. Consequently, as a rule of thumb,  $Q_{\text{tot}}$  can be considered as a measure for charge carrier shielding in case of doping profiles which have either same dopant concentrations near the surface or same profile depth: the higher  $Q_{\text{tot}}$ , the lower  $j_{0,\text{met,min}}$  is. If the doping profiles differ in both parameters, then  $Q_{\text{tot}}$  is no longer sufficient as an indicator for  $j_{0,\text{met,min}}$ .

Taking crystallites into consideration, the results from Fig. 5.15(b) show a vanishing influence of the dopant concentrations near the surface on  $j_{0,\text{met}}$ . Despite different  $j_{0,\text{met,min}}$  for the profile pairs with same depth (i.e. Gen3/Gen3–A and Gen3–B/Gen3–C),  $j_{0,\text{met}}$  is found to approach each other towards deeper crystallites up to virtually the same values. Obviously, the steep  $j_{0,\text{met}}$  increase for the profiles Gen3–B and Gen3–C occurs for significantly deeper crystallites. This means that deeper profiles are more robust against deeper crystallites up to the point when the crystallite tips reach a distance of about 250 nm to the virtual junction.

In literature,  $j_{0,\text{met}}$  values for boron-doped emitters and Ag-Al contacts are reported to be larger than about 2000 fA/cm<sup>2</sup> [215,216,242]. The simulation results suggest that these quite high  $j_{0,\text{met}}$  cannot be explained by simple loss of the whole passivated area below the metal contact during contact firing. Instead, metal crystallites with depths of at least several 100 nm are mandatory to create agreement between simulation and experimentally determined  $j_{0,\text{met}}$ . The existence of (such) deep crystallites has been shown in section 5.3.3; hence deep crystallites are most likely the origin for the observed high  $j_{0,\text{met}}$  for Ag-Al contacts on boron-doped emitters. The possibility of a layer-like metal penetration into the boron-doped surface is not excluded, but reasonable etching depths would not explain the experimentally measured  $j_{0,\text{met}}$ . Thus, also for a scenario in which the paste ingredients etch the boron-doped surface in a layer-like manner during contact firing, crystallites are still the objects that most probably trigger the high charge carrier recombination undoubtedly occurring on cell level.

Note that this is the first time that 3D-modeling has been used for this kind of contact geometry for the application in solar cell structures. Therein, the simulations touch the limits of contact modeling. Furthermore, only homogeneous distributions of crystallites and crystallite depths are considered. Nevertheless, the simulations give detailed insight into charge carrier recombination at 3D metal crystallites based on state-of-the-art physical models.

Based on the simulation study, valuable recommendations can be given with respect to achieving lower charge carrier recombination below metal contacts on boron-doped surfaces. Obviously, the task is to ensure that the metal crystallites' tips do not penetrate into a critical zone before the junction. If they do, an over-exponential increase in charge carrier recombination is triggered particularly at their tips. To call a quantity for the beginning of this critical zone, 250 nm before the junction could be an appropriate choice. However, this number depends strongly on crystallite coverage fraction and may vary from profile to profile. Altogether, there are two starting points, namely, on the one hand, the formation of deep doping profiles, which show a clear benefit in charge carrier shielding from the metal-silicon interface, and on the other hand, the optimization of the metal pastes in combination with the firing process to ensure the formation of only small crystallites. Of course, also a low-ohmic contact must be ensured for both scenarios. However, this requirement can be ensured even for small crystallites if they are present in sufficient numbers, as demonstrated by the analytical calculations performed in section 5.4.

## 5.7 Chapter summary

The state-of-the-art metallization technique to electrically contact the textured, boron-doped, and passivated emitter surface in *n*-type silicon solar cells with low contact resistance  $\rho_C$  is the screen printing of a silver paste containing aluminum (also called Ag-Al paste) and the subsequent contact firing in a short high temperature step. However, these Ag-Al contacts are reported to be highly recombination active, lowering particularly the open-circuit voltage. The experiments and simulations discussed in this chapter target at conveying a deeper understanding on the properties of the metal-silicon interface between Ag-Al contact bulk and highly boron-doped silicon.

Microstructural investigations, performed on the formerly metallized areas after wet-chemical etching, reveal the presence of large and deep crystallite imprints, which imply former metal crystallite presence at these locations. The extracted crystallite depths vary between several 100 nm and a few microns. The crystallite coverage fraction is determined to be in the range of about 1%. It is found that these metal crystallites play a very decisive role concerning both electrical contact and charge carrier recombination.

Lower  $\rho_C$  are experimentally determined for boron doping profiles with deeper junctions, which otherwise feature almost identical increasing curve progressions up to a depth of 60 nm before reaching the maximum dopant concentration  $N_{\max} \approx 8 \cdot 10^{19} \text{ cm}^{-3}$  (referred to as doping depletion zone). For instance,  $\rho_C$  is found to decrease from  $\rho_C = (3.7 \pm 0.8) \text{ m}\Omega\text{cm}^2$  for a 570 nm-deep profile to  $\rho_C = (2.0 \pm 0.4) \text{ m}\Omega\text{cm}^2$  for a 980 nm-deep one. From the theory of ideal planar contacts, it is known that  $\rho_C$  depends on the boron doping concentration at the surface; however, this is identical for the three examined profiles. To correlate this finding with deep penetrating metal crystallites, the application of an analytical model for calculating  $\rho_C$  proves to be a purposeful approach. Therein, direct current conduction between Ag-Al contact bulk, metal crystallites and boron-doped silicon is assumed. Considering physically reasonable input parameters, the calculated  $\rho_C$  can be brought into agreement with the experimentally determined values. The results obtained by the analytical calculations allow the conclusion that lower  $\rho_C$  for deeper junctions can be directly connected to metal crystallites with penetration depths of at least some 100 nm. Hence, apart from  $N_{\max}$ , also the junction depth of the doping profiles affects  $\rho_C$ . Furthermore, the calculations yield comparable  $\rho_C$  for doping profiles whether with

or without doping depletion zone close to the surface in case of metal crystallites, which are at least somewhat deeper than the depth of the depletion zone (i.e. deeper than  $d_{\text{cryst}} \approx 100$  nm for the examined profiles). This means that the doping depletion zone can be considered as being negligible with respect to  $\rho_C$ , as the observed crystallites clearly reach through this zone.

The benefit of deeper doping profiles for low  $\rho_C$  is also examined on the basis of further selected profiles. They differ pairwise either in  $N_{\max}$  or their junction depths. Despite considerably lowering  $N_{\max}$  from  $N_{\max} = (8.9 \pm 0.9) \text{ cm}^{-3}$  to  $N_{\max} = (1.8 \pm 0.2) \text{ cm}^{-3}$  for two of the profiles, almost the same  $\rho_C$  in the range of  $4 \text{ m}\Omega\text{cm}^2$  are measured, as the junction depth of the latter is increased by about 300 nm. This shows that low  $\rho_C$  can be maintained despite considerably lowering  $N_{\max}$  by increasing the junction depth.

To investigate charge carrier recombination below the metal contacts in more detail, synergies with a parallel ongoing PhD thesis prove as being very beneficial. This allows applying a novel numerical three-dimensional (3D) simulation approach, which considers charge carrier recombination at metal crystallites that penetrate the boron-doped silicon surface. The 3D simulations, which are performed with *Sentaurus Device*, yield a detailed insight into charge carrier recombination at the metal-silicon interface.

The simple loss of passivated area underneath the contacts—meaning that the paste ingredients etch the passivation layer completely during contact firing but no metal crystallites are formed—is not found to explain the dark saturation current densities  $j_{0,\text{met}}$  larger than about  $2000 \text{ fA/cm}^2$ , as they are reported in the literature for Ag-Al contacts on boron-doped surfaces. It is shown that such high  $j_{0,\text{met}}$  correlate with the presence of metal crystallites, which are at least so deep that their tips penetrate into a critical zone before the junction. The beginning of the critical zone is characterized by an over-exponential increase of charge carrier recombination particularly at the crystallites' tips. To quantify the beginning of this critical zone, 250 nm before the junction might be an appropriate number. Furthermore, the junction depth is found to be the crucial parameter with respect to charge carrier shielding from the metallized regions in case deep penetrating crystallites exist.

Hence, to obtain lower  $j_{0,\text{met}}$ , the task is to ensure that the metal crystallites' tips do not penetrate into this critical zone. On the one hand, deeper

doping profiles are a promising approach. On the other hand, optimization of both the utilized metal pastes in combination with contact firing processes might ensure the formation of only small crystallites. The presented analytical calculations show that for both approaches, a low-ohmic contact formation is still possible even for small crystallites, in case they are present in sufficient numbers.

# **6      Electrical Properties of the Backside Contacts of MWT Solar Cells**

## **6.1     Introduction**

By relocating the external contacts of the front to the backside in MWT solar cells, the external rear contacts, connected to the emitter by the front grid and metallized vias, directly overlap the silicon bulk with opposite polarity for the latest MWT cell architectures. Since no  $p$ - $n$ -junction is present in between, leakage currents under forward bias may occur. Such leakage currents reduce the energy conversion efficiency of the solar cells. The current under reverse bias is also of interest, not only with respect to potential module integration of the solar cells, but also to its impact on the cell properties in forward operation. In this chapter, several screen-printing pastes, developed to be used for metallization of the vias and of the external contacts, are examined with respect to their electrical contacting behavior utilizing special test structures. The bulk material for these test structures is chosen to be both  $n$ -type and  $p$ -type Cz-Si wafers in order to investigate if the bulk doping type influences the electrical contacting behavior of the used metal pastes. Furthermore, the test structures feature different surface topographies and different dielectric insulation layer systems. The in-depth characterization of the metal-insulation-semiconductor contacts is carried out both under forward and reverse bias operation. As discussed in Chapter 3.3, results from these examinations also contribute significantly to the ongoing development in  $p$ -type MWT technology.

## **6.2     Challenges for the MWT backside contact structure**

Typically, the external backside contacts and the vias in MWT solar cells are metallized simultaneously with a non-fire-through silver screen-printing

paste, called “via paste”. The term “non-fire-through” refers to the property of the paste to not fully penetrate  $\text{SiN}_x$  layers. In Chapter 3, it is discussed in detail that the major challenge in the fabrication of MWT solar cells is the use of a suitable via paste, depending on the cell structure of choice. The basic requirements of the via pastes and the basics of the contact system of interest will now be briefly reviewed.

### **Basic requirements of the via paste**

The via paste has to ensure reliable and continuous via metallization with low series resistance. For the latest *p*-type MWT solar cell types, namely the HIP–MWT+ (Fig. 3.6(a)) and the MWT–BSF+ structure (Fig. 3.6(b)), solely the non-fire-through property of the via pastes is no longer sufficient. In addition, the via pastes themselves have to prevent electrical contact formation not only when printed on top of an intermediate dielectric layer, but also when applied directly onto the bare *p*-type silicon bulk. In forward bias, i.e. normal operation mode, up to the open-circuit voltage no significant leakage current should occur to prevent fill factor and open-circuit voltage losses. The increased demands on the via paste originate from the fact that in these MWT structures no emitter layer, which formerly ensured the electrical contact separation, is present on the backside and within the vias. These higher requirements on the via paste also apply to the both novel *n*-type MWT solar cell structures *n*MWT and *n*MWT+ introduced in Chapter 3.5 and shown in Fig. 3.9. Therein, the configuration of the *n*MWT cell structure with high phosphorus doping also underneath the external *p*-type contact pads might represent a major challenge for suppressing leakage currents under forward operation. However, the formulation of the via pastes used for MWT cells should be such that no ohmic contact to silicon is formed. The contact system investigated within this chapter consists of a screen-printed and fired via paste with silver as conductive component, an intermediate dielectric layer, and the silicon wafer.

Since partial shading of a photovoltaic module can lead to reverse biasing the shaded cells [145], it is important that those cells are not harmed by the applied negative voltage and that the reverse behavior is not detrimental to the module. Therefore, the contacting behavior of the via pastes in reverse bias condition is of interest. MWT solar cells enabling sufficiently low reverse breakdown voltages can, however, represent an integrated by-

pass diode approach allowing a controlled reverse current flow with less external bypass diodes in the module [163].

### Review on screen-printed and fired silver-insulator-semiconductor contacts

Various models and explanations have been proposed within the photovoltaic community for the actual mechanisms of contact formation and current transport for screen-printed and fired silver contacts, commonly applied to electrically contact the front side phosphorus-doped emitter in *p*-type silicon solar cells, as e.g. in Refs. [111,221,229,230,243–246]. Tunnelling through a thin dielectric layer is assumed to be one of the major current transport mechanisms [243,245,246] leading to ohmic contact properties [247]. On the other hand, other works emphasize that the dominating current transport mechanism is more likely given by direct silicon-silver contacts [221,230].

One model to describe the electrical characteristics of the silver-insulator-semiconductor contact systems considered in this chapter is given by quantum mechanical tunneling of charge carriers through the intermediate dielectric layer [163,248]. Previous studies show the observation of nonlinear current-voltage (*I*-*V*) characteristics for screen-printed and fired contacts realized with via pastes on lightly doped *p*-type silicon [161,163,165]. In a joint publication with *Thaidigsmann* and further authors [163], these nonlinear *I*-*V* characteristics of such a via paste on lightly doped *p*-type Cz-Si with and without intermediate dielectric layers have been investigated in more detail. It is found that the dominating current transport mechanism is quantum mechanical tunneling of charge carriers through the dielectric layer between silver contact and silicon. Despite the fact that via pastes are designed not to penetrate  $\text{SiN}_x$  layers, samples with dielectric layer ( $\text{SiN}_x$  layer thickness of at least 50 nm, thus no significant tunneling current is expected) show areas of reduced dielectric layer thickness. These areas are supposed to enable significant charge carrier tunneling. Furthermore, the examinations indicate that the glass frit components of the via paste form a tunneling barrier (glass layer) during contact firing. It is also shown that both forward and reverse bias behavior of the via paste contacts can be modified by different intermediate dielectric layers [161,163,165] or the use of different via pastes [165].

Initial investigations on the electrical contact properties of via pastes for *n*-type Cz-Si within the thesis at hand reveal rather high leakage currents [165]. These examinations form the basis of the in-depth characterization of

state-of-the-art via pastes dealt with in this chapter. The performed experiments and obtained results are also published in Ref. [167]. Five via pastes from three paste manufacturers<sup>25</sup> and one standard fire-through reference silver paste—commonly used for the front metallization of *p*-type solar cells—are investigated on *n*-type and *p*-type Cz-Si test structures with various dielectric layers and two different surface topographies. In doing so, determining the influence of reverse bias load on occurring forward leakage currents is an important part of the examinations.

## 6.3 Methodology for characterization of the electrical contact behavior

### 6.3.1 Approach and test structure fabrication

In order to comprehensively investigate the electrical contact properties of the five via pastes V1–V5 and the fire-through reference paste R6, special test structures are fabricated from (100)-oriented *p*-type and *n*-type Cz-Si wafers as shown in Fig. 6.1 and Fig. 6.2, respectively. The front sides of the samples feature the metal contacts, the surface topographies, and the dielectric layer systems to be investigated, while the rear sides are fabricated such that they ensure an ohmic contact to the silicon bulk. The front surfaces are either alkaline saw-damage etched or alkaline textured. Table 6.1 summarizes the investigated different dielectric layer systems. It shows which sample type is investigated in combination with which dielectric layer system. The sample naming in the following is a combination of sample type and layer number, as e.g. *n3c*, which stands for *n*-type sample *n3* with a 75 nm-thick PECVD SiN<sub>x</sub> layer on the front side (layer number *c*).

The front sides of the *p*-type samples *p1* and *p3* in Fig. 6.1 correspond to the area of interest on the rear side of the *p*-type MWT cell structures in Fig. 3.6(b) and (a), respectively. On the other hand, the front sides of the *n*-type samples *n4* and *n8* in Fig. 6.2 correspond to the area of interest on the rear side of the *n*-type MWT cell structures in Fig. 3.9(b) and (a), respectively.

---

<sup>25</sup>The via pastes were provided by *DuPont Microcircuit Materials*, *Heraeus Precious Metals*, and *Murata*. Due to non-disclosure agreements, no information on the pastes' compositions can be specified.

### 6.3 Methodology for characterization of the electrical contact behavior

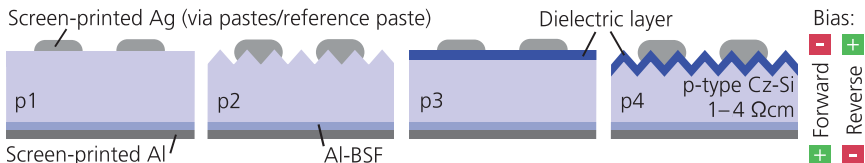


**Fig. 6.1.** Schematic cross sections of the *p*-type Cz-Si test structures for the investigation of electrical contact properties of screen-printed silver pastes without (*p*1, *p*2) and with (*p*3, *p*4) front dielectric layer as well as both alkaline saw-damage etched (*p*1, *p*3) and alkaline textured (*p*2, *p*4) front surfaces. The total silver contact area is  $2 \times 1.5 \text{ mm} \times 123 \text{ mm} \approx 3.7 \text{ cm}^2$ . The rear features a full-area screen-printed aluminum metallization. The electric polarities for both forward and reverse bias measurements are indicated on the right hand side.

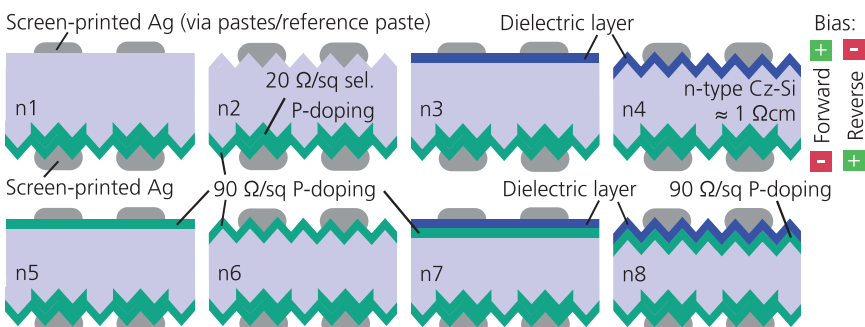


**Fig. 6.2.** Schematic cross sections of the *n*-type Cz-Si test structures. The front side of samples *n*1–*n*4 corresponds to the equivalent *p*-type samples in Fig. 6.1. For samples *n*5–*n*8, the front side features an additional phosphorus doping (drive-in temperature 820°C) with a sheet resistance  $R_{sh} \approx 90 \Omega/\text{sq}$  and a phosphorus surface concentration of  $N_s \approx 1.4 \cdot 10^{21} \text{ cm}^{-3}$  (measured by secondary ion mass spectroscopy). The rear sides of all samples feature a full-area phosphorus doping with  $R_{sh} \approx 90 \Omega/\text{sq}$  and a selective one ( $R_{sh} \approx 20 \Omega/\text{sq}$ ) underneath a contacting screen-printed silver metallization grid.

**Table 6.1.** Overview of the investigated four dielectric layer systems (abbreviated with layer number: “Layer no.”) and their nominal thicknesses (SiriON: silicon-rich oxynitride). The sample type refers to the samples shown in Fig. 6.1 and Fig. 6.2.

Sample type	Layer no.	Layer type
<i>p</i> 1, <i>p</i> 2, <i>n</i> 1, <i>n</i> 2, <i>n</i> 5, <i>n</i> 6	–	No dielectric
<i>p</i> 3, <i>p</i> 4, <i>n</i> 3, <i>n</i> 4, <i>n</i> 7, <i>n</i> 8	<i>a</i>	10 nm thermally grown $\text{SiO}_2$ + 40 nm PECVD $\text{SiO}_x$ + 50 nm PECVD $\text{SiN}_x$
<i>p</i> 3, <i>p</i> 4, <i>n</i> 3, <i>n</i> 4, <i>n</i> 7, <i>n</i> 8	<i>b</i>	10 nm PECVD $\text{Al}_2\text{O}_3$ + 65 nm PECVD $\text{SiN}_x$
<i>n</i> 3, <i>n</i> 4, <i>n</i> 7, <i>n</i> 8	<i>c</i>	75 nm PECVD $\text{SiN}_x$
<i>n</i> 3, <i>n</i> 4, <i>n</i> 7, <i>n</i> 8	<i>d</i>	10 nm PECVD SiriON + 65 nm PECVD $\text{SiN}_x$

The test structures allow for investigating the electrical contact properties of the silver (via) pastes without being influenced by the  $p$ - $n$ -junction of the solar cell. Three to five devices with a wafer edge length of 125 mm and an initial wafer thickness  $W = 200 \mu\text{m}$  ( $p$ -type Cz-Si) and  $W = 225 \mu\text{m}$  ( $n$ -type Cz-Si) are fabricated for each combination of bulk doping type, front surface topography, and front surface dielectric. As the results for the fabricated samples per variation are very similar, only representative measurements will be shown.

For each of the six silver pastes, two continuous busbar contacts with a width of 1.5 mm and a length of 123 mm are progressively screen printed next to each other onto the front side of the same sample, followed directly by a drying step; see Fig. 6.3. The  $p$ -type samples feature a screen-printed and alloyed full-area aluminum contact on the rear side serving as ohmic contact to the silicon bulk. A screen-printed H-pattern grid using a standard silver paste commonly used to contact highly phosphorus-doped surfaces forms the rear contact for the  $n$ -type samples. The selective laser doping below the contacts supports the ohmic contact formation.

Following screen printing, the contact firing process is performed in an industrial conveyor belt furnace. To ensure wafer temperatures of approximately 750°C (peak temperature time < 1 s) for all different samples, thermocouple measurements have been previously conducted.

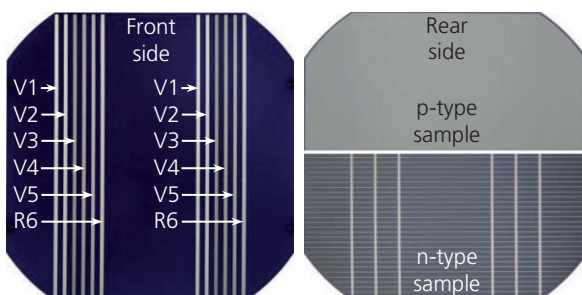


**Fig. 6.3.** Exemplary photographs of front (left) and rear sides (right) of the test structures with 125 mm edge length. The front side features six pairs of busbar contacts (pastes V1–V5 and R6) with a contact area of  $3.7 \text{ cm}^2$  for each contact pair. The rear side features either a full-area aluminum metallization ( $p$ -type samples) or a silver grid ( $n$ -type samples). For the latter, the busbar configuration is adapted for practical reasons for the current-voltage measurements.

## 6.3 Methodology for characterization of the electrical contact behavior

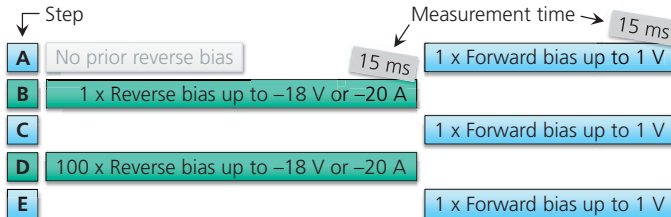


**Fig. 6.4.** Overview of the measurement sequence for determining the dark current–voltage characteristics. The duration for each measurement is 15 ms.

### 6.3.2 Procedure for current-voltage measurements

The dark forward and reverse  $I$ – $V$  characteristics of the test structures are measured with an industrial cell tester according to the measurement steps in Fig. 6.4. The electric polarities during the measurements—referred to as forward bias and reverse bias—are indicated on the right hand side in Fig. 6.1 and Fig. 6.2. The first measurement (A) is performed only under forward bias for all fabricated samples. Thus, the initial electrical behavior between the screen-printed and fired silver contacts and the silicon without prior reverse bias load can be evaluated. Note that the current measured under forward bias condition is referred to as leakage current<sup>26</sup> from now on. For the following measurements B–E, two samples of each variation are randomly selected. A second measurement in forward bias (C) follows a single measurement in reverse bias (B) to investigate the influence of a single reverse bias load on the leakage current in forward bias. To further test stability, 100 consecutive reverse bias measurements (D) are performed each with a break of one second in between. The resulting leakage currents in forward bias are subsequently measured again (E).

### 6.3.3 Leakage currents and their impact on forward current–voltage characteristics

Leakage currents have a negative impact on the conversion efficiency of solar cells. This impact can be calculated by subtracting the measured test structure leakage currents  $I_{\text{leak}}(V)$  from a reference  $I$ – $V$  curve of an illuminated solar cell  $j_{\text{cell}}(V)$ ; see Fig. 6.5. The resulting  $I$ – $V$  characteristic is given by

<sup>26</sup>The term leakage current is sometimes also used for current flow in the reverse direction. However, in this work, the term leakage current is used only for the forward direction.

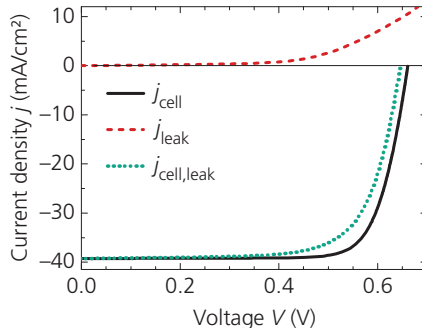


**Fig. 6.5.** Current-voltage characteristics for a *p*-type HIP–MWT solar cell under illumination, without ( $j_{\text{cell}}$ ) and with additional leakage current ( $j_{\text{cell},\text{leak}}$ ).

$$j_{\text{cell},\text{leak}}(V) = j_{\text{cell}}(V) + a_{\text{cell}} \underbrace{\frac{I_{\text{leak}}(V)}{A_{\text{test}}}}_{j_{\text{leak}}(V)}. \quad (6.1)$$

The reference solar cell used for the evaluation of Eq. (6.1) is a *p*-type HIP–MWT cell with a cell area of  $239 \text{ cm}^2$  and a conversion efficiency of 20.2% [12]. The area fraction of the external rear *n*-type contact pads on the reference cell is  $a_{\text{cell}} = 1.3\%$ . The metallized area on the test structures for each investigated paste is  $A_{\text{test}} = 3.7 \text{ cm}^2$ ; see Fig. 6.3.

The absolute losses both in fill factor  $\Delta FF^{27}$  and open-circuit voltage  $\Delta V_{\text{OC}}$  are determined by subtracting the  $FF$  and  $V_{\text{OC}}$  of the resulting  $I$ – $V$  curve from the ones of the reference  $I$ – $V$  curve. In the following sections, only the absolute fill factor loss  $\Delta FF$  is considered because it predominates clearly the loss in open-circuit voltage  $\Delta V_{\text{OC}}$ .

### 6.3.4 Thermal power dissipation under reverse bias load

The thermal power dissipation  $P_t$  and its spatial distribution across a solar cell under reverse bias load (which can occur if a cell is at least partially shaded in a photovoltaic module [145]) is of major importance for module reliability and safety. A solar module typically consists of a series connection of individual cell strings with connecting bypass diodes in parallel. Each cell string in turn consists of individual solar cells connected in series. The

<sup>27</sup>The leakage currents  $j_{\text{leak}}$  lead to a loss in pseudo fill factor  $\Delta pFF$  (see section 2.2.3), which directly translates into a fill factor loss  $\Delta FF$ .

number of cells per string limits the maximum reverse bias for a shaded cell.

For the test structures, the  $P_t$  under reverse bias load can be extracted from the measured  $I$ - $V$  characteristics. For the evaluation of the reverse characteristics, a string current of 10 A is used, which approximately corresponds to the short-circuit current of a MWT solar cell with  $239 \text{ cm}^2$  cell area. Furthermore, the area fraction of the external contact pads at the via contacts is considered with 1.3%. The assumed module bypass diode sets in if the current does not reach 10 A at a reverse bias of -15 V.

For H-pattern solar cells with a cell area of  $239 \text{ cm}^2$  it has been reported that a homogeneous power dissipation of 80 W is not harmful to the encapsulation material if an appropriate thermal coupling is provided to the module surface [249]. Since the external rear contacts of MWT cells are limited to a small portion of the cell rear surface, this value of 80 W has to be understood as an absolute upper limit. The assessment of the  $I$ - $V$  behavior in reverse direction with respect to module integration is anything but trivial, and more detailed investigations are required to determine the maximum allowable thermal power and its spatial density dissipation. Thus, the 80 W-limit has to be understood only as a rough estimate.

## 6.4 Results of the test structures for various MWT cell concepts

The calculated absolute fill factor losses  $\Delta FF$  for the dark  $I$ - $V$  characteristics measured on all different test structures mentioned in section 6.3.1 are summarized in Table 6.2. The calculated  $P_t$ , as product of voltage and current, are also given in column D. In this section, the dark  $I$ - $V$  characteristics are discussed only for the test structures featuring the rear contact structure of various *p*-type and *n*-type silicon MWT solar cell concepts.

### **p-type MWT-BSF+ cell concept**

The dark  $I$ - $V$  characteristics both in forward and reverse bias of sample *p1* with alkaline saw-damage etched (SDE) front surface and without dielectric layer—representing the test structure for the *p*-type MWT-BSF+ solar cell, Fig. 3.6(b)—are shown in Fig. 6.6. Without prior reverse bias load (measurement A), all via pastes V1–V5 show no leakage current at all and the calculated absolute fill factor losses are  $\Delta FF_A = 0\%$ , whereas for

**Table 6.2.** Calculated absolute fill factor losses  $\Delta FF$  and thermal power dissipations  $P_t$  from the measured dark  $I-V$  characteristics of the test structures for via pastes V1-V5 and reference paste R6 (mean values of two measured samples per variation). The measurements A, C, D, and E correspond to Fig. 6.4. For values marked with (/) no  $\Delta FF$  could be calculated due to very strong current flow and therefore not sufficiently recorded  $I-V$  characteristics—in these cases  $\Delta FF$  exceeds  $-10\%_{abs}$ . For measurement E, only those samples are considered, which show  $|\Delta FF_C| \leq 0.5\%_{abs}$  in measurement C. The bold marked values in D indicate that the maximum voltage of  $-15$  V is reached (FST: front surface topography; SDE: alkaline saw-damage etched, txt: alkaline textured, FSD: front surface doping, RBL: reverse bias load, SiON: silicon-rich oxynitride).

## 6.4 Results of the test structures for various MWT cell concepts

Sam-FST FSD ple	$(\Omega/\text{sq})$	Dielectric	(A) No prior RBL						(C) After single RBL <sub>L</sub>						(E) After 101 RBL <sub>S</sub>						(D) 101st RBL							
			$\Delta FF_A (\%)_{\text{abs}}$						$\Delta FF_C (\%)_{\text{abs}}$						$\Delta FF_E (\%)_{\text{abs}}$						$P_t (\text{W})$							
			V1	V2	V3	V4	V5	R6	V1	V2	V3	V4	V5	R6	V1	V2	V3	V4	V5	V1	V2	V3	V4	V5	V1	V2	V3	V4
<b>↓ n-type Cz-Si</b>																												
<i>n3a</i>	SDE	—	SiO <sub>2</sub> /SiO <sub>x</sub> /SiN <sub>x</sub>	0	0	0	0	-3.1	0	0	-0.2	0	-0.2	(/)	-0.1	0	-0.2	0	-0.2	10	1	11	0	10				
<i>n4a</i>	txt	—		0	0	0	0	-0.3	0	0	-1.4	0	-2.2	-4.7	-0.1	0	0	0	0	102	57	19						
<i>n7a</i>	SDE	90		0	0	-0.1	0	-0.1	(/)	-0.8	-0.2	(/)	-0.1	-5.5	(/)	-0.2	-0.1	-0.2	-0.1	5	0							
<i>n8a</i>	txt	90		0	0	-0.2	0	-0.1	(/)	-1.2	-0.5	-5.2	-0.7	-2.0	(/)	-0.5	-0.5	-0.5	-0.5	61	77							
<i>n3b</i>	SDE	—	Al <sub>2</sub> O <sub>3</sub> /SiN <sub>x</sub>	0	0	0	0	-3.9	-0.1	0	-4.1	-1.0	-2.0	(/)	-0.2	0	0	0	0	34	14							
<i>n4b</i>	txt	—		0	0	0	0	-0.8	0	-0.1	-2.2	-0.2	-0.3	-2.7	-0.1	-0.1	-0.1	-0.1	-0.1	22	9	81	65					
<i>n7b</i>	SDE	90		0	-0.2	-0.1	-0.2	-0.2	(/)	-1.5	-2.3	(/)	-5.7	-8.1	(/)													
<i>n8b</i>	txt	90		0	0	-0.1	-0.1	-0.3	(/)	-1.2	-0.4	-9.6	-1.7	-3.1	(/)	-1.5												
<i>n3c</i>	SDE	—	SiN <sub>x</sub>	0	0	0	0	-1.9	-0.2	-0.4	-1.2	0	-1.5	(/)	-0.3	-0.6	0	0	0	131	94	17						
<i>n4c</i>	txt	—		0	0	0	0	-0.3	-0.3	-0.2	-4.1	-0.2	-5.8	-2.3	-0.5	-0.6	-0.7	-0.7	-0.7	58	87	127						
<i>n7c</i>	SDE	90		0	0	-0.2	0	-0.1	(/)	-1.5	-0.7	(/)	-0.4	-6.3	(/)					-2.3		47						
<i>n8c</i>	txt	90		0	0	-0.1	0	-0.4	(/)	-2.0	-0.4	(/)	-0.5	-3.6	(/)	-1.9	-3.4	-3.4	-3.4	46	43							
<i>n3d</i>	SDE	—	Si <sub>x</sub> ON/SiN <sub>x</sub>	0	0	0	0	-1.2	-0.1	0	-0.3	0	-0.2	(/)	-0.2	-0.1	-0.4	-0.1	-0.2	70	132	12	27	58				
<i>n4d</i>	txt	—		0	0	0	0	-0.6	0	-0.2	-0.6	-0.1	-0.6	-3.8	-0.1	-0.5	-1.0	-0.6	-2.1	110	110	67	131	38				
<i>n7d</i>	SDE	90		0	0	-0.1	-0.1	-0.4	(/)	-1.6	-0.6	(/)	-0.3	-3.2	(/)					-2.1		48						
<i>n8d</i>	txt	90		0	0	-0.1	0	-0.2	(/)	-1.6	-0.5	(/)	-0.5	-4.0	(/)	-1.6	-2.6	-2.6	-2.6	49	47							

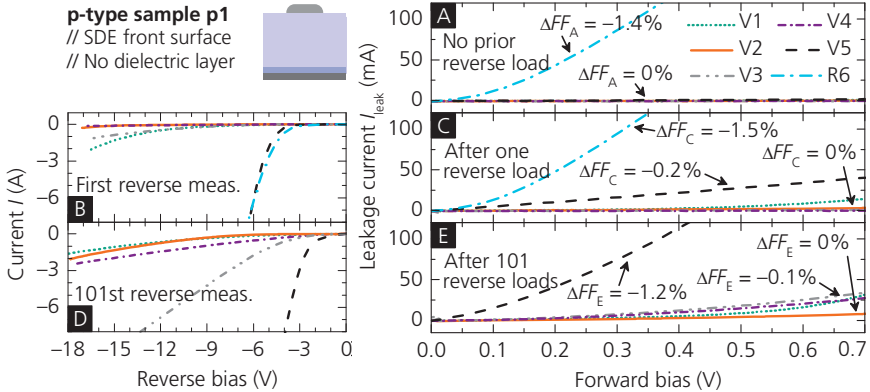


**Fig. 6.6.** Measured dark forward (right) and reverse (left)  $I$ - $V$  characteristics of  $p$ -type sample  $p1$  for via pastes V1–V5 and reference paste R6. The measurement procedure corresponds to Fig. 6.4. The calculated absolute fill factor losses  $\Delta FF$  are also specified. Paste R6 is not considered for measurements D and E.

reference paste R6 clearly higher current flow is measured ( $\Delta FF_A = -1.4\%$ ). The characteristics observed for the via pastes indicate that no electrical conductive contact is formed to the lightly doped  $p$ -type silicon. The glass components of the via pastes most likely formed a tunneling barrier (glass layer) during the contact firing process resulting in an electrically non-conducting contact system. For the first reverse bias measurement (B), via pastes V2 and V4 show almost no current flow up to a voltage of  $-18$  V, pastes V1 and V3 show somewhat higher currents, whereas a rather abrupt current increase is seen for pastes V5 and R6 from a voltage of  $-4$  V. The subsequently performed second forward measurements (C) show an increased leakage current for via paste V5 ( $\Delta FF_C = -0.2\%$ ), while the other via pastes are almost not affected ( $\Delta FF_C = 0\%$ ). After 100 further reverse bias loads (D), the currents in reverse bias increase for all via pastes, particularly for V3. The thermal power dissipation for V3 with  $P_t = 115$  W exceeds the aforementioned upper limit of 80 W, meaning that this paste might be critical in terms of reverse operation. For paste V5, the considered bypass diode limits the power dissipation to  $P_t = 45$  W. The final forward measurements (E) yield nonlinear  $I$ - $V$  characteristics for all via pastes. The leakage current of via paste V5 increased further ( $\Delta FF_E = -1.2\%$ ) and also via pastes V1, V3, and V4 show slightly increased currents ( $\Delta FF_E = -0.1\%$ ). Only via paste V2 is hardly affected ( $\Delta FF_E = 0\%$ ) and is therefore a very promising candidate for the fabrication of  $p$ -type MWT-BSF+ solar cells (the current in reverse bias is also almost the lowest).

In a joint publication with *Spribile* and further authors [250], via paste V2 is also examined on the cell level. To test stability against reverse bias load, the  $I$ - $V$  characteristics of a *p*-type MWT-BSF+ cell metallized with via paste V2 are measured for 1.000 times including initial reverse bias load for each single measurement. The observed absolute *FF* loss is lower than 0.2% in total. The currents under reverse bias  $I_{-12V}$ , which are measured at a voltage of -12 V, steadily increase during the 1.000 measurements reaching  $I_{-12V} \approx -10$  A. However, the increasing  $I_{-12V}$  do almost not affect the cell performance in forward bias, which is a promising result for an integrated bypass-diode approach. These results are in agreement with the results obtained for *p*-type test structure *p1*.

### **p-type HIP–MWT+ cell concept**

For the *p*-type HIP–MWT+ cell concept, Fig. 3.6(a), test structures *p3a* and *p3b* with alkaline saw-damage etched front surfaces and intermediate dielectric layers are of interest (layer *a*:  $\text{SiO}_2/\text{SiO}_x/\text{SiN}_x$ , layer *b*:  $\text{Al}_2\text{O}_3/\text{SiN}_x$ ). For both sample types, according to Table 6.2, all five via pastes show no electrical contact to *p*-type silicon after 101 reverse bias loads in forward operation ( $\Delta FF_E = 0\%$ ). In addition, no significant current flow in reverse direction occurs for all via pastes on sample *p3a* ( $P_t = 0$  W). On sample *p3b*,  $P_t$  is calculated to be in the range of 80 W for via pastes V1 and V2, indicating that these via pastes might not be an appropriate choice in case high reverse bias stability is aimed at on cell level for the applied dielectric layer *b*. On the other hand,  $P_t$  for via pastes V3–V5 is found to be considerably lower with  $P_t \leq 8$  W. Due to the additionally present intermediate dielectric layer (in comparison with the *p*-type MWT-BSF+ cell) the *p*-type HIP–MWT+ structure is clearly less sensitive with respect to the via paste applied. These findings are in agreement with examination results on cell level [166,167].

### **n-type MWT cell structure nMWT+**

For the *n*-type MWT cell structure *nMWT+*, Fig. 3.9(b), the  $I$ - $V$  results for sample *n4c* with alkaline textured front surface and  $\text{SiN}_x$  layer are shown in Fig. 6.7. An absolute stable electrical contact separation might be a challenge for all via pastes when using solely a  $\text{SiN}_x$  layer as intermediate dielectric, which is commonly used as rear passivation layer for *n*-type solar cells. Without prior reverse bias load (A), all via pastes show no leakage currents and thus, no fill factor losses ( $\Delta FF_A = 0\%$ ). The initial

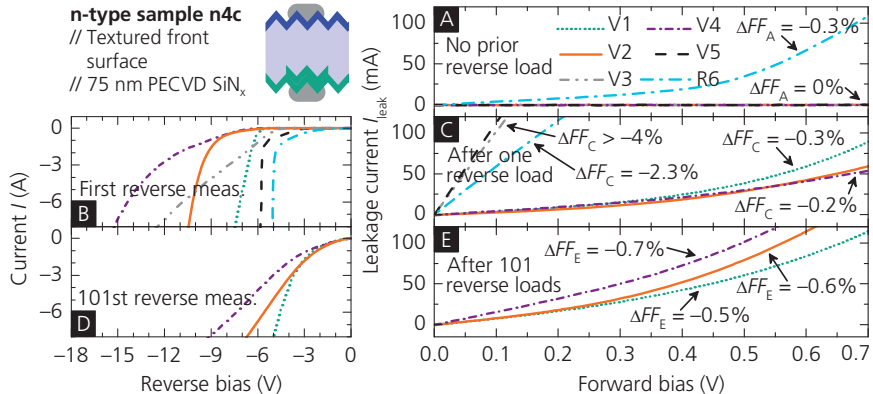


**Fig. 6.7.** Measured dark forward (right) and reverse (left)  $I$ - $V$  characteristics of  $n$ -type sample  $n4c$  including the calculated absolute fill factor losses  $\Delta FF$ . Pastes V3, V5, and R6 are not considered for measurements D and E, as the absolute fill factor losses  $\Delta FF_C$  after measurement C already exceed  $-2.3\%$ .

reverse bias load (B) reveals a non-stable reverse behavior for all via pastes. The following forward measurements (C) show drastically increased currents for via pastes V3 and V5 leading to fill factor losses  $\Delta FF_C = -4.1\%$  and  $\Delta FF_C = -5.8\%$ , respectively. The other three via pastes V1, V2, and V4 are much less affected; the  $\Delta FF_C$  values are between  $-0.2\%$  and  $-0.3\%$ . After 100 further reverse bias loads (D), the reverse  $I$ - $V$  characteristics already show an increase in current starting from reverse bias  $V = 0$  V (pastes V3 and V5 are not further considered). The leakage currents measured thereafter (E) increased again and fill factor losses  $\Delta FF_E$  between  $-0.5\%$  and  $-0.7\%$  result.

The other examined dielectrics on sample type  $n4$  provide an improved electrical contact separation for certain via pastes and fill factor losses  $|\Delta FF| \leq 0.1\%$  are found. However, these dielectric layers might either not be suitable as passivation layer for the rear phosphorus doping in  $n$ -type silicon solar cells or their potential integration into the fabrication process would trigger further challenges, drawbacks, or process effort. As  $\text{SiN}_x$  layers are known to effectively passivate phosphorus-doped surfaces, they will be used for the examined  $n$ -type MWT cells in Chapter 7. However, the obtained results show that it might not be a trivial task to ensure absolute stable electrical contact insulation for the  $n$ MWT+ cell structure.

### n-type MWT cell structure nMWT

A stable electrical contact separation for the *n*MWT cell structure, Fig. 3.9(a), with additional phosphorus doping below the intermediate dielectric layer and the external *p*-type contacts seems to be a challenging task. Besides the fact that some via pastes show no fill factor loss  $\Delta FF_A$  without prior reverse bias load for the corresponding sample type *n8*, all are more or less affected by reverse bias load. For sample *n8c* with  $\text{SiN}_x$  layer, the fill factor loss  $\Delta FF_E$  after 101 reverse bias loads is at least  $-1.9\%$ . Only sample *n8a* with thermally grown  $\text{SiO}_2$  layer and two PECVD capping layers shows moderate fill factor losses  $\Delta FF_E = -0.5\%$  for via paste V2. A stable electrical contact separation for the *n*MWT cell structure thus seems most likely to be not possible or at least anything but trivial.

### Discussion

The results indicate that it is mandatory to examine the influence of repeated reverse bias load on the leakage current in forward bias for MWT solar cells.

For the *p*-type HIP–MWT+ structure it is found that the cell performance is almost not impacted by reverse biasing. On the other hand, the *p*-type MWT–BSF+ and the *n*-type MWT cells are found to be impacted. After 101 reverse bias loads of *p*-type sample *p1* and *n*-type sample *n4c*—which are representative for the *p*-type MWT–BSF+ and the *n*-type *n*MWT+ cell structures, respectively—the latter shows clearly increased fill factor losses with an absolute difference in  $\Delta FF_E = -0.5\%$  or more. This indicates that the *n*-type sample is more susceptible to reverse bias load than the *p*-type one, which almost shows no leakage current for certain via pastes. Transferred to cell level this means that the electrical contact separation at the external contacts is most likely much more challenging for *n*-type MWT solar cells as for their *p*-type counterparts.

It is also found that the selection of a suitable via paste is important depending on the targeted application. The method to utilize test structures to examine the electrical contacting behavior of several via pastes on the same sample proves to be an efficient option for paste evaluation.

## 6.5 Study of impact factors on leakage current after reverse biasing

As shown in the previous section, reverse biasing the test structures leads to partially increased leakage currents in forward bias operation. Therein, reverse bias load appears to unequally influence the leakage currents for the *p*-type and *n*-type samples. In this section will be examined whether or not the different types of bulk dopings are responsible for the unequal influence of reverse biasing on the forward leakage current. Furthermore, the impact of surface topography, dielectric layer, and additional phosphorus doping in case of the *n*-type samples is investigated in more detail with respect to susceptibility against reverse stress.

### Impact of the type of bulk doping and the surface topography

To find out if the *p*-type and *n*-type Cz-Si samples are in general differently susceptible to reverse bias load, samples *p1* and *n1* (alkaline saw-damage etched front surface) as well as samples *p2* and *n2* (alkaline textured) are compared with each other. For all samples, the front side features no intermediate dielectric layer. To allow an evaluation, the sum of the absolute fill factor losses for all five via pastes of those samples is shown in Table 6.3. Note that the bulk doping concentration of the *n*-type samples is less than that of the *p*-type ones. For measurement A in forward bias, no significant difference in the cumulated fill factor losses can be identified. This means that the electrical contact properties without prior reverse bias load do not

**Table 6.3.** Sum of the absolute fill factor losses for the five via pastes for each sample without dielectric and alkaline saw-damage etched (SDE) or alkaline textured (txt) front surface (#sum of only three via pastes, since for the other two, no fill factor losses are calculated due to very strong leakage currents and therefore not sufficiently recorded *I*-*V* characteristics). Detailed values for each paste and sample are found in Table 6.2 (RBL: reverse bias load).

Sample	<i>p1</i>	<i>n1</i>	<i>p2</i>	<i>n2</i>
Type of bulk doping	<i>p</i>	<i>n</i>	<i>p</i>	<i>n</i>
Bulk doping concentration $N_{\text{bulk}}$ ( $10^{15}$ cm $^{-3}$ )	5.8	4.6	8.8	5.0
Front surface topography	SDE	SDE	txt	txt
$\downarrow$ Absolute fill factor losses after measurement				
A (no prior RBL): $\Delta FF_A$ (%)	0	-0.2	-0.1	-0.2
C (after one RBL): $\Delta FF_C$ (%)	-0.2	-16.3 <sup>#</sup>	-0.6	-10.3

significantly depend on the type of bulk doping or the front surface topography. All investigated via pastes show almost no electrical contact to *p*-type and *n*-type silicon. For measurement C after single reverse biasing, the cumulated fill factor losses of the *n*-type samples *n*1 and *n*2 exceed the values of the *p*-type samples *p*1 and *p*2 by more than a factor of 15, irrespective of the front surface topography. Hence, the different types of bulk dopings have a significant impact on the correlation between reverse bias load and forward leakage current. A clear trend regarding the front surface topography cannot be extracted. Keep in mind that the via pastes are differently affected by reverse bias load, as specified in Table 6.2.

The finding that particularly the *n*-type samples are affected by reverse biasing can be further confirmed by the results obtained for samples *p*3, *p*4, *n*3, and *n*4 with dielectric layer *a* ( $\text{SiO}_2/\text{SiO}_x/\text{SiN}_x$ ) or layer *b* ( $\text{Al}_2\text{O}_3/\text{SiN}_x$ ). The respective fill factor losses for the *p*-type and *n*-type samples for all five via pastes are accordingly added in Table 6.4. Without prior reverse bias load (A), no fill factor losses at all are observed for all samples and thus for all via pastes. After reverse bias load (C), the *p*-type samples are hardly affected with a maximum cumulated fill factor loss of only  $-0.1\%$  per sample. Again, the *n*-type samples are significantly more affected, whereas not every single via paste shows increased fill factor losses; see Table 6.2. Upon a closer inspection of the fill factor losses  $\Delta FF_C$  of all *n*-type samples after a single reverse bias load, also no clear trend between alkaline saw-damage etched and alkaline textured front surfaces concerning the calculated fill factor losses can be identified for comparable samples.

### Impact of the dielectric layer

Apart from the type of bulk doping, also the different dielectric layers affect the fill factor losses. For instance for samples *n*3*a* and *n*3*b* in Table 6.4,

**Table 6.4.** Sum of the absolute fill factor losses of the five via pastes for each sample with dielectric layer *a* ( $\text{SiO}_2/\text{SiO}_x/\text{SiN}_x$ ) or layer *b* ( $\text{Al}_2\text{O}_3/\text{SiN}_x$ ).

Sample	<i>p</i> 3 <i>a</i>	<i>p</i> 3 <i>b</i>	<i>p</i> 4 <i>a</i>	<i>p</i> 4 <i>b</i>	<i>n</i> 3 <i>a</i>	<i>n</i> 3 <i>b</i>	<i>n</i> 4 <i>a</i>	<i>n</i> 4 <i>b</i>
Type of bulk doping	<i>p</i>	<i>p</i>	<i>p</i>	<i>p</i>	<i>n</i>	<i>n</i>	<i>n</i>	<i>n</i>
Front surface topography	SDE	SDE	txt	txt	SDE	SDE	txt	txt
$\downarrow$ Absolute fill factor losses after measurement								
A (no prior RBL): $\Delta FF_A$ (%)	0	0	0	0	0	0	0	0
C (after one RBL): $\Delta FF_C$ (%)	0	0	-0.1	-0.1	-0.4	-7.2	-3.6	-2.8

which differ only in the dielectric layer, the first shows a cumulated fill factor loss which is lower by 6.8% absolute. This shows that not only the components of the via pastes but also the combination of via paste and dielectric layer play a decisive role to achieve the lowest possible fill factor losses.

### Impact of an additional phosphorus doping

To examine the influence of an additional  $90 \Omega/\text{sq}$  front surface phosphorus doping on the electrical contact properties for the  $n$ -type samples, only samples with alkaline textured front surface ( $n2$ ,  $n4$ ,  $n6$ , and  $n8$ )—which correspond to the  $n$ -type MWT structures in Fig. 3.9—are considered in Table 6.5 (via paste V3 is not included). After measurement A in forward bias, no or only moderate cumulated fill factor losses  $\Delta FF_A$  are observed for all samples, except for sample  $n6$  without dielectric layer and with front surface doping which shows already a value of  $-13.8\%$  for the sum of the four via pastes. In this case, an electrical conductive contact between the via pastes and the additionally phosphorus-doped front surface is already formed. The negative impact of reverse bias load is obvious for all samples after measurement C, but the samples with  $90 \Omega/\text{sq}$  front surface doping mostly show significant higher fill factor losses. A stable electrical contact insulation between the via pastes and  $n$ -type silicon with the additionally phosphorus-doped surface—as present in the  $n$ MWT cell structure in Fig. 3.9(a)—seems thus not feasible. Also without additional phosphorus doping, the absolute stable electrical contact insulation seems to be anything but trivial.

### Interim conclusion

Without prior reverse bias load, almost no electrical conductive contact between the via pastes and  $p$ -type as well as  $n$ -type Cz-Si is formed. The glass layer or the stack consisting of glass layer and additional dielectric

**Table 6.5.** Sum of the absolute fill factor losses for via pastes V1, V2, V4, and V5 for each  $n$ -type sample with alkaline textured front surface as well as no dielectric layer or layer  $a-d$ . For the sample marked with (/) no fill factor losses are calculated due to very strong currents and therefore not sufficiently recorded  $I-V$  curves.

Sample	$n2$	$n4a$	$n4b$	$n4c$	$n4d$	$n6$	$n8a$	$n8b$	$n8c$	$n8d$
Front surface doping ( $\Omega/\text{sq}$ )	—	—	—	—	—	90	90	90	90	90
$\downarrow$ Absolute fill factor losses after measurement										
A (no prior RBL): $\Delta FF_A$ (%)	-0.2	0	0	0	0	-13.8	-0.1	-0.4	-0.4	-0.2
C (after one RBL): $\Delta FF_C$ (%)	-9.2	-2.2	-0.6	-6.5	-0.9	(/)	-4.4	-6.4	-6.5	-6.6

layer probably provides the electrical insulation to the silicon. However, the insulating properties of the intermediate dielectrics seem to degrade more or less during reverse bias load dependent on the type of bulk doping or an additional phosphorus surface doping as examined for the *n*-type samples. This degradation is found to be not constant in general but depends rather on the combination of via paste and dielectric layer type. Significantly higher leakage currents are observed for the *n*-type samples even after only a single measurement in reverse bias compared with the corresponding *p*-type ones, irrespective of the front surface topography.

## 6.6 Detailed investigation of leakage current after reverse biasing

As shown in the previous sections, reverse bias load may lead to increased leakage currents in forward bias. Especially the *n*-type samples are more affected than the *p*-type ones. More comprehensive measurements are performed with selected test structures and via pastes (see Fig. 6.8) to investigate the causes of the observed behavior. These samples have been only measured once in forward bias so far—that means no reverse bias load has been applied before. Between consecutive measurements of the current under forward bias always up to a voltage of 0.7 V, the current in reverse bias is measured up to gradually increased negative voltages starting with -1 V (nominal step size -1 V).

### Test structures with different type of bulk doping

Two almost identical samples (*p1, n1*) both with alkaline saw-damage etched front surface, no dielectric layer, and with similar bulk doping concentration  $N_{\text{bulk}} \approx 5 \cdot 10^{15} \text{ cm}^{-3}$  are investigated for via pastes V2–V4. The only dif-

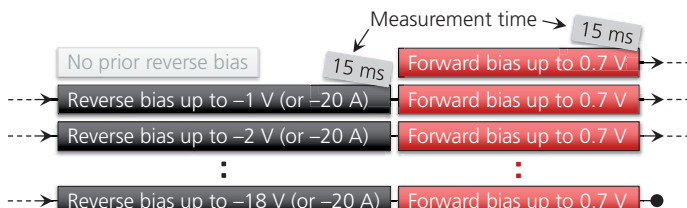


**Fig. 6.8.** Overview of the measurements of the dark  $I$ - $V$  characteristics. The reverse bias is gradually increased with a step size of -1 V after each forward measurement. The maximum measured current in reverse bias is limited to -20 A. The duration for each measurement is 15 ms, with an interval of several seconds in between.

ference is the bulk dopant type. Despite the basically same sample structure, *p*-type sample *p1* shows a completely different behavior than *n*-type sample *n1*; see Fig. 6.9. Obviously, the measured currents under forward and reverse bias are significantly different.

For sample *p1*, no current flow occurs for via pastes V2 and V4 and thus, no electrical contact to the underlying bare *p*-type silicon can be assumed. For via paste V3, the current under reverse bias slightly increases with increasing negative voltages, whereas the leakage current remains on a negligible level. In contrast, the currents under reverse bias abruptly rise for the *n*-type sample *n1* in the range of only a few volts. This comes along with an abrupt rise of the leakage currents under forward bias for all three via pastes. This illustrates that leakage currents only occur as soon as current flow sets in under reverse bias. In contrast, current flow under reverse bias does not necessarily lead to leakage currents in forward bias (as e.g. for via paste V3 on sample *p1*).

### Possible reasons for the different behavior of *p*-type and *n*-type samples

As can be concluded from Fig. 6.9, the electrical contact separation degrades especially for the *n*-type sample *n1*. One possible reason could be

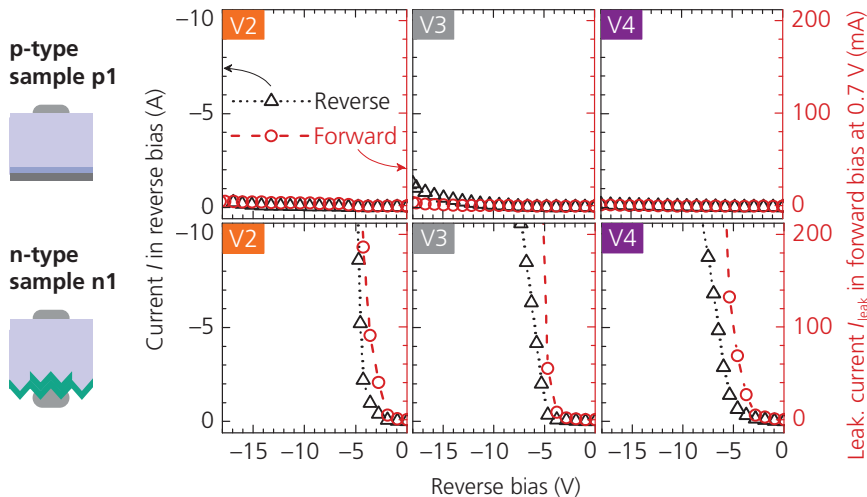


**Fig. 6.9.** Measured currents in forward and reverse bias for via pastes V2–V4 on samples *p1* (top) and *n1* (bottom) with alkaline saw-damage etched front surface. The current in forward bias is measured at a voltage of 0.7 V after each gradual increase of the reverse bias by nominal  $-1\text{ V}$ .

the direction of the applied reverse bias. The current directions under reverse bias are different for the two bulk doping types: for *n*-type silicon, electrons flow from the metal to the silicon, whereas for *p*-type silicon, the electron flow is vice versa (i.e. from the silicon to the metal). Hot electrons or hot holes can enable the formation of defects within the intermediate dielectric layer system<sup>28</sup> [251–253]. This defect formation or the electrical breakdown of dielectric layers are described in the literature based on biased percolation models [254,255]. *Watanabe et al.* [252] reported a dependence of defect formation within an SiO<sub>2</sub> layer on *n*-type silicon on the polarity of the applied stressing bias. Only if the *n*-type sample is stressed with a positive bias (corresponding to reverse bias in the present work), defects are created within the SiO<sub>2</sub> layer, whereas no formation of defects is observed for negative sample bias (corresponding to forward bias in the present work). However, further studies have to be performed to find the responsible mechanisms, which can explain the observed behavior.

### Test structures with different intermediate dielectrics

Further measurements with *n*-type samples are carried out in order to examine if the suspected defect formation within the insulation layer and thus, the current flow under reverse bias is constant for different applied dielectric layers. Fig. 6.10 shows the results for the *n*-type samples *n3c* and *n3d* with alkaline saw-damage etched front surface and PECVD SiN<sub>x</sub> and PECVD SiriON/SiN<sub>x</sub> layers, respectively. Again, as long as no current flow occurs under reverse bias, no forward leakage currents are measured. For via paste V1, the currents for reverse and forward bias do almost not differ for both dielectrics. A clear difference occurs for via paste V2. For sample *n3c* (SiN<sub>x</sub>) the leakage current increases significantly once current in reverse bias sets in. The leakage current for sample *n3d* (SiriON/SiN<sub>x</sub>) is almost not affected although the current flow under reverse bias is significant. Such a behavior is very interesting with respect to an integrated bypass-diode approach on module level. For via paste V4, the currents under reverse bias for both dielectrics are clearly lower compared with the other two via pastes. Almost no leakage currents occur. This shows again the possibility to keep the occurring leakage currents as small as possible by using adapted via paste ingredients in combination with suitable dielectric insulation layers.

---

<sup>28</sup>The samples last discussed in Fig. 6.9 do not feature an extra-applied dielectric layer. Here, also the glass layer formed below the via pastes during contact firing is addressed when referring to the intermediate dielectric layer system.

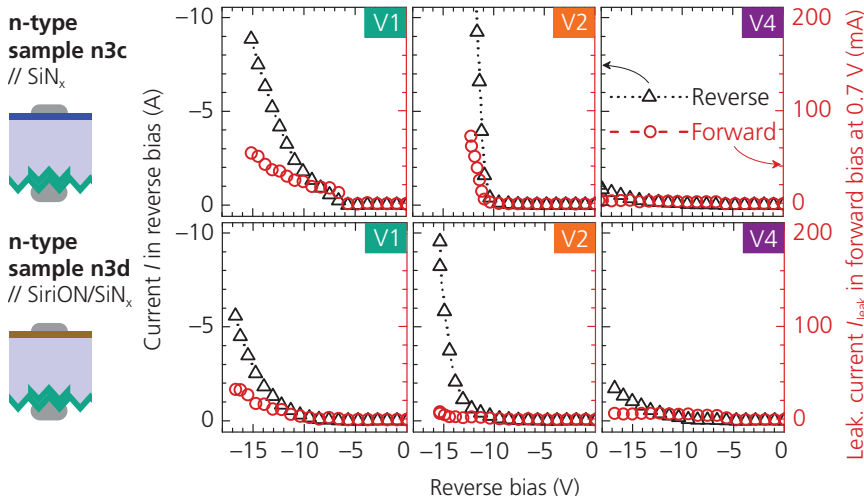


**Fig. 6.10.** Measured currents in forward and reverse bias for via pastes V1, V2, and V4 on samples *n3c* (top) and *n3d* (bottom) with alkaline saw-damage etched front surface and with different dielectric layers.

## 6.7 Chapter summary

The key component of MWT silicon solar cells, irrespective of the bulk doping type, is the metal-insulator-silicon contact in the area of the external rear contacts that are connected to the emitter by the front grid and metallized vias. In this chapter, the examinations focused on the electrical contact properties of screen-printed and fired silver contacts on *p*-type and *n*-type Cz-Si utilizing special test structures. Five via pastes and one reference paste each with silver as conductive component thereby formed the metal contacts. In contrast to the reference paste, the via pastes must not form an electrically conductive contact to the silicon surface on which they are applied. The impact of (i) different intermediate dielectric layers and (ii) different surface topographies (alkaline saw-damage etched and alkaline textured) on the electrical contact properties are analyzed.

Dark current-voltage (*I-V*) measurements reveal that initially, i.e. without prior reverse bias load, no electrical conductive contact between all examined via pastes and *p*-type as well as *n*-type Cz-Si is formed. A single measurement in reverse bias can lead to significant forward leakage currents for the *n*-type samples, whereas the corresponding *p*-type samples are al-

ways much less affected—irrespective of the surface topography. The  $I$ – $V$  measurements also reveal significant impact of the via paste on the  $I$ – $V$  characteristics. Leakage currents in forward bias only occur as soon as current flow appears under reverse bias condition. In contrast, current flow under reverse bias does not necessarily lead to leakage currents in forward direction.

The examinations revealed a promising via paste for the metallization of  $p$ -type MWT–BSF+ solar cells without rear emitter showing no significant leakage currents even after repeated reverse biasing. Despite the fact that the current under reverse condition increases up to  $-10\text{ A}$  at a voltage of  $-12\text{ V}$  during repeated  $I$ – $V$  measurements, no significant effect on cell performance is observed. This indicates that the current flow in reverse bias condition solely is not a suitable criterion for determining the quality of MWT solar cells as the high currents in reverse mode might be utilized for an integrated bypass-diode approach at the module level.

The investigations indicate—especially for the  $n$ -type test structures—that the electrical insulation between the via pastes and the silicon surfaces degrades during reverse biasing. Hence, the electrical contact separation between via paste and silicon bulk is found to be much more challenging for  $n$ -type MWT cells compared with  $p$ -type ones. For the former, high currents in reverse bias condition most likely cause increased forward leakage currents leading to degradation of the cell performance. The investigations further reveal that the continuous phosphorus BSF configuration of the  $n$ MWT cell structure might represent a major challenge for maintaining high (pseudo) fill factors and shunt resistances after reverse biasing due to high risk of leakage currents in forward operation in the area of the external  $p$ -type contacts. Also for the  $n$ MWT+ structure, an absolute stable behavior against reverse stress, i.e. no increased leakage current at all, seems to be a challenging task. However, the leakage currents can be considerably reduced by the use of a suitable combination of via paste and dielectric insulation layer.

Via paste V2 is found to be the most promising and versatile paste for fabrication of  $n$ -type MWT solar cells with alkaline textured rear surface and will be used for cell fabrication in the next chapter.



# **7 Solar Cell Results and Loss Mechanisms**

## **7.1 Introduction**

This chapter gives an overview on the development of large-area *n*-type Cz-Si MWT solar cells with 156 mm edge length during the course of this thesis. As reference, also *n*-type Cz-Si H-pattern cells are fabricated to identify MWT-specific challenges. The improvements in terms of current-voltage characteristics and energy conversion efficiencies achieved within various development cycles are discussed. A selection of detailed investigations aims at identifying the major loss mechanisms. As a continuation of the studies from Chapter 6, the current flow under reverse bias load and its impact on the forward characteristics of the H-pattern and the MWT solar cells is examined. These investigations of the reverse bias behavior are also important for potential module integration of the fabricated solar cells. Several process optimizations, including the findings from the Chapters 4 and 5, as well as process simplifications are implemented into the fabrication of *n*-type MWT solar cells. Finally, an estimate for the energy conversion efficiency potential of *n*-type MWT solar cells is performed, which might be achieved by integration of further technological progresses.

## **7.2 Development of the energy conversion efficiency**

The optimization of solar cells can be investigated using various test samples. Such test samples have been used within this work for, e.g. the optimization of  $\text{BBr}_3$  diffusion processes (Chapter 4) or the characterization of the electrical properties of the external rear contact structure for MWT solar cells (Chapter 6). Up to a certain point, test samples provide opportunities to characterize and to optimize individual issues, processes,

or process clusters without the need to fabricate complete and complex solar cells. But in the end, there is interest in, of course, the performance of both fully functional solar cells and the developed processes which have been implemented into their fabrication.

During the period of this thesis, numerous *n*-type Cz-Si H-pattern solar cells and *n*-type Cz-Si MWT solar cells have been fabricated in various runs. The respective schematic cross sections of the cell structures can be found in Fig. 3.2(b) and Fig. 3.9. Exemplary images of some of the completed solar cells illustrate Fig. 3.7(b) and Fig. 3.11. Throughout the performed experiments, the H-pattern solar cells—representing a “standard” cell structure—serve as reference on the more novel *n*-type MWT cell concept. The utilized fabrication sequences are based on the process sequence introduced in Fig. 3.10. The progression of achieved solar cell parameters is shown in Fig. 7.1 for a selection of experiments A–E and gives an impression of the steady improvement and stabilization due to various optimizations of the fabrication process. Such a dynamic progress points out the large potential of the rather new *n*-type MWT solar cell technology. The data given refer to measurements performed without applying reverse bias load. The difference between the two MWT cell structures is that the *n*MWT cell has a full-area phosphorus-doped back surface field (BSF) on the rear side (see Fig. 3.9(a)) whereas the rear side of the *n*MWT+ cell is not highly doped in the area of the external *p*-type contacts (see Fig. 3.9(b)). For more information about the *n*MWT and the *n*MWT+ cell structures, refer to Chapter 3.5.

As the *n*-type solar cells feature a grid structure on the rear side, light may be also incident from the rear. Thus, the surface underneath the cells during the current-voltage (*I*–*V*) measurements affects the *I*–*V* data. Refer to Appendix B.1 for further information concerning the procedure of *I*–*V* measurements of these bifacial solar cells within this thesis. The box plot data in Fig. 7.1, initially measured with an industrial cell tester, is corrected with respect to measurements performed at *Fraunhofer ISE CalLab PV Cells* on black-foil-coated measurement chucks. The *I*–*V* data of some most efficient solar cells are also given for *CalLab* measurements performed either on gold-plated or white-foil-covered surfaces (depicted as open symbols) to account for a reflective surface underneath the cells. Note that the results given in Fig. 7.1 are to be used to extract a general trend on the improvement achieved over time. The data is not suitable to conclude on small differences between the different cell technologies (this will be done

in the Chapters 7.4 to 7.6), as the boxes for each experiment and the different cell types do not always include solar cells, which have been fabricated using comparable process steps.

A continuous improvement is seen for all four characteristic parameters: energy conversion efficiency  $\eta$ , fill factor  $FF$ , open-circuit voltage  $V_{OC}$ , and short-circuit current density  $j_{SC}$ . Consider first the box plot data representing the  $I$ - $V$  results for the MWT cells obtained on black foil. Starting from mean conversion efficiencies in the range of 17%, they could be increased to over 19.5% in experiment E. The most efficient MWT cells achieve  $\eta = 20.0\%$  ( $n$ MWT) and  $\eta = 19.9\%$  ( $n$ MWT+). Likewise the increase in  $V_{OC}$  by

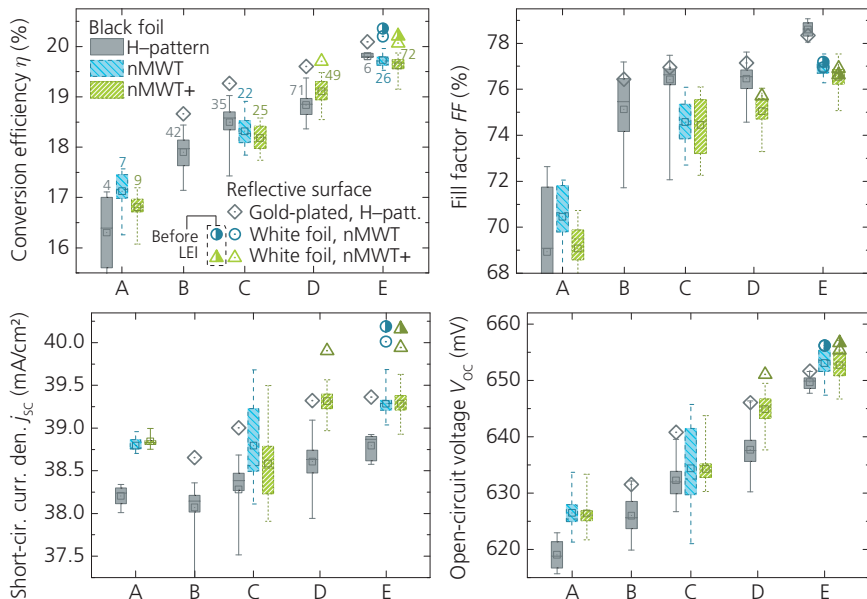


**Fig. 7.1.** Development of the solar cell parameters energy conversion efficiency  $\eta$ , fill factor  $FF$ , short-circuit current density  $j_{SC}$ , and open-circuit voltage  $V_{OC}$  from selected experiments A–E during the thesis period (after laser edge isolation (LEI) without previous reverse bias load). The box plot data, initially measured with an industrial cell tester, is corrected with respect to measurements performed on black-foil-coated chucks at *Fraunhofer ISE CalLab PV Cells* (description of box plot see Fig. 5.3, the number above the boxes indicates the group size). Each open symbol represents a *CalLab* measurement on the stated reflective chuck surface for the most efficient solar cells per cell type. The half-filled symbols in experiment E refer to measurements before LEI. All solar cells are made of  $n$ -type Cz-Si wafers with 156 mm edge length (except experiment A with 125 mm edge length).

nearly 30 mV up to mean values of 653 mV shows the successful improvement in the formation and passivation of the highly doped surface layers as well as their metallization. This steady improvement is also apparent for the *FF*, which could be increased by 10% relative to values just below 77%, and the  $j_{SC}$  with mean values of up to  $39.3 \text{ mA/cm}^2$ .

The results shown in Fig. 7.1 allow the following conclusions: First, the MWT cell concepts show clearly higher  $j_{SC}$  due to less metal coverage on the front surface compared with the H-pattern reference cells. Second, the  $V_{OC}$  of the MWT cells is at least equal to that of the H-pattern cells, indicating that the MWT concept does not contain any serious additional recombination channels. Third, the rise of the *FF* for the MWT cells to a level comparable to that of the H-pattern cells is a remaining challenge. However, the lower *FF* for the MWT structure is not surprising as additional series resistance contributions arise from the transfer of the external front contacts to the rear side. These additional series resistance contributions might originate from the thinner (pseudo-) busbars on the cell's front and rear side, the via contacts, the lateral current flow within the base in the area of the external *p*-type contacts, and the lower number of external contacts per contact row (for the latter see Appendix B.1). These issues will be discussed in detail in Chapter 7.4.4. Fourth and last, the achievable conversion efficiencies and the other parameters for the *nMWT* and the *nMWT+* cell structures prior to applying reverse bias load are found to be almost equal.

Some most efficient solar cells have also been measured at the *CalLab* on chucks with either gold-plated or white-foil-covered surface (open symbols). Due to their significant higher surface reflectivity (see Fig. B.1 in Appendix B.1),  $j_{SC}$  is increased between 1% and 1.5% relative compared with the measurements performed on black foil. This gain in  $j_{SC}$  transfers almost completely on  $\eta$ , since *FF* and  $V_{OC}$  remain nearly unchanged. The thus measured cells achieve maximum conversion efficiencies of  $\eta = 20.2\%$  (*nMWT*) and  $\eta = 20.1\%$  (*nMWT+*). By default, laser edge isolation on the front side is performed at the end of the fabrication process to electrically separate front and rear sides, so that the solar cells do not shunt at the wafer edges. This leads mostly to a significant increase in shunt resistance  $R_P$ , accompanied by an increase in pseudo fill factor *pFF* and *FF* in case  $R_P$  limits both quantities to a large extent. On the other hand, laser edge isolation reduces the effective current collecting cell area, which leads to reduction in  $j_{SC}$  of up to  $0.2 \text{ mA/cm}^2$ . To determine the potential of the

solar cells also prior to laser edge isolation, some of the solar cells have been also measured prior to this process step. In experiment E, the  $I$ - $V$  measurements on white foil prior to laser edge isolation revealed the highest  $\eta$  being measured at all within this thesis, specifically  $\eta = 20.4\%$ <sup>29</sup> (*nMWT*) and  $\eta = 20.2\%$  (*nMWT+*). As discussed in Chapter 3.2.2, *ECN* and *Yingli Green Energy* also work on the development of *n*-type Cz-Si MWT solar cells. From  $\eta = 19.7\%$  in 2011 [16], they have recently been able to increase the cell efficiency to  $\eta = 21.0\%$ <sup>30</sup> (measured on reflective underground) [256]. Comparing the  $I$ - $V$  data given in the footnotes 29 and 30, it is clear that  $j_{SC}$  and  $V_{OC}$  are virtually identical. However, the most efficient *n*-type MWT solar cell from *ECN* and *Yingli Green Energy* shows a significant higher  $FF$ , which originates to a large extent from the applied metallization layout that is based on 6/7 external *p*-type/*n*-type contact rows [256]. In comparison, the most efficient *nMWT* and *nMWT+* solar cells from this work feature a metallization layout with four external contact rows per polarity; see Fig. 3.11(b). It is noted that especially the *nMWT* structure is very susceptible to reverse bias load, as this is tested in detail on cells from experiment C in the following section. Excerpts from the experiments D and E will be discussed in more detail in the sections 7.4 to 7.6. The issue concerning the influence of reverse bias load is taken up again in section 7.6 for the latest cells from experiment E.

### 7.3 Impact of reverse bias load on cell characteristics

The studies in this section focus on the reverse bias behavior of the *n*-type Cz-Si H-pattern and *n*-type Cz-Si MWT solar cells (*nMWT*, *nMWT+*) from experiment C in Fig. 7.1. The performed investigations and the obtained results are also published in Ref. [257]. The current under reverse bias as well as its impact on  $\eta$ <sup>31</sup> are examined utilizing two boron-doped emitters with different doping profiles. In addition, shunting caused by the front side metallization—relevant to both the H-pattern as well as the MWT solar cells—is addressed by comparison of respective cells featuring these emitters. In addition to global measurements of forward and reverse  $I$ - $V$  characteristics, dark lock-in thermography (DLIT) [258] measurements are performed which depict the current flow spatially resolved.

<sup>29</sup>Further  $I$ - $V$  data:  $j_{SC} = 40.2 \text{ mA/cm}^2$ ,  $V_{OC} = 656 \text{ mV}$ ,  $FF = 77.2\%$ ,  $R_P = 6.5 \text{ k}\Omega\text{cm}^2$ .

<sup>30</sup>Further  $I$ - $V$  data:  $j_{SC} = 40.3 \text{ mA/cm}^2$ ,  $V_{OC} = 656 \text{ mV}$ ,  $FF = 79.4\%$ .

<sup>31</sup>The conclusions drawn within this chapter refer always to an illumination intensity of 1 sun. For lower illumination levels, however, the conclusions may change.

For both  $n$ -type MWT cell concepts, a silver-based via paste is applied for metallization of the vias and the external contact pads. To avoid shunting at the external  $p$ -type contacts, the via paste must not form an electrically conductive contact to the adjacent  $n$ -type-doped region during the firing process. In the previous Chapter 6, special test structures are used to examine the influence of reverse biasing on the electrical contact insulation between  $n$ -type-doped bulk silicon and external  $p$ -type contacts. A strong degradation of the electrical contact insulation is observed on the rear contact setup corresponding to cell type  $n$ MWT. Here, the shunting behavior of the two different backside structures for the  $n$ -type MWT cells is investigated on cell level.

### 7.3.1 Cell fabrication and measurement methods

The H-pattern and MWT solar cells are fabricated according to the procedure depicted in Fig. 7.2 using pseudo-square  $n$ -type Cz-Si wafers with an edge length of 156 mm, a diameter of 200 mm, an initial thickness of  $W = 200 \mu\text{m}$ , and a specific bulk resistance of  $\rho_{\text{bulk}} \approx 5 \Omega\text{cm}$ . The final solar cells of either type feature three external busbar contacts on both front and back; see Fig. 3.7(b) and Fig. 3.11(a).

Following alkaline texturing, the boron-doped front side and the phosphorus-doped rear side are formed by  $\text{BBr}_3$  and  $\text{POCl}_3$  tube furnace diffusion,

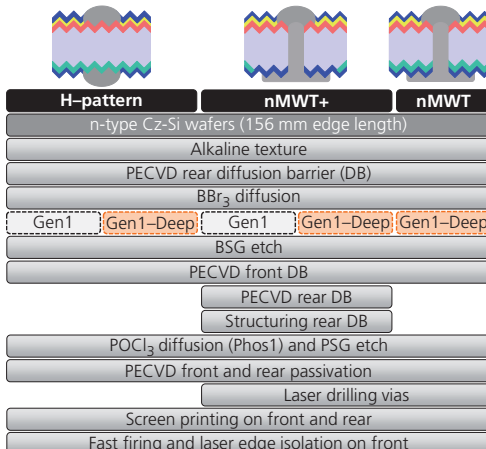


**Fig. 7.2.** Process sequence for fabrication of  $n$ -type Cz-Si H-pattern and MWT solar cells (DB: diffusion barrier).

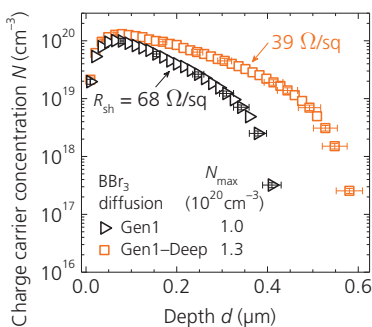


**Fig. 7.3.** Boron doping profiles, determined by ECV measurements on alkaline saw-damage etched surfaces. Exemplary error bars are shown. The sheet resistances  $R_{\text{sh}}$  and the maximum dopant concentrations  $N_{\text{max}}$  are stated.

respectively. For  $\text{BBr}_3$  diffusion, process Gen1 from Chapter 4.3 and a variation of this with higher peak temperature Gen1–Deep are applied. The emitter doping profiles, depicted in Fig. 7.3, are determined by electrochemical capacitance-voltage (ECV) measurements on alkaline saw-damage etched surfaces; see Appendix B.2. The temperature difference results in doping profiles with different maximum dopant concentrations  $N_{\max}$  and different junction depths<sup>32</sup>  $d = (500 \pm 50)$  nm (Gen1), and  $d = (680 \pm 68)$  nm (Gen1–Deep). The resulting emitter sheet resistances on the both-sides textured wafers are  $R_{\text{sh}} = (72 \pm 4)$   $\Omega/\text{sq}$  for Gen1, and  $R_{\text{sh}} = (41 \pm 2)$   $\Omega/\text{sq}$  for Gen1–Deep. The applied  $\text{POCl}_3$  diffusion process is referred to as Phos1 and yields  $R_{\text{sh}} = (73 \pm 4)$   $\Omega/\text{sq}$  with  $N_{\max} = (3.4 \pm 0.3) \cdot 10^{20}$   $\text{cm}^{-3}$ , and  $d = (440 \pm 44)$  nm. The surfaces that should not to be doped during the respective diffusion processes are masked with a diffusion barrier layer stack consisting of 50 nm-thick  $\text{SiO}_x$  and 30 nm-thick  $\text{SiN}_x$ , both applied by PECVD. As shown in Chapter 4.5, the boron doping profiles do not significantly change during  $\text{POCl}_3$  diffusion Phos1. For the nMWT+ solar cells, the rear diffusion barrier layer is structured prior to  $\text{POCl}_3$  diffusion using inkjet-printed masking resist and buffered hydrofluoric acid (HF); see Appendix C.1. In this experiment, the front diffusion barrier layer for  $\text{POCl}_3$  diffusion is already applied prior to structuring the rear diffusion barrier layer. Hence, a full-area inkjet-printed masking resist is applied on the front side as protection against the HF.

Following each diffusion, the borosilicate glass (BSG) or phosphosilicate glass (PSG) layers are removed in HF solution along with the diffusion barrier layers. The front passivation and anti-reflective coating consists of  $\text{Al}_2\text{O}_3$  and  $\text{SiN}_x$  layers, both applied by PECVD. PECVD  $\text{SiN}_x$  passivates the rear side. Subsequently, laser-drilling of the vias of the MWT cells is performed.

For screen printing, commercial metal pastes are used. The H-pattern cells are metallized with a three-busbar grid on both sides by applying a fire-through Ag-Al paste on the front (paste Ag-Al1 from Chapter 5) and a fire-through silver paste (paste Ag1) on the back (both are of electrically contacting nature). The rear side of the MWT cells is metallized by a two-step screen printing process. First, the finger structures are printed with silver paste Ag1, followed by the simultaneous printing of the external

---

<sup>32</sup>In this section, the junction depth  $d$  is estimated at a dopant concentration  $N = 9.2 \cdot 10^{14}$   $\text{cm}^{-3}$ , which corresponds to the bulk doping concentration of the wafers used for cell fabrication.

*p*-type and *n*-type contacts as well as the vias with a non-fire-through silver via paste (via paste V2 from Chapter 6). The front MWT grid with three thin pseudo-busbars is applied with paste Ag-Al1. Therein, the front grids for the different cell types have the same finger number. The finger number is also identical for the respective rear grids. For solar cells with boron-doped emitters Gen1 or Gen1–Deep, the same grid structures, i.e. the same finger numbers, are applied. Finally, contact formation with the same process conditions for all solar cells takes place in a fast firing furnace, followed by laser edge isolation on the front side.

### Current-voltage measurements

First, measurements of the global forward and reverse *I*–*V* characteristics are performed. The *n*-type Cz-Si H-pattern and MWT cells are tested with an industrial cell tester with non-reflective underground, following the measurement steps outlined in Fig. 7.4. Initially, the cells are tested without applying prior reverse bias. In order to characterize the influence of reverse bias load on the forward *I*–*V* characteristics, the measurement direction alternates between reverse and forward measurement (20 times in total).

### Dark lock-in thermography measurements

For typical silicon solar cells, DLIT images recorded at a phase of  $-90^\circ$  are proportional to the locally dissipated power [258], generated by local current flow. Hence, current flow is depicted spatially, which can help to better understand the globally measured *I*–*V* data and to find critical areas. As different measurement procedures are used, the procedures are explained when the respective DLIT measurements are discussed.

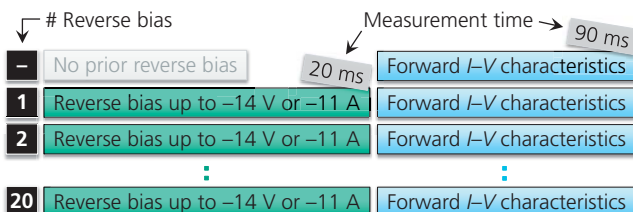


**Fig. 7.4.** Overview of the performed *I*–*V* measurements. The measurements in reverse bias are performed in the dark (duration 20 ms), whereas the forward measurements are performed under illumination (duration 90 ms). The interval in between each of the measurements is 4 s.

### 7.3.2 Current-voltage characteristics

As just mentioned, the  $I$ - $V$  measurements are performed following the procedure depicted in Fig. 7.4. The measured conversion efficiencies  $\eta$  are found to be between 18% and 19% for the investigated H-pattern and MWT cells; see also the  $I$ - $V$  data for experiment C in Fig. 7.1.

In order to extract the impact of reverse bias load on the forward behavior of the examined solar cells, certain  $I$ - $V$  characteristics after the first and the 20th reverse measurement are compared with the initial values (cells are not stressed in reverse yet). Therefore, the absolute losses in  $\eta$ , fill factor  $FF$ , and pseudo fill factor  $pFF$  are summarized in Table 7.1. The shunt resistances  $R_p$  are given in absolute numbers. Refer to Chapter 2.2.3 for further information on the single  $I$ - $V$  parameters. The losses in open-circuit voltage  $V_{OC}$  are very small ( $|\Delta V_{OC}| < 0.4\%\text{rel}$ ) and are therefore not shown. That means that no significant increase of the dark saturation current density  $j_{01}$  of the first diode in the two-diode model is observed due to reverse biasing. The short-circuit current densities  $j_{SC}$  are constant throughout and thus, are also not shown.

**Table 7.1.** Mean absolute losses in conversion efficiency  $\eta$ , fill factor  $FF$ , and pseudo fill factor  $pFF$  in relation to the initial measurements performed without prior reverse bias. The shunt resistance  $R_p$  is given in absolute numbers. The numbers in parenthesis indicate the number of cells per variation.

Cell type	BBR <sub>3</sub> diffusion	#Reverse bias	$\Delta\eta$ (% <sub>abs</sub> )	$\Delta FF$ (% <sub>abs</sub> )	$\Delta pFF$ (% <sub>abs</sub> )	$R_p$ (k $\Omega$ cm <sup>2</sup> )
H-pattern	Gen1 (3)	–		<i>Initial values</i>		9.1
		1	−0.1	−0.2	−0.2	4.6
		20	−0.1	−0.3	−0.2	4.2
	Gen1–Deep (3)	–		<i>Initial values</i>		46.8
		1	0.0	−0.1	0.0	27.9
		20	0.0	−0.2	−0.1	26.5
<i>n</i> MWT+	Gen1 (1)	–		<i>Initial values</i>		8.6
		1	−0.1	−0.2	−0.2	4.4
		20	−0.1	−0.3	−0.3	3.5
	Gen1–Deep (3)	–		<i>Initial values</i>		41.8
		1	0.0	−0.1	−0.1	24.2
		20	0.0	−0.2	−0.2	20.8
<i>n</i> MWT	Gen1–Deep (3)	–		<i>Initial values</i>		33.1
		1	−0.1	−0.3	−0.4	3.3
		20	−0.3	−1.0	−1.3	1.3

All cells with boron emitter Gen1 show initial shunt resistance values of  $R_p \approx 9 \text{ k}\Omega\text{cm}^2$  for the first measurement without prior reverse load. In contrast, the cells with emitter Gen1–Deep exhibit clearly higher shunt resistances with  $R_p > 30 \text{ k}\Omega\text{cm}^2$ . The significant difference in  $R_p$  shows that the cells with emitter Gen1–Deep are less sensitive to shunting than cells featuring emitter Gen1. Among the different cell structures, no significant difference in  $R_p$  is observed for the respective emitters. It is noteworthy that the  $R_p$  of the *nMWT* cells is at a comparable level with both the H-pattern and *nMWT+* cells for the very first measurement (i.e. the measurement without prior reverse bias).

For the forward measurement after the first reverse bias load,  $R_p$  decreases to slightly more than half of its initial value for the H-pattern and *nMWT+* cells, irrespective of the emitter. For the *nMWT* cells with emitter Gen1–Deep,  $R_p$  decreases to approximately a tenth of its original value. The rather moderate losses in *pFF* are  $|\Delta pFF| \leq 0.4\%_{\text{abs}}$ . Losses in *FF* are almost equivalent. The *nMWT* cells with emitter Gen1–Deep show the most pronounced *pFF* loss, whereas the H-pattern and *nMWT+* cells each with emitter Gen1–Deep show the least.

In principle, the observed losses in *pFF* can be caused by increased leakage currents and/or increased non-ideal recombination, which both leads to an increase of the dark saturation current density  $j_{02}$  of the second diode in the two-diode model; see Chapter 2.2. The decrease of  $R_p$ <sup>33</sup> shows that the ohmic (linear) leakage currents have definitely increased. However, application of the two-diode model suggests that the losses in *pFF* for the H-pattern and *nMWT+* cells with emitter Gen1–Deep are mainly caused by slightly increased  $j_{02}$  contributions, since the  $R_p$  are still sufficiently high (i.e. the ohmic leakage currents are still sufficiently low). This potential increase in  $j_{02}$  can originate from increased non-ideal recombination, as stated above, or from nonlinear leakage currents. For emitter Gen1, both increased ohmic leakage currents and slightly higher  $j_{02}$  are needed to justify the losses in *pFF* corresponding to the two-diode model.

Comparing  $R_p$  of the first measurement after initial reverse bias with the 20th measurement for the H-pattern and *nMWT+* cells and both emitters, it is seen that  $R_p$  hardly varies. This indicates that the ohmic leakage currents are particularly changed by the very first reverse load for those

<sup>33</sup>As described in Chapter 2.2.3,  $R_p$  is determined at the voltage zero point of the dark *I–V* curve and it is a measure for ohmic (linear) leakage currents.

two cell structures. The maximum observed  $FF$  loss between initial measurement without reverse bias and last measurement with reverse bias is given by  $\Delta FF = -0.3\%_{abs}$  for the H-pattern and  $n$ MWT+ cells with emitter Gen1; the maximum  $FF$  loss for the respective cells with emitter Gen1–Deep is somewhat lower with  $\Delta FF = -0.2\%_{abs}$ . Thus, the conversion efficiencies  $\eta$  are almost not affected by reverse bias stress for the H-pattern and  $n$ MWT+ cells and both emitters ( $|\Delta\eta| \leq 0.1\%_{abs}$ ).

In contrast to these two cell types, cell structure  $n$ MWT shows a higher sensitivity towards reverse biasing. As already mentioned,  $R_p$  decreases from initially larger than  $30 \text{ k}\Omega\text{cm}^2$  to approximately a tenth after single reverse load ( $R_p \approx 3 \text{ k}\Omega\text{cm}^2$ ). Further reverse biasing leads to further increased ohmic leakage currents at the external  $p$ -type contacts, as will be shown later. Consequently, an additional drop in  $R_p$  down to  $R_p \approx 1 \text{ k}\Omega\text{cm}^2$  occurs. As a result,  $pFF$  and  $FF$  drop by about  $1\%_{abs}$  compared with the initial measurement, and  $\eta$  is decreased by  $0.3\%_{abs}$ .

A possible explanation for the higher  $R_p$  (i.e. lower ohmic leakage currents) for cells with emitter Gen1–Deep could be less shunting of the  $p$ - $n$ -junction by metal crystallites below the Ag-Al contacts on the front side. The presence of metal crystallites, which form during the contact firing process, with penetration depths up to several microns have been already discussed in Chapter 5.3.3. Hence, some of the crystallites are deep enough to penetrate through the emitter region into the silicon bulk. It seems that emitter Gen1–Deep is less affected by this fact compared with emitter Gen1 likely due to its deeper junction. As higher  $R_p$  values for selectively doped and thus, deeper boron-doped emitters have been also reported by e.g. Schiele *et al.* [259], it seems reasonable to conclude that a deeper boron-doped emitter gives rise to higher  $R_p$  prior to and following reverse bias load. However, the two investigated boron doping profiles Gen1 and Gen1–Deep differ not only in junction depth, but also in  $N_{max}$ . This means that the cause for the difference in  $R_p$  cannot be doubtlessly only attributed to the junction depth as a single parameter.

### 7.3.3 Dark reverse current-voltage characteristics and dark lock-in thermography measurements I

Fig. 7.5 shows the dark  $I$ - $V$  characteristics under reverse bias of the first and the 20th measurement for the examined solar cells from Table 7.1. A significant current increase occurs at voltages below  $V \approx -4 \text{ V}$  for the H-pat-

tern and  $n$ MWT+ cells with shallower boron-doped emitter Gen1, whereas the cells with the deeper emitter Gen1–Deep show significantly lower currents; see Fig. 7.5(a)–(d). No significant differences between first and 20th reverse bias measurements are observed for those cells. Thus, emitter Gen1–Deep results in lower current flow under reverse bias condition. No clear differences are obvious between the H-pattern and the  $n$ MWT+ solar cells in terms of current flow under reverse bias stress. This means that the challenges for the  $n$ MWT+ cells concerning reverse bias behavior are found to be comparable with those of common  $n$ -type Cz-Si H-pattern cells.

Several works show that in  $n$ -type Cz-Si solar cells in general, currents occurring under reverse bias are, on the one hand, strongly dependent on the fabrication process, but on the other hand, can be significantly higher than those observed for  $p$ -type Cz-Si solar cells [137,260–262]. The two classic breakdown mechanisms of reverse-biased  $p$ - $n$ -junctions are the tunneling (Zener) effect and avalanche multiplication (impact ionization) [108, pp. 96–108]. Considering also the observed metal crystallites penetrating through the  $p$ - $n$ -junction, as discussed in Chapter 5.3.3, an assessment of the actual causes of the occurring breakdowns is not possible without further detailed investigations, which could be interesting for future work.

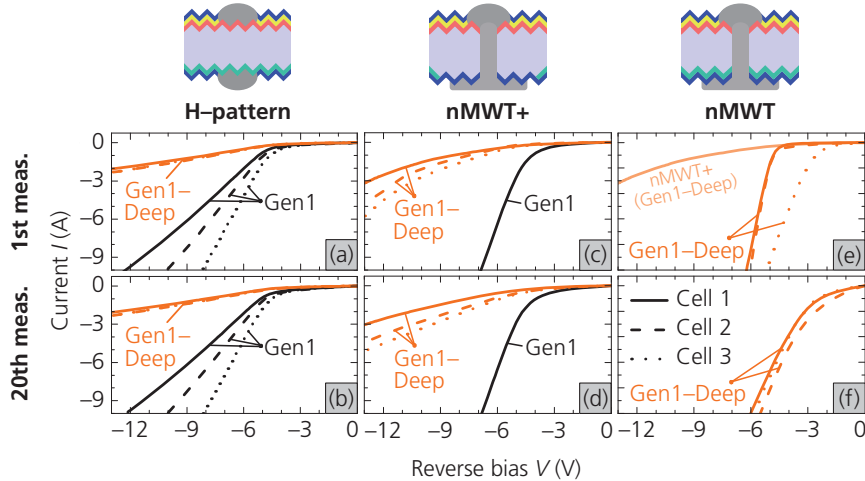


**Fig. 7.5.** Dark  $I$ - $V$  characteristics under reverse bias for the first (top) and the 20th (bottom) measurement of the  $n$ -type Cz-Si H-pattern and MWT cells from Table 7.1. Each curve represents one cell. For reasons of comparison, one curve from a  $n$ MWT+ cell of image (c) with emitter Gen1–Deep is also shown in (e).

By comparing the dark reverse  $I$ - $V$  characteristics for emitter Gen1-Deep of the  $n$ MWT+ cells (Fig. 7.5(c)) and the  $n$ MWT cells (Fig. 7.5(e)), the curves for the first reverse bias measurement are similar up to a voltage of  $V \approx -4$  V (at least for two of the  $n$ MWT cells). For more negative voltages, a strong current increase is observed for the  $n$ MWT cells. This strong current increase can mainly be attributed to the external  $p$ -type contact pads metallized with the silver via paste, as illustrated by the DLIT image in Fig. 7.6(e). The 20th reverse bias measurement in Fig. 7.5(f) reveals an even earlier current increase for the  $n$ MWT cells compared with the first reverse bias measurement in Fig. 7.5(e). This is in contrast to the findings for the H-pattern and  $n$ MWT+ cells in Fig. 7.5(a)–(d).

The DLIT images in Fig. 7.6 depict the current flow under reverse bias spatially resolved. The H-pattern and  $n$ MWT+ cells with emitter Gen1, Fig. 7.6(a) and (c), show an area with current flow close to the wafer center. The causes for the occurrence of such rather “well-defined” local current-carrying areas have not been clearly identified so far. One hypothesis for their origin is that the emitter profile depths in these areas are lower in

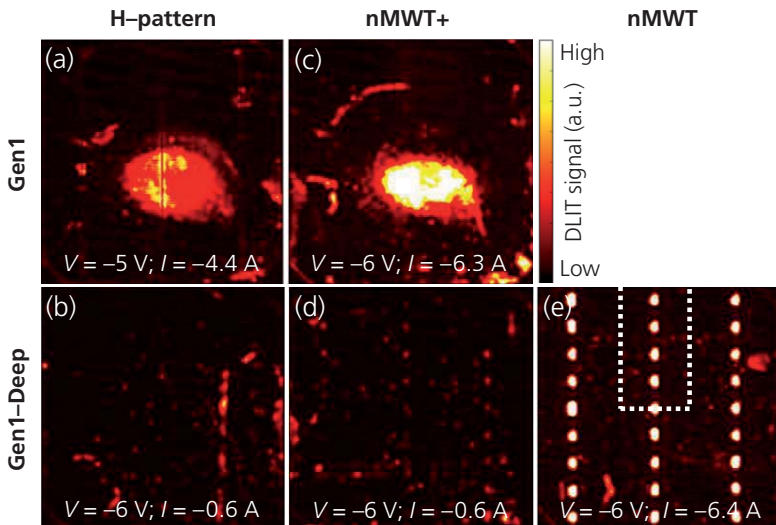


**Fig. 7.6.** DLIT images recorded at a phase of  $-90^\circ$  obtained at voltages of  $-5$  V or  $-6$  V for the different cell structures and emitters. The overall current  $I$  is also specified. In (e), the three rows with the external  $p$ -type contact pads for the  $n$ MWT cell are clearly visible. The white dotted lines in (e) define the cutout of the DLIT images depicted in Fig. 7.7.

comparison with those on the remaining front surface. This might lead to higher current flow under reverse bias condition. In experiment D, which will be discussed in more detail in section 7.4, also emitter Gen1 is utilized, but such rather “well-defined” local structures are not observed. However, the global reverse  $I$ - $V$  behavior measured for the cells in experiment D is consistent with the discussed cells with emitter Gen1 in this section. For emitter Gen1–Deep, the signal strengths of the H-pattern and the  $n$ MWT+ cells are comparable with each other in Fig. 7.6(b) and (d). The vertically aligned signals for the H-pattern cell are not within range of a busbar contact. For the  $n$ MWT+ cells, weak signals can be partly correlated with the external  $p$ -type contact pads. For the  $n$ MWT cell in Fig. 7.6(e), high signals are evident at the  $p$ -type contacts.

### 7.3.4 Dark lock-in thermography measurements II

In order to distinguish between the previously discussed contributions of  $R_P$  and  $j_{02}$  to the observed  $pFF$  losses after reverse biasing, detailed DLIT measurements are performed. The decrease in  $pFF$  is either caused by increased  $j_{02}$  contributions, whose signals should be prominent in DLIT images taken at a voltage of +0.5 V but not for -0.5 V, or by more pronounced shunts which are linear in voltage (ohmic shunts) that should exhibit the same current flow at voltages of +/-0.5 V. The performed DLIT measurement sequences start with images taken at voltages of +/-0.5 V using initially not reverse-loaded cells. Subsequently, DLIT images with stepwise increased negative voltages up to at least -6 V are recorded, followed by the repeated measurements at voltages of +/-0.5 V.

#### **nMWT+ and nMWT solar cells**

The performed DLIT measurement sequences for initially non reverse-loaded  $n$ MWT+ and  $n$ MWT cells with emitter Gen1–Deep are depicted in Fig. 7.7. No clear signals at voltages of +/-0.5 V are observed for cell  $n$ MWT in the lower row in Fig. 7.7(a) and (b). For cell  $n$ MWT+, very weak signals at the external  $p$ -type contact pads are observed for a voltage of +0.5 V, but not for -0.5 V. This indicates that slightly higher charge carrier recombination occurs in these areas (less charge carrier shielding of the metallized pads by the non-existing phosphorus doping in comparison with cell  $n$ MWT). Up to this point, both MWT cells show no significant ohmic shunts.

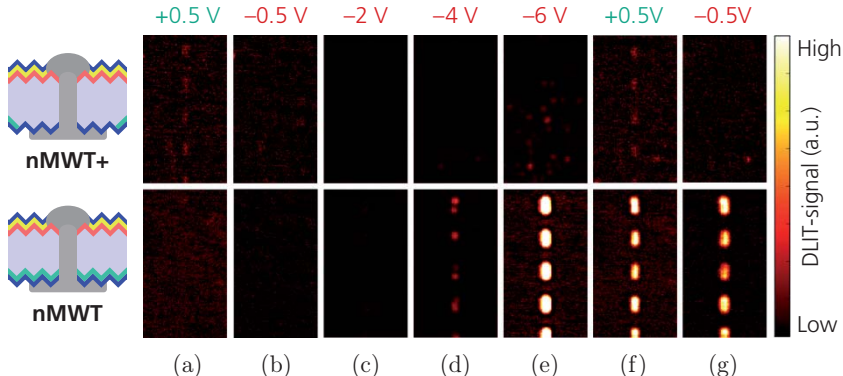


**Fig. 7.7.** DLIT images recorded at a phase of  $-90^\circ$  obtained for a  $n\text{MWT}^+$  and a  $n\text{MWT}$  cell with emitter Gen1–Deep, which have not been exposed to reverse load previously. Only the upper half of the middle contact row with the external  $p$ -type contact pads is shown—as indicated in Fig. 7.6(e)—for each applied voltage. The measurement sequences start with (a) and end with (g). For the  $n\text{MWT}^+$  cell,  $-8$  V and  $-10$  V are applied as well (not shown). The images in (c)–(e) have a different scaling compared with the other images (the signal strength is ten times higher).

At a voltage of  $-4$  V, weak signals at the external  $p$ -type contact pads begin to appear for the  $n\text{MWT}$  cell; distinct signals and thus high current flow arise for the measurement at  $-6$  V. For the  $n\text{MWT}^+$  cell, weak signals only occur at  $-6$  V, which are partly not correlated to the external  $p$ -type contact pads. This also applies to the measurements at  $-8$  V and  $-10$  V for the  $n\text{MWT}^+$  cell, which are not shown.

The subsequently repeated measurements at voltages of  $+/-0.5$  V are shown in Fig. 7.7(f) and (g). For the  $n\text{MWT}$  cell, significantly higher current flow occurs in the area of the external  $p$ -type contact pads compared with the initial measurements in (a) and (b). The same signal strength is detected for  $+0.5$  V and for  $-0.5$  V. That is the same power dissipation and thus, magnitude of the current flow, regardless of the sign of the applied voltage. This ohmic shunting behavior originates from the stress of the reverse biasing that was experienced by the  $n\text{MWT}$  structure. For the  $n\text{MWT}^+$  cell, the DLIT images at  $+/-0.5$  V after reverse bias stress almost do not differ from the corresponding images before reverse loading.

This examination clearly demonstrates that reverse biasing leads to the degradation of the electrical contact insulation between phosphorus-doped BSF and external  $p$ -type contact pads for the  $n\text{MWT}$  cells. This is in

agreement with the results obtained on the respective test structures in Chapter 6. The found increased leakage currents in forward operation at the external *p*-type contact pads contribute significantly to the losses in *pFF* of more than 1%<sub>abs</sub> for the *n*MWT cells; see Table 7.1.

### H-pattern solar cell

The described DLIT measurement sequence is also applied to an H-pattern cell with the shallower emitter Gen1, which had not been reverse biased before. This is done in order to exemplarily investigate the influence of reverse bias load on shunting at the cell's front side in more detail. Again, DLIT images are recorded at voltages of  $+/-0.5$  V before and after reverse bias load of up to  $-7$  V is applied in steps. For this investigation, an H-pattern cell from experiment D in Fig. 7.1 is utilized. The only difference in the fabrication process of this cell to the cells in this section is the  $\text{POCl}_3$  diffusion process (Phos2 instead of Phos1). However, also during  $\text{POCl}_3$  diffusion Phos2, the boron doping profile is not significantly changed as discussed in Chapter 4.5.

By comparing the respective DLIT images captured at  $+0.5$  V (Fig. 7.8(a) and (d)), and  $-0.5$  V (Fig. 7.8(b) and (e)), new ohmic shunts are clearly vis-

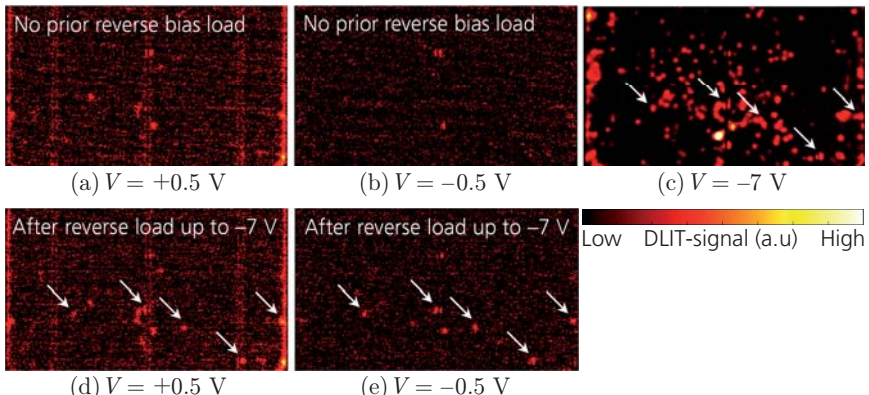


**Fig. 7.8.** DLIT images recorded at a phase of  $-90^\circ$  obtained for an H-pattern cell with emitter Gen1, which has not been exposed to reverse load previously. The images show a representative cutout over the entire cell width. The examined cell comes from an almost equally processed cell batch (experiment D, Fig. 7.1). Emerging ohmic shunts, while/after reverse bias load, are marked with arrows in (c)–(e). The image in (c) has a different scaling compared with the other images (the signal strength is ten times higher).

ible (marked with arrows) after reverse bias load has been applied. These ohmic shunts are also visible in the image taken at  $-7$  V in Fig. 7.8(c).

When studying the difference image resulting from Fig. 7.8(a) and (d) (not shown), it is seen that only clear signals remain at the spots, where the newly-created ohmic shunts are marked by the arrows. This also applies to the difference image of Fig. 7.8(b) and (e), which is also not shown. By calculating the difference image of the shunt-corrected DLIT images of Fig. 7.8(a) and (d), no clear signals, besides noise, remain. Thus,  $j_{02}$  does not significantly increase locally after reverse bias stress. Based on these findings, the loss in  $pFF = -0.2\%$  (Table 7.1) found for the H-pattern cells with emitter Gen1 after reverse biasing might be explained by increased ohmic leakage currents at the front sides of the cells. This may also apply to the *n*MWT+ solar cells with emitter Gen1 as well as to the other cells featuring the deeper emitter Gen1–Deep.

### 7.3.5 Section summary

This section deals with studying the current flow under reverse bias mode and its impact on the conversion efficiency for *n*-type Cz-Si H-pattern and *n*-type Cz-Si MWT solar cells. Shunting is studied, on the one hand, in dependence on the emitter doping profile by using two different boron diffusion processes and, on the other hand, by comparing two different phosphorus-doped BSF configurations in case of the MWT solar cells.

Less ohmic shunting is observed for the solar cells with boron-doped emitters Gen1–Deep (junction depth  $d \approx 680$  nm, maximum dopant concentration  $N_{\max} \approx 1.3 \cdot 10^{20} \text{ cm}^{-3}$ ) compared with the cells with emitters Gen1 ( $d \approx 500$  nm,  $N_{\max} \approx 1.0 \cdot 10^{20} \text{ cm}^{-3}$ ). The cells with the deeper boron doping profiles have initial shunt resistances of  $R_p > 30 \text{ k}\Omega\text{cm}^2$  (without prior reverse load), while the cells with shallower emitters exhibit initial values of  $R_p \approx 9 \text{ k}\Omega\text{cm}^2$ , irrespective of the cell type. However, the two boron emitters differ also in  $N_{\max}$ . This means that the cause for the different  $R_p$  values cannot be undoubtedly attributed to the junction depth only.

Reverse stress causes different effects on the investigated solar cell structures. A drop of  $R_p$  to approximately half of its initial value after single reverse biasing is observed for the H-pattern cells and the *n*MWT+ cells with structured BSF, independent of the emitter doping profile. Further reverse stressing leads to no further substantial degradation in  $R_p$ . The de-

terminated losses in pseudo fill factor  $pFF$  and energy conversion efficiency  $\eta$  due to reverse stressing are quite small with  $|\Delta pFF| \leq 0.3\%_{abs}$  and  $|\Delta\eta| \leq 0.1\%_{abs}$ . For the  $n$ MWT solar cells with full-area BSF and the deeper emitter,  $R_p$  drops to  $R_p \approx 3 \text{ k}\Omega\text{cm}^2$  after single reverse biasing and thus, to a tenth of its initial value. Further reverse stressing leads to a further reduction down to  $R_p \approx 1 \text{ k}\Omega\text{cm}^2$ . As a result,  $pFF$  and  $\eta$  are significantly decreased and the losses are given by  $|\Delta pFF| = 1.3\%_{abs}$  and  $|\Delta\eta| = 0.3\%_{abs}$ . The majority of the observed  $pFF$  losses for the  $n$ MWT cell occur due to significantly increased ohmic leakage currents in the forward direction in the area of the external  $p$ -type contact pads. This result is in agreement with the findings for the respective test structures from Chapter 6. On the other hand, also reverse-bias-induced shunting on the front side might contribute to this  $pFF$  loss, as this has been demonstrated for an exemplarily H-pattern cell. This shunting at the front side might also contribute to the observed  $pFF$  losses for the  $n$ MWT+ cells.

Regarding the behavior under reverse bias, the results indicate that the deeper boron doping profile with the higher  $N_{max}$  results in significantly lower current flow. The high currents observed for the  $n$ MWT solar cells might be potentially used for an integrated bypass-diode approach, in case the forward leakage current can be sufficiently reduced. As also revealed, high currents in reverse operation do not inevitably lead to reduced conversion efficiencies. No significant differences are found in terms of the amount and the spatial distribution of current flow in reverse mode between the H-pattern and the  $n$ MWT+ solar cells. This means that the challenges in terms of the reverse behavior and its suitability for module integration are similar for both cell structures.

## 7.4 Decrease of metallization-losses and discussion of MWT-specific issues

This section deals with an excerpt from experiment D in Fig. 7.1 examining  $n$ -type H-pattern solar cells (Fig. 3.2(b)) and  $n$ MWT+ solar cells with structured phosphorus-doped BSF (Fig. 3.9(b)). The performed investigations and the obtained results are partly published in Ref. [263]. The focus of this experiment is set on two subject matters: first, the implementation of electrically non-contacting silver-based busbar contacts on the front side for the H-pattern cells, also known as floating busbars and second, the comparison of laser-drilling the vias at different points in time within the

fabrication process for *n*MWT+ solar cells. Both approaches aim at identifying options to reduce metallization-related voltage losses. Furthermore, the single series resistance contributions for both cell concepts are calculated based on experimental data. With this and further studies, MWT-specific issues are discussed.

#### 7.4.1 Cell fabrication and basic process characterization

The H-pattern and *n*MWT+ solar cells are fabricated using pseudo-square *n*-type Cz-Si wafers with an edge length of 156 mm, a diameter of 200 mm, an initial thickness of  $W = 205 \mu\text{m}$ , and a specific bulk resistance of  $\rho_{\text{bulk}} \approx 1.5 \Omega\text{cm}$ . The final H-pattern cells feature three external busbar contacts on either side; see Fig. 3.7(b). A four-busbar layout is used for the *n*MWT+ cells; see Fig. 3.11(b). For the H-pattern cells, electrically contacting external front busbars are compared against electrically non-contacting (floating) busbars. In case of the *n*MWT+ cells, via-drilling is performed either before application of the passivation layers (including wet-chemical cleaning after laser processing) or after.

The solar cells are fabricated according to the procedure depicted in Fig. 7.9, which is very similar to that in the preceding section. Here, for  $\text{BBr}_3$  diffusion, only process Gen1 is considered, while for  $\text{POCl}_3$  diffusion an optimized process is applied (Phos2). As shown in Chapter 4.5, the boron doping profile

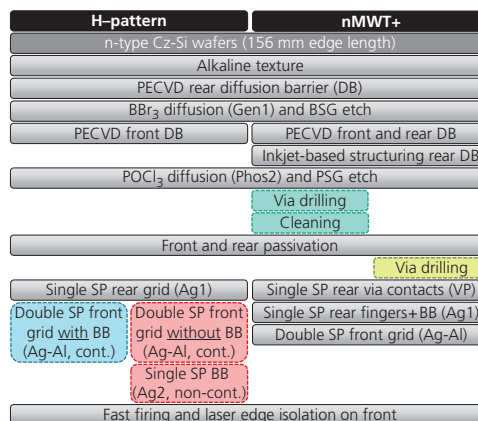


**Fig. 7.9.** Process sequence for fabrication of *n*-type Cz-Si H-pattern and *n*MWT+ solar cells (DB: diffusion barrier, SP: screen printing, VP: via paste, BB: busbar).

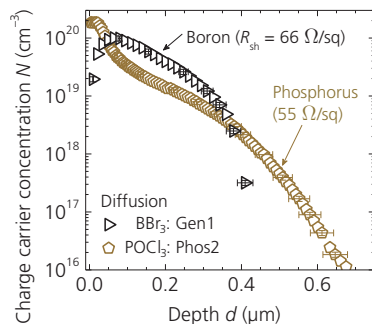


**Fig. 7.10.** Doping profiles, determined by ECV measurements on alkaline saw-damage etched surfaces. Exemplary error bars are shown. The sheet resistances  $R_{\text{sh}}$  are stated.

does not alter significantly during  $\text{POCl}_3$  diffusion Phos2. The resulting front- and rear-side sheet resistances on the both-sides textured wafers after  $\text{BBr}_3$  and  $\text{POCl}_3$  diffusions are  $R_{\text{sh}} = (70 \pm 4) \Omega/\text{sq}$  and  $R_{\text{sh}} = (60 \pm 4) \Omega/\text{sq}$ , respectively. The respective doping profiles, determined by ECV measurements on alkaline saw-damage etched surfaces, are depicted in Fig. 7.10. The boron-doped emitter Gen1 has a maximum dopant concentration  $N_{\text{max}} = (1.0 \pm 0.1) \cdot 10^{20} \text{ cm}^{-3}$  and a profile depth<sup>34</sup>  $d = (480 \pm 48) \text{ nm}$ . For the phosphorus-doped BSF Phos2, the values are given by  $N_{\text{max}} = (1.9 \pm 0.2) \cdot 10^{20} \text{ cm}^{-3}$  and  $d = (750 \pm 75) \text{ nm}$ .

Laser-drilling the vias of the  $n\text{MWT+}$  cells is performed either (i) before passivation followed by wet-chemical SC1-SC2 cleaning, or (ii) after passivation without any post treatment. The front passivation and anti-reflective coating consists of ALD  $\text{Al}_2\text{O}_3$  and PECVD  $\text{SiN}_x$  layers. The rear side is passivated by PECVD  $\text{SiN}_x$ .

The rear side grid for the H-pattern cells with finger and busbar contacts is applied by screen printing a fire-through and electrically contacting silver paste (paste Ag1). The front grid is applied with a variation in busbar metallization. For the first group, both the finger and the busbar contacts are double-printed with a fire-through and electrically contacting Ag-Al paste (paste Ag-Al1 from Chapter 5). For the second group, only the finger contacts are double-printed with the Ag-Al paste, followed by single-printing the busbar contacts with a non-fire-through and electrically non-contacting silver paste (paste Ag2). The rear side metallization of the  $n\text{MWT+}$  cells is formed by applying a two-step screen printing process. First, the vias and the external  $p$ -type contact pads are metallized with a non-fire-through and electrically non-contacting silver via paste (via paste V2 from Chapter 6). Second, the finger and the external  $n$ -type contacts are screen printed with the contacting silver paste Ag1. The front grid with fingers and thin pseudo-busbars is double-printed with the contacting Ag-Al paste.

Finally, contact formation takes place in a fast firing furnace with the same process conditions for all solar cells, followed by laser edge isolation on the front side. The number of fingers and the finger widths  $w_f$  are equal for both cell types on the respective side. The finger widths are measured after firing with a light microscope on 15 solar cells at six different positions per

<sup>34</sup>In this section, the profile depth  $d$  is estimated at a dopant concentration  $N = 3.3 \cdot 10^{15} \text{ cm}^{-3}$ , which corresponds to the bulk doping concentration of the wafers used for cell fabrication.

## 7.4 Decrease of metallization-losses and discussion of MWT-specific issues

**Table 7.2.** Percentage of metallized area for the different structures. The values are calculated based on measured structure sizes after firing. The given errors are estimated with respect to the standard deviation of the finger widths. For the H-pattern cells, either the front metal structures A or B are applied.

Cell type	Side	Metal structures	Paste type	Met. area $F_M$ (%)
H-pattern	Front-A	Fingers and busbars	Ag-Al	$5.8 \pm 0.7$
	Front-B	Fingers only	Ag-Al	$3.4 \pm 0.4$
	Front-B	Busbars only	Ag2	$2.4 \pm 0.1$
	Rear	Fingers and busbars	Ag1	$7.2 \pm 0.6$
<i>n</i> MWT+	Front	Fingers and pseudo-busbars	Ag-Al	$3.5 \pm 0.4$
	Rear	Fingers and busbars	Ag1	$6.1 \pm 0.6$
	Rear	<i>p</i> -type contact pads	Via paste	$0.49 \pm 0.02$

cell and side. The average finger widths on the front and rear sides are  $w_f = (58 \pm 7) \mu\text{m}$  and  $w_f = (76 \pm 11) \mu\text{m}$ , respectively. Table 7.2 summarizes the percentages of metallized areas, which are calculated based on measured structure sizes. These metallization fractions for the front and rear sides of the H-pattern and the *n*MWT+ solar cells will be useful for the discussion in the following sections.

Symmetric  $j_0$  samples fabricated in parallel to the solar cells—using the same corresponding processes—allow for the determination of dark saturation current densities  $j_0$  of the highly doped and alkaline textured surfaces after firing by quasi-steady state photoconductance (QSSPC) measurements; see also the Chapters 2.2.2 and 4.3.4. In case of the boron emitter, Fig. 4.3(c) shows the schematic cross section of the symmetric  $j_{0e}$  sample. The symmetric  $j_{0BSF}$  sample for the phosphorus BSF features both-sided phosphorus doping, whereby a PECVD SiN<sub>x</sub> layer ensures surface passivation on either side. The  $j_0$  for the boron emitter and the phosphorus BSF are found to be  $j_{0e} = (77 \pm 5) \text{ fA/cm}^2$  and  $j_{0BSF} = (116 \pm 12) \text{ fA/cm}^2$ , respectively.

Two samples per group are measured by QSSPC prior to metallization to determine the  $V_{OC}$  potential of the passivated (non-metallized) cell precursors, whose schematic cross sections are shown in Fig. 7.11. Prior to the QSSPC measurements, the surface passivation has been activated in a firing process. As introduced in Chapter 2.2.3, the extracted implied open-circuit voltages  $iV_{OC}$  represent an upper limit for the cells'  $V_{OC}$  after application of metal contacts. Hence, the difference between  $iV_{OC}$  and  $V_{OC}$  of the final cells allows for determining the voltage losses, which are caused by the metallization.

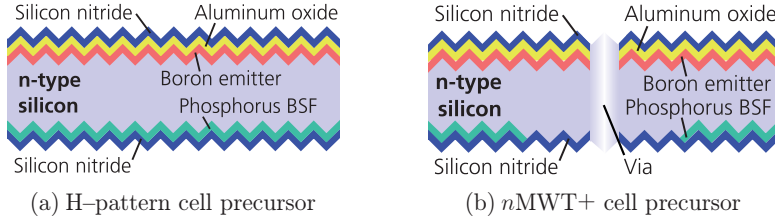


**Fig. 7.11.** Schematic cross sections of an (a) H-pattern and (b) nMWT+ cell precursor prior to metallization (not to scale), also designated as  $iV_{OC}$  samples in the following. Note that the via in (b) is indicated in simplified manner.

**Table 7.3.** Dimensions of the external  $p$ -type contact structure for nMWT+ solar cells with four busbars per polarity on pseudo-square silicon wafers with 156 mm edge length and a thickness of  $W = 190 \mu\text{m}$ . The values are given for a metallization geometry with 24 round  $p$ -type contacts with a BSF gap diameter of 3.3 mm, a pad diameter of 2.5 mm, and two via contacts per contact pad. The via diameters are 70  $\mu\text{m}$  and 140  $\mu\text{m}$  on front and rear side, respectively.

Total wafer surface $A_{\text{wafer}}$ (mm $^2$ )	Area BSF gaps $A_{\text{gaps}}$ (mm $^2$ )	Area $p$ -type contact pads $A_{\text{pads}}$ (mm $^2$ )	Area inside the vias $A_{\text{vias}}$ (mm $^2$ )	$\frac{A_{\text{gaps}}}{A_{\text{wafer}}}$ (%)	$\frac{A_{\text{pads}}}{A_{\text{wafer}}}$ (%)	$\frac{A_{\text{vias}}}{A_{\text{wafer}}}$ (%)
23895	205.3	117.8	3.1	0.9	0.5	0.01

Note that the schematic cross section of the nMWT+  $iV_{OC}$  sample in Fig. 7.11(b) is not drawn to scale. To give an impression on the real proportions, the areas of the structures of interest are given in Table 7.3, both with their absolute values and relative to the total wafer surface. The gap area in the rear phosphorus BSF is actually only 0.9% from the total wafer area. Furthermore, the proportion of the surface within the vias relative to the total wafer surface is very small with only 0.01%.

#### 7.4.2 Current-voltage characteristics

The determined  $I$ - $V$  characteristics of the fabricated solar cells are summarized in Table 7.4. Apart from mean values, also the data for the most efficient cells of each variation are stated. The given values correspond to measurements performed on black-foil-coated (non-reflective) measurement chucks. The conversion efficiencies  $\eta$  for the most efficient H-pattern and nMWT+ cells are 19.4% and 19.5%, respectively. These two cells are also measured with reflective measurement chucks at the *CalLab*, resulting in a gain in short-circuit current density  $j_{SC}$  of about 1%<sub>rel</sub> for both cell types. Con-

sequently,  $\eta$  increases by 0.2%<sub>abs</sub> to 19.6% for the H-pattern and to 19.7% for the nMWT+ cell. In the following discussion, only the  $I$ - $V$  data from Table 7.4 is considered, which correspond to results obtained on black foil.

### H-pattern solar cells

When comparing the two groups of H-pattern solar cells, it is seen that the reduced Ag-Al metallization fraction on the front side by application of electrically non-contacting (floating) busbars is advantageous. The cells with floating Ag2 busbars (about 3.4% of the front area is metallized with contacting Ag-Al paste; Table 7.2) reach a mean conversion efficiency  $\eta = (19.2 \pm 0.2)\%$  in comparison with  $\eta = (19.0 \pm 0.1)\%$  for the cells with contacting Ag-Al busbars (about 5.8% metallized front area). For the most efficient cells, this difference is even larger with  $\eta = 19.4\%$  (floating busbars) and  $\eta = 19.1\%$  (contacting busbars). These  $\eta$  differences between the two groups are mainly due to differences in the open-circuit voltage  $V_{OC}$ . For instance, the most efficient cell with floating Ag2 busbars has a  $V_{OC} = 646$  mV, which is 7 mV higher than that of the best cell with contacting Ag-Al bus-

**Table 7.4.**  $I$ - $V$  data for  $n$ -type Cz-Si H-pattern and nMWT+ solar cells (cell area: 239 cm<sup>2</sup>). All cells are tested after laser edge isolation with an industrial cell tester without reverse bias load. The two cells marked with # are also measured at *Fraunhofer ISE CalLab PV cells* on black-foil-coated measurement chucks. The data for the other cells is corrected with respect to the *CalLab* measurements, i.e. all data correspond to measurements on black foil. Indicated are mean values, standard deviation, group size in brackets, and data of the *best cell* per group.

Cell type	Front busbars	Via drilling	$\eta$ (%)	$V_{OC}$ (mV)	$j_{SC}$ (mA/cm <sup>2</sup> )	FF (%)	pFF (%)	$R_P$ (k $\Omega$ cm <sup>2</sup> )	$R_S$ ( $\Omega$ cm <sup>2</sup> )
H-pattern	Contacting (Ag-Al)	–	Mean (5)	19.0 $\pm$ 0.1	638 $\pm$ 2	38.8 $\pm$ 0.1	76.6 $\pm$ 0.2	80.2 $\pm$ 0.5	3.4 $\pm$ 1.4
			<i>Best cell</i>	19.1	639	38.9	76.9	80.6	3.5
	Floating (Ag2)	–	Mean (5)	19.2 $\pm$ 0.2	644 $\pm$ 2	38.8 $\pm$ 0.1	76.5 $\pm$ 0.5	81.0 $\pm$ 0.4	5.8 $\pm$ 3.3
			<i>Best cell</i>	19.4#	646	39.0	77.1	81.4	9.8
nMWT+	–	Before pass.	Mean (7)	19.4 $\pm$ 0.1	648 $\pm$ 1	39.4 $\pm$ 0.1	75.4 $\pm$ 0.3	80.2 $\pm$ 0.5	3.0 $\pm$ 1.4
			<i>Best cell</i>	19.5#	650	39.6	75.7	80.4	3.8
	–	After pass.	Mean (7)	19.3 $\pm$ 0.1	646 $\pm$ 1	39.3 $\pm$ 0.1	75.5 $\pm$ 0.3	80.3 $\pm$ 0.3	3.2 $\pm$ 0.9
			<i>Best cell</i>	19.4	648	39.4	75.7	80.3	2.9

bars. The short-circuit current densities  $j_{SC}$  are almost identical, as the shaded area amounts to  $F_M \approx 5.8\%$  for both cell groups. The fill factors  $FF$  are also nearly identical with values close to 77%, as the differences in series resistance  $R_S$  and pseudo fill factor  $pFF$  compensate for each other. The slightly higher  $R_S$  for the cells with floating busbars originate particularly from both higher line resistance and lower height of the busbar contacts. Furthermore, the  $FF$  values are also limited by  $pFF$  values below 81.5%, whereby the H-pattern cells with floating busbars show a higher  $pFF$  by about 0.8%<sub>abs</sub>. This difference in  $pFF$  cannot be explained solely by the different shunt resistances  $R_P$  for these two groups. Considering the best cell of each group for an estimate on the basis of the two-diode model, the increase of  $R_P$  towards infinity starting from  $R_P = 3.5 \text{ k}\Omega\text{cm}^2$  or  $R_P = 9.8 \text{ k}\Omega\text{cm}^2$  only leads to a gain in  $pFF \lesssim 0.4\%$ <sub>abs</sub> in both cases. This means that  $R_P$  is not the dominating loss term for  $pFF$ . Hence, other non-ideal recombination channels—summarized in the dark saturation current density  $j_{02}$  of the second diode in the two-diode model—limit the  $pFF$  particularly for the H-pattern cells with contacting busbars. A hasty conclusion might be to fully ascribe the causes for the  $pFF$  difference to the higher metallization fraction with Ag-Al contacts of the H-pattern cells with contacting busbars. As also the  $pFF$  for the nMWT+ solar cells—which have similar Ag-Al metallization fraction as the H-pattern cells with floating busbars ( $F_M \approx 3.5\%$ )—show comparable low  $pFF$  in the range of 80.5%, the real causes for the observed  $pFF$  difference between H-pattern cells with floating and contacting busbars could not be identified. As will be shown in section 7.5, this difference in  $pFF$  between H-pattern cells with floating busbars and nMWT+ cells is no longer observed.

### nMWT+ solar cells

For the nMWT+ solar cells, laser-drilling the vias has been performed either before or after passivation. For the cells with via drilling before passivation, a wet-chemical SC1-SC2 cleaning followed the laser process. By comparing the  $I-V$  data of the two cell groups, only a minor difference is observed for both mean and best values, resulting in almost the same maximum  $\eta$  of 19.4% and 19.5%. The small differences in  $j_{SC}$  and  $V_{OC}$ —which are actually not significant comparing the mean values of both groups—might originate from marginally changed doping profiles due to the wet-chemical cleaning for the MWT cells with via drilling before passivation. Furthermore, the values for  $FF$ ,  $pFF$ ,  $R_P$ , and  $R_S$  are also nearly identical.

Hence, the process sequence with via drilling directly before metallization is found to show no serious drawbacks and thus, it is a very promising approach to fabricate  $n$ MWT+ solar cells with respect to both process simplicity and industrial implementation.

The  $n$ MWT+ cells benefit from a clearly higher  $j_{SC}$  (up to  $+0.6$  mA/cm $^2$  on average) due to less front side shading compared with the H-pattern cells. Furthermore, the  $V_{OC}$  for the  $n$ MWT+ cells is also slightly higher than that for the H-pattern cells with floating busbars. Since the front side metallization fraction for the contacting Ag-Al paste is similar for the  $n$ MWT+ and the H-pattern cells with floating busbars, the slightly higher  $V_{OC}$  for the  $n$ MWT+ cells might originate from their lower metallization fraction on the rear side (contacting paste Ag1:  $F_M \approx 6.1\%$  for  $n$ MWT+ cells,  $F_M \approx 7.2\%$  for H-pattern cells). But also statistical variations in  $iV_{OC}$  of the cell precursors prior to metallization might explain, at least partly, the present  $V_{OC}$  difference; see section 7.4.3. It is particularly noteworthy that no significant negative effect of the via metallization is observed on  $V_{OC}$  for the  $n$ MWT+ cells. The lower  $FF$  of about  $1\%_{abs}$  in comparison with the H-pattern cells originates mainly from the thinner (pseudo-) busbar contacts on the front and rear side in conjunction with the lower number of contact points during  $I$ - $V$  testing; more details on this, see section 7.4.4. As already mentioned, the values for  $pFF$  and  $R_p$  are similar to those of the H-pattern cells with contacting Ag-Al busbars. Hence, the increase in  $pFF$  and  $R_p$  is a general challenge for both the  $n$ MWT+ and the H-pattern solar cells.

#### 7.4.3 Implied open-circuit voltages and metallization-related voltage losses

For two samples per group, implied open-circuit voltages  $iV_{OC}$  are determined by QSSPC prior to metallization at the five marked points in Fig. 4.8 per wafer. Fig. 7.12 shows the  $iV_{OC}$  of these samples and the  $V_{OC}$  of the finished solar cells. By calculating the difference, the loss in open-circuit voltage  $\Delta V_{OC} = V_{OC} - iV_{OC}$ , caused by the front and rear side metallization, can be quantified. These losses are also specified in Fig. 7.12. The upper limit for the implied open-circuit voltage  $iV_{OC,limit} = (666 \pm 2)$  mV is calculated according to Eq. (2.20) and the procedure described in Chapter 2.2.1.<sup>35</sup>

---

<sup>35</sup>Used parameters:  $j_{0e}$  and  $j_{0BSF}$  from section 7.4.1, wafer thickness  $W = 190$   $\mu\text{m}$ , bulk lifetime  $\tau_{bulk} = 1.5$  ms, injection density  $\Delta p = 2.1 \cdot 10^{15}$  cm $^{-3}$  (corresponding approximately to the injection level of the  $iV_{OC}$  samples at 1 sun),  $j_{ph} = 39$  mA/cm $^2$ , and  $T = 25^\circ\text{C}$ .

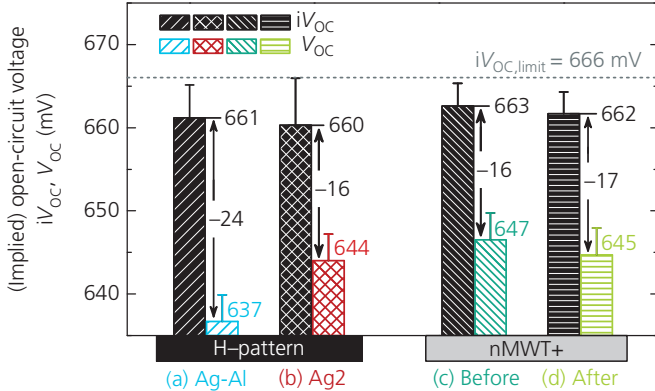


**Fig. 7.12.** Mean (implied) open-circuit voltage  $iV_{OC}$ ,  $V_{OC}$  of two cells per group, and respective losses in open-circuit voltage  $\Delta V_{OC} = V_{OC} - iV_{OC}$  caused by front and rear side metallization. Pastes for busbar metallization of the H-pattern cells: (a) contacting Ag-Al, (b) non-contacting (floating) Ag2. For the nMWT+ solar cells, laser-drilling the vias is performed either (c) before or (d) after passivation. The  $iV_{OC,\text{limit}}$  is calculated based on the measured  $j_{0e}$  and  $j_{0\text{BSF}}$  and the parameters given in the text. The error bars for  $iV_{OC}$  represent the standard deviation, whereas for  $V_{OC}$  they indicate the measurement uncertainty (assumed to be 0.5% relative).

The measured  $iV_{OC}$  range from  $iV_{OC} = (660 \pm 6)$  mV to  $(663 \pm 3)$  mV and are thus close to the value for  $iV_{OC,\text{limit}} = (666 \pm 2)$  mV. In section 7.4.2, it has been discussed that the slightly higher  $V_{OC}$  of the nMWT+ solar cells might partly originate from statistical variations in  $iV_{OC}$ . In consideration of the  $iV_{OC}$  given in Fig. 7.12, this seems to be quite possible.

The H-pattern cells with contacting Ag-Al busbars show the highest voltage loss with  $\Delta V_{OC} = -(24 \pm 5)$  mV. In case of the H-pattern cells with floating Ag2 busbars, the voltage loss is only  $\Delta V_{OC} = -(16 \pm 6)$  mV, and therefore 8 mV less. The losses of the nMWT+ cells with  $\Delta V_{OC} = -(16 \pm 4)$  mV and  $\Delta V_{OC} = -(17 \pm 4)$  mV are as high as those of the H-pattern cells with floating Ag2 busbars. These results show that the reduction of the Ag-Al metallized area fraction on the cell's front side leads to a significant decrease in  $\Delta V_{OC}$ .

### Microstructure analysis of formerly metallized areas

Fig. 7.13 shows scanning electron microscope (SEM) images taken on the fabricated solar cells after wet-chemically etching<sup>36</sup> of the different metal con-

<sup>36</sup>The etching procedure is the one which has been used in Chapter 5.3.3.

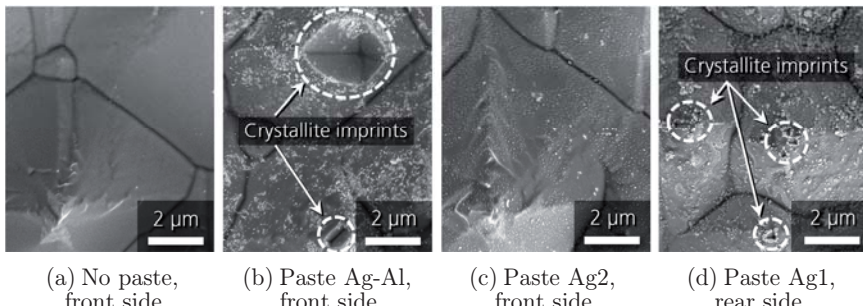


**Fig. 7.13.** SEM images of alkaline textured silicon surfaces after removal of metal contacts, passivation, and glass layer. (a) No metal paste was present in this area. (b) Two crystallite imprints (a very large and a smaller one) are apparent for the Ag-Al contact. (c) No crystallite imprints are observed for the electrically non-contacting Ag2 paste. (d) Small imprints are visible for the contacting paste Ag1.

tacts (Ag-Al, Ag1, and Ag2), the passivation layers, and the glass layers. The image in Fig. 7.13(a), taken in an area not metallized before, shows the random pyramids of the alkaline textured surface and serves as reference. As expected from the studies in Chapter 5.3.3, large crystallite imprints are found for the Ag-Al contact in Fig. 7.13(b). In contrast, no crystallite imprints are found for the electrically non-contacting busbar paste Ag2 in Fig. 7.13(c), whereby the image is very similar to the image without prior metallization. For the electrically-contacting paste Ag1 on the phosphorus-doped rear side, many small crystallite imprints are visible in Fig. 7.13(d), which are significantly smaller than the imprints observed for the Ag-Al contact on the boron emitter.

The observation for the Ag-Al contact is in line with the results from Chapter 5.3.3, where also large and deeply penetrating metal crystallites are detected underneath the Ag-Al contacts on boron-doped surfaces. These deep metal crystallites are most likely the cause for dark saturation current densities  $j_{0,\text{met}}$  in the range of several  $1000 \text{ fA/cm}^2$  for Ag-Al contacts, as shown by the simulations of charge carrier recombination at the metal-silicon interface in Chapter 5.6. This  $j_{0,\text{met}}$ -range is in agreement with experimental data published by other authors [215,216,242]. In contrast,  $j_{0,\text{met}}$  values reported for phosphorus-doped surfaces and silver metallization are only about  $1000 \text{ fA/cm}^2$  [264]. The observation of only small imprints for paste Ag1 also suggests that  $j_{0,\text{met}}$  is significantly lower for these contacts than that of the front Ag-Al contacts. The SEM images further confirm

the electrically non-contacting property of paste Ag2 on microscopic level with respect to both current transport by and recombination at metal crystallites. Considering also the higher  $V_{OC}$  obtained for the H-pattern cells with non-contacting busbars,  $j_{0,met}$  below the Ag2 contacts on the boron emitter side is significantly lower than that for the Ag-Al contacts.

#### 7.4.4 Series resistance contributions and MWT-specific losses

As shown in Table 7.4, the  $n$ MWT+ solar cells feature a higher total series resistance  $R_S$  compared with the  $n$ -type H-pattern reference cells ( $R_S$  is higher by about  $0.2 \Omega\text{cm}^2$ ). Using the analytical simulation tool *Gridmaster* [265], the total  $R_S$  and individual  $R_S$  contributions are calculated for both the H-pattern cells with contacting front busbars and the  $n$ MWT+ cells. The employed input parameters, which base on experimentally determined values, are summarized in Table D.1 in Appendix D. Table 7.5(a) and (b) show the calculated  $R_S$  contributions; columns (c) and (d) give the respective differ-

**Table 7.5.** Calculated series resistance  $R_S$  contributions for (a)  $n$ -type H-pattern cells with contacting front busbars and (b)  $n$ MWT+ cells. The values are calculated with the analytical simulation tool *Gridmaster* using the input parameters summarized in Table D.1 in Appendix D. Column (c) shows the differences  $\Delta R_S$  for each  $R_S$  contribution with respect to the  $n$ MWT+ cell, whereas column (d) states the respective impact on fill factor  $\Delta FF \approx -5.5\% \cdot (\Delta R_S / \Omega\text{cm}^2)$ . Positive  $\Delta R_S$  correspond to higher  $R_S$  (lower  $FF$ ) for the  $n$ MWT+ device and vice versa.

	Cell type, $R_S$ contributions		Differences	
	(a) H-pattern	(b) $n$ MWT+	(c) $\Delta R_S =$	(d) $\Delta FF$
	$R_{S,H\text{-pattern}}$ ( $\Omega\text{cm}^2$ )	$R_{S,n\text{MWT}+}$ ( $\Omega\text{cm}^2$ )	$R_{S,n\text{MWT}+} - R_{S,H\text{-pattern}}$ ( $\Omega\text{cm}^2$ )	(%) <sub>abs</sub>
<i>Front side</i>	Emitter	0.200	0.195	-0.005
	Fingers	0.088	0.051	-0.037
	(Pseudo-) Busbars	0.011	0.151	+0.140
	Contact	0.150	0.150	0
	Vias	-	0.020	+0.020
<i>Rear side</i>	BSF	0.138	0.136	-0.002
	Fingers	0.073	0.042	-0.031
	Busbars	0.012	0.129	+0.117
	Contact	0.072	0.072	0
<i>Bulk</i>	Vertical	0.029	0.029	0
	Lateral	-	0.004	+0.004
$\sim$ Total		0.773	0.979	+0.206
				-1.13

ences in  $R_S$  ( $\Delta R_S$ ) and fill factor  $FF$  ( $\Delta FF$ ) between the  $n$ MWT+ and the H-pattern cells. The calculated total  $R_S \approx 0.77 \Omega\text{cm}^2$  (H-pattern) and  $R_S \approx 0.98 \Omega\text{cm}^2$  ( $n$ MWT+) are in accordance with the values given in Table 7.4, indicating a quite accurate description of the  $R_S$  contributions for both cell structures. The increased total  $R_S$  for the  $n$ MWT+ cell with  $\Delta R_S \approx 0.2 \Omega\text{cm}^2$  causes a  $FF$  loss of  $\Delta FF \approx -1.1\%_{\text{abs}}$  in comparison with the H-pattern cell.

The benefit from the higher busbar number of the  $n$ MWT+ cell is particularly given by lower  $R_S$  contributions from the finger contacts on both sides:  $\Delta R_S = -0.068 \Omega\text{cm}^2$  ( $\Delta FF = +0.37\%_{\text{abs}}$ ). However, these gains are over-compensated by increased  $R_S$  contributions especially from the front and rear side (pseudo-) busbar contacts because of their smaller widths and a smaller number of external contact points per polarity:  $\Delta R_S = +0.257 \Omega\text{cm}^2$  ( $\Delta FF = -1.41\%_{\text{abs}}$ ). The front pseudo-busbars are linearly tapered starting from the via contacts with a width between 0.2 mm and 0.1 mm, whereas the rear busbar contacts have been applied with a continuous width of 0.5 mm (equivalent to one third of the H-pattern busbar width). The number of contact points per busbar and polarity is 11 for the H-pattern cell, whereas the  $n$ MWT+ cell features only 6/5 contact points for each *p*-type/*n*-type contact row. The  $R_S$  contribution of  $0.004 \Omega\text{cm}^2$  from the lateral flow of majority charge carriers in the bulk in the area of the rear external *p*-type contacts for the  $n$ MWT+ cells is found to be negligible. An also rather small contribution to the total  $R_S$  of  $0.02 \Omega\text{cm}^2$  results for the via contacts, which corresponds to  $\Delta FF \approx -0.1\%_{\text{abs}}$ . The via resistances are measured on complete  $n$ MWT+ solar cells [266], and the mean resistance of a single via contact is found to be about  $4 \text{ m}\Omega$  for both the vias whether drilled before or after passivation.

For both cell types, the contact resistances between the metal contacts and the highly doped surface layers contribute in sum  $0.222 \Omega\text{cm}^2$  to the total  $R_S$ . The measured specific contact resistances are  $\rho_C = (4.5 \pm 0.7) \text{ m}\Omega\text{cm}^2$  for the Ag-Al contact on the boron emitter, and  $\rho_C = (3.0 \pm 1.0) \text{ m}\Omega\text{cm}^2$  for the silver contact on the phosphorus BSF. For screen-printed and fired metallization, both  $\rho_C$  are already on a quite low level.

In summary, the  $R_S$  related lower  $FF$  of about  $1\%_{\text{abs}}$  for the  $n$ MWT+ cells in comparison with the H-pattern reference cells originates mainly from the metallization layout on the rear side with a rather low number of external contact pads per contact row. One option to reduce this  $FF$  difference is the increase of the number of external contact pads, as will be shown in section 7.7.

**Influence of the vias on the (implied) open-circuit voltage for nMWT+ cells**

Considering the obtained results so far from the  $iV_{OC}$  samples as well as from the fabricated solar cells, there is no evidence for significant via recombination for the  $n$ MWT+ cell precursors and final solar cells. However, this section aims at clarifying whether or not the vias have a fundamental contribution to recombination.

To determine the impact of the vias on recombination within the silicon bulk—and hence on  $V_{OC}$  as well as on  $iV_{OC}$ —the effective minority charge carrier lifetime  $\tau_{\text{eff}}$  is considered, which includes recombination within the silicon bulk and recombination due to the vias themselves. These recombination channels can be expressed by their inverse lifetimes

$$\frac{1}{\tau_{\text{eff}}} = \frac{1}{\tau_{\text{bulk}}} + \frac{1}{\tau_{\text{via}}}, \quad (7.1)$$

where  $\tau_{\text{bulk}}$  describes the minority charge carrier lifetime in the silicon bulk including the surfaces without vias, and  $\tau_{\text{via}}$  the minority charge carrier lifetime limited due to via recombination.

Assuming maximum recombination of the vias, i.e. maximum effective surface recombination velocity  $S_{\text{via}}$  at the vias ( $S_{\text{via}} \rightarrow \infty$ ),  $\tau_{\text{via}}$  for regularly arranged vias can be approximated by [267]

$$\tau_{\text{via}} \approx \frac{1}{2\pi D_p n_{\text{via}}} [-\ln(r_{\text{via}}\sqrt{n_{\text{via}}}) - 1.17]. \quad (7.2)$$

Using minority charge carrier diffusion coefficient  $D_p = 11.8 \text{ cm}^2/\text{s}$  ( $n$ -type silicon with specific bulk resistance of  $1.5 \Omega\text{cm}$ ), via density  $n_{\text{via}} = 0.2 \text{ cm}^{-2}$ , and via radius  $r_{\text{via}} = 70 \mu\text{m}$ , Eq. (7.2) yields  $\tau_{\text{via}} = 308 \text{ ms}$ .

Since the via arrangement is not uniform over the cell area for the investigated  $n$ MWT+ cells, this calculation has to be considered as a rough estimation. Nevertheless, as  $\tau_{\text{via}}$  is more than an order of magnitude larger than  $\tau_{\text{bulk}}$  (usually in the range of a few milliseconds), the recombination at the via surfaces can be neglected even for  $S_{\text{via}} \rightarrow \infty$ . Hence, via recombination is not significant for the fabricated  $n$ MWT+ solar cells and thus, has no impact on the achievable  $V_{OC}$  or  $iV_{OC}$ .

### Influence of regions without phosphorus BSF on (implied) open-circuit voltage for nMWT+ cells

The characteristic feature of the *n*MWT+ solar cells is the gap within the rear phosphorus BSF in the area of the external *p*-type contact pads, see Fig. 7.14(a). In the region without BSF, the PECVD SiN<sub>x</sub> layer directly passivates the exposed silicon bulk surface. The surface recombination velocity  $S_{\text{gap}}$  of this gap region is extracted from symmetrical *n*-type Cz-Si lifetime samples with alkaline textured surfaces and PECVD SiN<sub>x</sub> as passivation layer. The effective lifetime  $\tau_{\text{eff}}$  after firing measured by QSSPC on six samples with four measurements each is given by  $\tau_{\text{eff}} = (300 \pm 98) \mu\text{s}$ <sup>37</sup>. By using Eqs. (2.15) and (2.17)<sup>38</sup>,  $\tau_{\text{eff}}$  can be converted into  $S_{\text{gap}}$  yielding  $S_{\text{gap}} = (26 \pm 10) \text{ cm/s}$ , which implies high quality surface passivation considering respective literature values for textured surfaces [119]. The measured  $j_{0\text{BSF}}$  for the highly phosphorus-doped area can be also expressed in terms of a surface recombination velocity  $S_{\text{BSF}}$  by using Eq. (2.13), what results in  $S_{\text{BSF}} = (51 \pm 5) \text{ cm/s}$ . Hence, the passivated gap region features lower recombination as the passivated BSF region. However, since all gap regions together only have an area fraction of  $a_{\text{gaps}} = 0.9\%$  of the total rear side surface (prior to metallization), their lower recombination has no significant impact on the effective rear side recombination.

In order to estimate an upper limit for the voltage loss caused by the external *p*-type contact pads applied within the BSF gaps, the effective dark saturation current density  $j_{0\text{b,eff}}$  of the base is used. For calculation of  $j_{0\text{b,eff}}$ , the pad coverage fraction  $a_{\text{pads}}$  and the surface recombination velocity underneath the pads  $S_{\text{pad}}$  (linked to the dark saturation current density  $j_{0\text{pad}}$  by means of Eq. (2.13)) are varied. Thereby, the difference between BSF gap radius and pad radius is kept constant with 0.4 mm. For the passivated BSF area, no metallization is considered. The area weighted summation of the three contributions to  $j_{0\text{b,eff}}$  is performed as follows:

$$j_{0\text{b,eff}} = j_{0\text{b,pad}} a_{\text{pads}} + j_{0\text{b,gap}} (a_{\text{gaps}} - a_{\text{pads}}) + j_{0\text{b,BSF}} (1 - a_{\text{gaps}}). \quad (7.3)$$

Therein, the single  $j_{0\text{b}}$ -parameters are calculated from the respective surface recombination velocities  $S$  according to Eqs. (2.5) and (2.6).  $S_{\text{pad}}$  is varied up to 600 cm/s, which corresponds to  $j_{0\text{pad}} = 1370 \text{ fA/cm}^2$ . This value is in the range of a contacting silver paste as discussed in section 7.4.3.

<sup>37</sup> $\tau_{\text{eff}}$  is extracted at the same injection density  $\Delta p = 2.1 \cdot 10^{15} \text{ cm}^{-3}$  as considered for  $iV_{\text{OC,limit}}$ .

<sup>38</sup>Used parameters:  $\tau_{\text{bulk}} = 1.5 \text{ ms}$ ,  $W = 190 \mu\text{m}$ ,  $D_{\text{amb}} = 14 \text{ cm}^2/\text{s}$ .

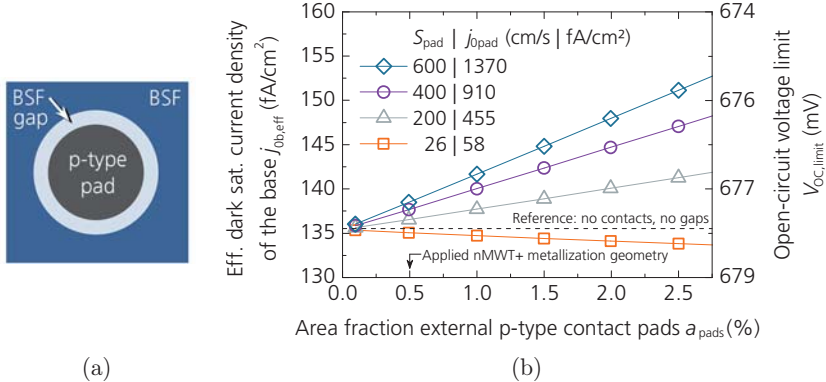


**Fig. 7.14.** (a) Schematic illustration of the *n*MWT+ rear contact layout consisting of the *p*-type contact pad, the BSF gap (not highly doped with phosphorus), and the highly phosphorus-doped BSF. (b) Estimation of the effective dark saturation current density  $j_{0b,eff}$  of the base for the *n*MWT+ solar cells according to Eq. (7.3). Varied is the area fraction of the pads  $a_{pads}$  and their recombination properties  $S_{pad}$  or  $j_{0pad}$ . The difference between BSF gap radius and pad radius is kept constant with 0.4 mm. The  $V_{OC,limit}$  is calculated according to Eq. (2.20) utilizing  $j_{ph} = 39 \text{ mA}/\text{cm}^2$ .

The results are shown in Fig. 7.14(b). In case no pads and no BSF gaps are present ( $a_{pads} = a_{gaps} = 0$ )—representing a full-area phosphorus-doped and passivated BSF— $j_{0b,eff}$  is equal to  $j_{0b,BSF} = 136 \text{ fA}/\text{cm}^2$ . In case the pad metallization induces no additional recombination at all ( $S_{pad} = S_{gap} = 26 \text{ cm/s}$ ),  $j_{0b,eff}$  slightly decreases with increasing  $a_{pads}$ , as the BSF area with higher  $S_{BSF} = 51 \text{ cm/s}$  decreases. However, this scenario is rather unlikely. More realistic scenarios represent the results obtained for higher  $S_{pad}$ , which result in an increase in  $j_{0b,eff}$ . The area fraction of the external *p*-type contact pads for the fabricated *n*MWT+ cells is  $a_{pads} = 0.5\%$ . Even for the highest  $S_{pad}$  considered, the voltage loss caused by the pad contacts with respect to the open-circuit voltage limit  $V_{OC,limit}$  is found to be below 1 mV and is thus not significant. With increasing  $a_{pads}$ , the voltage loss increases slightly, but even for  $a_{pads} = 2.5\%$  and  $S_{pad} = 600 \text{ cm/s}$ , the calculated loss is lower than 3 mV.

In summary this means that neither the BSF gaps nor the pad metallization present in fabricated *n*MWT+ solar cells do significantly increase the total recombination at the rear side of the cells and are thus no limiting factors for  $V_{OC}$ .

### 7.4.5 Section summary

This section addresses three subject matters: (i) the reduction of metallization-induced recombination losses on the cell's front side by decreasing the electrically contacted area, (ii) the comparison of laser-drilling the vias at different points in time within the fabrication process for *n*MWT+ solar cells, and (iii) the determination of MWT-specific loss mechanisms in terms of series resistance and properties of the rear side contact configuration.

Concerning point one, it is shown that the decrease in area fraction contacted with Ag-Al paste on the boron emitter leads to a significant gain in  $V_{OC}$  of up to 8 mV. The loss in  $V_{OC}$ , caused by front and rear side metallization, is found to be -16 mV for the *n*MWT+ cells as well as for the *n*-type H-pattern cells with electrically non-contacting (floating) silver busbars. The use of electrically contacting Ag-Al busbars for the H-pattern cells leads to a significantly higher total  $V_{OC}$  loss of -24 mV. Based upon microstructural investigations it is concluded that the Ag-Al contact on the front side exhibits significantly higher  $j_{0,met}$  as the silver contact on the rear side. This is most likely triggered by deep crystallite formation below the Ag-Al contact bulk during contact firing. This conclusion is supported by the simulation results from Chapter 5.6.

Peak energy conversion efficiencies of  $\eta = 19.5\%$  and  $\eta = 19.7\%$  are measured for the most efficient *n*MWT+ solar cell on chucks covered by black and white foil, respectively. For the measurement on black foil, short-circuit current density  $j_{SC}$ , open-circuit voltage  $V_{OC}$ , and fill factor  $FF$  are 39.6 mA/cm<sup>2</sup>, 650 mV, and 75.7%, respectively. The most efficient H-pattern reference cell achieves  $\eta = 19.4\%$ ,  $j_{SC} = 39.0$  mA/cm<sup>2</sup>,  $V_{OC} = 646$  mV, and  $FF = 77.1\%$  on black foil. Due to less front side shading compared with the H-pattern cells,  $j_{SC}$  for the *n*MWT+ cells is up to 0.6 mA/cm<sup>2</sup> higher. For the *n*MWT+ cells it is further found that the via metallization has a negligible impact on  $V_{OC}$ , regardless of whether the vias are drilled prior to or after passivation. Hence, laser-drilling the vias directly before metallization and hence, without any post treatment, can be used without serious drawbacks.

The lower  $FF$  of somewhat more than 1%<sub>abs</sub>, measured for the *n*MWT+ cells in comparison with the H-pattern cells, originates mainly from the applied metallization layout with a rather low number of external contact pads per contact row. MWT-specific series resistance contributions from

both lateral current flow in the bulk and the via contacts result in a cumulated *FF* loss of about 0.1%<sub>abs</sub> and hence, can be almost neglected for the fabricated *nMWT+* solar cells. Furthermore, the studies concerning recombination properties at the rear external *p*-type contact pads of the *nMWT+* cells reveal that neither the passivated gap areas—where no phosphorus BSF is present—nor the metallized contact pads have a significant impact on total recombination. Hence, the optimization of the metallization layout with respect to a higher number of external contact pads is surely a very promising option to reduce the series resistance of *nMWT+* solar cells.

## 7.5 Solar cells utilizing the latest $\text{BBr}_3$ diffusion processes

This section presents some of the variations carried out in experiment E from Fig. 7.1. Again, the studies are performed utilizing *n*-type H-pattern and *nMWT+* solar cells. The main focus is set on the implementation of the latest  $\text{BBr}_3$  diffusion processes from Chapter 4 to form the boron emitter and to study their performance on the cell level. These  $\text{BBr}_3$  diffusion processes base on process generation Gen3 and allow for significantly lower  $j_{0e}$  at the passivated emitter surfaces. Based on the results concerning electrical contactability and charge carrier recombination at the metal contacts from Chapter 5, these emitters have the potential to boost the conversion efficiency of therewith fabricated solar cells.

As shown in the previous section, a fundamental optimization of the grid layout would be necessary for the *nMWT+* solar cells in order to decrease the series resistance contributions originating mainly from the rather low number of external contact points. As the arrangement of the external contacts has to be matched with the measurement chuck used for *I–V* testing, changes in their number and location require the manufacturing of such a suitable new chuck. At the time of the investigations, however, such an optimized measurement chuck was not available. Hence, the four-busbar layout from the previous section is again utilized for the *nMWT+* cells, with partial changes in the finger number and the rear side busbar width. For the H-pattern reference solar cells, a novel five-busbar layout on front and rear side is applied—instead of the three-busbar layout used previously.

### 7.5.1 Cell fabrication and process characterization

The H-pattern and  $n\text{MWT}^+$  solar cells are fabricated according to the procedure in Fig. 7.15 using pseudo-square  $n$ -type Cz-Si wafers with an edge length of 156 mm, a diameter of 200 mm, an initial thickness of  $W = 200 \mu\text{m}$ , and a specific bulk resistance of  $\rho_{\text{bulk}} \approx 3.5 \Omega\text{cm}$ . For the  $n\text{MWT}^+$  cells, the four  $\text{BBr}_3$  diffusion processes Gen3, Gen3-A, Gen3-B, and Gen3-C are applied. Their naming is changed compared with Chapter 4 for reasons of simplicity, but their assignment is as shown in Table 7.6. These terms have also been used for the four processes in the Chapters 5.5 and 5.6. For the H-pattern cells, only processes Gen3 and Gen3-A are used.

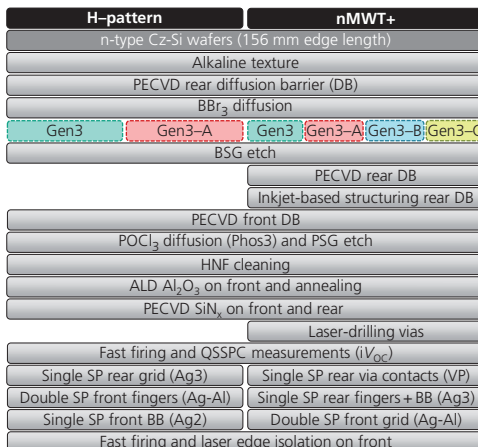


**Fig. 7.15.** Process sequence for fabrication of  $n$ -type Cz-Si H-pattern and  $n\text{MWT}^+$  solar cells (DB: diffusion barrier, SP: screen printing, VP: via paste, BB: busbar).

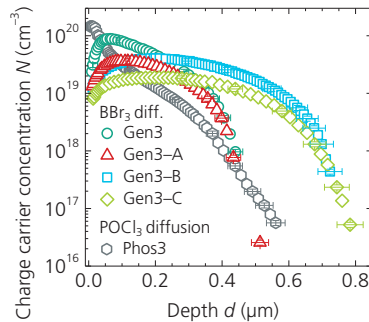


**Fig. 7.16.** Doping profiles, determined by ECV measurements on alkaline saw-damage etched surfaces. Exemplary error bars are shown. Data on the boron profiles on the front side, see Table 7.6. Phosphorus profile Phos3 on the rear side:  $N_{\text{max}} = (1.5 \pm 0.2) \cdot 10^{20} \text{ cm}^{-3}$ ,  $R_{\text{sh}} \approx 62 \Omega/\text{sq}$ .

**Table 7.6.** Summary of characteristic parameters for the different Gen3-based  $\text{BBr}_3$  diffusion processes obtained from alkaline saw-damage etched ECV samples ( $R_{\text{sh}}$ ,  $N_{\text{max}}$ ,  $d$ ), and from alkaline textured  $j_{\text{oe}}$  samples after passivation and firing. The profile depth  $d$  is estimated at a dopant concentration  $N = 1.3 \cdot 10^{15} \text{ cm}^{-3}$ , which corresponds to the bulk doping concentration of the wafers used for cell fabrication.

Designation	$\text{BBr}_3$ diffusion processes	$R_{\text{sh}}$	$N_{\text{max}}$	$d$	$j_{\text{oe}}$
This chapter	Chapter 4	( $\Omega/\text{sq}$ )	( $10^{19} \text{ cm}^{-3}$ )	( $\mu\text{m}$ )	( $\text{fA}/\text{cm}^2$ )
Gen3	Gen3	$\approx 65$	$8.9 \pm 0.9$	$580 \pm 58$	$60 \pm 6$
Gen3-A	Gen3-PO2-LT	$\approx 111$	$3.6 \pm 0.4$	$570 \pm 57$	$38 \pm 3$
Gen3-B	Gen3-DrIn1-PO6	$\approx 62$	$4.1 \pm 0.4$	$820 \pm 82$	$54 \pm 2$
Gen3-C	Gen3-PO5	$\approx 108$	$1.8 \pm 0.2$	$840 \pm 84$	$30 \pm 3$

The doping profiles, measured by the ECV technique on alkaline saw-damage etched surfaces, are illustrated in Fig. 7.16. The associated characteristic parameters like sheet resistance  $R_{\text{sh}}$ , maximum dopant concentration  $N_{\text{max}}$ , and junction depth  $d$  are summarized in Table 7.6. The  $\text{BBr}_3$  diffusion processes are selected such that the resulting doping profiles exhibit pairwise either the same  $N_{\text{max}}$  or the same  $d$ . Doping profile Gen3–A has the same  $d$  but lower  $N_{\text{max}}$  compared with Gen3. The  $N_{\text{max}}$  of profile Gen3–A is almost equal to that of Gen3–B, but the latter has a significant deeper junction. Profile Gen3–C shows a further decreased  $N_{\text{max}}$  while having more or less the same  $d$  as Gen3–B. The resulting  $R_{\text{sh}}$  for the both-sides textured wafers are somewhat higher than those measured on the ECV samples, namely  $R_{\text{sh}} = (70 \pm 2) \Omega/\text{sq}$  (Gen3),  $R_{\text{sh}} = (131 \pm 7) \Omega/\text{sq}$  (Gen3–A),  $R_{\text{sh}} = (68 \pm 2) \Omega/\text{sq}$  (Gen3–B), and  $R_{\text{sh}} = (125 \pm 4) \Omega/\text{sq}$  (Gen3–C). The dark saturation current densities  $j_{0e}$  of the textured and boron-doped surfaces, extracted from parallel processed symmetric  $j_{0e}$  samples after passivation and firing, are also stated in Table 7.6.

In this experiment, the front diffusion barrier layer for the  $n\text{MWT}^+$  cells is applied subsequent to the inkjet-based structuring of the rear diffusion barrier layer. For the formation of the phosphorus-doped BSF, the further optimized  $\text{POCl}_3$  diffusion Phos3 is applied. As shown in Chapter 4.5, the boron doping profile does not get altered significantly during  $\text{POCl}_3$  diffusion Phos3. The resulting phosphorus doping profile is also shown in Fig. 7.16. The corresponding  $R_{\text{sh}}$  measured on the textured wafers is  $(70 \pm 3) \Omega/\text{sq}$ , while  $j_{0\text{BSF}}$  is extracted to be  $(81 \pm 9) \text{fA}/\text{cm}^2$ . All wafers undergo HNF cleaning prior to the deposition of the ALD  $\text{Al}_2\text{O}_3$  passivation layer onto the boron emitters. An annealing step follows directly afterwards in a tube furnace process with a peak zone at  $550^\circ\text{C}$  for 10 min in nitrogen ambient, which is reported to suppress potential blistering of the  $\text{Al}_2\text{O}_3$  layer during contact firing [203]. Laser-drilling the vias for the  $n\text{MWT}^+$  cells is directly performed prior to metallization without any post-treatment. In this experiment, all wafers are additionally fired and measured by QSSPC prior to metallization to obtain the  $iV_{\text{OC}}$  of the so far passivated but not yet metallized cell precursors; see also the samples' cross sections in Fig. 7.11.

The contact grid of the H-pattern cells has five busbar contacts with a width of 0.6 mm each on either side; the contact grid for the  $n\text{MWT}^+$  cells is still based on the one with four busbars. Due to the higher  $R_{\text{sh}}$  of boron emitters Gen3–A and Gen3–C, Table 7.6, a higher finger number is applied onto the front sides of the respective cells (100 fingers instead of 84

**Table 7.7.** Percentage of metallized area for the different structures. The values are calculated based on measured structure sizes after firing. The given errors are estimated with respect to the standard deviation of the finger widths. For the front finger contacts, two different finger numbers are applied depending on the  $R_{\text{sh}}$  of the boron emitter: 84 fingers (Gen3/Gen3-B) || 100 fingers (Gen3-A/Gen3-C).

Cell type	Side	Metal structures	Paste type	Met. area $F_M$ (%)
H-pattern	Front	Fingers only	Ag-Al	$3.7 \pm 0.5 \parallel 4.4 \pm 0.6$
	Front	Busbars only	Ag2	$1.9 \pm 0.1$
	Rear	Fingers and busbars	Ag3	$8.6 \pm 0.6$
$n\text{MWT}^+$	Front	Fingers and pseudo-busbars	Ag-Al	$4.1 \pm 0.5 \parallel 4.8 \pm 0.6$
	Rear	Fingers and busbars	Ag3	$8.7 \pm 0.7$
	Rear	$p$ -type contact pads	Via paste	$0.49 \pm 0.02$

fingers). For all cells of either cell type, also the finger number on the rear side is increased compared with the cells in the previous section (this time 130 fingers instead of 93 fingers). The utilized silver paste to contact the phosphorus BSF is the successor of paste Ag1, referred to as Ag3, the other pastes are the same. Last but not least, the width of the  $n$ -type busbar contacts on the rear side of the  $n\text{MWT}^+$  cells is increased by 30% to 0.65 mm. This is particularly done to ensure the same degree of metallization with paste Ag3 on the rear sides for both cell structures.

The finger widths are measured after firing with a light microscope on three wafers at six different positions per wafer and side. The average finger widths including standard deviation on the front and rear sides are  $w_f = (69 \pm 9) \mu\text{m}$  and  $w_t = (83 \pm 8) \mu\text{m}$ , respectively, and are thus slightly wider than in the previous experiment. The metallized areas are calculated based on measured structure sizes. The resulting percentages of metallized surface area for the front and rear sides of the H-pattern and the  $n\text{MWT}^+$  solar cells, summarized in Table 7.7, will be useful for the discussion in the following sections.

### 7.5.2 Current-voltage characteristics

The determined  $I$ - $V$  characteristics of the fabricated solar cells are illustrated in Fig. 7.17. Shown are the data for measurements on black foil as well as on reflective surface (golden/white foil). The data on the most efficient solar cells for the measurements on reflective surface are also summarized in Table 7.8. Both cell structures exhibit a maximum conversion effi-

**Table 7.8.**  $I\text{-}V$  data for the most efficient  $n$ -type Cz-Si H-pattern and  $n\text{MWT+}$  solar cells (cell area: 239 cm<sup>2</sup>) with the different boron emitters on reflective surfaces (H-pattern: gold-plated,  $n\text{MWT+}$ : white foil). The two cells marked with  $\#$  are measured at *Fraunhofer ISE CalLab PV cells*. For the H-pattern cells, the  $FF$  is taken from the cell tester measurements. For further details on the  $I\text{-}V$  measurements, see the description text in Fig. 7.17 or Appendix B.1 (BB: busbar).

Cell type	Boron emitter	$\eta$ (%)	$V_{OC}$ (mV)	$j_{SC}$ (mA/cm <sup>2</sup> )	$FF$ (%)	$pFF$ (%)	$R_P$ (k $\Omega$ cm <sup>2</sup> )	$R_S$ ( $\Omega$ cm <sup>2</sup> )
H-pattern (5 BB)	Gen3 $\#$	20.0	648	39.3	78.7	81.4	21.7	0.55
	Gen3-A	20.1	650	39.3	78.5	81.2	7.7	0.55
$n\text{MWT+}$ (4 BB)	Gen3	20.0	653	39.9	76.6	81.4	31.2	0.83
	Gen3-A	19.7	651	40.0	75.7	80.7	14.9	0.86
	Gen3-B	20.0	654	39.8	77.0	81.3	17.9	0.76
	Gen3-C $\#$	20.1	656	40.0	76.6	81.4	31.0	0.84

ciency  $\eta = 20.1\%$ . For the measurements on black foil, the respective maximum  $\eta$  are given by 19.9%. Compared to the experiments in the previous section 7.4, this means that  $\eta$  could be increased by about 0.5%<sub>abs</sub>.

Comparing the  $I\text{-}V$  results in Fig. 7.17 for the different surfaces underneath the cells for each cell structure, it is seen that the reflective surfaces particularly lead to higher  $j_{SC}$ . The benefit from a reflective surface underneath the cell in the long wavelength regime is apparent by comparing the internal quantum efficiency (IQE) [155,268] measured for a  $n\text{MWT+}$  solar cell both on black and white foil; see Fig. 7.18(a). The other  $I\text{-}V$  parameters change, if at all, only a little. Hence, in the following discussion, only the  $I\text{-}V$  data belonging to the measurements on reflective surfaces, i.e. golden/white foil, are considered from Fig. 7.17.

It is striking that the mean pseudo fill factor  $pFF$  of 80.2% for the  $n\text{MWT+}$  cells with emitter Gen3-A is lower by about 1%<sub>abs</sub> compared with the other mean  $pFF$  of just below 81.5%, which are basically on the same level for both cell structures and the other emitters. As the H-pattern cells with emitter Gen3-A do not show this strong  $pFF$  drop, the lower  $pFF$  for the  $n\text{MWT+}$  cells can only be partially ascribed to emitter Gen3-A. The lower  $pFF$  originate most probably from process instabilities. The shunt resistances  $R_P$  for these  $n\text{MWT+}$  cells are in a value range (1 k $\Omega$ cm<sup>2</sup>  $\lesssim R_P \lesssim$  15 k $\Omega$ cm<sup>2</sup>), where ohmic leakage currents have an impact on  $pFF$ , particularly for  $R_P < 5$  k $\Omega$ cm<sup>2</sup>. The higher mean  $R_P \approx 25$  k $\Omega$ cm<sup>2</sup> for the  $n\text{MWT+}$  cells with emitters Gen3-B and Gen3-C indicate that the ohmic leakage

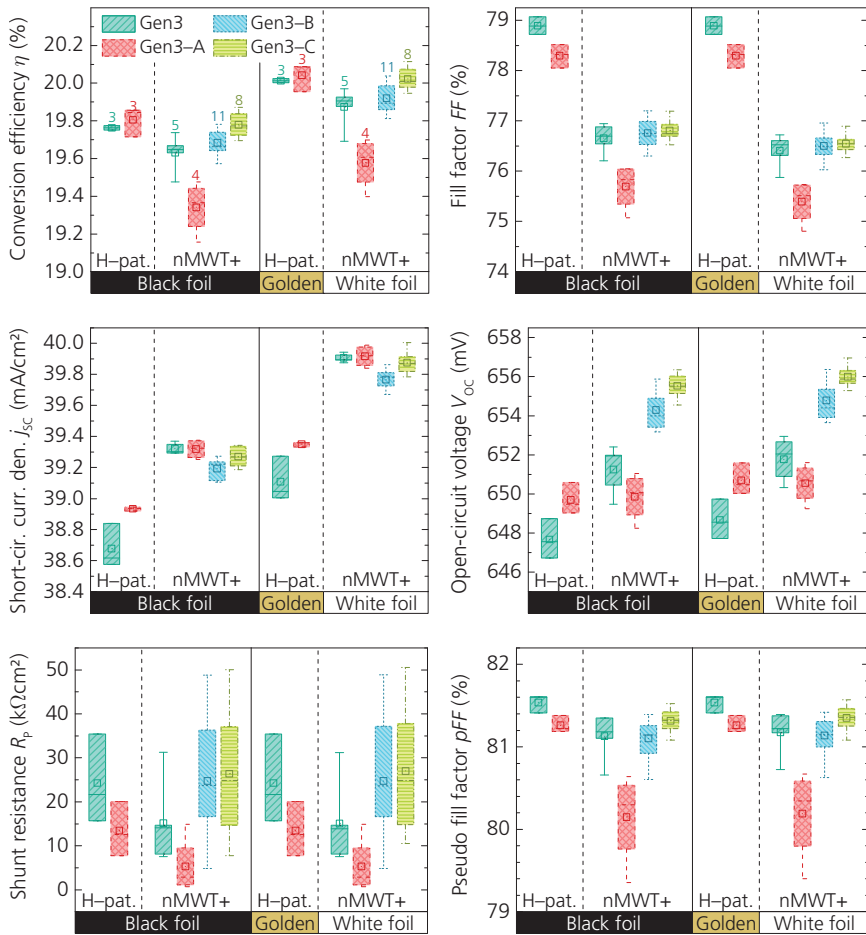


**Fig. 7.17.**  $I-V$  data for the  $n$ -type Cz-Si H-pattern and nMWT+ solar cells (cell area:  $239 \text{ cm}^2$ ) with the different boron emitters on different surfaces (black foil/gold-plated/white foil). All cells are initially tested after laser edge isolation with an industrial cell tester without reverse bias load; see also Appendix B.1. Some of the most efficient cells are then measured at *Fraunhofer ISE CalLab PV cells*. The data for the other cells is corrected with respect to the corresponding *CalLab* measurements. For the H-pattern cells, no black measuring chuck with five busbar contacts was available at the *CalLab*. Hence, their data with respect to black foil are corrected by considering respective correction values from previous investigations. For all H-pattern data, the  $FF$  values are taken from the cell tester measurements.

currents are significantly lower as those for the *n*MWT+ cells with emitter Gen3–A. This also holds when comparing with the *n*MWT+ cells with emitter Gen3 ( $R_p \approx 15 \text{ k}\Omega\text{cm}^2$ ). Hence, the deeper junctions of the emitters Gen3–B and Gen3–C might lead to lower ohmic shunting, but show no significant benefit with respect to *pFF*. The challenges for an increase in *pFF* are basically the same for both the H–pattern and the *n*MWT+ solar cells. In other words, the results do not suggest that the *n*MWT+ cell structure suffer more from either non-ideal recombination or nonlinear leakage currents than the H–pattern structure to the current state of development.

The lower *pFF* for the *n*MWT+ cells with emitter Gen3–A directly translates into a correspondingly lower *FF* with a mean value of 75.4%. For the other *n*MWT+ cells, the mean values are on the same level with  $FF \approx 76.5\%$ , what equates to an increase in *FF* of more than 1%<sub>abs</sub> in comparison with the *n*MWT+ cells from the previous section. This increase is mainly due to the higher *pFF*, but also the series resistance  $R_s$  could be decreased by about  $0.05 \text{ }\Omega\text{cm}^2$  to  $R_s \approx 0.85 \text{ }\Omega\text{cm}^2$ . Remember that the finger number on the front side is higher for the cells with emitters Gen3–A and Gen3–C to counteract their higher  $R_{sh}$ ; see Table 7.7. The specific contact resistances  $\rho_c$  for the Ag-Al contacts on the applied boron emitters are in the range between  $3 \text{ m}\Omega\text{cm}^2 \lesssim \rho_c \lesssim 5 \text{ m}\Omega\text{cm}^2$  (Fig. 5.13). For paste Ag3 on the phosphorus-doped BSF Phos3,  $\rho_c$  is found to be approximately  $5 \text{ m}\Omega\text{cm}^2$ . Despite considerably changing the doping profiles on either cell side,  $\rho_c$  could be maintained on a quite low level utilizing the identical contact firing process as before. The *FF* for the H–pattern cells amounts to between 78% and 79% ( $0.5 \text{ }\Omega\text{cm}^2 \lesssim R_s \lesssim 0.6 \text{ }\Omega\text{cm}^2$ ). Consequently, the difference in *FF* between the H–pattern and the *n*MWT+ solar cells increased to about 2%<sub>abs</sub>. However, this is not surprising as the H–pattern cells are fabricated with a five-busbar layout in this study. Nevertheless,  $R_s$  still remains the parameter in which the *n*MWT+ solar cells need to be further improved, as already discussed.

On the other hand, the *n*MWT+ cells are clearly superior to the H–pattern cells with respect to short-circuit current density  $j_{sc}$ . The *n*MWT+ cells reach mean  $j_{sc}$  between  $39.8 \text{ mA/cm}^2$  and  $39.9 \text{ mA/cm}^2$ , whereas  $j_{sc}$  for the H–pattern cells is between  $39.1 \text{ mA/cm}^2$  and  $39.3 \text{ mA/cm}^2$ . Note that the gold-plated chuck has a somewhat different reflectivity; see Appendix B.1. Nevertheless,  $j_{sc}$  is higher for the *n*MWT+ cells by about  $0.6 \text{ mA/cm}^2$ . Looking at the  $j_{sc}$ -results for the *n*MWT+ cells more closely, it is seen that  $j_{sc}$  for emitter Gen3–B is about  $0.1 \text{ mA/cm}^2$  lower in comparison to the other emitters, for which  $j_{sc} = 39.9 \text{ mA/cm}^2$  is identical. Despite

the higher front side shading (higher finger number) of the cells with emitters Gen3-A and Gen3-C, their  $j_{\text{SC}}$  is equal to that of the cells with emitter Gen3. The causes of both findings can be explained by the IQE data for the  $n\text{MWT}^+$  cells with the different emitters, which are shown in Fig. 7.18(b). The IQE differ clearly in the short wavelength regime. As incident light with short wavelengths is absorbed within the emitter volume, the IQE obtained at short wavelengths is a characteristic emitter property. It is found that the IQE for emitter Gen3-B up to a wavelength of  $\lambda \approx 600$  nm is lower than that of emitter Gen3, which explains the lower  $j_{\text{SC}}$  for these cells. On the other hand, the emitters Gen3-A and Gen3-C show a higher IQE as emitter Gen3. Hence, despite higher front side shading by the contact finger metallization,  $j_{\text{SC}}$  is not decreased for the  $n\text{MWT}^+$  cells with these emitters. The reason for lower  $j_{\text{SC}}$  for the H-pattern cells with emitter Gen3 (mean  $j_{\text{SC}} = 39.1 \text{ mA/cm}^2$ ) compared with that of the cells with emitter Gen3-A ( $j_{\text{SC}} = 39.3 \text{ mA/cm}^2$ ) can be attributed to the screen printing process. During printing the front side grid onto the H-pattern precursors with emitter Gen3, it came to a partial transfer of significantly wider fingers contacts, what results in an unintended higher metallization fraction for these cells.

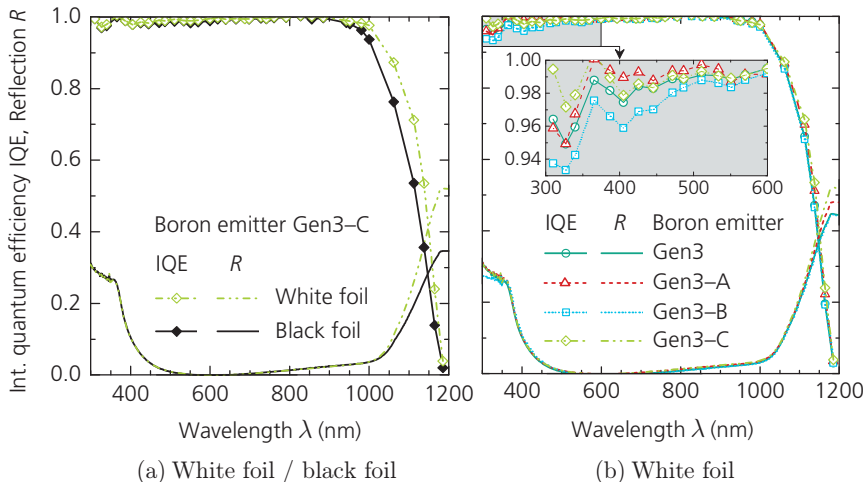


**Fig. 7.18.** Internal quantum efficiency IQE and reflection  $R$  determined on  $n\text{MWT}^+$  solar cells as a function of the wavelength  $\lambda$ . (a) Data for measurements on white and black foil for a  $n\text{MWT}^+$  cell with emitter Gen3-C. (b) Data for measurements on white foil for  $n\text{MWT}^+$  cells with the four different boron-doped emitters. The higher reflection for the cells with emitters Gen3-A and Gen3-C for long wavelengths is due to lower parasitic absorption in the emitter regions.

The mean open-circuit voltages  $V_{OC}$  for the  $n$ MWT+ cells are between 651 mV (emitter Gen3–A) and 656 mV (Gen3–C), which corresponds to an absolute increase of up to 10 mV compared with the  $n$ MWT+ cells from the previous experiment. The visible trend in  $V_{OC}$  for the  $n$ MWT+ cells and the different emitters will be discussed in more detail in section 7.5.3. The  $V_{OC}$  of the H-pattern cells with emitter Gen3–A are on the same level as those for the  $n$ MWT+ cells with emitter Gen3–A. In contrast,  $V_{OC}$  for the H-pattern cells with emitter Gen3 is lower compared with the respective  $n$ MWT+ cells, what is initially contradictory. For the same reason as stated above concerning the transfer of wider finger contacts during screen printing, the lower  $V_{OC}$  for the H-pattern cells with emitter Gen3 can be explained.

In summary, the implementation of the optimized  $BBr_3$  and  $POCl_3$  diffusion processes in conjunction with further adaptions of the fabrication process resulted in the fabrication of a  $n$ MWT+ solar cell achieving  $\eta = 20.1\%$ ,  $V_{OC} = 656$  mV,  $j_{SC} = 40.0$  mA/cm<sup>2</sup>, and  $FF = 76.6\%$ . It is shown that particularly  $R_S$  needs to be decreased, and that the challenges for further increasing the  $pFF$  is not MWT-specific to the current state of development.

### 7.5.3 Metallization-related voltage losses

On all cell precursors,  $iV_{OC}$  values are determined after firing by QSSPC measurements prior to metallization at the five marked points in Fig. 4.8 per wafer. Fig. 7.19 shows the  $iV_{OC}$  and  $V_{OC}$  of the H-pattern and  $n$ MWT+ solar cells grouped by the applied boron emitters. The losses in open-circuit voltage  $\Delta V_{OC} = V_{OC} - iV_{OC}$ , caused by front and rear side metallization, are also stated. The  $iV_{OC,\text{limit}}$  are calculated according to Eq. (2.20) and the procedure described in Chapter 2.2.1.<sup>39</sup>

In comparison to  $iV_{OC,\text{limit}} = (666 \pm 2)$  mV from the previous experiment in section 7.4, the implementation of the optimized  $BBr_3$  and  $POCl_3$  diffusion processes result in a gain in  $iV_{OC,\text{limit}}$  between 7 mV and 12 mV; see Fig. 7.19. The highest  $iV_{OC,\text{limit}} = (678 \pm 2)$  mV arises for the cell precursors with boron emitter Gen3–C. The measured  $iV_{OC}$  on all cell precursors are close to the values for  $iV_{OC,\text{limit}}$  and hence, the progress with respect to lower  $j_{0e}$  for the Gen3-based boron emitters, Table 7.6, and the lower  $j_{0BSF}$  reflects

<sup>39</sup>Used parameters:  $j_{0e}$  from Table 7.6,  $j_{0BSF}$  from Chapter 7.5.1, wafer thickness  $W = 175$  µm, bulk lifetime  $\tau_{\text{bulk}} = 1.5$  ms, injection density  $\Delta p = 3.4 \cdot 10^{15}$  cm<sup>-3</sup> (corresponding approximately to the injection level of the  $iV_{OC}$  samples at 1 sun),  $j_{ph} = 39$  mA/cm<sup>2</sup>, and  $T = 25^\circ\text{C}$ .

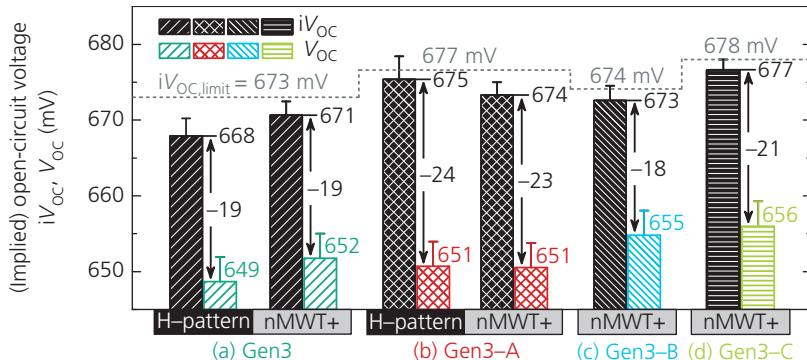


**Fig. 7.19.** Mean (implied) open-circuit voltage  $iV_{OC}$ ,  $V_{OC}$  of all cells per group, as well as respective losses in open-circuit voltage  $\Delta V_{OC} = V_{OC} - iV_{OC}$  caused by front and rear side metallization. Applied boron emitters on the front side (a) Gen3, (b) Gen3-A, (c) Gen3-B, and (d) Gen3-C. The  $iV_{OC,limit}$  are calculated based on the measured  $j_{oe}$  and  $j_{oBSF}$  and the parameters given in the text. The error bars for  $iV_{OC}$  represent the standard deviation, whereas for  $V_{OC}$  they indicate the measurement uncertainty (assumed to be 0.5% relative).

directly in higher  $iV_{OC}$ . Comparable values yield the H-pattern and the nMWT+ cell precursors for the respective emitters. The highest  $iV_{OC} = (677 \pm 1)$  mV show the nMWT+ cell precursors with boron emitter Gen3-C, which is 14 mV higher as the highest  $iV_{OC}$  measured in the previous experiment; see Fig. 7.12. However, the absolute voltage losses  $\Delta V_{OC}$  with values between  $-(18 \pm 4)$  mV and  $-(24 \pm 4)$  mV are somewhat higher as those observed previously ( $\Delta V_{OC} \approx -17$  mV). This is not surprising, as the metallization fractions on both cell sides are higher for the cells discussed in this section.

To assess the recombination at the metal contacts for the four different boron emitters on the nMWT+ cells in more detail, the two different metallization fractions on the cells' front sides must be taken into account. For this purpose,  $\Delta V_{OC}$  is normalized to the front side metallization fractions given in Table 7.7. The resulting normalized voltage losses  $\Delta V_{OC,norm}$  are summarized in Table 7.9, which include the recombination at the rear side contacts (the same for all four groups) and the different recombination contributions from the emitter contacts. It is seen that the cells with emitters Gen3 and Gen3-A are impacted most by metallization-related recombination with  $\Delta V_{OC,norm} \approx -4.7$  mV and  $\Delta V_{OC,norm} \approx -4.8$  mV, respectively. The impact of their different maximum dopant concentrations  $N_{max}$  (see Fig. 7.16)

## 7 Solar Cell Results and Loss Mechanisms

---

**Table 7.9.** Normalized voltage losses  $\Delta V_{OC,norm}$  for the  $n$ MWT+ solar cells with the four different boron emitters caused by recombination at the front and rear side metal contacts. The  $\Delta V_{OC,norm}$  considers the different metallization fractions  $F_{M,front}$  of the boron emitters, as specified in Table 7.7 (the cells' rear sides are identical).

Boron emitter →	Gen3	Gen3-A	Gen3-B	Gen3-C
$\Delta V_{OC,norm} = \Delta V_{OC}/F_{M,front}$ (mV)	$-4.7 \pm 0.2$	$-4.8 \pm 0.2$	$-4.4 \pm 0.2$	$-4.3 \pm 0.2$

on  $\Delta V_{OC,norm}$  cannot be assessed. For a higher junction depth  $d \approx 840$  nm, as this is apparent for the cells with boron emitters Gen3-B and Gen3-C, the recombination at the metal contacts can be lowered by up to 10%. Thus, the junction depth of the boron doping profile is the parameter, which mainly determines the magnitude of charge carrier recombination. This experimental finding is in agreement with the simulations of charge carrier recombination underneath the metal contacts in Chapter 5.6, which considered deep penetrating metal crystallites at the interface between the Ag-Al contact and the boron-doped surface.

A more intuitive quantity to account for metallization-related recombination is the dark saturation current density  $j_{0,met}$  in the metallized areas. By knowing  $j_{0,met}$  either for the front or the rear side contacts,  $j_{0,met}$  for the respective other side can be approximately calculated. For this purpose, the total  $j_{01}$  (Eq. (2.3)) is derived by area-weighted addition of the contributions from passivated and metallized areas for front (Eq. (2.8)) and rear side (Eq. (2.9)), respectively. For the rear side, also the external  $p$ -type contact pads and the respective passivated BSF gap areas are considered according to Eq. (7.3). Using Eq. (2.20), the determined total  $j_{01}$  allows the calculation of  $V_{OC}$ . In order to estimate  $j_{0,met}$  for the unknown contact, its value is adjusted so that the calculated  $V_{OC}$  matches with the measured  $V_{OC}$  of the fabricated cells. The aim now is to estimate the dark saturation current density in the metallized areas for the different boron emitters  $j_{0e,met}$  on the basis of the fabricated  $n$ MWT+ cells. Since the rear side is identical for all  $n$ MWT+ cells, the dark saturation current density  $j_{0BSF,met}$  in the metallized areas of the phosphorus BSF is used as input variable as its exact value is unknown. According to results for screen-printed and fired silver contacts on phosphorus-doped surfaces published by other authors [215,264],  $j_{0BSF,met}$  is assumed to be between  $500$  fA/cm $^2$  and  $1500$  fA/cm $^2$ . For the external  $p$ -type contact pads, the via paste used is of electrically non-contacting nature and hence,  $j_{0pad}$  is considered to be lower as for the silver paste used to contact the BSF, i.e.  $j_{0pad} = 500$  fA/cm $^2$  is used. For the passivated BSF gap areas,  $j_{0gap} = 58$  fA/cm $^2$  is applied, as it is determined in section 7.4.4.

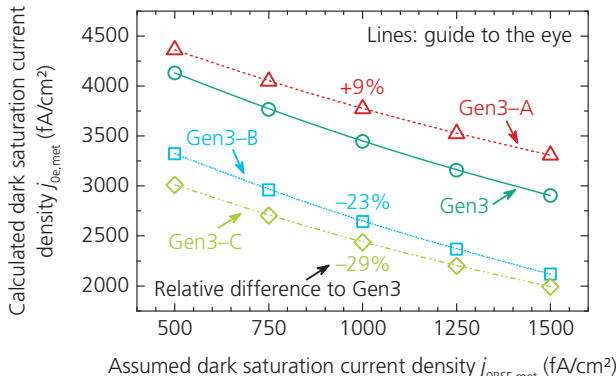


**Fig. 7.20.** Calculated dark saturation current densities  $j_{\text{oe,met}}$  of the metallized boron emitters as function of assumed dark saturation current densities  $j_{\text{OBSF,met}}$  of the metallized phosphorus BSF. The calculations are performed on basis of  $n\text{MWT+}$  cells with Gen3-based boron emitters and the procedure described in the text. The relative differences to emitter Gen3 are exemplified for  $j_{\text{OBSF,met}} = 1000 \text{ fA}/\text{cm}^2$ .

The results for the calculations of  $j_{\text{oe,met}}$  in dependence on  $j_{\text{OBSF,met}}$  are shown in Fig. 7.20. The  $j_{\text{oe,met}}$  values are found to be roughly between  $2000 \text{ fA}/\text{cm}^2$  and  $4500 \text{ fA}/\text{cm}^2$  for the utilized Ag-Al paste. It is immediately evident that boron-doped emitter Gen3-A has the highest  $j_{\text{oe,met}}$  irrespective of what  $j_{\text{OBSF,met}}$  is assumed. For  $j_{\text{OBSF,met}} = 1000 \text{ fA}/\text{cm}^2$ ,  $j_{\text{oe,met}}$  for emitter Gen3-A is  $\approx 9\%$  higher than  $j_{\text{oe,met}}$  for emitter Gen3. On the other hand, emitters Gen3-B and Gen3-C show superior performance with respect to  $j_{\text{oe,met}}$  in comparison with emitter Gen3:  $j_{\text{oe,met}}$  is lower by  $\approx 23\%$  and  $\approx 29\%$  for  $j_{\text{OBSF,met}} = 1000 \text{ fA}/\text{cm}^2$ , respectively. Hence, lowering of  $N_{\max}$  and increasing the junction depth is found to be a promising approach to achieve lower metallization-related recombination at Ag-Al contacts on boron-doped surfaces.

### 7.5.4 Section summary

Main focus in this section is set on testing the latest Gen3-based  $\text{BBr}_3$  diffusion processes from Chapter 4 on the cell level utilizing  $n$ -type Cz-Si H-pattern and  $n\text{MWT+}$  solar cells. On the one hand, the objective is to improve the energy conversion efficiency  $\eta$  in comparison to the previous experiments in section 7.4. On the other hand, examinations of the interplay between the boron doping profiles and metallization-related voltage losses aim at generating experimental data to validate the simulations of charge carrier recombination underneath the metal contacts from Chapter 5.6.

The maximum  $\eta$ , measured on reflective surface, could be increased to 20.1% for both the H-pattern and the *n*MWT+ solar cells. Note that the H-pattern cells feature a five-busbar layout, whereas the *n*MWT+ cells are still fabricated with the four-busbar-based layout as used before. The measurements on non-reflective surface yield respective maximum  $\eta = 19.9\%$ . Compared with the previous experiment,  $\eta$  could be increased by about 0.5%<sub>abs</sub>. For the most efficient *n*MWT+ cell with  $\eta = 20.1\%$ , short-circuit current density  $j_{SC}$ , open-circuit voltage  $V_{OC}$  and fill factor  $FF$  are 40.0 mA/cm<sup>2</sup>, 656 mV, and 76.6%, respectively. Compared with the H-pattern cells, the *n*MWT+ cells benefit particularly from higher  $j_{SC}$  by about 0.5 mA/cm<sup>2</sup>. Concerning  $V_{OC}$ , the *n*MWT+ cells show slightly higher values, but which are more or less on the same level with those of the H-pattern cells. Lowering of series resistance contributions remains the major task for further improving the  $FF$  in order to minimize the  $FF$  gap to the H-pattern cells of currently about 2%<sub>abs</sub>. It is also found that the challenges for an increase in pseudo fill factor  $pFF$ —currently  $pFF \approx 81.5\%$ —are basically the same for both the H-pattern and the *n*MWT+ cells. Based on the current state of development, the *n*MWT+ cell structure is found to not trigger significant higher  $j_{02}$  contributions in comparison with the H-pattern structure, which are characterized by either non-ideal recombination or nonlinear leakage currents.

A substantial contribution to the achieved increase in  $\eta$  is the successful implementation of the optimized Gen3-based BBr<sub>3</sub> diffusions from Chapter 4 into the cell fabrication process in conjunction with a further optimized POCl<sub>3</sub> diffusion process. For non-metallized passivated *n*MWT+ cell precursors, the implied open-circuit voltages iV<sub>OC</sub> could be increased by up to 14 mV compared with the previous experiment, resulting in peak iV<sub>OC</sub> = (677 ± 1) mV. However, the absolute loss in  $V_{OC}$  due to front and rear side metallization increased slightly by a few millivolts to about -20 mV, as both metallization fractions are somewhat higher in this study. Nevertheless,  $V_{OC}$  could be boosted by up to 10 mV on the finished solar cells compared with the previous ones.

The data obtained for metallization-related charge carrier recombination with respect to the doping profiles of the boron emitters matches with the results from the simulations in Chapter 5.6. The examinations are performed by means of pairwise varying the boron doping profiles to feature either same maximum dopant concentration  $N_{max}$  or same junction depth  $d$ . The reference doping profile features  $N_{max} = (8.9 \pm 0.9) \cdot 10^{19}$  cm<sup>-3</sup>,  $d = (580 \pm 58)$  nm,

and a dark saturation current density below the Ag-Al contacts  $j_{0,\text{met}} \approx 3500 \text{ fA/cm}^2$ . It is shown that lowering  $N_{\max}$  to  $N_{\max} = (3.6 \pm 0.4) \cdot 10^{19} \text{ cm}^{-3}$ , while keeping  $d$  constant, leads to an increase in  $j_{0,\text{met}}$  by about 10%. For two deeper boron doping profiles with  $d \approx 840 \text{ nm}$ ,  $j_{0,\text{met}}$  is found to be lower by up to 30% (or about 1000 fA/cm<sup>2</sup>) in comparison with the reference profile. These results validate the simulation results from Chapter 5.6 that the junction depths of the boron emitters are the parameters which mainly determine the magnitude of charge carrier recombination below the metal contacts in case deep penetrating metal crystallites are present. Furthermore, the *nMWT+* cells with the deep boron emitter which has the lowest  $N_{\max} = (1.8 \pm 0.2) \cdot 10^{19} \text{ cm}^{-3}$  show no drawbacks with respect to  $j_{\text{SC}}$  as this emitter features a very high internal quantum efficiency. Hence, lowering of  $N_{\max}$  and increasing the junction depth is found to be a promising approach for improving the cells' front sides. These findings are of high relevance not only for *nMWT+* solar cells, but also for any kind of solar cell with boron-doped surfaces contacted by screen-printed and fired Ag-Al metallization.

## 7.6 Simplified fabrication process for n-type MWT solar cells

As shown in section 7.3, the rear side configuration of the *nMWT+* solar cells without phosphorus doping underneath the external *p*-type contacts is necessary to ensure that no significant increase in leakage current occurs in these areas after reverse bias stress. Up to this point, the structuring of the phosphorus BSF is realized by masking the respective areas during  $\text{POCl}_3$  diffusion. Therefor, prior to  $\text{POCl}_3$  diffusion, the rear side diffusion barrier layers are structured by means of inkjet-printing a masking resist onto the areas of the *p*-type contact where no diffusion is desired; see Fig. C.1 in Appendix C.1. Wet-chemical etching removes the diffusion barrier layer where no masking resist is present. However, the applied structuring approach is quite elaborate, which makes it rather not relevant when it comes to industrial mass production.

The study in this section aims at testing laser processes for structuring the rear side to reduce the number of process steps needed for fabrication of *nMWT+* solar cells. More specifically, the novel approach is based on the structuring of the phosphorus-doped surfaces by laser irradiation subsequent to  $\text{POCl}_3$  diffusion and PSG etching. Two different laser-based ap-

proaches are examined on solar cells, enabling the investigation of the performance of thus fabricated  $n$ MWT+ solar cells in both forward and reverse operation. These approaches are referred to as “laser drive-in” and “laser ablation”. The used laser types and some of their characteristic parameters are summarized in Table C.1 in Appendix C.2.

### 7.6.1 Cell fabrication and process characterization

The laser-structured  $n$ MWT+ solar cells have been fabricated also in experiment E parallel with the  $n$ MWT+ cells with inkjet-based structuring discussed in the previous section 7.5. Fig. 7.21 shows the part of the fabrication sequence which is varied; otherwise the cells are fabricated according to the sequence depicted in Fig. 7.15. Schematic cross sections at the different process steps for the laser structuring are shown in Fig. C.2. In addition,  $n$ MWT solar cells with full-area phosphorus BSF (without structuring) are fabricated as reference.

The general idea for both approaches is to significantly reduce the maximum phosphorus doping concentration, which results in lower electrical conductivity between the silicon and the applied external  $p$ -type contacts; see Fig. A.2. For the laser drive-in process, the dopants are redistributed deeper into the silicon wafer by thermally excited diffusion processes [194], while the initially alkaline textured surface is locally leveled; see Fig. 7.22(a). As the ECV measurement in Fig. 7.23(a) shows, the maximum phosphorus dopant concentration  $N_{\max}$  could be lowered by two orders of magnitude from initially  $N_{\max} \approx 1.5 \cdot 10^{20} \text{ cm}^{-3}$  to  $N_{\max} \approx 2.9 \cdot 10^{18} \text{ cm}^{-3}$ , while the profile depth is increased to more than 4  $\mu\text{m}$ . For laser ablation, the highly phosphorus-doped surface layer is locally ablated [194]. Due to the rough surface caused by the laser ablation (Fig. 7.22(b)), reliable measurements of the resulting doping profile after laser ablation are not possible by means of ECV. To check anyway if the phosphorus BSF is completely removed, the surface is smoothed with the laser drive-in process—which leads to a comparable surface topography as shown in Fig. 7.22(a)—and an ECV measurement is performed thereafter. The resulting doping profile is shown in Fig. 7.23(b). Obviously, the measured dopant concentration  $N \lesssim 10^{18} \text{ cm}^{-3}$  remain higher as the bulk doping concentration  $N_{\text{bulk}} \approx 1.3 \cdot 10^{15} \text{ cm}^{-3}$ , which means that the laser ablation process has not ablated the entire highly phosphorus-doped layer. As it is seen, the depths of both resulting profiles are almost similar which originates from the laser drive-in process leading to a strong redistribution of phosphorus atoms. For the combined process,  $N$  is

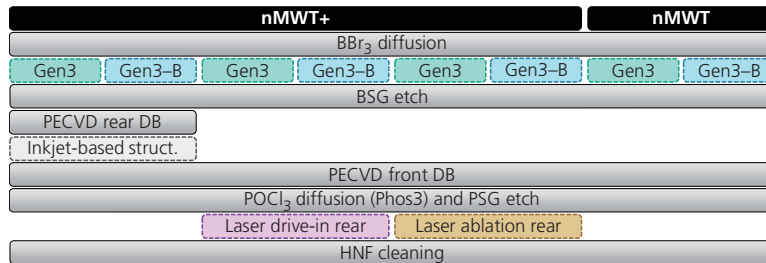


**Fig. 7.21.** Extract from the process flow for fabrication of *n*-type MWT solar cells with varying process steps for structuring of the rear phosphorus-doped surfaces (DB: diffusion barrier). Previous und subsequent processes see Fig. 7.15.

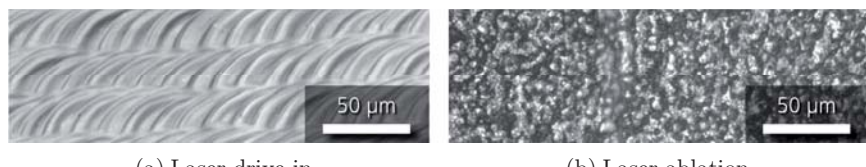


**Fig. 7.22.** Light microscope images of laser-processed areas via the processes (a) laser drive-in and (b) laser ablation. For both approaches, the laser pulses overlap each other, which is clearly visible especially in image (a).

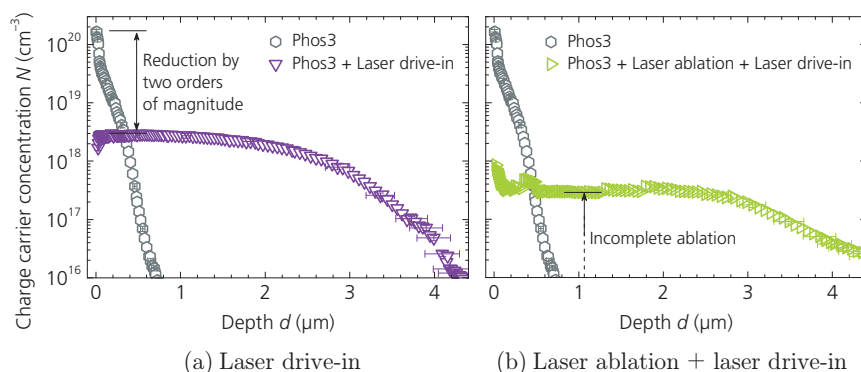


**Fig. 7.23.** Doping profiles, determined by ECV measurements on initially alkaline textured and phosphorus-doped surfaces for (a) laser drive-in and (b) laser ablation. As no reliable ECV measurements can be made on the rough surface in Fig. 7.22(b), a laser drive-in step is additionally performed in (b) to obtain a suitable surface. Exemplary error bars are shown.

significantly lower as for the single laser drive-in process, what indicates that a significant amount of the silicon surface has been ablated. However, it is not possible to extract to which depth or likewise to which  $N_{\max}$  the silicon surface has been solely removed by laser ablation. Nevertheless, both approaches can significantly decrease  $N_{\max}$ . Recall that Fig. 7.23(b) does not represent the doping profile of the  $n$ MWT+ cells with laser ablation.

### 7.6.2 Current-voltage characteristics

The trend with respect to the  $I$ - $V$  parameters for the different structuring methods is similar for the fabricated MWT cells with boron emitters Gen3 and Gen3-B. Thus, only the  $I$ - $V$  data for the MWT cells with emitter Gen3-B will first be discussed with respect to their performance in forward operation. An overview on the measurement data obtained on white foil can be found in Fig. C.3 in Appendix C.2. For the investigation of the current flow in reverse mode, also the cells with emitter Gen3 will be considered.

The following discussion of the  $I$ - $V$  characteristics in forward operation for the differently structured MWT cells is based on the most efficient cells, whose  $I$ - $V$  data with boron emitter Gen3-B are summarized in Table 7.10 (the respective mean values show the same trend). The three differently structured  $n$ MWT+ cells and the  $n$ MWT cell with full-area phosphorus BSF show almost the same characteristic parameters with  $\eta = 20.0\%$  and  $\eta = 20.1\%$  for the initial measurements without prior reverse bias load. The differences in shunt resistance  $R_P$  have no significant impact on the  $I$ - $V$  data as the values are sufficiently high to not affect the  $pFF$  considerably. Also, the variations in series resistance  $R_S$  are rather small and originate

**Table 7.10.**  $I$ - $V$  data on white foil for the most efficient  $n$ -type Cz-Si  $n$ MWT+ and  $n$ MWT solar cells (cell area:  $239 \text{ cm}^2$ ) with boron emitter Gen3-B and different rear-side structuring. All cells are initially tested after laser edge isolation with an industrial cell tester without reverse bias load. The given data is corrected with respect to measurements performed at *Fraunhofer ISE CalLab PV cells*.

Cell type	BSF structuring	$\eta$ (%)	$V_{\text{OC}}$ (mV)	$j_{\text{SC}}$ ( $\text{mA}/\text{cm}^2$ )	FF (%)	$pFF$ (%)	$R_P$ ( $\text{k}\Omega\text{cm}^2$ )	$R_S$ ( $\Omega\text{cm}^2$ )
$n$ MWT+	Inkjet-based	20.0	654	39.8	77.0	81.3	17.9	0.76
	Laser drive-in	20.0	657	39.7	76.7	81.5	60.2	0.84
	Laser ablation	20.0	654	39.8	76.7	81.2	32.2	0.78
$n$ MWT	-	20.1	654	39.8	77.1	81.5	74.4	0.76

most likely from process fluctuations during screen printing. The use of both laser processes shows no impact on the achievable cell performance in forward operation.

In order to examine the impact of reverse bias load on the  $I$ - $V$  characteristics, one MWT cell per group is biased in reverse 20 times in total with respective forward measurements in between (i.e. the same measurement procedure as used in section 7.3, Fig. 7.4). The differences to the initial measurements without prior reverse bias load are summarized for the MWT cells with emitter Gen3-B in Table 7.11 with respect to  $\eta$ ,  $FF$ ,  $pFF$ , and  $R_p$ . For reference, also an H-pattern cell with emitter Gen3 from the previous section 7.5 is considered. The losses in  $V_{OC}$  are very small ( $|\Delta V_{OC}| < 0.3\%$ <sub>rel</sub>) and are therefore not shown, as well as the  $j_{SC}$  values which are constant throughout. The  $R_p$  values are given in absolute numbers, while for the other parameters the absolute differences are specified.

Irrespective of the structuring method applied, the  $n$ MWT+ cells show a loss in  $\eta$  of  $-0.1\%$ <sub>abs</sub> after the 20th reverse bias load. The same loss in  $\eta$  is observed for the H-pattern cell. As expected from the results in section 7.3, the  $n$ MWT cell is much more impacted by reverse stress and  $\eta$

**Table 7.11.** Mean absolute losses in conversion efficiency  $\eta$ , fill factor  $FF$ , and pseudo fill factor  $pFF$  in relation to the initial measurements performed without prior reverse bias for one cell per group. The shunt resistance  $R_p$  is given in absolute numbers.

Cell type (Boron emitter)	BSF structuring	#Reverse bias	$\Delta\eta$ (% <sub>abs</sub> )	$\Delta FF$ (% <sub>abs</sub> )	$\Delta pFF$ (% <sub>abs</sub> )	$R_p$ (k $\Omega$ cm $^2$ )
<i>n</i> MWT+ (Gen3-B)	Inkjet-based	—	<i>Initial values</i>			25.1
		1	-0.1	-0.2	-0.2	16.5
		20	-0.1	-0.4	-0.4	16.0
	Laser drive-in	—	<i>Initial values</i>			22.6
		1	-0.1	-0.3	-0.4	12.8
		20	-0.1	-0.4	-0.5	11.5
	Laser ablation	—	<i>Initial values</i>			45.0
		1	-0.1	-0.1	-0.2	29.3
		20	-0.1	-0.3	-0.4	24.0
<i>n</i> MWT (Gen3-B)	—	—	<i>Initial values</i>			16.7
		1	-0.2	-0.7	-0.7	9.1
		20	-0.3	-1.1	-1.1	6.9
H-pattern (Gen3)	—	—	<i>Initial values</i>			11.7
		1	-0.1	-0.2	-0.2	10.1
		20	-0.1	-0.4	-0.4	9.8

decreases by in total  $-0.3\%_{\text{abs}}$ . The observed losses originate from decreased  $pFF$  values, which translates into lower  $FF$ . The decrease of  $R_p$  by reverse stressing is evident. However, the  $R_p = 6.9 \text{ k}\Omega\text{cm}^2$  for the  $n$ MWT cell here is significantly higher than  $R_p = 1.3 \text{ k}\Omega\text{cm}^2$  measured in section 7.3. This might originate from the fact that the area fraction of the external  $p$ -type contact pads is 0.5% of the total cell area in this experiment and thus lower compared with 1.3% for the former  $n$ MWT cells. Application of the two-diode model reveals that the dominating loss mechanism in  $pFF$  for the  $n$ MWT cell examined in this study is an increase in  $j_{02}$  (ohmic leakage currents contribute only about  $0.1\%_{\text{abs}}$  to the loss in  $pFF$ ). The higher  $j_{02}$  is most likely caused by increased nonlinear leakage currents. In summary, these results show that the  $n$ MWT+ solar cells—*independent of the structuring method*—are significantly less affected by reverse bias stress as the  $n$ MWT cells, whereby they show the same losses as observed for the H-pattern reference cell. Hence, the potential for a significant simplification of the fabrication process of  $n$ MWT+ solar cells by integration of laser processes for structuring the phosphorus BSF is demonstrated.

The  $I$ – $V$  characteristics for the 20th measurement in reverse bias are shown in Fig. 7.24. The curve progressions for the different cells are very similar for both boron emitters Gen3 and Gen3–B. It seems that the higher junction depth of emitter Gen3–B (about 300 nm deeper than that of emitter Gen3) is somehow compensated by its significantly lower  $N_{\text{max}}$  with respect to current flow under reverse operation. On the other hand, all investigated cells show strongly increased current starting from a voltage of approximately  $-4 \text{ V}$ . The earliest increase in current is seen for the  $n$ MWT cells. For the differently structured  $n$ MWT+ cells, the current increase sets in a bit later and the resulting curves are more or less similar. The determined  $I$ – $V$  curve

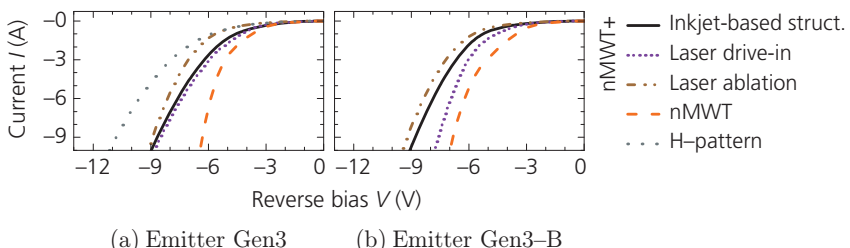


**Fig. 7.24.** Dark  $I$ – $V$  characteristics under reverse bias for the 20th measurement of the indicated  $n$ -type Cz-Si solar cells with emitter (a) Gen3 and (b) Gen3–B. No H-pattern cell with emitter Gen3–B has been fabricated.

for the H-pattern cell with emitter Gen3 in Fig. 7.24(a) shows the lowest currents for increasing negative voltages. However, the general curve progression is quite similar to the other curves (especially to those of the *n*MWT+ cells). This result is in accordance with the results from section 7.3, where it has been also found that the challenges considering the reverse behavior are similar for both the H-pattern and the *n*MWT+ solar cell structures.

The local current flow in reverse bias at  $-7$  V, determined by DLIT measurements, shows Fig. 7.25 for the MWT cells with emitter Gen3-B and the H-pattern cell with emitter Gen3. For all MWT cells, signals are visible in the area of the external *p*-type contact pads, while the signals are most pronounced for the *n*MWT cell in Fig. 7.25(d). But also signals in the rest of the cell area are seen (as also for the H-pattern cell). Also these results are in agreement with the results from section 7.3. Comparing the signal strengths of the *n*MWT+ cells in (a)–(c) with those of the *n*MWT cell in (d), it is seen that lowering of  $N_{\max}$  yields lower current flow in the area of the external *p*-type contacts. The signal strengths are comparable for the *n*MWT+ cells with inkjet-based structured BSF in (a) and laser-ablated BSF in (c). For the *n*MWT+ cell fabricated with laser drive-in in (b), the signal strengths at the pads are somewhat higher. Further reduction in current density at the pads is most likely possible by optimizing the laser drive-in process.

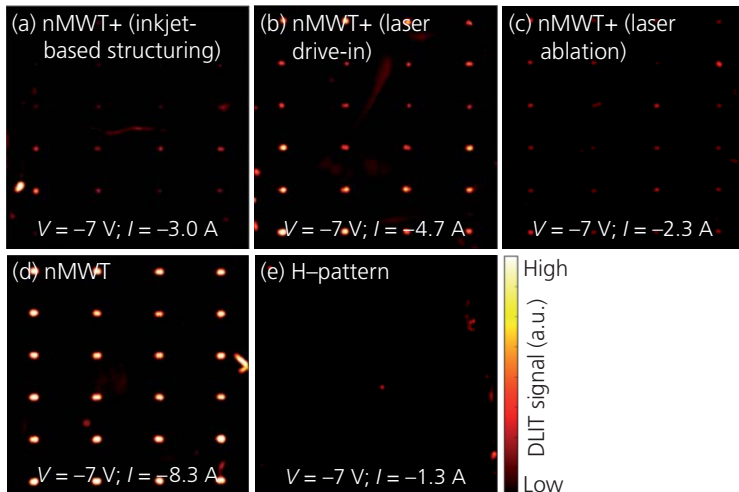


**Fig. 7.25.** DLIT images recorded at a phase of  $-90^\circ$  obtained at voltages of  $-7$  V for the indicated solar cell structures. The overall current  $I$  is also specified. The MWT cells feature boron emitter Gen3-B, while the H-pattern cell has emitter Gen3.

### 7.6.3 Section summary and conclusion

Under forward and reverse operation, the laser-structured  $n$ MWT+ cells are found to show very similar performance as  $n$ MWT+ cells with inkjet-based BSF structuring. The peak energy conversion efficiency  $\eta$ , measured on white foil without prior reverse bias load, is the same for these cells with  $\eta = 20.0\%$ . After 20 measurements with reverse bias load,  $\eta$  decreases by  $-0.1\%_{\text{abs}}$  irrespective of the structuring method. The same loss in  $\eta$  is also found for an examined H-pattern reference cell. Concerning the behavior in reverse operation, the same current flow as function of the applied voltage is more or less observed for the differently structured  $n$ MWT+ cells and also for the H-pattern cell. A strong current increase begins to develop for all cells for voltages exceeding  $-4$  V. As the determined reverse behavior of the H-pattern cell is very similar to that of the  $n$ MWT+ cells this means that the properties of the cells' front sides most likely dominate the global reverse behavior of the fabricated cells. However, for the  $n$ MWT+ cells, some current flow in reverse operation is observed in the areas of the external  $p$ -type contacts pads. Such local current flow for  $n$ MWT+ cells has been also observed in section 7.3. For the  $n$ MWT cells without structured phosphorus BSF,  $\eta = 20.1\%$  is measured prior the reverse biasing. As expected, reverse stress leads to a loss in  $\eta$  by  $0.3\%_{\text{abs}}$  and high current flow is observed at the external  $p$ -type contact pads under reverse operation. This local current flow is significantly higher as that observed for the  $n$ MWT+ cells no matter which structuring approach has been applied. Hence, the potential for a significant process simplification for fabrication of  $n$ MWT+ solar cells by implementation of laser processes for structuring the phosphorus BSF is demonstrated.

However, the observed overall high currents in reverse operation might be not compatible with conventional solar module technology where quite low current flow is required. This applies to both the H-pattern and the various  $n$ MWT+ solar cells examined. As also other authors as e.g. Cabal *et al.* report on high currents for  $n$ -type Cz-Si H-pattern cells under reverse bias load [137], the lowering of current flow in reverse operation might be a general challenge for  $n$ -type silicon solar cells. The task for future studies is to identify the reasons for this high current flow under reverse operation, which might be caused to a large extent from non-optimal properties of the cells' front sides. On the other hand, the high currents in reverse mode might be utilized for a cell-integrated bypass-diode approach at the module level, in case the thermal power triggered by the current flow and

its spatial density dissipation allows for this. For such an approach, reverse stress must also not significantly affect the forward performance. This has been demonstrated for all fabricated  $n$ MWT+ solar cells, even for those with significantly simplified process sequences by implementation of laser-based structuring of the phosphorus BSF.

## 7.7 Estimation of conversion efficiency potential

The energy conversion efficiency potential for  $n$ MWT+ solar cells is estimated for expected technological improvements. For this purpose, analytical device modelling is used which is based, on the one hand, on the tool *Gridmaster* [265] for calculation of  $R_s$  contributions. On the other hand, the procedure described in section 7.5.3 is used for determination of the total  $j_{01}$  of complete solar cells. Therein, the total  $j_{01}$  is determined by area-weighted addition of the contributions from passivated and metallized areas for both the front and the rear sides of the cell (the contributions from the bulk are also taken into account). Using Eq. (2.20), the determined total  $j_{01}$  allows the calculation of  $V_{OC}$ .

The estimation of the efficiency potential starts with the  $I$ - $V$  data of the most efficient  $n$ MWT+ solar cell from section 7.5 with  $\eta = 20.1\%$  and boron emitter Gen3-C; see Table 7.8. The input parameters of the utilized models are adjusted so that the output  $I$ - $V$  data fit to the measured ones for this  $n$ MWT+ cell. Subsequently, the expected technological improvements are considered by gradually adapting the respective input parameters in order to determine their impact on the  $I$ - $V$  characteristics. Fig. 7.26 shows the expected increase in energy conversion efficiency  $\eta$ .

The first improvement is an adaption of the rear contact layout to five contact rows per polarity each featuring 10 external contact pads. This includes the increase of the number of pseudo-busbar contacts to five on the front side. In order not to change the metallization fractions of the emitter and the BSF, the finger widths on front and rear sides are correspondingly reduced. Due to the doubling of the number of external contact pads, a reduction of  $R_s$  by  $0.2 \Omega\text{cm}^2$  is expected. This leads to an efficiency increase of  $\Delta\eta \approx 0.3\%_{\text{abs}}$ . The loss in  $V_{OC}$  due to twice the number of external  $p$ -type contacts is found to be only 0.2 mV, as shown in Fig. 7.14(b). Further progress in contacting the highly doped surfaces is expected in terms of lower charge carrier recombination below the metal contacts. For the boron

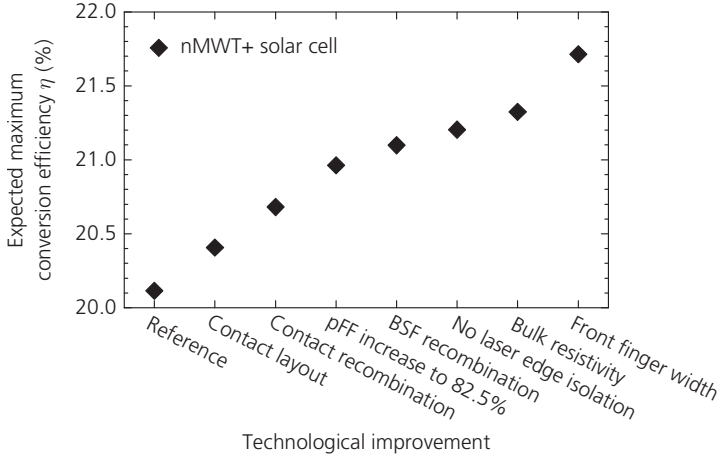


**Fig. 7.26.** Conversion efficiency for *n*MWT+ solar cells calculated with *Gridmaster* and the procedure described in the text for assumed technological improvements.

emitter and the phosphorus BSF, the dark saturation current density below the metal contacts is assumed to decrease to  $j_{0e,met} = 1000 \text{ fA/cm}^2$  (formerly  $2400 \text{ fA/cm}^2$ ) and to  $j_{0BSF,met} = 500 \text{ fA/cm}^2$  (formerly  $1000 \text{ fA/cm}^2$ ), respectively. This might be achieved by implementation of selective dopings below the metal contacts [216,259] or improved metal paste compositions. In case of the boron emitter, the assumed lower  $j_{0e,met}$  equals the value which is simulated for emitter Gen3-C in Chapter 5.6 without presence of metal crystallites. All in all, this leads to a further possible increase of  $\Delta\eta \approx 0.3\%_{abs}$ . Another gain of  $\Delta\eta \approx 0.3\%_{abs}$  results from an improvement in *pFF* to a value of 82.5% (formerly 81.4%), which is assumed to result from further optimized fabrication processes. Further progress in phosphorus diffusion is expected to decrease  $j_{0BSF}$  to  $40 \text{ fA/cm}^2$  (formerly  $80 \text{ fA/cm}^2$ ) and thus, to a comparable level as  $j_{0e}$  for the boron emitter. This results in an increase of  $\Delta\eta \approx 0.1\%_{abs}$ . A gain in  $j_{SC}$  of  $0.2 \text{ mA/cm}^2$  is assumed in case laser edge isolation is no longer necessary to electrically separate front and rear sides (larger active cell area), which enhances  $\eta$  by about  $0.1\%_{abs}$ . Up to this point, a total increase of  $\Delta\eta \approx 1.1\%_{abs}$  is estimated from the so far considered technological improvements leading to an efficiency potential of  $\eta = 21.2\%$ .

Furthermore, an adaption of the bulk material is beneficial. The model predicts an efficiency increase of about  $0.1\%_{abs}$  to  $\eta = 21.3\%$  in case the bulk resistivity is decreased to  $0.5 \Omega\text{cm}$  (formerly  $3.5 \Omega\text{cm}$ ). Due to the higher bulk doping density, it is assumed that  $j_{SC}$  is decreased by  $0.3 \text{ mA/cm}^2$ . A

further gain of  $\Delta\eta \approx 0.4\%_{\text{abs}}$  to  $\eta = 21.7\%$  is predicted by the model for the reduction of the front finger width to 40  $\mu\text{m}$  (formerly 67  $\mu\text{m}$ ) while maintaining their height. The higher  $R_s$  of about  $0.08 \Omega\text{cm}^2$  is more than compensated by the increase in both  $V_{\text{OC}}$  (+ 3.4 mV) and  $j_{\text{SC}}$  (+ 0.8 mA/cm<sup>2</sup>), which is due to the lower metal coverage on the front side. These calculations highlight the high energy conversion efficiency potential of about 22% for MWT solar cells fabricated from *n*-type Cz-Si material.

## 7.8 Chapter summary

This chapter discusses the results obtained for *n*-type Cz-Si solar cells with 156 mm edge length within various development cycles during the course of this thesis. Apart from MWT solar cells, also H-pattern cells are fabricated, which serve as reference for the more novel *n*-type MWT cell concept. The fabrication process used is based on sequential tube furnace diffusion processes with  $\text{BBr}_3$  and  $\text{POCl}_3$  as liquid dopant precursors. In detailed studies, loss mechanisms of the fabricated solar cells are identified. These losses could be partly decreased by different approaches and the energy conversion efficiency could be significantly increased.

The optimization of the  $\text{BBr}_3$  diffusion processes carried out in Chapter 4 enabled implied open-circuit voltages of up to  $iV_{\text{OC}} = (677 \pm 1)$  mV measured on passivated but not yet metallized cell precursors. Charge carrier recombination underneath the metal contacts on front and rear side are found to lead to a total loss in open-circuit voltage  $V_{\text{OC}}$  of about -20 mV for the finished solar cells for both the MWT and the H-pattern structure. This means that no significant metallization-related MWT-specific losses in  $V_{\text{OC}}$  are observed. The dark saturation current density  $j_{0e,\text{met}}$  below the Ag-Al contacts on the boron-doped emitter could be decreased by about 30% to  $j_{0e,\text{met}} \approx 2500 \text{ fA/cm}^2$  by increasing the junction depth of the boron doping by approximately 300 nm to  $d \approx 850 \text{ nm}$ . At the same time, the near-surface maximum dopant concentration  $N_{\text{max}}$  is lowered to  $N_{\text{max}} = (1.8 \pm 0.2) \cdot 10^{19} \text{ cm}^{-3}$ , while the specific contact resistance is kept constant with  $\rho_C \approx 4 \text{ m}\Omega\text{cm}^2$ , as shown in Chapter 5.5. In agreement with the simulation results of charge carrier recombination at metal contacts in Chapter 5.6, the emitter junction depth is found to be the parameter which mainly determines the magnitude of  $j_{0e,\text{met}}$  for the observed partly deep penetrating metal crystallites. Hence, lowering  $N_{\text{max}}$  and increasing the junction depth of the boron emitter is found to be a promising approach

for improving the performance of the cells' front sides contacted by screen-printed and fired Ag-Al metallization.

These findings contribute substantially to the fabrication of *n*-type MWT solar cells exceeding energy conversion efficiencies  $\eta$  of 20% (for comparison, the first cells fabricated at the beginning of this work reached  $\eta = 17.5\%$ ). The most efficient *n*-type MWT solar cell measured prior to laser edge isolation features  $\eta = 20.4\%$ , a short-circuit current density  $j_{SC} = 40.2 \text{ mA/cm}^2$ ,  $V_{OC} = 656 \text{ mV}$ , and a fill factor  $FF = 77.2\%$ . To ensure that the solar cells do not shunt at the edges, laser edge isolation is performed by default at the end of the fabrication process, which results in  $\eta = 20.2\%$  for this MWT cell. This cell features a full-area phosphorus-doped back surface field (BSF) and is called a *nMWT* solar cell. Reverse biasing of such *nMWT* solar cells reveals that the backside *p*-type contact structures—which consist of a fired via paste, an intermediate  $\text{SiN}_x$  passivation layer, and the highly doped phosphorus BSF—cannot withstand the applied negative voltages. This results in formation of local shunts at these external contacts, which is in agreement with the findings for the respective test structures from Chapter 6. For the performance in forward direction, the occurring leakage currents mean most notably a loss in pseudo fill factor  $pFF$  of at least  $1\%_{abs}$  ( $FF$  decreases accordingly) and a loss in  $\eta$  by about  $0.3\%_{abs}$ . For the reverse direction, quite high current flow occurs locally at these contact areas.

For the other investigated *n*-type MWT cell structure, called *nMWT+*, the phosphorus BSF is either completely omitted underneath the external *p*-type contacts or its maximum surface doping concentration is clearly lowered. These *nMWT+* cells are found to be significantly less susceptible to reverse bias load compared with the *nMWT* cells. Furthermore, the current at the external *p*-type contacts under reverse operation reveal to be significantly lower for the *nMWT+* cells. On the other hand, their efficiency potential prior to applying reverse bias is basically the same as for the *nMWT* cell structure. The most efficient *nMWT+* solar cell features  $\eta = 20.1\%$ ,  $j_{SC} = 40.0 \text{ mA/cm}^2$ ,  $V_{OC} = 656 \text{ mV}$ , and  $FF = 76.6\%$  (after laser edge isolation). The finding that the efficiency potential is equal for both MWT concepts follows also from studying the different rear side configurations in terms of respective losses. After reverse biasing, the losses for the *nMWT+* cells result to  $\Delta pFF \leq 0.5\%_{abs}$  and  $\Delta\eta \leq 0.1\%_{abs}$ , which are clearly lower as those observed for the *nMWT* cells. The H-pattern cells suffer also from reverse bias load and the absolute losses are comparable to those of the *nMWT+* cells. For the H-pattern cells, the formation of reverse bias

induced new shunts on the cells' front sides is observed, which might explain the found losses. Hence, the reverse-bias-induced losses determined for the *n*MWT+ cells most likely do not completely originate from increased shunting on the cells' rear sides. In terms of the total current in reverse mode, the H-pattern cells show comparable values as the *n*MWT+ cells. This means that the challenges in terms of the reverse behavior and its suitability for module integration are similar for both cell structures to the current state of development.

The most efficient *n*-type H-pattern reference cell achieves  $\eta = 20.1\%$ ,  $j_{SC} = 39.3 \text{ mA/cm}^2$ ,  $V_{OC} = 650 \text{ mV}$ , and  $FF = 78.8\%$  (after laser edge isolation, prior to reverse biasing). Obviously,  $j_{SC}$  is higher by  $\approx 0.5 \text{ mA/cm}^2$  for the *n*-type MWT solar cells due to less shaded front side area. Also  $V_{OC}$  for the MWT solar cells is found to be higher by a few millivolts. The studies concerning recombination properties at the external *p*-type contacts reveal that these MWT-specific areas have no significant impact on the cells' total recombination. For the  $FF$  it is found that lowering of series resistance  $R_S$  contributions for the MWT cells is one of the major tasks for their further improvement in  $\eta$ . The  $FF$  difference from the H-pattern cells of currently about  $2\%_{\text{abs}}$  originates mainly from the applied MWT metallization layout with a rather low number of external contacts. MWT-specific  $R_S$  contributions from both lateral current flow in the bulk and the via contacts are quite small and yield a cumulated  $FF$  loss of only  $0.1\%_{\text{abs}}$ . Hence, the increase in number of external contacts for optimized MWT metallization layouts is imperative.

Finally, the efficiency potential of *n*MWT+ solar cells is estimated by assuming further technological progress. Optimizing the contact layout and reduction in charge carrier recombination underneath the metal contacts might be the first most promising steps. The performed analytical calculations show a high efficiency potential of about 22% for *n*-type Cz-Si MWT solar cells.



## 8 Summary

In this thesis, the transfer of the metal wrap through (MWT) solar cell concept from *p*-type to *n*-type Cz-Si is investigated. As research mainly focused on *p*-type silicon MWT solar cells in the past, the challenges coming with the transfer to *n*-type Cz-Si are examined. The findings provide important knowledge on the functionality of *n*-type MWT devices and point out the issues that need to be dealt with when it comes to industrial implementation. For this purpose, also conventional *n*-type Cz-Si H-pattern solar cells serve as reference. The solar cells investigated feature a front side *p-n*-junction, screen-printed metallization, and 156 mm edge length.

Due to the change of the substrate material from *p*-type to *n*-type Cz-Si, novel process technologies and process sequences need to be examined for cell fabrication. The chosen process sequence to form the different highly doped surfaces is based on sequential tube furnace diffusion processes. Following the formation of the boron-doped emitter on the front side utilizing boron tribromide ( $\text{BBr}_3$ ) as liquid dopant precursor, the phosphorus-doped back surface field (BSF) is formed utilizing phosphorus oxychloride. With respect to process development, the focus is set on optimizing  $\text{BBr}_3$  diffusion processes in connection with the electrical contacting of the boron-doped surfaces by screen-printed and fired metal contacts. New diffusion processes with integrated post-oxidation are developed to form deep driven-in boron diffusion profiles with low surface concentration in a single process step. The emitters formed therewith feature low dark saturation current density of  $(30 \pm 3) \text{ fA/cm}^2$  on textured surface passivated by an  $\text{Al}_2\text{O}_3/\text{SiN}_x$  layer stack and a sheet resistance of about  $120 \Omega/\text{sq}$  at a junction depth of almost 850 nm. Despite low maximum dopant concentration  $N_{\max}$  of only  $(1.8 \pm 0.2) \cdot 10^{19} \text{ cm}^{-3}$ , low specific contact resistance  $\rho_c$  of less than  $4 \text{ m}\Omega\text{cm}^2$  is obtained for screen-printed and fired silver-aluminum (Ag-Al) contacts. From the theory of ideal planar contacts, it is known that  $\rho_c$  depends on  $N_{\max}$ . However, it is experimentally shown, for the first time, that the depth-dependent course of the dopant concentration also contri-

butes to a low-ohmic contact formation. This is due to presence of metal crystallites underneath the bulk of the Ag-Al contacts with penetration depths between several 100 nm and a few microns. This means that from two doping profiles with the same  $N_{\max}$  but different junction depths, the one with the deeper junction can be contacted with lower  $\rho_C$ . The correlation between junction depth and  $\rho_C$  could be also demonstrated by means of an analytical model which is based on metal crystallites.

The optimization of the  $\text{BBr}_3$  diffusion processes enabled implied open-circuit voltages of up to  $iV_{\text{OC}} = (677 \pm 1)$  mV for passivated but not yet metallized cell precursors. Charge carrier recombination underneath the metal contacts on front and rear side are found to lead to a total loss in open-circuit voltage  $V_{\text{OC}}$  of about -20 mV for the finished  $n$ -type Cz-Si solar cells. Since this applies to both the MWT as well as the H-pattern structure, thus no significant MWT-specific metallization-related losses in  $V_{\text{OC}}$  are observed. The dark saturation current density  $j_{0e,\text{met}}$  below the Ag-Al contacts on the above discussed boron emitter is estimated to be about 2500 fA/cm<sup>2</sup>. Comparing the results of MWT cells with different emitter doping profiles reveals that the junction depth is the parameter which mainly determines the magnitude of  $j_{0e,\text{met}}$ . Hence, deep driven-in emitters enable a significant reduction in  $j_{0e,\text{met}}$ . The application of a novel numerical three-dimensional simulation approach, resulting from cooperation with a parallel ongoing PhD thesis, allows detailed insight into charge carrier recombination below the metal contacts. It is shown that  $j_{0e,\text{met}}$  exceeding 1300 fA/cm<sup>2</sup> correlate with the presence of metal crystallites, which are at least so deep that an over-exponential increase of charge carrier recombination sets in particularly at their tips.

The key component of MWT solar cells—irrespective of the bulk doping type—is the metal-insulator-silicon contact in the area of the external rear contacts that are connected to the emitter by the front grid and metallized vias. The vias and these rear contacts are metallized by screen-printed silver-based via pastes, which should not form electrical contact with the underlying silicon during contact firing to prevent the occurrence of leakage currents. To examine the challenges coming with the transfer of the MWT concept from  $p$ -type to  $n$ -type Cz-Si, special test structures with both substrate types are utilized. It is found that the electrical contact separation, and thus the avoidance of leakage currents, is clearly more demanding on the  $n$ -type substrates. Nevertheless, the obtained results reveal a promising via paste for the application in  $n$ -type MWT solar cells. The acquired knowledge could also be brought into the ongoing development in  $p$ -type MWT technology.

All these findings contributed substantially to the fabrication of *n*-type Cz-Si MWT solar cells exceeding energy conversion efficiencies  $\eta$  of 20%. Two *n*-type MWT cell structures, named *nMWT* and *nMWT+*, are developed which might serve as a basis for further development. The *nMWT* cells feature a full-area BSF and achieve a peak efficiency of 20.2% for the initial current-voltage measurement without previous reverse bias load. For the *nMWT+* cells, the BSF is either completely omitted underneath the external *p*-type contacts or its maximum surface doping concentration is clearly lowered. Nevertheless, the peak efficiency with 20.1% is comparable with that of the *nMWT* cells. Reverse biasing the cells reveals for the *nMWT+* structure that the induced leakage currents result in a loss in  $\eta$  that does not exceed 0.1%<sub>abs</sub>. This loss is at least three times lower than the one observed for the *nMWT* structure. The H-pattern reference cells, which also achieve peak efficiencies of 20.1%, suffer the same from reverse biasing as the *nMWT+* cells and the absolute losses are found to be similar. Also in terms of the total current in reverse mode, the H-pattern cells show comparable values as the *nMWT+* cells. However, the observed currents might be too high for conventional module technology. Hence, the challenges in terms of the reverse behavior and its suitability for module integration are similar for both cell structures to the current state of development.

The most efficient *nMWT+* cell, with  $\eta = 20.1\%$ , features a short-circuit current density  $j_{SC} = 40.0 \text{ mA/cm}^2$ , a  $V_{OC} = 656 \text{ mV}$ , and a fill factor  $FF = 76.6\%$  prior to reverse biasing. In comparison with the most efficient H-pattern cell, the *nMWT+* cell benefits from a higher  $j_{SC}$  by about 0.5  $\text{mA/cm}^2$  due to less shaded front side area. Also the  $V_{OC}$  is higher by a few millivolts. On the other hand, the  $FF$  is lower by approximately 2%<sub>abs</sub>, which originates mainly from series resistance contributions of the applied MWT metallization layout with only 20/24 external *n*-type/*p*-type contact pads. Thus, the increase in the number of external contacts for the MWT metallization layouts is imperative to further increase the  $FF$ . By default, laser edge isolation is performed at the end of the fabrication process prior to current-voltage testing. However, some cells have also been tested prior to laser edge isolation. The highest efficiency that has been achieved during the course of this thesis is 20.4%, measured for a *nMWT* solar cell before edge isolation.

The studies demonstrate the successful transfer of the MWT concept to *n*-type Cz-Si. With respect to current flow, the cell behavior in reverse mode is shown to be the major challenge, which has to be overcome for a reliable operation after module encapsulation.

## 9 Outlook

The estimation of the energy conversion efficiency potential of *n*MWT+ solar cells by assumed technological progress yields a value of about 22%. Optimizing the contact layout and reduction in charge carrier recombination underneath the metal contacts may be the first most promising steps. The task to decrease the charge carrier recombination underneath the metal contacts on the boron emitter is to ensure that the metal crystallites' tips do not come too close to the *p-n*-junction. On the one hand, deeper and optional selective dopings are a promising approach. On the other hand, optimization of both the utilized metal pastes in combination with contact firing processes might ensure the formation of only small crystallites. Even for small crystallites it is shown that a low-ohmic contact formation is possible in case their density is sufficiently high.

Another topic of intensive research within the PV community to reduce costs is the simplification of the process sequences, which are needed to form the two different highly doped surfaces in *n*-type silicon solar cells. One of these approaches is, e.g. co-diffusion. Therein, a solid dopant source on one wafer side is used during a high-temperature gas phase diffusion of the other dopant atoms on the other wafer side. The usage of implantation processes is another option. No matter which process sequence is applied, the *n*MWT+ cell structure can still be realized by using laser processes to structure the rear phosphorus doping after its formation.

Concerning the *p*-type contact structure and reverse bias stress, further optimization of the via pastes and the intermediate dielectric layers might lead to even lower current in these MWT-specific areas. Apart from further improving the cell efficiency, also the reduction of current in reverse mode should be focused on for future work. However, in case of low breakdown voltages and an adequate spatial distribution of the current flow, the early breakdown behavior can be potentially used as an integrated bypass diode approach at the module level.

## 10 Deutsche Zusammenfassung

Diese Arbeit beschäftigt sich mit dem Übertrag des „Metal Wrap Through“ (MWT) Solarzellenkonzepts von *p*-dotiertem auf *n*-dotiertes Cz-Si. Da sich die Forschung in der Vergangenheit hauptsächlich auf MWT-Solarzellen aus *p*-dotiertem Silicium fokussiert hat, werden die Herausforderungen untersucht, die mit dem Übertrag auf *n*-dotiertes Cz-Si einhergehen. Die gewonnenen Erkenntnisse stellen wichtiges Wissen über die Funktionsweise von MWT-Solarzellen aus *n*-dotiertem Silicium bereit und weisen auf die Fragestellungen hin, die bei einer industriellen Umsetzung zu berücksichtigen sind. Hierfür werden auch Solarzellen aus *n*-dotiertem Cz-Si mit Standardkontakteierung als Referenz herangezogen. Die untersuchten Solarzellen weisen einen vorderseitigen *p-n*-Übergang, siebgedruckte Metallisierung und eine Kantenlänge von 156 mm auf.

Der Wechsel des Substratmaterials von *p*-dotiertem zu *n*-dotiertem Cz-Si bedingt die Untersuchung neuartiger Prozesstechnologien und Prozessabläufe zur Solarzellenherstellung. Der gewählte Ansatz zur Ausbildung der unterschiedlich stark dotierten Oberflächen basiert auf einander folgenden Rohrofen-Diffusionsprozessen. Nach Ausbildung des Bor-dotierten Emitters auf der Vorderseite mittels Bortribromid ( $\text{BBr}_3$ ) als flüssige Dotierstoffquelle wird das Phosphor-dotierte „Back Surface Field“ (BSF) mittels Phosphoroxychlorid ausgebildet. Der Schwerpunkt der Prozessentwicklung liegt auf der Optimierung von  $\text{BBr}_3$ -Diffusionsprozessen in Verbindung mit der elektrischen Kontaktierung der Bor-dotierten Oberflächen mittels siebgedruckter und gefeuerter Metallkontakte. Neue Diffusionsprozesse mit integrierter Nachoxidation werden entwickelt, um tief eingetriebene Bordotierungen mit geringer Oberflächenkonzentration in einem einzigen Prozessschritt auszubilden. Die damit hergestellten Emitter weisen eine geringe Dunkelsättigungsstromdichte von  $(30 \pm 3) \text{ fA/cm}^2$  für eine texturierte und mittels  $\text{Al}_2\text{O}_3/\text{SiN}_x$  passivierte Oberfläche auf, sowie einen Schichtwiderstand von ungefähr  $120 \Omega/\text{sq}$  bei einer Profiltiefe von nahezu 850 nm. Trotz geringer maximaler Dotierkonzentration  $N_{\max}$  von nur  $(1,8 \pm 0,2) \cdot 10^{19} \text{ cm}^{-3}$

ergeben sich geringe spezifische Kontaktwiderstände  $\rho_C$  kleiner  $4 \text{ m}\Omega\text{cm}^2$  für siebgedruckte und gefeuerte Silber-Aluminium (Ag-Al) Kontakte. Aus der Theorie idealer planer Kontakte ist bekannt, dass  $\rho_C$  von  $N_{\max}$  abhängt. Erstmalig wird experimentell gezeigt, dass der tiefenabhängige Verlauf der Dotierung ebenfalls zu einer niederohmigen Kontaktausbildung beiträgt. Die Ursache hierfür liegt darin, dass Metallkristallite unterhalb der Ag-Al-Kontakte vorhanden sind, die einige 100 nm bis einige Mikrometer tief eindringen. Dies bedeutet, dass von zwei Dotierprofilen mit demselben  $N_{\max}$  aber unterschiedlicher Profiltiefe jenes mit dem tieferen Profil mit geringerem  $\rho_C$  kontaktiert werden kann. Der Zusammenhang zwischen Profiltiefe und  $\rho_C$  konnte ebenfalls unter Verwendung eines analytischen Modells nachgewiesen werden, welches auf Metallkristalliten beruht.

Die Optimierung der  $\text{BBr}_3$ -Diffusionsprozesse ermöglichte implizierte Leerlaufspannungen von bis zu  $iV_{OC} = (677 \pm 1) \text{ mV}$  für passivierte aber noch nicht metallisierte Zell-Vorläufer. Ein Gesamtverlust in der Leerlaufspannung  $V_{OC}$  von etwa  $-20 \text{ mV}$  ergibt sich für die fertiggestellten Solarzellen aus  $n$ -dotiertem Cz-Si aufgrund von Ladungsträgerrekombination unterhalb der Metallkontakte auf Vorder- und Rückseite. Da dies sowohl auf die MWT- als auch auf die Standardstruktur zutrifft, werden somit keine signifikanten MWT-spezifischen Metallisierungsverluste für  $V_{OC}$  beobachtet. Für den zuvor behandelten Bor-dotierten Emitter wird die Dunkelsättigungsstromdichte  $j_{0e,met}$  unterhalb der Ag-Al Kontakte zu etwa  $2500 \text{ fA/cm}^2$  abgeschätzt. Ein Vergleich der Ergebnisse von MWT-Solarzellen mit unterschiedlichen Emitter-Dotierprofilen zeigt, dass hauptsächlich die Profiltiefe der Parameter ist, welcher die Größe von  $j_{0e,met}$  bestimmt. Tief eingetriebene Emittoren ermöglichen somit eine signifikante Verringerung von  $j_{0e,met}$ . In Zusammenarbeit mit einer parallel laufenden Doktorarbeit ermöglicht die Anwendung eines neuartigen numerischen dreidimensionalen Simulationsansatzes detaillierte Einblicke in die Ladungsträgerrekombination unterhalb der Metallkontakte. Gezeigt wird, dass  $j_{0e,met}$ -Werte von mehr als  $1300 \text{ fA/cm}^2$  mit dem Auftreten von Metallkristalliten zusammenhängen, die so tief eindringen, dass die Ladungsträgerrekombination vor allem an deren Spitzen überexponentiell ansteigt.

Die wichtigste Komponente von MWT-Solarzellen – unabhängig vom Typ der Basisdotierung – ist der Metall-Isolator-Silicium-Kontakt in den Gebieten der externen rückseitigen Kontakte, die mit dem Emitter durch die Vorderseitenmetallisierung und den Durchkontaktierungen (Vias) verbunden sind. Die Vias und diese rückseitigen Kontakte werden mittels siebgedruckter

silber-basierter Via-Pasten metallisiert, welche während des Kontaktfeuerschritts keinen elektrischen Kontakt zum angrenzenden Silicium ausbilden dürfen, um das Auftreten von Leckströmen zu vermeiden. Zur Bestimmung der Herausforderungen, die der Übertrag des MWT-Konzepts von *p*-dotiertem auf *n*-dotiertes Cz-Si mit sich bringt, werden spezielle Teststrukturen mit beiden Basisdotierungen untersucht. Die elektrische Kontakt trennung, und somit die Vermeidung von Leckströmen, zeigt sich für die *n*-dotierten Proben als deutlich anspruchsvoller. Trotzdem weisen die gewonnenen Erkenntnisse eine vielversprechende Via-Paste für die Verwendung in MWT-Solarzellen mit *n*-Basisdotierung aus. Das erworbene Wissen konnte ebenfalls in die laufende Entwicklung der MWT-Solarzellentechnologie auf *p*-Substraten eingebracht werden.

Alle bisherigen Erkenntnisse trugen maßgeblich zur Herstellung von MWT-Solarzellen aus *n*-dotiertem Cz-Si mit einem Wirkungsgrad  $\eta$  von über 20% bei. Zwei *n*-dotierte MWT-Solarzellenstrukturen, als *nMWT* und *nMWT+* bezeichnet, werden entwickelt und können als Ausgangspunkt für weitere Entwicklungen dienen. Die *nMWT*-Solarzellen besitzen ein vollflächiges BSF und erreichen einen Spitzenwirkungsgrad von 20,2% aus der initialen Strom-Spannungs-Messung ohne vorherige Rückwärtsbelastung. Für die *nMWT+*-Solarzellen ist das BSF unterhalb der externen *p*-Kontakte entweder vollständig ausgespart oder in seiner maximalen Oberflächendotierung deutlich abgesenkt. Gleichwohl ist der Spitzenwirkungsgrad mit 20,1% vergleichbar mit dem der *nMWT*-Solarzellen. Die aufgrund angelegter Rückwärtsspannung hervorgerufenen Leckströme für die *nMWT+*-Struktur resultieren in einem Wirkungsgradverlust von kleiner 0,1%<sub>abs</sub>. Dieser Verlust ist mindestens um einen Faktor drei geringer als der für die *nMWT*-Struktur. Die Referenzzellen mit Standardkontakteierung, die ebenfalls Spitzenwirkungsgrade von 20,1% erzielen, sind für Rückwärtslast gleich anfällig wie die *nMWT+*-Solarzellen und die absoluten Verluste sind nahezu gleich. Auch die Gesamtstromstärken unter Rückwärtslast sind für die Solarzellen mit Standardkontakteierung und für die *nMWT+*-Solarzellen vergleichbar. Für die konventionelle Modultechnologie sind die auftretenden Stromstärken womöglich zu hoch. Somit sind zum aktuellen Entwicklungsstand die Herausforderungen bezüglich Rückwärtsverhalten und dessen Eignung für die Modulintegration für beide Zellstrukturen ähnlich.

Die effizienteste *nMWT+*-Solarzelle mit  $\eta = 20,1\%$  weist vor Rückwärtsbelastung eine Kurzschlussstromdichte  $j_{SC} = 40,0 \text{ mA/cm}^2$ , einen  $V_{OC} = 656 \text{ mV}$  und einen Füllfaktor  $FF = 76,6\%$  auf. Im Vergleich zur effizientesten Solar-

zelle mit Standardkontakteierung profitiert die *n*MWT+-Solarzelle von einem etwa  $0,5 \text{ mA/cm}^2$  höheren  $j_{SC}$ , da die Zellvorderseite geringer abgeschattet ist. Auch der  $V_{OC}$  ist um einige Millivolt höher. Andererseits ist der  $FF$  etwa 2%<sub>abs</sub> geringer, was hauptsächlich an Serienwiderstandsbeiträgen des verwendeten MWT-Metallisierungslayouts liegt, welches nur 20/24 externe *n*-/*p*-Kontakte zählt. Somit ist die Erhöhung der Anzahl an externen Kontakten für das MWT-Metallisierungslayout zwingend erforderlich, um den  $FF$  weiter zu steigern. Standardmäßig wird am Ende des Herstellungsprozesses vor der Strom-Spannungs-Messung die Laserkantenisolierung durchgeführt. Dennoch wurden einige Zellen auch vor jener Kantenisolierung gemessen. Die höchste Effizienz, die im Laufe dieser Arbeit erreicht wurde, erzielte in diesen Messungen eine *n*MWT-Solarzelle mit 20,4%.

Die Untersuchungen demonstrieren den erfolgreichen Übertrag des MWT-Konzepts auf *n*-dotiertes Cz-Si. In Bezug auf den Stromfluss ist das Rückwärtsverhalten der Solarzellen die größte Herausforderung, die für einen zuverlässigen Betrieb nach Moduleinkapselung überwunden werden muss.

# Appendix

## A Current transport models and specific contact resistance

This section deals with the theoretical calculation of specific contact resistances  $\rho_C$  for the different current transport mechanisms introduced in Chapter 2.4. These are the thermionic emission (TE), the thermionic field emission (TFE), and the field emission (FE); see also Fig. 2.11.

An effect which needs to be considered in practical metal-semiconductor contacts is the lowering of the Schottky barrier height  $q\phi_b$  due to image forces, when an electrical field is present. Consider a metal-vacuum system first. An electron at distance  $x$  from the metal induces a positive charge of same magnitude on the metal surface. The resulting force of attraction between electron and induced positive charge is equivalent to the force resulting between the electron and an equal fictive positive charge with distance  $-x$  from the metal surface, the so-called image charge. This scenario can also be applied to metal-semiconductor contacts, leading to a reduction of the Schottky barrier height of [105,108]

$$q\Delta\phi_b = q \left( \frac{q^3 N \left( V_{bi} - V_{ext} - \frac{k_B T}{q} \right)}{8\pi^2 (\varepsilon_r \varepsilon_0)^3} \right)^{1/4}, \quad (A.1)$$

with elementary charge  $q$ , semiconductor charge carrier concentration  $N$ , built-in potential  $V_{bi}$  (Eq. (2.41)), externally applied potential  $V_{ext}$ , Boltzmann constant  $k_B$ , temperature  $T$ , circle number  $\pi$ , dielectric constant of the semiconductor  $\varepsilon_r$ , and permittivity of the vacuum  $\varepsilon_0$ . For calculating the specific contact resistance  $\rho_C$ ,  $V_{ext} = 0$  V (according to the definition of  $\rho_C$  in Eq. (A.3)).

The effective Schottky barrier height  $q\phi_b'$  is then given by

$$q\phi_b' = q\phi_b - q\Delta\phi_b. \quad (A.2)$$

## Appendix

---

In general,  $\rho_C$  is defined as the inverse of the derivative of the function of current density  $j$  and voltage  $V$  at the voltage zero point ( $V = 0$  V),

$$\rho_C = \left( \frac{\partial j}{\partial V} \right)_{V=0\text{ V}}^{-1}. \quad (\text{A.3})$$

The resulting formulae for calculating  $\rho_C$  for each of the three current transport mechanisms are summarized in Table A.1. The equations for TFE and FE are only valid for certain value ranges of  $N$ , as described in the literature, e.g. in Ref. [104].

The characteristic energies  $E_0$  and  $E_{00}$  are defined as [109]

$$E_0 = E_{00} \coth\left(\frac{E_{00}}{k_B T}\right), \text{ and} \quad (\text{A.4})$$

$$E_{00} = \frac{q\hbar}{2} \left( \frac{N}{m_t^* \varepsilon_r \varepsilon_0} \right)^{1/2}, \quad (\text{A.5})$$

with reduced Plank's constant  $\hbar$ , and effective charge carrier tunneling mass  $m_t^*$  (given as fraction of the electron mass  $m_0$ ).

$E_0$  and  $E_{00}$  can also be referred to as tunneling energies, which means that above a certain charge carrier concentration  $N$ , tunneling processes are important; see Fig. A.1. This is reflected by the increase of  $E_{00}$  with  $N$ , indicating the barrier getting thinner for higher doping concentrations. The ratio  $k_B T/E_{00}$  can be used as a measure of the relative importance of TE

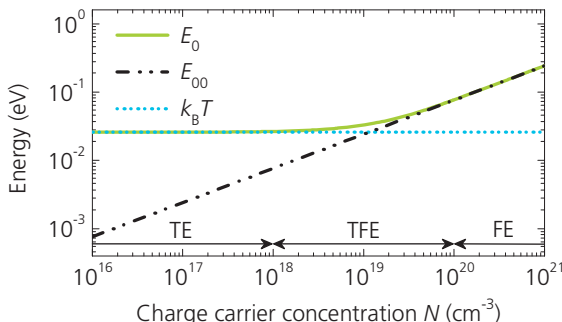


**Fig. A.1.** Tunneling energies  $E_0$  (Eq. (A.4)) and  $E_{00}$  (Eq. (A.5)) for silicon as function of doping concentration  $N$  at  $T = 300$  K (used parameters:  $m_t^* = 0.5 m_0$ ,  $\varepsilon_r = 11.7$  [269]; see also Table 5.2). The thermal energy  $k_B T$  is also shown.

## A Current transport models and specific contact resistance

---

**Table A.1.** Formulae for calculating  $\rho_C$  for the different current transport mechanisms between metal and semiconductor (effective Richardson constant  $A^*$ , Euler number  $e$ , constants  $c_{\text{TFE}}$  and  $c_{\text{FE}}$ , characteristic energies  $E_0$  (Eq. (A.4)) and  $E_{00}$  (Eq. (A.5)), and Fermi energy  $E_F$  with respect to the energy band edge (Eqs. (A.12) and (A.13)).

Current transport mechanism / Specific contact resistance $\rho_C$
~ Thermionic emission (TE) [108, p. 304]
$\rho_C(\text{TE}) = \frac{k_B}{qA^*T} \exp\left(\frac{q\phi_b'}{k_B T}\right) \quad (\text{A.6})$
~ Thermionic field emission (TFE) [104,238]
$\rho_C(\text{TFE}) = c_{\text{TFE}} \frac{k_B}{qA^*T} \exp\left(\frac{q\phi_b'}{E_0}\right) \quad (\text{A.7})$
with $c_{\text{TFE}} = \frac{k_B T \cosh\left(\frac{E_{00}}{k_B T}\right) \sqrt{\coth\left(\frac{E_{00}}{k_B T}\right)}}{\sqrt{\pi(q\phi_b' + E_F) E_{00}}} \exp\left(\frac{E_F}{E_0} - \frac{E_F}{k_B T}\right) \quad (\text{A.8})$
~ Field emission (FE) [104,238]
$\rho_C(\text{FE}) = c_{\text{FE}} \frac{k_B}{qA^*T} \exp\left(\frac{q\phi_b'}{E_{00}}\right) \quad (\text{A.9})$
with $c_{\text{FE}} = \left[ \frac{\pi}{\sin\left(\frac{\pi k_B T}{2E_{00}} \ln\left(\frac{4q\phi_b'}{E_F}\right)\right)} - \frac{2E_{00}}{k_B T \ln\left(\frac{4q\phi_b'}{E_F}\right)} \exp\left(-\frac{E_F \ln\left(\frac{4q\phi_b'}{E_F}\right)}{2E_{00}}\right) \right]^{-1} \quad (\text{A.10})$

processes with respect to FE (tunneling) processes: TE dominates for lightly doped semiconductors where  $k_B T/E_{00} \gg 1$ , whereas FE dominates for heavily doped semiconductors where  $k_B T/E_{00} \ll 1$ . In between, TFE dominates for semiconductors with intermediate doping where  $k_B T/E_{00} \approx 1$ . It is clear that  $E_0$  connects the TE regime with the FE regime.

*Varahramyan and Verret* [238] combined the TFE and FE tunneling mechanisms into a unified model for  $\rho_C$ ,

$$\rho_C(\text{TFE/FE}) = \bar{c} \frac{k_B}{qA^*T} \exp\left(\frac{q\phi_b'}{E_0}\right), \quad (\text{A.11})$$

with doping-type dependent constant  $\bar{c}$  being 0.425 for  $n$ -type silicon, and 0.355 for  $p$ -type silicon, using Boltzmann statistics to determine the charge carrier distribution at  $T = 300$  K.

To the author's knowledge, in all publications dealing with the calculation of  $\rho_C$  for metal-silicon contacts by using the different current transport mechanisms, Boltzmann statistics is used throughout for determination of the charge carrier distribution and thus, for the calculation of the location of the Fermi energy  $E_F$  relative to the corresponding band edge. Considering all dopants to be ionized, the location of  $E_F$  relative to the conduction band edge energy  $E_C$  in  $n$ -doped silicon is given by [108, p. 27]

$$E_C - E_F = k_B T \ln\left(\frac{N_C}{N}\right). \quad (\text{A.12})$$

and relative to the valence band edge energy  $E_V$  in  $p$ -doped silicon by

$$E_F - E_V = k_B T \ln\left(\frac{N_V}{N}\right). \quad (\text{A.13})$$

$N_C$  and  $N_V$  are the densities of states in the conduction band and in the valence band, respectively.

However, for highly doped silicon (i.e.  $N > 10^{19} \text{ cm}^{-3}$ ), the charge carrier distribution by Boltzmann statistics is inaccurate in determining  $E_F$  [270, 271]. A more accurate model to describe the charge carrier distribution is given by, e.g. the Joyce-Dixon approximation [270] reflecting Fermi-Dirac statistics. To be consistent with literature, Boltzmann statistics is used within this work to calculate  $E_F$  according to Eq. (A.12) and Eq. (A.13). For the analytical calculations of  $\rho_C$  performed in Chapter 5.4, the maximum dopant concentrations  $N$  are lower than  $9 \cdot 10^{19} \text{ cm}^{-3}$ . Hence, the inaccuracy in determination of the  $E_F$  location by using Boltzmann statistics is still rather low for the occurring range of dopant concentrations [271].

In Eq. (A.12) and Eq. (A.13), the density of states in the conduction band  $N_C$  and in the valence band  $N_V$  are required. The former is  $N_C = 2.86 \cdot 10^{19} \text{ cm}^{-3}$  for silicon at  $T = 300$  K [46]. To determine  $N_V$ , consider the intrinsic charge carrier density  $n_i$  of a semiconductor first, which is given by [108, p. 19]

$$n_i^2 = N_C N_V \exp\left(-\frac{E_g}{k_B T}\right). \quad (\text{A.14})$$

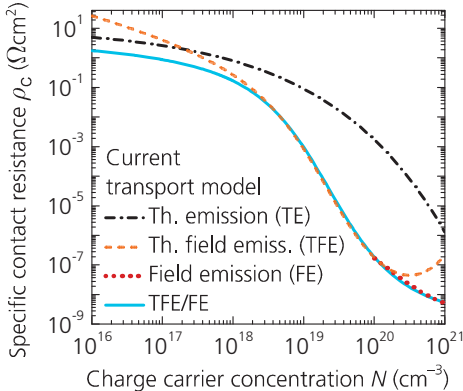


**Fig. A.2.** Specific contact resistances  $\rho_C$  on  $p$ -doped silicon as function of charge carrier concentration  $N$  for the different current transport models (used parameters: see Table 5.2). Image force barrier lowering is taken into account.

With the values for silicon of  $n_i = 9.65 \cdot 10^9 \text{ cm}^{-3}$  [232], and  $E_g = 1.1242 \text{ eV}$  [107], the density of states in the valence band calculates to  $N_V = 2.503 \cdot 10^{19} \text{ cm}^{-3}$ .

Fig. A.2 exemplarily shows the calculated  $\rho_C$  for  $p$ -doped silicon as function of  $N$  for the discussed different current transport models and the input parameters summarized in Table 5.2. As it is clear,  $\rho_C$  decreases significantly with increasing  $N$ . Because of that, it is important to dope the silicon surfaces sufficiently in order to achieve low  $\rho_C$ . The unified model for  $\rho_C$  from Varahramyan and Verret (TFE/FE, Eq. (A.11)) describes the TFE (Eq. (A.7)) and FE (Eq. (A.9)) very well for  $N > 10^{18} \text{ cm}^{-3}$ . On the other hand, for  $N \leq 10^{18} \text{ cm}^{-3}$ , this unified model does not consider TE (Eq. (A.6)), which is becoming more and more important towards lower  $N$ .

## B Measurement and characterization methods

This section describes some of the measurement and characterization methods used within this thesis. The methods used, which are not listed in the following, have been already introduced within the chapters.

### B.1 Current-voltage measurements of bifacial n-type solar cells

The  $n$ -type solar cells investigated feature a grid structure on both sides, as shown in Fig. 3.7(b) and Fig. 3.11. That means that light can penetrate

the cells not only from the front but also from the rear side. In this work, the fabricated solar cells are illuminated from the front side only. Due to their bifacial property, the surface present underneath the cells during current-voltage ( $I-V$ ) measurements (performed according to the standard test conditions [50], see also Chapter 2.2.3) impacts the results. In particular, the higher the surface reflection, the higher the short-circuit current density  $j_{SC}$ . Fig. B.1 depicts the reflectivity of three different chuck surfaces, as they have been used for measuring  $n$ -type H-pattern and  $n$ -type MWT solar cells. The black foil reflects less than 5% from the incident light over the wavelength range between  $\lambda = 200$  nm and  $\lambda = 1200$  nm. In contrast, the white foil and the gold-plated surface have significantly higher reflectivity, whereby the white-foil-coated chuck has the surface with the highest reflectivity over almost the entire wavelength range considered.

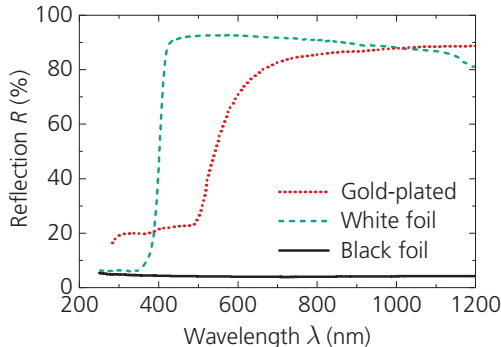


**Fig. B.1.** Measured reflectivity of different solar cell mounting chuck surfaces. The data from the gold-plated chuck is taken from Ref. [272].

**Table B.1.** Summary of different measurement setups for determining current-voltage data for  $n$ -type solar cells within this work. Every fabricated solar cell is measured with an industrial cell tester at *Fraunhofer ISE PV-TEC*. The best performing cells are also measured at *Fraunhofer ISE CalLab PV Cells*. The measurement uncertainty on conversion efficiency is 3% (*PV-TEC*) and 2% relative (*CalLab*).

Cell type	Location	Cell measurement on	Electr. conductive chuck
H-pattern	<i>PV-TEC</i>	Conveyor belt (ind. cell tester)	–
	<i>CalLab</i>	Chuck with <i>black</i> foil	No
MWT	<i>PV-TEC</i>	Chuck with <i>gold-plated</i> surface	Yes
	and <i>CalLab</i>	Chuck with <i>black</i> foil	No
		Chuck with <i>white</i> foil	No

A summary of the used  $I$ - $V$  measurement setups shows Table B.1. All  $n$ -type H-pattern cells with three external busbar contacts on either side are initially tested on the conveyer belt of an industrial and fully automated cell tester “A” at *Fraunhofer ISE PV-TEC*. Contact bars with local contact units contact the busbars on front and rear side (i.e. one pin for current and voltage each). Each front contact bar has 15 contact units, whereas the rear contact bars only have 8 contact units due to the conveyer belt. Also, the  $n$ -type H-pattern cells with five busbar contacts on either side are initially tested with an industrial cell tester “B”, but this cell tester measures the cells placed in a holder with 11 contact units per contact row and side. Subsequently, a selection of the best performing H-pattern cells is measured at *Fraunhofer ISE CalLab PV Cells* on chucks either with black-foil-coated or gold-plated surface [272]. Both chucks use vacuum suction to fix the cells; the number of contact units per contact row for each polarity is given in Table B.2. For both chucks, contact bars with 11 local contact units contact the cells’ front busbars. On the black-foil-coated chuck, the rear busbar contacts are also contacted by 11 local contact units embedded into the chuck surface. For the measurement on the gold-plated chuck, the rear side grid completely contacts the electrically conductive chuck surface. This leads to an overestimation of the fill factor  $FF$ . To account for this issue, the  $FF$  obtained from the measurements on the black-foil-coated chuck are considered also for the measurements on the gold-plated surface. Finally, based on the *CalLab* data for the measurements on black foil, the cell tester  $I$ - $V$  results are corrected accordingly for each individual H-pattern solar cell. Note that no *CalLab* measurements on black foil are performed for the H-pattern cells with five busbar contacts. How-

**Table B.2.** Summary of the number of local contact units (#CU) for each contact row for the measurements performed on different chucks (*n.m.* means *not measured*). Each local contact unit consists of in sum two to three measurement pins for current and voltage. The  $p$ -type contact ( $p$ ) corresponds to the emitter contact, the  $n$ -type contact ( $n$ ) to that of the phosphorus doping. The  $n$ -type polarity is contacted by the gold-plated (conductive) chuck on its entire metallized area.

Cell type (#Contact rows for each polarity)	Black foil		White foil		Gold-plated
	#CU( $p$ )	#CU( $n$ )	#CU( $p$ )	#CU( $n$ )	#CU( $p$ )
H-pattern (3)	11	11	<i>n.m.</i>	<i>n.m.</i>	11
H-pattern (5)	<i>n.m.</i>	<i>n.m.</i>	<i>n.m.</i>	<i>n.m.</i>	11
MWT (3)	9	8	<i>n.m.</i>	<i>n.m.</i>	—
MWT (4)	6	5	6	5	—

ever, for these cells  $I$ - $V$  data on black foil is also given in Fig. 7.1. This data is corrected with respect to the current offset between gold-plated and black-foil-coated chuck observed for the three-busbar H-pattern cells.

The  $n$ -type MWT solar cells are also initially tested with the industrial cell tester “A” on chucks with black or white foil. These chucks differ from the above mentioned chucks, as both polarities have to be locally contacted on the rear side of the MWT cells [273]. The fixation of the MWT cells on the chuck is also realized by vacuum suction; the number of local contact units per contact row for each polarity is given in Table B.2. As illustrated in Fig. 3.11, MWT solar cells with three or four contact rows per polarity are fabricated within this thesis. Again, the best performing MWT cells are measured at the *CalLab*, and the cell tester  $I$ - $V$  results are also corrected with respect to these data.

When the performance of H-pattern solar cells is compared with that of MWT solar cells within this work, it has to be noted that the white foil and the gold-plated surface differ somewhat in their reflectivities.

From Table B.2 it is also seen that during the  $I$ - $V$  measurements, the MWT solar cells are contacted by a lower number of contact units per contact row compared with the H-pattern cells. This fact results in higher series resistance for the MWT solar cells. In principle, this number of contact units per contact row can be increased, but would necessitate the making of a suitable measurement chuck. By the transition from three to four contact rows for the MWT cells (see also Fig. 3.11), such a new chuck was made. Further adaption of the metallization geometry with respect to the external contact pads has not been performed throughout this work. The room for improvement in terms of lower series resistances is investigated by other authors, see e.g. the references [197,198], and it is also shown in Chapter 7.7.

## B.2 Electrochemical capacitance-voltage measurement

Depth dependent charge carrier concentrations  $N(d)$  close to the surface of a sample are determined by means of the electrochemical capacitance-voltage (ECV) method [81]. The resulting profiles  $N(d)$  are also referred to as *doping profiles* within this work, as the measured  $N(d)$  at a given depth equals approximately the dopant concentration. Refer to Ref. [31, pp. 61–106] for a detailed description of the ECV technique for its application on silicon surfaces and its limitations.

The near surface charge carrier concentration  $N$  for a certain depth  $d$  is determined by capacitance-voltage measurements and reads

$$N = \frac{2}{q\epsilon_r\epsilon_0 A^2 \frac{d}{dV} C^{-2}}, \quad (\text{B.1})$$

with the elementary charge  $q$ , the dielectric constant of the semiconductor  $\epsilon_r$ , the permittivity of the vacuum  $\epsilon_0$ , and the contact area between the sample and an electrolyte  $A$ . The capacitance  $C$  is measured by periodic variation of the voltage  $V$  between the semiconductor and the electrolyte. The assumed contact area  $A$ , which depends on the sample's surface topography and the area of the sealing ring  $A_0$ ,

$$A = f_A A_0, \quad (\text{B.2})$$

is one major source of uncertainty. The area factor  $f_A$  denotes the ratio of the sample's surface area to an absolutely planar surface. The typically applied values are  $1.0 \leq f_A \leq 1.1$  for alkaline saw-damage etched surfaces and  $1.6 \leq f_A \leq 1.7$  for alkaline textured ones [274]. Throughout this work,  $f_A$  is adapted so that the profile's calculated sheet resistance matches the measured sheet resistance at the test position prior to ECV measurement. The value for  $A_0$  is determined by optical microscopy of the etch crater. In order to obtain depth-resolved measurements, controlled etching steps are performed between two consecutive capacitance-voltage measurements.

The ECV measurements are performed with the automated system *WEP CVP21*. The assumed errors specified in the graphs which show ECV measurements are  $\pm 5\%$  for the depth  $d$  and  $\pm 10\%$  for the charge carrier concentration  $N(d)$ . For extracted values of  $d$  from the graphs, the total error is assumed to be  $\pm 10\%$ .

### B.3 Inductive sheet resistance measurement

With the inductive measuring method, sheet resistances of samples can be determined contactless [275]. The method is applied to control the quality/stability of high-temperature diffusion processes. For this purpose, the bulk sheet resistance  $R_{\text{sh,bulk}}$  of the samples is measured prior to diffusion, and the total sheet resistance  $R_{\text{sh,tot}}$  after diffusion. For the calculation of the sheet resistance  $R_{\text{sh}}$  of the highly doped surface layers, a parallel con-

nection of the differently doped layers is assumed [199]. Depending on the symmetry of the sample,  $R_{sh}$  is calculated by

$$R_{sh} = \frac{R_{sh,bulk} R_{sh,tot}}{R_{sh,bulk} - R_{sh,tot}} \quad \text{for one-sided diffusion,} \quad (\text{B.3})$$

$$R_{sh} = 2 \frac{R_{sh,bulk} R_{sh,tot}}{R_{sh,bulk} - R_{sh,tot}} \quad \text{for double-sided diffusion.} \quad (\text{B.4})$$

Within this work, two different measuring devices are used to obtain  $R_{sh}$  for the boron- and phosphorus-doped surface layers after  $\text{BBr}_3$  and  $\text{POCl}_3$  diffusion, respectively. This is because the diffusion processes are performed in different tube furnace systems with separate characterization devices. The schematic measurement patterns of both inductive measuring devices shows Fig. B.2. The sheet resistance  $R_{sh,w}$  of a single wafer  $w$  is measured by three sensors  $s$  with a diameter of 25 mm and a sensor-to-sensor distance of (a) 52 mm or (b) 35 mm. Every sensor records (a) 36 or (b) 24 measurement points  $p$  while the sample is moving over the sensors parallel to the horizontal wafer edges. The mean sheet resistance for a single wafer is given by

$$R_{sh,w} = \frac{1}{3p} \left( \sum_{s=1}^3 \sum_{i=1}^p R_{sh,s,i} \right), \quad (\text{B.5})$$

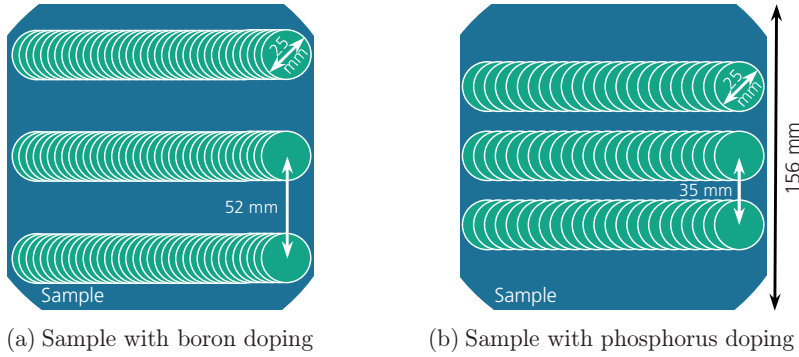


**Fig. B.2.** Pattern of  $R_{sh}$  measurements based on inductive coupling. Depending on the doping type of the highly doped surfaces, different measuring devices are used in (a) and (b). The sample with 156 mm edge length moves parallel to the horizontal wafer edges over three stationary coils with a diameter of 25 mm each and a distance of (a) 52 mm or (b) 35 mm. The number of measurement points per row is (a) 36 and (b) 24.

wherein it is  $p = 36$  for the samples with boron doping and  $p = 24$  for the samples with phosphorus doping. The relative standard deviation

$$\sigma_w = \frac{\left( \frac{1}{3p} \sum_{s=1}^3 \sum_{i=1}^p (R_{\text{sh},s,i} - R_{\text{sh},w})^2 \right)^{1/2}}{R_{\text{sh},w}}, \quad (\text{B.6})$$

is defined as the standard deviation of all measured  $R_{\text{sh},s,i}$  of a single wafer relative to the wafer's mean sheet resistance  $R_{\text{sh},w}$ . In this work,  $R_{\text{sh},w}$  and  $\sigma_w$  are simply named  $R_{\text{sh}}$  and  $\sigma$  in case of inductive measurements.

#### B.4 Transmission line model

For the experimental determination of specific contact resistances  $\rho_C$ , the transmission line model (TLM) is utilized [201,202]. The TLM measurement is based on the 4-point-probe technique. This means that one pin pair introduces the measuring current into the sample while another pin pair measures the voltage drop present in between.

The contact structure applied for the TLM measurements is shown in Fig. B.3(a). The respective samples are cut out directly from complete solar cells. The measured total resistance  $R_{\text{tot}}$  between two adjoined finger contacts is the sum of two times the contact resistance  $R_C$  and the sheet resistance  $R_{\text{sh}}$  between the both,

$$R_{\text{tot}} = 2R_C + R_{\text{sh}}. \quad (\text{B.7})$$

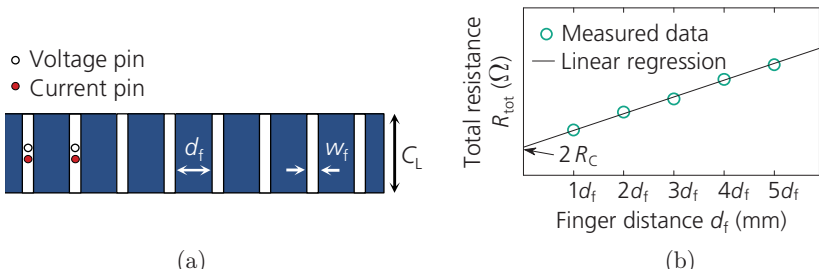


**Fig. B.3.** (a) Schematic of the top view of a TLM sample illustrating an exemplary pin configuration for determining the total contact resistance  $R_{\text{tot}}$ . (b) Evaluation method to extract the contact resistance  $R_C$  from the various measurements of  $R_{\text{tot}}$  for increasing finger distances  $d_f$ . The intersection of the linear regression with the y-axis corresponds to twice the  $R_C$ .

Further measurements are performed with successively increased distances between the two fingers which are contacted by the pins. Based on these measurements,  $R_C$  can be extracted from the  $y$ -intercept by linear regression as shown in Fig. B.3(b). It is given by

$$R_C = \frac{1}{2} R_{\text{tot}}(d_f = 0). \quad (\text{B.8})$$

In order to compare different samples with different contact lengths  $C_L$ , contact widths  $w_f$ , and contact distances  $d_f$ , it is meaningful to express  $R_C$  as specific contact resistance  $\rho_C$ . Utilizing the transfer length  $L_T$ ,  $\rho_C$  reads [31, p. 141]

$$\rho_C = R_C \cdot C_L \cdot L_T \cdot \tanh\left(\frac{w_f}{L_T}\right). \quad (\text{B.9})$$

The transfer length  $L_T$  defines the distance below the contact fingers, after which the voltage is decreased to  $1/e$  in comparison with its initial value at the beginning of the contact finger. More information on the determination of  $L_T$  can be found, e.g. in Ref. [31, pp. 140–143]. Sometimes, this model to determine  $\rho_C$  is also referred to as transfer length method, emphasizing the importance of the transfer length  $L_T$ .

For the TLM measurements, a measuring current of 10 mA is applied. The TLM samples have a width of  $C_L = 10$  mm. Eight fingers are considered for a single measurement of  $\rho_C$ , which is performed by utilizing a fully automated system.

## C Structuring methods for the rear phosphorus doping

To fabricate  $n$ -type MWT solar cells with structured phosphorus doping underneath the external  $p$ -type contacts, as present in the  $n$ MWT+ cell structure, Fig. 3.9(b), several structuring options are available (see also the discussion in section 3.5).

The first method pursued within this work is the structuring of the diffusion barrier layers prior to  $\text{POCl}_3$  diffusion using inkjet-printed masking resist and wet-chemical etching. The second method employed is the structuring of the phosphorus-doped surfaces by laser irradiation subsequent to  $\text{POCl}_3$  diffusion.

### C.1 Inkjet-assisted structuring of diffusion barrier layers

The employed approach to structure the diffusion barrier layers prior to  $\text{POCl}_3$  diffusion is based on inkjet printing a masking resist and subsequent wet-chemical etching of the uncovered areas in buffered HF [191–193]. A corresponding schematic process sequence is illustrated in Fig. C.1. Following  $\text{BBr}_3$  diffusion and BSG etching, the rear side of the wafers is coated with the diffusion barrier layer applied by PECVD. The masking resist is locally applied by means of inkjet printing prior to the wet-chemical etching of the exposed diffusion barrier layer in buffered HF. Subsequently, the masking resist is stripped in baths with acetone and isopropanol, followed by the application of the front PECVD diffusion barrier layer. Finally, the phosphorus-doped BSF is formed during  $\text{POCl}_3$  diffusion, and both the PSG as well as the diffusion barrier layers on either side are removed in the PSG etch.

The undercutting of the resist during etch in buffered HF is negligible for the diffusion barrier layer and the structure dimensions used within this work. For example, the round contact pads for the four-busbar layout, Fig. 3.11(b), have a diameter of 2.5 mm. The diameter of the inkjet-printed round pads is about 3.3 mm. The diameters of the resulting structured areas are in any case larger than 3.2 mm. Hence, the alignment during screen printing with respect to these not highly phosphorus-doped areas does not constitute a challenge for the utilized structure dimensions and clearances.

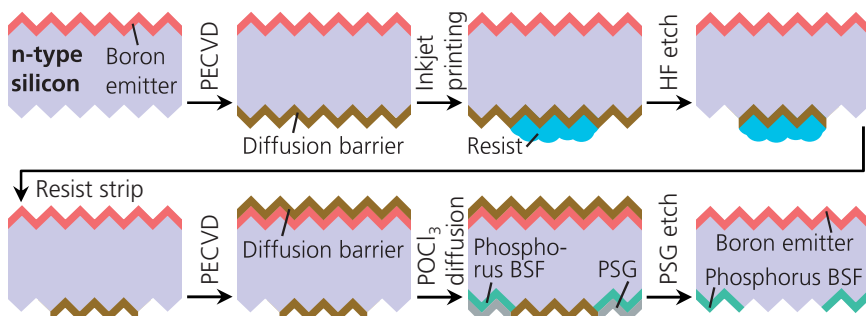


**Fig. C.1.** Schematic process sequence to realize structured rear side phosphorus dopings by means of inkjet-assisted structuring of diffusion barrier layers and subsequent  $\text{POCl}_3$  diffusion. In case the boron-doped front side is already covered with a diffusion barrier layer, then the masking resist need to be also applied on the complete front side surface.

## C.2 Redistribution of phosphorus doping by laser irradiation

Another method to realize structured phosphorus dopings on the rear side of *n*-type MWT solar cells is based on the use of laser processes. A schematic process sequence utilizing two different approaches is illustrated in Fig. C.2. Initially, the PECVD diffusion barrier layer is applied onto the already boron-doped front surface. The phosphorus BSF and the PSG layer are formed on the rear side during the subsequently performed  $\text{POCl}_3$  diffusion. In the PSG etch, both the front diffusion barrier layer and the rear PSG layer are removed. Thus, the cell precursor features full-area boron- and phosphorus-doped surfaces on front and rear side, respectively.

Two different approaches are employed, namely “laser drive-in”, Fig. C.2(a), and “laser ablation”, Fig. C.2(b). The used laser types and some of their characteristic parameters are summarized in Table C.1. For laser drive-in, the dopants are redistributed deeper into the silicon wafer by thermally excited diffusion processes [194] and the surface is locally leveled; see Fig. C.2(a) and Fig. 7.22(a). This leads to both a decrease in maximum dopant concentration at the surface and to a deepening of the doping profile; see Fig. 7.23(a). In case of laser ablation, the highly phosphorus-doped

**Table C.1.** Some characteristic parameters of the lasers used to structure the phosphorus-doped surface on the rear side.

Approach	Laser type	Wavelength	Frequency
Laser drive-in	Jenoptik IR50	1030 nm	20 kHz
Laser ablation	Lumera Super Rapid	532 nm	100 kHz

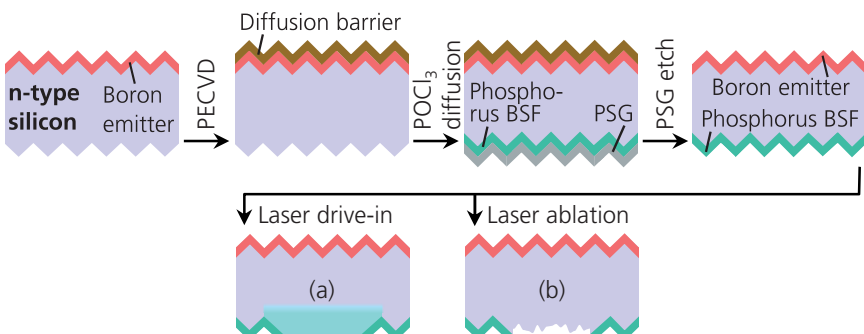


**Fig. C.2.** Schematic process sequence to realize a structured phosphorus doping by means of laser irradiation after  $\text{POCl}_3$  diffusion: (a) laser drive-in and (b) laser ablation.

layer is locally vaporized [194], and a rather rough and disordered surface remains; see Fig. C.2(b) and Fig. 7.22(b).

The  $I$ - $V$  characteristics obtained on white foil from the experiment in Chapter 7.6, in which these structuring methods are tested on  $n$ -type Cz-Si MWTSolar cells along with two other reference groups, are summarized in Fig. C.3.

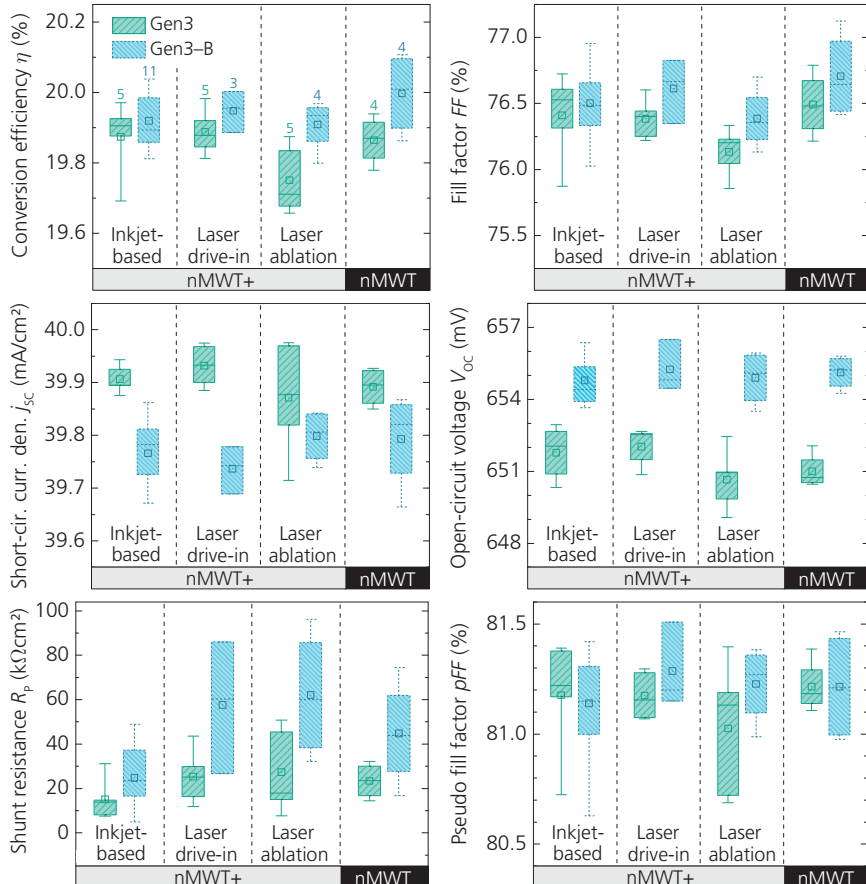


**Fig. C.3.**  $I$ - $V$  data on white foil for the  $n$ -type Cz-Si nMWT+ and nMWT solar cells (cell area: 239 cm<sup>2</sup>) with boron emitters Gen3 and Gen3-B and different rear-side structuring from the experiment in Chapter 7.6. All cells are initially tested after laser edge isolation with an industrial cell tester without reverse bias load. Some of the most efficient cells are then measured at *Fraunhofer ISE CalLab PV cells*. The data for the other cells is corrected with respect to the corresponding *CalLab* measurements.

## D Parameters for calculation of series resistance contributions

**Table D.1.** Summary of values for the analytical calculation of series resistance contributions for  $n$ -type H-pattern and nMWT+ solar cells in Table 7.5 (page 166) using the tool *Gridmaster* [265]. The data given are determined experimentally (in case measurements are required). Structures marked with \* have been double printed.

	Unit	Cell type	
		H-pattern	$n$ MWT+
Wafer edge length	(mm)	156	
Wafer thickness	( $\mu\text{m}$ )	190	
Specific bulk resistance	( $\Omega\text{cm}$ )	1.5	
(Pseudo-) Busbar number per polarity	1	3	4
<i>Front side</i>	Sheet resistance boron emitter (Gen1)	( $\Omega/\text{sq}$ )	70
	Finger number	1	84
	Finger width	( $\mu\text{m}$ )	58
	Finger height	( $\mu\text{m}$ )	27*
	Busbar width (tapered for $n$ MWT+)	(mm)	1.5      0.1 – 0.2
	(Pseudo-) Busbar height	( $\mu\text{m}$ )	18*      22*
	Specific line resistance (Ag-Al1)	( $\mu\Omega\text{cm}$ )	3.0
	Specific contact resistance (Ag-Al1)	( $\text{m}\Omega\text{cm}^2$ )	4.5
	Number contact pins per busbar	1	11      –
<i>Rear side</i>	Via resistance	( $\text{m}\Omega$ )	–      4
	Sheet resistance phosphorus BSF (Phos2)	( $\Omega/\text{sq}$ )	60
	Finger number	1	93
	Finger width	( $\mu\text{m}$ )	76
	Finger height	( $\mu\text{m}$ )	18
	Busbar width	(mm)	1.5      0.5
	Busbar height	( $\mu\text{m}$ )	12
	Specific line resistance (Ag1)	( $\mu\Omega\text{cm}$ )	2.5
	Specific contact resistance (Ag1)	( $\text{m}\Omega\text{cm}^2$ )	3.0
	Number contact pins per busbar	1	11      –
	Number $p$ -type / $n$ -type contact pads	1	–      24 / 20
	Radius BSF gap / contact gap	(mm)	–      1.65 / 1.9

# Bibliography

- [1] Bundesanstalt für Geowissenschaften und Rohstoffe (BGR), “Energiestudie 2014 - Reserven, Ressourcen und Verfügbarkeit von Energierohstoffen (18)”, Hannover, Germany, 2014.
- [2] P. Würfel, “Physics of solar cells - from principles to new concepts”, *Wiley-VCH*, Weinheim, Germany, 2005.
- [3] SolarPower Europe, “Global market outlook for solar power 2015 – 2019”, *URL*: <http://www.solarpowereurope.org> (last visited on September 30, 2015).
- [4] ITRPV, “International Technology Roadmap for Photovoltaic (ITRPV) - Results 2014”, *URL*: <http://www.itrpv.net/Reports/Downloads/2015/> (last visited on September 30, 2015).
- [5] M. Metayer, C. Breyer, and H.-J. Fell, “The projections for the future and quality in the past of the World Energy Outlook for solar PV and other renewable energy technologies”, in *Proceedings of the 31st European Photovoltaic Solar Energy Conference and Exhibition*, Hamburg, Germany, 2015, pp. 3212–3238.
- [6] J. Czochralski, “Ein neues Verfahren zur Messung der Kristallisationsgeschwindigkeit der Metalle”, *Zeitschrift für Physikalische Chemie*, no. 92, pp. 219–221, 1918.
- [7] D. Macdonald, and L. J. Geerligs, “Recombination activity of interstitial iron and other transition metal point defects in *p*- and *n*-type crystalline silicon”, *Applied Physics Letters*, vol. 85, no. 18, pp. 4061–4063, 2004.
- [8] S. Wilking, J. Engelhardt, S. Ebert, C. Beckh, A. Herguth, and G. Hahn, “High speed regeneration of BO-defects: improving long-term solar cell performance within seconds”, in *Proceedings of the 29th European Photovoltaic Solar Energy Conference and Exhibition*, Amsterdam, Netherlands, 2014, pp. 366–372.

- [9] B. J. Hallam, P. G. Hamer, S. Wang, L. Song, N. Nampalli, M. D. Abbott, C. E. Chan, D. Lu, A. M. Wenham, L. Mai, N. Borojevic, A. Li, D. Chen, M. Y. Kim, A. Azmi, and S. Wenham, “Advanced hydrogenation of dislocation clusters and boron-oxygen defects in silicon solar cells”, *Energy Procedia*, vol. 77, pp. 799–809, 2015.
- [10] E. van Kerschaver, R. Einhaus, J. Szlufcik, J. Nijs, and R. Mertens, “A novel silicon solar cell structure with both external polarity contacts on the back surface”, in *Proceedings of the 2nd World Conference on Photovoltaic Energy Conversion*, Vienna, Austria, 1998, pp. 1479–1482.
- [11] E. Lohmüller, B. Thaidigsmann, M. Pospischil, U. Jäger, S. Mack, J. Specht, J. Nekarda, M. Retzlaff, A. Krieg, F. Clement, A. Wolf, D. Biro, and R. Preu, “20% efficient passivated large-area metal wrap through solar cells on boron-doped Cz silicon”, *IEEE Electron Device Letters*, vol. 32, no. 12, pp. 1719–1721, 2011.
- [12] B. Thaidigsmann, M. Linse, A. Wolf, F. Clement, D. Biro, and R. Preu, “The path to industrial production of highly efficient metal wrap through silicon solar cells”, *Green: The International Journal of Sustainable Energy Conversion and Storage*, vol. 2, no. 4, pp. 171–176, 2012.
- [13] W. Yin, X. Wang, F. Zhang, and L. Zhang, “19.6% cast mono-MWT solar cells and 268 W modules”, *IEEE Journal of Photovoltaics*, vol. 3, no. 2, pp. 697–701, 2013.
- [14] B. Thaidigsmann, M. Hendrichs, S. Nold, E. Lohmüller, A. Wolf, F. Clement, D. Biro, and R. Preu, “P-type MWT solar cells: current status and future expectations”, in *Proceedings of the 28th European Photovoltaic Solar Energy Conference and Exhibition*, Paris, France, 2013, pp. 1099–1104.
- [15] N. Guillemin, L. J. Geerligs, R. C. G. Naber, W. Eerenstein, and A. W. Weeber, “High Efficiency *n*-type metal wrap through Si solar cells for low-cost industrial production”, in *Proceedings of the 25th European Photovoltaic Solar Energy Conference and Exhibition*, Valencia, Spain, 2010, pp. 1429–1431.
- [16] N. Guillemin, B. J. B. Heurtault, L. J. Geerligs, and A. W. Weeber, “Development towards 20% efficient Si MWT solar cells for low-cost industrial production”, *Energy Procedia*, vol. 8, pp. 9–16, 2011.
- [17] W. Shockley, “The theory of *p-n* junctions in semiconductors and *p-n* junction transistors”, *Bell System Technical Journal*, vol. 28, no. 3, pp. 435–489, 1949.
- [18] W. van Roosbroeck, and W. Shockley, “Photon-radiative recombination of electrons and holes in germanium”, *Physical Review*, vol. 94, no. 6, pp. 1558–1560, 1954.

- 
- [19] T. Trupke, M. A. Green, P. Würfel, P. P. Altermatt, A. Wang, J. Zhao, and R. Corkish, "Temperature dependence of the radiative recombination coefficient of intrinsic crystalline silicon", *Journal of Applied Physics*, vol. 94, no. 8, pp. 4930–4937, 2003.
  - [20] A. Richter, F. Werner, A. Cuevas, J. Schmidt, and S. W. Glunz, "Improved parameterization of Auger recombination in silicon", *Energy Procedia*, vol. 27, pp. 88–94, 2012.
  - [21] W. Shockley, and W. Read, "Statistics of the recombinations of holes and electrons", *Physical Review*, vol. 87, no. 5, pp. 835–842, 1952.
  - [22] R. Hall, "Electron-hole recombination in germanium", *Physical Review*, vol. 87, no. 2, p. 387, 1952.
  - [23] D. Chan, and J. Phang, "Analytical methods for the extraction of solar-cell single- and double-diode model parameters from  $I$ - $V$  characteristics", *IEEE Transactions on Electron Devices*, vol. 34, no. 2, pp. 286–293, 1987.
  - [24] K. R. McIntosh, "Lumps, humps and bumps: three detrimental effects in the current-voltage curve of silicon solar cells", *PhD thesis*, University of New South Wales, Sydney, Australia, 2001.
  - [25] A. Wolf, D. Biro, J. Nekarda, S. Stumpp, A. Kimmerle, S. Mack, and R. Preu, "Comprehensive analytical model for locally contacted rear surface passivated solar cells", *Journal of Applied Physics*, vol. 108, no. 12, pp. 124510-1–124510-13, 2010.
  - [26] A. Kimmerle, M. Rüdiger, A. Wolf, M. Hermle, and D. Biro, "Validation of analytical modelling of locally contacted solar cells by numerical simulations", *Energy Procedia*, vol. 27, pp. 219–226, 2012.
  - [27] D. E. Kane, and R. M. Swanson, "Electron-hole collisions in concentrator solar cells", in *Proceedings of the 20th IEEE Photovoltaic Specialists Conference*, Las Vegas, USA, 1988, pp. 512–517.
  - [28] A. B. Sproul, "Dimensionless solution of the equation describing the effect of surface recombination on carrier decay in semiconductors", *Journal of Applied Physics*, vol. 76, no. 5, pp. 2851–2854, 1994.
  - [29] R. A. Sinton, A. Cuevas, and M. Stuckings, "Quasi-steady-state photoconductance, a new method for solar cell material and device characterization", in *Proceedings of the 25th IEEE Photovoltaic Specialists Conference*, Washington DC, USA, 1996, pp. 457–460.
  - [30] A. Cuevas, M. Stocks, D. Macdonald, and R. Sinton, "Applications of the quasi-steady-state photoconductance technique", in *Proceedings of the 2nd World Conference on Photovoltaic Energy Conversion*, Vienna, Austria, 1998.

- [31] D. K. Schroder, "Semiconductor material and device characterization", Third Edition, *John Wiley & Sons*, Hoboken, USA, 2006.
- [32] R. Sinton, and D. Macdonald, "WCT-120 photoconductance lifetime tester and optional Suns- $V_{OC}$  stage user manual", *Sinton Instruments*, 2012.
- [33] F. Dannhäuser, "Die Abhängigkeit der Trägerbeweglichkeit in Silizium von der Konzentration der freien Ladungsträger – I", *Solid-State Electronics*, vol. 15, no. 12, pp. 1371–1375, 1972.
- [34] J. Krausse, "Die Abhängigkeit der Trägerbeweglichkeit in Silizium von der Konzentration der freien Ladungsträger – II", *Solid-State Electronics*, vol. 15, no. 12, pp. 1377–1381, 1972.
- [35] G. Masetti, M. Severi, and S. Solmi, "Modeling of carrier mobility against carrier concentration in arsenic-, phosphorus-, and boron-doped silicon", *IEEE Transactions on Electron Devices*, vol. 30, no. 7, pp. 764–769, 1983.
- [36] D. B. M. Klaassen, "A unified mobility model for device simulation – I. Model equations and concentration dependence", *Solid-State Electronics*, vol. 35, no. 7, pp. 953–959, 1992.
- [37] H. Nagel, C. Berge, and A. G. Aberle, "Generalized analysis of quasi-steady-state and quasi-transient measurements of carrier lifetimes in semiconductors", *Journal of Applied Physics*, vol. 86, no. 11, pp. 6218–6221, 1999.
- [38] A. Cuevas, and D. Macdonald, "Measuring and interpreting the lifetime of silicon wafers", *Solar Energy*, vol. 76, no. 1-3, pp. 255–262, 2004.
- [39] D. E. Kane, and R. M. Swanson, "Measurement of the emitter saturation current by a contactless photoconductivity decay method", in *Proceedings of the 18th IEEE Photovoltaic Specialists Conference*, Las Vegas, USA, 1985, pp. 578–583.
- [40] A. L. Blum, J. S. Swirhun, R. A. Sinton, and A. Kimmerle, "An updated analysis to the WCT-120 QSSPC measurement system using advanced device physics", in *Proceedings of the 28th European Photovoltaic Solar Energy Conference and Exhibition*, Paris, France, 2013, pp. 1521–1523.
- [41] A. Kimmerle, P. Rothhardt, A. Wolf, and R. Sinton, "Increased reliability for  $J_0$ -analysis by QSSPC", *Energy Procedia*, vol. 55, pp. 101–106, 2014.
- [42] A. Kimmerle, J. Greulich, and A. Wolf, "Carrier-diffusion corrected  $J_0$ -analysis of charge carrier lifetime measurements for increased consistency", *Solar Energy Materials and Solar Cells*, vol. 142, pp. 116–122, 2015.

- [43] J. R. Haynes, and W. Shockley, "The mobility and life of injected holes and electrons in germanium", *Physical Review*, vol. 81, no. 5, pp. 835–843, 1951.
- [44] A. B. Sproul, and M. A. Green, "Intrinsic carrier concentration and minority-carrier mobility of silicon from 77 to 300 K", *Journal of Applied Physics*, vol. 73, no. 3, pp. 1214–1225, 1993.
- [45] P. P. Altermatt, A. Schenk, F. Geelhaar, and G. Heiser, "Reassessment of the intrinsic carrier density in crystalline silicon in view of band-gap narrowing", *Journal of Applied Physics*, vol. 93, no. 3, pp. 1598–1604, 2003.
- [46] M. A. Green, "Intrinsic concentration, effective densities of states, and effective mass in silicon", *Journal of Applied Physics*, vol. 67, no. 6, pp. 2944–2954, 1990.
- [47] A. Schenk, "Finite-temperature full random-phase approximation model of band gap narrowing for silicon device simulation", *Journal of Applied Physics*, vol. 84, no. 7, pp. 3684–3695, 1998.
- [48] A. Goetzberger, B. Voß, and J. Knobloch, "Sonnenenergie: Photovoltaik - Physik und Technologie der Solarzelle", Second Edition, *Teubner-Studienbücher Physik*, Stuttgart, Germany, 1997.
- [49] M. Hörteis, "Fine-line printed contacts on crystalline silicon solar cells", *PhD thesis*, University of Constance, Germany, 2009.
- [50] International Electrotechnical Commission, "IEC 60904-3, URL: <http://www.iec.ch> (last visited on September 30, 2015).
- [51] M. A. Green, "Solar cell fill factors: general graph and empirical expressions", *Solid-State Electronics*, vol. 24, no. 8, pp. 788–789, 1981.
- [52] R. A. Sinton, and A. Cuevas, "A quasi-steady-state open-circuit voltage method for solar cell characterization", in *Proceedings of the 16th European Photovoltaic Solar Energy Conference*, Glasgow, UK, 2000, pp. 1152–1155.
- [53] J. Greulich, M. Glatthaar, and S. Rein, "Fill factor analysis of solar cells' current-voltage curves", *Progress in Photovoltaics: Research and Applications*, vol. 18, no. 7, pp. 511–515, 2010.
- [54] A. Fick, "Ueber Diffusion", *Annalen der Physik*, vol. 170, no. 1, pp. 59–86, 1855.
- [55] S. M. Sze, "Semiconductor devices - physics and technology", Second Edition, *John Wiley & Sons*, New York, USA, 2002.
- [56] G. L. Pearson, and J. Bardeen, "Electrical properties of pure silicon and silicon alloys containing boron and phosphorus", *Physical Review*, vol. 75, no. 5, pp. 865–883, 1949.

- [57] F. H. Horn, “Densitometric and electrical investigation of boron in silicon”, *Physical Review*, vol. 97, no. 6, pp. 1521–1525, 1955.
- [58] P. Pichler, “Intrinsic point defects, impurities, and their diffusion in silicon”, *Springer-Verlag*, Wien, Austria, 2004.
- [59] R. B. Fair, and P. N. Pappas, “Diffusion of ion-implanted B in high concentration P- and As-doped silicon”, *Journal of the Electrochemical Society*, vol. 122, no. 9, pp. 1241–1244, 1975.
- [60] S. M. Hu, “Formation of stacking faults and enhanced diffusion in the oxidation of silicon”, *Journal of Applied Physics*, vol. 45, no. 4, pp. 1567–1573, 1974.
- [61] W. Windl, M. M. Bunea, R. Stumpf, S. T. Dunham, and M. P. Massquelier, “First-principles study of boron diffusion in silicon”, *Physical Review Letters*, vol. 83, no. 21, pp. 4345–4348, 1999.
- [62] A. Ural, P. B. Griffin, and J. D. Plummer, “Fractional contributions of microscopic diffusion mechanisms for common dopants and self-diffusion in silicon”, *Journal of Applied Physics*, vol. 85, no. 9, pp. 6440–6446, 1999.
- [63] Jung, M. Y. L., R. Gunawan, R. D. Braatz, and E. G. Seebauer, “Pair diffusion and kick-out: contributions to diffusion of boron in silicon”, *AICHE Journal*, vol. 50, no. 12, pp. 3248–3256, 2004.
- [64] A. Bentzen, “Phosphorus diffusion and gettering in silicon solar cells”, *PhD thesis*, University of Oslo, Norway, 2006.
- [65] S. Mirabella, D. de Salvador, E. Napolitani, E. Bruno, and F. Priolo, “Mechanisms of boron diffusion in silicon and germanium”, *Journal of Applied Physics*, vol. 113, no. 3, pp. 031101-1–031101-21, 2013.
- [66] S. F. Guo, and W. S. Chen, “A model for boron deposition in silicon using a  $\text{BBr}_3$  source”, *Journal of the Electrochemical Society*, vol. 129, no. 7, pp. 1592–1596, 1982.
- [67] K. Taniguchi, K. Kurosawa, and M. Kashiwagi, “Oxidation enhanced diffusion of boron and phosphorus in (100) silicon”, *Journal of the Electrochemical Society*, vol. 127, no. 10, pp. 2243–2248, 1980.
- [68] P. Stolk, A. van Brandenburg, and A. Montree, “Oxidation enhanced diffusion during the growth of ultrathin oxides”, *Materials Science in Semiconductor Processing*, vol. 2, no. 1, pp. 29–33, 1999.
- [69] G. L. Vick, and K. M. Whittle, “Solid solubility and diffusion coefficients of boron in silicon”, *Journal of the Electrochemical Society*, vol. 116, no. 8, pp. 1142–1144, 1969.
- [70] R. B. Fair, “Boron diffusion in silicon - Concentration and orientation dependence, background effects, and profile estimation”, *Journal of the Electrochemical Society*, vol. 122, no. 6, pp. 800–805, 1975.

- 
- [71] M. Uematsu, "Simulation of boron, phosphorus, and arsenic diffusion in silicon based on an integrated diffusion model, and the anomalous phosphorus diffusion mechanism", *Journal of Applied Physics*, vol. 82, no. 5, pp. 2228–2246, 1997.
  - [72] A. S. Grove, O. Leistikko, and C. T. Sah, "Redistribution of acceptor and donor impurities during thermal oxidation of silicon", *Journal of Applied Physics*, vol. 35, no. 9, pp. 2695–2701, 1964.
  - [73] D. Nobili, and D. de Cogan, "Solubility of B, Al, Ga, In, Tl, P, As and Sb in c-Si", *Properties of Crystalline Silicon*, no. 20, pp. 620–635, 1999.
  - [74] S. Solmi, A. Parisini, R. Angelucci, A. Armigliato, D. Nobili, and L. Moro, "Dopant and carrier concentration in Si in equilibrium with monoclinic SiP precipitates", *Physical Review B*, vol. 53, no. 12, pp. 7836–7841, 1996.
  - [75] W. Kuzmicz, "Ionization of impurities in silicon", *Solid-State Electronics*, vol. 29, no. 12, pp. 1223–1227, 1986.
  - [76] P. Negrini, "Boron predeposition in silicon using  $\text{BBr}_3$ ", *Journal of the Electrochemical Society*, vol. 125, no. 4, pp. 609–613, 1978.
  - [77] O. V. Aleksandrov, N. N. Afonin, and O. M. Arshinov, "Redistribution of boron in the subsurface region of silicon in diffusion from borosilicate glass", *Technical Physics*, vol. 39, no. 6, pp. 573–575, 1994.
  - [78] M. A. Kessler, T. Ohrdes, B. Wolpensinger, R. Bock, and N.-P. Harder, "Characterisation and implications of the boron rich layer resulting from open-tube liquid source  $\text{BBr}_3$  boron diffusion processes", in *Proceedings of the 34th IEEE Photovoltaic Specialists Conference*, Philadelphia, USA, 2009, pp. 1556–1561.
  - [79] M. A. Kessler, T. Ohrdes, B. Wolpensinger, and N.-P. Harder, "Charge carrier lifetime degradation in Cz silicon through the formation of a boron-rich layer during  $\text{BBr}_3$  diffusion processes", *Semiconductor Science and Technology*, vol. 25, no. 5, pp. 1–9, 2010.
  - [80] S. W. Jones, "Diffusion in silicon", *IC Knowledge LLC*, 2000.
  - [81] E. Peiner, A. Schlachetzki, and D. Krüger, "Doping profile analysis in Si by electrochemical capacitance-voltage measurements", *Journal of the Electrochemical Society*, vol. 142, no. 2, pp. 576–580, 1995.
  - [82] Y. Schiele, S. Fahr, S. Joos, G. Hahn, and B. Terheiden, "Study on boron emitter formation by  $\text{BBr}_3$  diffusion for *n*-type Si solar cell applications", in *Proceedings of the 28th European Photovoltaic Solar Energy Conference and Exhibition*, Paris, France, 2013, pp. 1242–1247.

- [83] K. Ryu, A. Upadhyaya, H.-J. Song, C.-J. Choi, A. Rohatgi, and Y.-W. Ok, “Chemical etching of boron-rich layer and its impact on high efficiency *n*-type silicon solar cells”, *Applied Physics Letters*, vol. 101, no. 7, pp. 073902-1–073902-4, 2012.
- [84] S. P. Phang, W. Liang, B. Wolpensinger, M. A. Kessler, and D. Macdonald, “Tradeoffs between impurity gettering, bulk degradation, and surface passivation of boron-rich layers on silicon solar cells”, *IEEE Journal of Photovoltaics*, vol. 3, no. 1, pp. 261–266, 2013.
- [85] E. Arai, H. Nakamura, and Y. Terunuma, “Interface reactions of  $\text{B}_2\text{O}_3\text{-Si}$  system and boron diffusion into silicon”, *Journal of the Electrochemical Society*, vol. 120, no. 7, pp. 980–987, 1973.
- [86] J. Libal, R. Petres, T. Buck, R. Kopecek, G. Hahn, R. Ferre, M. Vetter, I. Martin, K. Wambach, I. Roever, and P. Fath, “N-Type multicrystalline silicon solar cells:  $\text{BBr}_3$ -diffusion and passivation of *p*+ diffused silicon surfaces”, in *Proceedings of the 20th European Photovoltaic Solar Energy Conference*, Barcelona, Spain, 2005, pp. 793–796.
- [87] J.-H. Guo, and J. E. Cotter, “Optimizing the diffused regions of interdigitated backside buried contact solar cells”, *Progress in Photovoltaics: Research and Applications*, vol. 15, no. 3, pp. 211–223, 2007.
- [88] G. Masetti, D. Nobili, and S. Solmi, “Profiles of phosphorus predeposition in silicon and carrier concentration in equilibrium with SiP precipitates”, *Semiconductor Silicon*, vol. 77-2, pp. 648–657, 1977.
- [89] P. M. Fahey, P. B. Griffin, and J. D. Plummer, “Point defects and dopant diffusion in silicon”, *Reviews of Modern Physics*, vol. 61, no. 2, pp. 289–384, 1989.
- [90] M. Binnewies, R. Gläum, M. Schmidt, and P. Schmidt, “Chemical vapor transport reactions”, *De Gruyter*, Berlin, Germany, 2012.
- [91] A. Kimmerle, R. Woehl, A. Wolf, and D. Biro, “Simplified front surface field formation for back contacted silicon solar cells”, *Energy Procedia*, vol. 38, pp. 278–282, 2013.
- [92] S. Werner, E. Lohmüller, S. Maier, A. Kimmerle, A. Spribille, S. Wasmer, F. Clement, and A. Wolf, “Process optimization for the front side of *p*-type silicon solar cells”, in *Proceedings of the 29th European Photovoltaic Solar Energy Conference and Exhibition*, Amsterdam, Netherlands, 2014, pp. 1342–1347.
- [93] W. Schottky, “Halbleitertheorie der Sperrsicht”, *Die Naturwissenschaften*, vol. 26, no. 52, p. 843, 1938.
- [94] W. Schottky, “Zur Halbleitertheorie der Sperrsicht- und Spitzengleichrichter”, *Zeitschrift für Physik*, vol. 113, no. 5–6, pp. 367–414, 1939.

- 
- [95] W. Schottky, "Vereinfachte und erweiterte Theorie der Randschichtgleichrichter", *Zeitschrift für Physik*, vol. 118, no. 9–10, pp. 539–592, 1942.
  - [96] N. F. Mott, "Note on the contact between a metal and an insulator or semi-conductor", *Mathematical Proceedings of the Cambridge Philosophical Society*, vol. 34, no. 4, pp. 568–572, 1938.
  - [97] N. F. Mott, "The theory of crystal rectifiers", *Proceedings of the Royal Society of London, Series A: Mathematical, Physical & Engineering Sciences*, vol. 171, pp. 27–38, 1939.
  - [98] J. Bardeen, "Surface states and rectification at a metal semi-conductor contact", *Physical Review*, vol. 71, no. 10, pp. 717–727, 1947.
  - [99] A. M. Cowley, and S. M. Sze, "Surface states and barrier height of metal-semiconductor systems", *Journal of Applied Physics*, vol. 36, no. 10, pp. 3212–3220, 1965.
  - [100] C. R. Crowell, H. B. Shore, and E. E. LaBate, "Surface-state and interface effects in Schottky barriers at *n*-type silicon surfaces", *Journal of Applied Physics*, vol. 36, no. 12, pp. 3843–3850, 1965.
  - [101] C. R. Crowell, and S. M. Sze, "Current transport in metal-semiconductor barriers", *Solid-State Electronics*, vol. 9, pp. 1035–1048, 1966.
  - [102] C. R. Crowell, "Metal-semiconductor interfaces", *Surface Science*, vol. 13, no. 1, pp. 13–16, 1969.
  - [103] C. R. Crowell, and V. L. Rideout, "Normalized thermionic-field (T-F) emission in metal-semiconductor (Schottky) barriers", *Solid-State Electronics*, vol. 12, no. 2, pp. 89–105, 1969.
  - [104] A. Yu, "Electron tunneling and contact resistance of metal-silicon contact barriers", *Solid-State Electronics*, vol. 13, no. 2, pp. 239–247, 1970.
  - [105] D. K. Schroder, and D. L. Meier, "Solar cell contact resistance - a review", *IEEE Transactions on Electron Devices*, vol. 31, no. 5, pp. 637–647, 1984.
  - [106] E. H. Rhoderick, and R. H. Williams, "Metal-semiconductor contacts", Second Edition, *Clarendon Press*, Oxford, UK, 1988.
  - [107] W. Bludau, A. Onton, and W. Heinke, "Temperature dependence of the band gap of silicon", *Journal of Applied Physics*, vol. 45, no. 4, pp. 1846–1848, 1974.
  - [108] S. M. Sze, "Physics of semiconductor devices", Second Edition, *John Wiley & Sons*, New York, USA, 1981.
  - [109] F. A. Padovani, and R. Stratton, "Field and thermionic-field emission in Schottky barriers", *Solid-State Electronics*, vol. 9, no. 7, pp. 695–707, 1966.

- [110] G. Schubert, F. Huster, and P. Fath, “Physical understanding of printed thick-film front contacts of crystalline Si solar cells—Review of existing models and recent developments”, *Solar Energy Materials and Solar Cells*, vol. 90, pp. 3399–3406, 2006.
- [111] G. Schubert, “Thick film metallisation of crystalline silicon solar cells”, *PhD thesis*, University of Constance, Germany, 2006.
- [112] C. Ballif, D. M. Huljic, A. Hessler-Wyser, and G. Willeke, “Nature of the Ag-Si interface in screen-printed contacts”, in *Proceedings of the 29th IEEE Photovoltaic Specialists Conference*, New Orleans, USA, 2002, pp. 360–363.
- [113] ITRPV, “International Technology Roadmap for Photovoltaics (ITRPV) - Results 2011, URL: <http://www.itrpv.net/Reports/Downloads/2012/> (last visited on September 30, 2015).
- [114] H. Hannebauer, T. Falcon, R. Hesse, T. Dullweber, and R. Brendel, “18.9%-efficient screen-printed solar cells applying a print-on-print process”, in *Proceedings of the 26th European Photovoltaic Solar Energy Conference and Exhibition*, Hamburg, Germany, 2011, pp. 1607–1610.
- [115] A. W. Blakers, A. Wang, A. M. Milne, J. Zhao, and M. A. Green, “22.8% efficient silicon solar cell”, *Applied Physics Letters*, vol. 55, no. 13, pp. 1363–1365, 1989.
- [116] S. Gatz, H. Hannebauer, R. Hesse, F. Werner, A. Schmidt, T. Dullweber, J. Schmidt, K. Bothe, and R. Brendel, “19.4%-efficient large-area fully screen-printed silicon solar cells”, *Physica Status Solidi RRL*, vol. 5, no. 4, pp. 147–149, 2011.
- [117] T. Böscke, R. Hellriegel, T. Wütherich, L. Bornschein, A. Helbig, R. Carl, M. Dupke, D. Stichtenoth, T. Aichele, R. Jesswein, T. Roth, C. Schöllhorn, T. Geppert, A. Grohe, J. Lossen, and H.-J. Krokoszinski, “Fully screen-printed PERC cells with laser-fired contacts—An industrial cell concept with 19.5% efficiency”, in *Proceedings of the 37th IEEE Photovoltaic Specialists Conference*, Seattle, USA, 2011, pp. 3663–3666.
- [118] B. Thaidigsmann, E. Lohmüller, U. Jäger, S. Mack, F. Lottspeich, A. Spribille, K. Birmann, D. Erath, A. Wolf, F. Clement, D. Biro, and R. Preu, “Large-area *p*-type HIP–MWT silicon solar cells with screen printed contacts exceeding 20% efficiency”, *Physica Status Solidi RRL*, vol. 5, no. 8, pp. 286–288, 2011.
- [119] J. Schmidt, F. Werner, B. Veith, D. Zielke, S. Steingrube, P. P. Altermatt, S. Gatz, T. Dullweber, and R. Brendel, “Advances in the surface passivation of silicon solar cells”, *Energy Procedia*, vol. 15, pp. 30–39, 2012.

- 
- [120] R. Preu, S. W. Glunz, S. Schäfer, R. Lüdemann, W. Wetling, and W. Pfleging, “Laser ablation—a new low-cost approach for passivated rear contact formation in crystalline silicon solar cell technology”, in *Proceedings of the 16th European Photovoltaic Solar Energy Conference*, Glasgow, UK, 2000, pp. 1181–1184.
  - [121] G. Agostinelli, J. Szlufcick, P. Choulat, and G. Beaucarne, “Local contact structures for industrial PERC-type solar cells”, in *Proceedings of the 20th European Photovoltaic Solar Energy Conference*, Barcelona, Spain, 2005, pp. 942–945.
  - [122] E. Schneiderlöchner, R. Preu, R. Lüdemann, S. W. Glunz, and G. Wilkele, “Laser-fired contacts (LFC)”, in *Proceedings of the 17th European Photovoltaic Solar Energy Conference*, Munich, Germany, 2001, pp. 1303–1306.
  - [123] J. Nekarda, S. Stumpf, L. Gautero, M. Hörteis, A. Grohe, D. Biro, and R. Preu, “LFC on screen printed aluminium rear side metallization”, in *Proceedings of the 24th European Photovoltaic Solar Energy Conference and Exhibition*, Hamburg, Germany, 2009, pp. 1441–1445.
  - [124] P. Engelhart, D. Manger, B. Klöter, S. Hermann, A. A. Stekolnikov, S. Peters, H.-C. Ploigt, A. Eifler, C. Klenke, A. Mohr, G. Zimmermann, B. Barkenfels, K. Suva, J. Wendt, T. Kaden, S. Rupp, D. Rychtarik, M. Fischer, and J. W. Müller, “Q.ANTUM – Q-Cells next generation high-power silicon solar cell & module concept”, in *Proceedings of the 26th European Photovoltaic Solar Energy Conference and Exhibition*, Hamburg, Germany, 2011, pp. 821–826.
  - [125] K. A. Münzer, J. Schöne, A. Teppe, M. Hein, R. E. Schlosser, M. Hanke, J. Maier, A. Yodyungyong, J. Isenberg, T. Friess, C. Ehling, K. Varner, S. Keller, and P. Fath, “Towards 19.5% industrial crystalline silicon solar cells”, in *Proceedings of the 26th European Photovoltaic Solar Energy Conference and Exhibition*, Hamburg, Germany, 2011, pp. 843–848.
  - [126] S. W. Glunz, S. Rein, J. Y. Lee, and W. Warta, “Minority carrier lifetime degradation in boron-doped Czochralski silicon”, *Journal of Applied Physics*, vol. 90, no. 5, pp. 2397–2404, 2001.
  - [127] K. Bothe, R. Sinton, and J. Schmidt, “Fundamental boron-oxygen-related carrier lifetime limit in mono- and multicrystalline silicon”, *Progress in Photovoltaics: Research and Applications*, vol. 13, pp. 287–296, 2005.
  - [128] R. Hull, “Properties of crystalline silicon”, *INSPEC, The Institution of Electrical Engineers*, no. 20, London, UK, 1999.
  - [129] J. Schmidt, “Light-induced degradation in crystalline silicon solar cells”, *Solid State Phenomena*, vol. 95–96, pp. 187–196, 2003.

- [130] K. Hoshi, N. Isawa, T. Suzuki, and Y. Ohkubo, "Czochralski silicon crystals grown in a transverse magnetic field", *Journal of the Electrochemical Society*, vol. 132, no. 3, pp. 693–700, 1985.
- [131] S. W. Glunz, S. Rein, J. Knobloch, W. Wetling, and T. Abe, "Comparison of boron- and gallium-doped *p*-type Czochralski silicon for photovoltaic application", *Progress in Photovoltaics: Research and Applications*, vol. 7, no. 6, pp. 463–469, 1999.
- [132] H. Kodera, "Diffusion coefficients of impurities in silicon melt", *Japanese Journal of Applied Physics*, vol. 2, no. 4, pp. 212–219, 1963.
- [133] A. Herguth, G. Schubert, M. Kaes, and G. Hahn, "A new approach to prevent the negative impact of the metastable defect in boron doped Cz silicon solar cells", in *Proceedings of the 4th World Conference on Photovoltaic Energy Conversion*, Waikoloa, Hawaii, USA, 2006, pp. 940–943.
- [134] A. R. Burgers, L. J. Geerligs, A. J. Carr, A. Gutjahr, D. S. Saynova, X. Xiong, L. Li, X. Zhuo, W. Hongfang, A. Haijiao, H. Hu, P. R. Venema, and A. Vloojswijk, "19.5% efficient *n*-type Si solar cells made in production", in *Proceedings of the 26th European Photovoltaic Solar Energy Conference and Exhibition*, Hamburg, Germany, 2011, pp. 1144–1147.
- [135] B. Hoex, J. Schmidt, R. Bock, P. P. Altermatt, M. C. M. van de Sanden, and W. M. M. Kessels, "Excellent passivation of highly doped *p*-type Si surfaces by the negative-charge-dielectric  $\text{Al}_2\text{O}_3$ ", *Applied Physics Letters*, vol. 91, no. 11, pp. 112107-1–112107-3, 2007.
- [136] R. Cabal, J. Jourdan, B. Grange, Y. Veschetti, and D. Heslinga, "Investigation of the potential of boron doped oxide deposited by PECVD - Application to advanced solar cells fabrication processes", in *Proceedings of the 24th European Photovoltaic Solar Energy Conference and Exhibition*, Hamburg, Germany, 2009, pp. 1605–1608.
- [137] R. Cabal, F. Dauzou, V. Sanzone, P. Brand, and Y. Veschetti, "Industrial process leading to 19.1% on *n*-type Cz silicon", in *Proceedings of the 26th European Photovoltaic Solar Energy Conference and Exhibition*, Hamburg, Germany, 2011, pp. 1164–1167.
- [138] A. Edler, V. D. Mihailetti, R. Kopecek, R. Harney, T. Böscke, D. Stichtenthal, J. Lossen, K. Meyer, R. Hellriegel, T. Aichele, and H.-J. Krokszinski, "Improving screen printed metallization for large area industrial solar cells based on *n*-type material", *Energy Procedia*, vol. 8, pp. 493–497, 2011.

- 
- [139] Yingli Green Energy, "Yingli Green Energy unveils high-efficiency monocrystalline Panda module at Intersolar trade shows", *Press Release*, 2010, URL: <http://ir.yinglisolar.com/phoenix.zhtml?c=213018&p=irol-newsArticle&ID=1435603> (last visited on September 30, 2015).
  - [140] R. Kopecek, T. Buck, J. Libal, R. Petres, I. Röver, K. Wambach, R. Kinderman, L. J. Geerligs, and P. Fath, "Large area  $n$ -type multi-crystalline silicon solar cells with B-emitter: Efficiencies exceeding 14%", in *Proceedings of the 15th International Photovoltaic Science and Engineering Conference*, Shanghai, China, 2005, pp. 892–893.
  - [141] H. Kerp, S. Kim, R. Lago, F. Recart, I. Freire, L. Pérez, K. Albertsen, C. Jiméno, and A. Shaikh, "Development of screen printable contacts for P emitters in bifacial solar cells", in *Proceedings of the 21st European Photovoltaic Solar Energy Conference*, Dresden, Germany, 2006, pp. 892–894.
  - [142] R. Lago, L. Pérez, H. Kerp, I. Freire, I. Hoces, N. Azkona, F. Recart, and J. C. Jimeno, "Screen printing metallization of boron emitters", *Progress in Photovoltaics: Research and Applications*, vol. 18, no. 1, pp. 20–27, 2010.
  - [143] A. Richter, M. Hörteis, J. Benick, S. Henneck, M. Hermle, and S. W. Glunz, "Towards industrially feasible high-efficiency  $n$ -type Si solar cells with boron-diffused front side emitter - combining firing stable  $\text{Al}_2\text{O}_3$  passivation and fine-line printing", in *Proceedings of the 35th IEEE Photovoltaic Specialists Conference*, Honolulu, Hawaii, USA, 2010, pp. 3587–3592.
  - [144] G. Laudisio, P. J. Willmott, M. Rose, and R. J. S. Young, "Improved c-Si cell performance through metallizations adapted to reduce recombination effects", in *Proceedings of the 24th European Photovoltaic Solar Energy Conference and Exhibition*, Hamburg, Germany, 2009, pp. 1446–1448.
  - [145] F. Fertig, S. Rein, M. Schubert, and W. Warta, "Impact of junction breakdown in multi-crystalline silicon solar cells on hot spot formation and module performance", in *Proceedings of the 26th European Photovoltaic Solar Energy Conference and Exhibition*, Hamburg, Germany, 2011, pp. 1168–1178.
  - [146] A. Schneider, L. Rubin, and G. Rubin, "Solar cell efficiency improvement by new metallization techniques - the Day4 electrode concept", in *Proceedings of the 4th World Conference on Photovoltaic Energy Conversion*, Waikoloa, Hawaii, USA, 2006, pp. 1095–1098.
  - [147] S. Braun, G. Micard, and G. Hahn, "Solar cell improvement by using a multi busbar design as front electrode", *Energy Procedia*, vol. 27, pp. 227–233, 2012.

## Bibliography

---

- [148] F. Granek, “High efficiency back-contact back-junction solar cells”, *PhD thesis*, University of Freiburg, Germany, 2009.
- [149] P. J. Cousins, D. D. Smith, H.-C. Luan, J. Manning, T. D. Dennis, A. Waldhauer, K. E. Wilson, G. Harley, and W. P. Mulligan, “Generation 3: improved performance at lower cost”, in *Proceedings of the 35th IEEE Photovoltaic Specialists Conference*, Honolulu, Hawaii, USA, 2010, pp. 275–278.
- [150] F. Clement, “Die Metal Wrap Through Solarzelle - Entwicklung und Charakterisierung”, *PhD thesis*, University of Freiburg, Germany, 2009.
- [151] F. Clement, M. Menkoe, D. Erath, T. Kubera, R. Hoenig, W. Kwapil, W. Wolke, D. Biro, and R. Preu, “High throughput via-metallization technique for multi-crystalline metal wrap through (MWT) silicon solar cells exceeding 16% efficiency”, *Solar Energy Materials and Solar Cells*, vol. 94, no. 1, pp. 51–56, 2010.
- [152] K. Meyer, M. Menkoe, H.-J. Krokszinski, T. Wütherich, M. Dupke, and R. Jesswein, “MWT cells with Al–BSF on Cz silicon with efficiencies up to 19.4%”, in *Proceedings of the 26th European Photovoltaic Solar Energy Conference and Exhibition*, Hamburg, Germany, 2011, pp. 984–988.
- [153] F. Dross, E. van Kerschaver, C. Alleb  , A. van der Heide, J. Szlufcik, G. Agostinelli, P. Choulat, H. Dekkers, and G. Beaucarne, “Impact of rear-surface passivation on MWT performances”, in *Proceedings of the 4th World Conference on Photovoltaic Energy Conversion*, Waikoloa, Hawaii, USA, 2006, pp. 1291–1294.
- [154] F. Dross, C. Alleb  , Y. Ma, H. Dekkers, G. Agostinelli, P. Choulat, X. Loozen, E. van Kerschaver, J. Szlufcik, and G. Beaucarne, “High-efficiency (average 16.0%) industrial-type rear-contacts multicrystalline silicon solar cells”, in *Proceedings of the 17th International Photovoltaic Science and Engineering Conference*, Fukuoka, Japan, 2007, pp. 410–411.
- [155] B. Thaidigsmann, A. Wolf, F. Clement, D. Biro, and R. Preu, “Combining the advantages of wrap through metallization and rear surface passivation into industrial MWT–PERC devices”, in *Proceedings of the 25th European Photovoltaic Solar Energy Conference and Exhibition*, Valencia, Spain, 2010, pp. 2227–2230.
- [156] J. Specht, K. Zengerle, M. Pospischil, D. Erath, J. Haunschild, F. Clement, and D. Biro, “High aspect ratio front contacts by single step dispensing of metal pastes”, in *Proceedings of the 25th European Photovoltaic Solar Energy Conference and Exhibition*, Valencia, Spain, 2010, pp. 1867–1870.

- [157] F. Clement, M. Lutsch, T. Kubera, M. Kasemann, W. Kwapil, C. Harmel, N. Mingirulli, D. Erath, H. Wirth, D. Biro, and R. Preu, "Processing and comprehensive characterisation of screen-printed mc-Si metal wrap through (MWT) solar cells", in *Proceedings of the 22nd European Photovoltaic Solar Energy Conference*, Milan, Italy, 2007, pp. 1399–1402.
- [158] M. Neidert, F. Clement, M. Menkoe, R. Höning, A. Henning, W. Zhang, D. Biro, and R. Preu, "Development of via pastes for high efficiency MWT cells with a low shunting behaviour", in *Proceedings of the 24th European Photovoltaic Solar Energy Conference and Exhibition*, Hamburg, Germany, 2009, pp. 1424–1429.
- [159] R. S. Watt, G. Laudisio, Y. Wang, H. Hsueh, J. Mo, and A. C. Street, "A metallization system for metal wrap through solar cells", in *Proceedings of the 26th European Photovoltaic Solar Energy Conference and Exhibition*, Hamburg, Germany, 2011, pp. 2174–2176.
- [160] B. Thaidigsmann, F. Clement, A. Wolf, E. Lohmüller, F. Fertig, D. Biro, and R. Preu, "HIP–MWT: A simplified structure for metal wrap through solar cells with passivated rear surface", *Energy Procedia*, vol. 8, pp. 498–502, 2011.
- [161] B. Thaidigsmann, S. Werner, S. Gutscher, F. Fertig, F. Clement, A. Wolf, and D. Biro, "Manipulation of the reverse bias behaviour of silicon solar cells", in *Proceedings of the 21st International Photovoltaic Science and Engineering Conference*, Fukuoka, Japan, 2011.
- [162] B. Thaidigsmann, A. Spribille, H. Plagwitz, G. Schubert, F. Fertig, F. Clement, A. Wolf, D. Biro, and R. Preu, "HIP–MWT - A new cell concept for industrial processing of high-performance metal wrap through silicon solar cells", in *Proceedings of the 26th European Photovoltaic Solar Energy Conference and Exhibition*, Hamburg, Germany, 2011, pp. 817–820.
- [163] B. Thaidigsmann, E. Lohmüller, F. Fertig, F. Clement, and A. Wolf, "Characterization and modeling of screen-printed metal insulator semiconductor tunnel junctions for integrated bypass functionality in crystalline silicon solar cells", *Journal of Applied Physics*, vol. 113, no. 21, pp. 214502-1–214502-9, 2013.
- [164] Yingli Green Energy, "Yingli Green Energy, ECN and Amtech join efforts to develop n-type MWT high efficiency PV cell and module", *Press Release*, 2011, URL: <http://ir.yinglisolar.com/phoenix.zhtml?c=213018&p=irol-newsArticle&ID=1604184> (last visited on September 30, 2015).

- [165] E. Lohmüller, B. Thaidigsmann, S. Werner, F. Clement, A. Wolf, D. Biro, and R. Preu, "Evaluation of via pastes for *p*- and *n*-type metal wrap through (MWT) solar cells", in *Proceedings of the 27th European Photovoltaic Solar Energy Conference and Exhibition*, Frankfurt, Germany, 2012, pp. 590–595.
- [166] B. Thaidigsmann, "Entwicklung und Charakterisierung hocheffizienter MWT-PERC-Solarzellen aus *p*-dotiertem, kristallinem Silicium", *PhD thesis*, University of Tübingen, Germany, 2013.
- [167] E. Lohmüller, M. Thanasa, B. Thaidigsmann, F. Clement, and D. Biro, "Electrical properties of the rear contact structure of MWT silicon solar cells", *Solar Energy Materials and Solar Cells*, vol. 137, pp. 293–302, 2015.
- [168] D. Biro, R. Preu, S. W. Glunz, S. Rein, J. Rentsch, G. Emanuel, I. Brucker, T. Faasch, C. Faller, G. Willeke, and J. Luther, "PV-TEC: Photovoltaic technology evaluation center - design and implementation of a production research unit", in *Proceedings of the 21st European Photovoltaic Solar Energy Conference*, Dresden, Germany, 2006, pp. 621–624.
- [169] P. Rothhardt, "Co-diffusion for bifacial n-type solar cells", *PhD thesis*, University of Freiburg, Germany, 2014.
- [170] R. Cabal, B. Grange, L. Bounaas, R. Monna, N. Plassat, E. Pihan, and Y. Veschetti, "20% PERT technology adapted to *n*-type mono-like silicon: simplified process and narrowed cell efficiency distribution", in *Proceedings of the 29th European Photovoltaic Solar Energy Conference and Exhibition*, Amsterdam, Netherlands, 2014, pp. 648–652.
- [171] S. Miyajima, J. Irikawa, A. Yamada, and M. Konagai, "Hydrogenated aluminum oxide films deposited by plasma enhanced chemical vapor deposition for passivation of *p*-type crystalline silicon", in *Proceedings of the 23rd European Photovoltaic Solar Energy Conference and Exhibition*, Valencia, Spain, 2008, pp. 1029–1032.
- [172] P. Saint-Cast, J. Benick, D. Kania, L. Weiss, M. Hofmann, J. Rentsch, R. Preu, and S. W. Glunz, "High-efficiency c-Si solar cells passivated with ALD and PECVD aluminum oxide", *IEEE Electron Device Letters*, vol. 31, no. 7, pp. 695–697, 2010.
- [173] D. Kania, P. Saint-Cast, D. Wagenmann, M. Hofmann, J. Rentsch, and R. Preu, "Industrial negatively charged c-Si surface passivation by inline PECVD AlO<sub>x</sub>", in *Proceedings of the 24th European Photovoltaic Solar Energy Conference*, Hamburg, Germany, 2009, pp. 2275–2278.
- [174] P. Saint-Cast, E. Billot, P. Olwal, S. Kühnhold, A. Richter, M. Hofmann, J. Rentsch, and R. Preu, "Surface passivation of highly and lowly doped *p*-type silicon surfaces with PECVD Al<sub>2</sub>O<sub>3</sub> for industrially applicable solar cell concepts", in *Proceedings of the 26th European Photovoltaic Solar Energy Conference and Exhibition*, Hamburg, Germany, 2011, pp. 1125–1128.

- [175] J. Benick, A. Richter, M. Hermle, and S. W. Glunz, "Thermal stability of the  $\text{Al}_2\text{O}_3$  passivation on *p*-type silicon surfaces for solar cell applications", *Physica Status Solidi RRL*, vol. 3, no. 7–8, pp. 233–235, 2009.
- [176] A. Richter, S. Henneck, J. Benick, M. Hörteis, M. Hermle, and S. W. Glunz, "Firing stable  $\text{Al}_2\text{O}_3/\text{SiN}_x$  layer stack passivation for the front side boron emitter of *n*-type silicon solar cells", in *Proceedings of the 25th European Photovoltaic Solar Energy Conference and Exhibition*, Valencia, Spain, 2010, pp. 1453–1459.
- [177] J. Schmidt, B. Veith, and R. Brendel, "Effective surface passivation of crystalline silicon using ultrathin  $\text{Al}_2\text{O}_3$  films and  $\text{Al}_2\text{O}_3/\text{SiN}_x$  stacks", *Physica Status Solidi RRL*, pp. 287–289, 2009.
- [178] A. Usami, Y. Fujii, and K. Monoka, "The effect of swirl defects on the minority carrier lifetime in heat-treated silicon crystals", *Journal of Physics D: Applied Physics*, vol. 10, no. 6, pp. 899–910, 1977.
- [179] V. V. Voronkov, "The mechanism of swirl defects formation in silicon", *Journal of Crystal Growth*, vol. 59, no. 3, pp. 625–643, 1982.
- [180] D. Walter, B. Lim, R. Falster, J. Binns, and J. Schmidt, "Understanding lifetime degradation in Czochralski-grown *n*-type silicon after high-temperature processing", in *Proceedings of the 28th European Photovoltaic Solar Energy Conference and Exhibition*, Paris, France, 2013, pp. 699–702.
- [181] J. Schön, M. C. Schubert, W. Warta, H. Savin, and A. Haarahiltunen, "Analysis of simultaneous boron and phosphorus diffusion gettering in silicon", *Physica Status Solidi A*, vol. 207, no. 11, pp. 2589–2592, 2010.
- [182] J. Schön, V. Vähäniemi, A. Haarahiltunen, M. C. Schubert, W. Warta, and H. Savin, "Main defect reactions behind phosphorus diffusion gettering of iron", *Journal of Applied Physics*, vol. 116, no. 24, pp. 244503-1–244503-7, 2014.
- [183] R. S. Bonilla, C. Reichel, M. Hermle, and P. R. Wilshaw, "Electric field effect surface passivation for silicon solar cells", *Solid State Phenomena*, vol. 205–206, pp. 346–351, 2013.
- [184] W. Kern, and D. Puotinen, "Cleaning solutions based on hydrogen peroxide for use in silicon semiconductor technology", *RCA Review*, vol. 31, pp. 187–205, 1970.
- [185] H. Kobayashi, Asuha, O. Maida, M. Takahashi, and H. Iwasa, "Nitric acid oxidation of Si to form ultrathin silicon dioxide layers with a low leakage current density", *Journal of Applied Physics*, vol. 94, no. 11, pp. 7328–7335, 2003.

- [186] H. Kobayashi, K. Imamura, W.-B. Kim, S.-S. Im, and Asuha, “Nitric acid oxidation of Si (NAOS) method for low temperature fabrication of  $\text{SiO}_2/\text{Si}$  and  $\text{SiO}_2/\text{SiC}$  structures”, *Applied Surface Science*, vol. 256, no. 19, pp. 5744–5756, 2010.
- [187] A. G. Aberle, and R. Hezel, “Progress in low-temperature surface passivation of silicon solar cells using remote-plasma silicon nitride”, *Progress in Photovoltaics: Research and Applications*, vol. 5, no. 1, pp. 29–50, 1997.
- [188] A. Richter, J. Benick, M. Hermle, and S. W. Glunz, “Excellent silicon surface passivation with 5 Å thin ALD  $\text{Al}_2\text{O}_3$  layers: Influence of different thermal post-deposition treatments”, *Physica Status Solidi RRL*, vol. 5, no. 5-6, pp. 202–204, 2011.
- [189] M. König, M. Deckelmann, A. Henning, R. Hoenig, F. Clement, and M. Hörtelis, “Dual screen printing featuring novel framed busbar screen layout and non-contacting Ag busbar paste”, *Energy Procedia*, vol. 27, pp. 510–515, 2012.
- [190] E. Lohmüller, B. Thaidigsmann, F. Clement, A. Wolf, and D. Biro, “Transfer of the HIP–MWT solar cell concept to *n*-type silicon”, *Energy Procedia*, vol. 38, pp. 436–442, 2013.
- [191] D. Biro, D. Erath, U. Belledin, J. Specht, D. Stüwe, A. Lemke, M. Aleman, N. Mingirulli, J. Rentsch, R. Preu, R. Schlosser, B. Bitnar, and H. Neuhaus, “Inkjet printing for high definition industrial masking processes for solar cell production”, in *Proceedings of the 17th International Photovoltaic Science and Engineering Conference*, Fukuoka, Japan, 2007.
- [192] N. Mingirulli, R. Keding, J. Specht, A. Fallisch, D. Stuwe, and D. Biro, “Hot-melt inkjet as masking technology for back-contacted cells”, in *Proceedings of the 34th IEEE Photovoltaic Specialists Conference*, Philadelphia, USA, 2009, pp. 1064–1068.
- [193] J. Specht, D. Biro, N. Mingirulli, M. Aleman, U. Belledin, R. Efinger, D. Erath, L. Gautero, A. Lemke, D. Stüwe, J. Rentsch, and R. Preu, “Using hotmelt-inkjet as a structuring method for higher efficiency industrial silicon solar cells”, in *Proceedings 24th International Conference on Digital Printing Technologies*, Pittsburgh, USA, 2008, pp. 912–917.
- [194] A. Grohe, “Einsatz von Laserverfahren zur Prozessierung von kristallinen Silizium-Solarzellen”, *PhD thesis*, University of Constance, Germany, 2007.
- [195] A. Spribile, F. Clement, D. Erath, J. Specht, D. Biro, and R. Preu, “Dispensing of etching paste and inkjetting of diffusion barrier for MWT solar cell processing”, in *Proceedings of the 25th European Photovoltaic Solar Energy Conference and Exhibition*, Valencia, Spain, 2010, pp. 2654–2658.

- [196] A. Spribile, J. Greulich, E. Lohmüller, F. Clement, J. Specht, D. Biro, R. Preu, O. Doll, C. Tüshaus, W. Stockum, and I. Köhler, “MWT solar cell processing by use of Isishape® SolarEtch® SiD for rear contact and edge isolation”, in *Proceedings of the 27th European Photovoltaic Solar Energy Conference and Exhibition*, Frankfurt, Germany, 2012, pp. 2001–2006.
- [197] K. Meyer, H.-J. Krokoszinski, D. Lahmer, T. Wuetherich, M. Dupke, R. Jesswein, J. Lossen, P. Zerrer, and A. Prießner, “Novel MWT cell design on monocrystalline silicon wafers”, in *Proceedings of the 25th European Photovoltaic Solar Energy Conference and Exhibition*, Valencia, Spain, 2010, pp. 1774–1777.
- [198] M. Hendrichs, B. Thaidigsmann, T. Fellmeth, S. Nold, A. Spribile, P. Herrmann, M. Mittag, I. Hädrich, U. Eitner, F. Clement, D. Biro, and R. Preu, “Cost-optimised metallization layout for metal wrap through (MWT) solar cells and modules”, in *Proceedings of the 28th European Photovoltaic Solar Energy Conference and Exhibition*, Paris, France, 2013, pp. 1524–1528.
- [199] M. Spitz, U. Belledin, and S. Rein, “Fast inductive inline measurement of the emitter sheet resistance in industrial solar cell fabrication”, in *Proceedings of the 22nd European Photovoltaic Solar Energy Conference*, Milan, Italy, 2007, pp. 47–50.
- [200] C. S. Fuller, “Resistivity charges in silicon induced by heat treatment”, *Physical Review*, vol. 96, p. 833, 1954.
- [201] H. Murrmann, and D. Widmann, “Current crowding on metal contacts to planar devices”, *IEEE Transactions on Electron Devices*, vol. 16, no. 12, pp. 1022–1024, 1969.
- [202] H. H. Berger, “Contact resistance and contact resistivity”, *Journal of the Electrochemical Society*, vol. 119, no. 4, pp. 507–514, 1972.
- [203] B. Vermang, H. Goverde, A. Lorenz, A. Uruena, J. Das, P. Choulat, E. Cornagliotti, A. Rothschild, J. John, J. Poortmans, and A. Merten, “On the blistering of  $\text{Al}_2\text{O}_3$  passivation layers for Si solar cells”, in *Proceedings of the 26th European Photovoltaic Solar Energy Conference and Exhibition*, Hamburg, Germany, 2011, pp. 1129–1131.
- [204] X. Li, L. Tao, Z. Xia, Z. Yang, J. Dong, W. Song, B. Zhang, R. Sidhu, and G. Xing, “Boron diffused emitter etch back and passivation”, in *Proceedings of the 38th IEEE Photovoltaic Specialists Conference*, Austin, USA, 2012, pp. 1073–1076.

## Bibliography

---

- [205] G. J. M. Janssen, M. Koppes, Y. Komatsu, J. Anker, J. Liu, A. Gutjahr, A. A. Mewe, C. J. J. Tool, I. G. Romijn, O. Siarheyeva, M. Ernst, B. W. H. van de Loo, and W. Kessels, "Front side improvements for  $n$ -Pasha cells", in *Proceedings of the 29th European Photovoltaic Solar Energy Conference and Exhibition*, Amsterdam, Netherlands, 2014, pp. 812–815.
- [206] A. Moldovan, K. Birnmann, J. Rentsch, M. Zimmer, T. Gitte, and J. Fittkau, "Combined ozone/HF/HCl based cleaning and adjusted emitter etch-back for silicon solar cells", *Solid State Phenomena*, vol. 195, pp. 305–309, 2013.
- [207] K. R. Williams, and R. S. Muller, "Etch rates for micromachining processing", *Journal of Microelectromechanical Systems*, vol. 5, no. 4, pp. 256–269, 1996.
- [208] V. Doo, "Silicon nitride, a new diffusion mask", *IEEE Transactions on Electron Devices*, vol. 13, no. 7, pp. 561–563, 1966.
- [209] E. Lohmüller, S. Werner, J. Schön, M. Thanasa, S. Mack, W. Wolke, A. Wolf, F. Clement, and D. Biro, "Depletion of boron-doped surfaces protected with barrier layers during  $\text{POCl}_3$ -diffusion", in *Proceedings of the 28th European Photovoltaic Solar Energy Conference and Exhibition*, Paris, France, 2013, pp. 1043–1047.
- [210] G. Schumicki, and P. Seegerbrecht, "Prozesstechnologie: Fertigungsverfahren für integrierte MOS-Schaltungen", *Springer-Verlag*, Berlin, Germany, 1991.
- [211] Synopsys TCAD, "Sentaurus Process", *Release G-2012.06*, Synopsys, <http://www.synopsys.com>.
- [212] J. Schön, A. Abdollahinia, R. Müller, J. Benick, M. Hermle, W. Warta, and M. C. Schubert, "Predictive simulation of doping processes for silicon solar cells", *Energy Procedia*, vol. 38, pp. 312–320, 2013.
- [213] F. D. Heinz, M. Breitwieser, P. Gundel, M. König, M. Hörteis, W. Warta, and M. C. Schubert, "Microscopic origin of the aluminium assisted spiking effects in  $n$ -type silicon solar cells", *Solar Energy Materials and Solar Cells*, vol. 131, pp. 105–109, 2014.
- [214] Y.-W. Ok, A. Upadhyaya, F. Zimbardi, Y. Tao, I. B. Cooper, A. Rothagi, A. F. Carroll, and T. Suess, "Effect of Al content on the performance of Ag/Al screen printed  $n$ -type Si solar cells", in *Proceedings of the 39th IEEE Photovoltaic Specialists Conference*, Tampa, USA, 2013, pp. 2247–2249.
- [215] A. Edler, V. D. Mihailetchi, L. J. Koduvvelikulathu, C. Comparotto, R. Kopecsek, and R. Harney, "Metallization-induced recombination losses of bifacial silicon solar cells", *Progress in Photovoltaics: Research and Applications*, vol. 23, pp. 620–627, 2014.

- [216] F. Kiefer, R. Peibst, T. Ohrdes, J. Krügener, H. J. Osten, and R. Brendel, "Emitter recombination current densities of boron emitters with silver/aluminum pastes", in *Proceedings of the 40th IEEE Photovoltaic Specialists Conference*, Denver, USA, 2014, pp. 2808–2812.
- [217] S. Fritz, M. König, S. Riegel, A. Herguth, M. Hörteis, and G. Hahn, "Formation of Ag/Al screen-printing contacts on B emitters", *IEEE Journal of Photovoltaics*, vol. 5, no. 1, pp. 145–151, 2015.
- [218] S. Riegel, F. Mutter, G. Hahn, and B. Terheiden, "Contact formation in the silver/aluminum thick film firing process – a phenomenological approach", in *Proceedings of the 25th European Photovoltaic Solar Energy Conference and Exhibition*, Valencia, Spain, 2010, pp. 2353–2356.
- [219] M. König, A. Rudl, N. Georg, and M. Hörteis, "Advanced model for the contact formation of Al-containing Ag thick film paste on boron-doped emitter of Si solar cells", presented at the *3rd nPV Workshop*, Chambéry, France, 2013.
- [220] S. Kontermann, A. Ruf, R. Preu, and G. Willeke, "Simulating the interface morphology of silver thick film contacts on *n*-type Si-(100) and Si-(111)", *Applied Physics Letters*, vol. 101, no. 12, pp. 121907-1–121907-4, 2012.
- [221] E. Cabrera, S. Olibet, J. Glatz-Reichenbach, R. Kopecik, D. Reinke, and G. Schubert, "Experimental evidence of direct contact formation for the current transport in silver thick film metallized silicon emitters", *Journal of Applied Physics*, vol. 110, no. 11, pp. 114511-1–114511-5, 2011.
- [222] S. Seyedmohammadi, E. Graddy, and A. Shaik, "Screen printable Ag-Al metal pastes for *p*+ silicon application in solar cells", in *Proceedings of the 35th IEEE Photovoltaic Specialists Conference*, Honolulu, Hawaii, USA, 2010, pp. 3600–3603.
- [223] A. Frey, J. Engelhart, S. Fritz, S. Gloger, G. Hahn, and B. Terheiden, "N-type bi-facial solar cells with boron emitters from doped PECVD layers", in *Proceedings of the 29th European Photovoltaic Solar Energy Conference and Exhibition*, Amsterdam, Netherlands, 2014.
- [224] T. Buck, J. Theobald, M. Nejati, D. Rudolph, A. Helfricht, G. Schubert, V. D. Mihailescu, and R. Harney, "Engineering and characterization of metal contacts to *p*+‐doped silicon", in *Proceedings of the 29th European Photovoltaic Solar Energy Conference and Exhibition*, Amsterdam, Netherlands, 2014, pp. 401–405.
- [225] S. Fritz, S. Riegel, S. Gloger, D. Kohler, M. König, M. Hörteis, and G. Hahn, "Influence of emitter properties on contact formation to *p*+ silicon", *Energy Procedia*, vol. 38, pp. 720–724, 2013.

- [226] V. Cosslett, "Fifty years of instrumental development of the electron microscope", *Advances in Optical Technologies*, pp. 215–267, 1988.
- [227] E. Lohmüller, S. Werner, R. Hoenig, J. Greulich, and F. Clement, "Impact of boron doping profiles on the specific contact resistance of screen printed Ag-Al contacts on silicon", *Solar Energy Materials and Solar Cells*, vol. 142, pp. 2–11, 2015.
- [228] E. Cabrera, S. Olibet, D. Rudolph, P. E. Vullum, R. Kopecek, D. Reinke, C. Herzog, D. Schwaderer, and G. Schubert, "Impact of excess phosphorus doping and Si crystalline defects on Ag crystallite nucleation and growth in silver screen-printed Si solar cells", *Progress in Photovoltaics: Research and Applications*, vol. 23, no. 3, pp. 367–375, 2015.
- [229] S. Kontermann, "Characterization and modeling of contacting crystalline silicon solar cells", *PhD thesis*, University of Constance, Germany, 2009.
- [230] R. Hoenig, "Evaluation and microstructure analysis of thick film contacts for industrial silicon solar cells", *PhD thesis*, University of Freiburg, Germany, 2014.
- [231] C. Y. Chang, Y. K. Fang, and S. M. Sze, "Specific contact resistance of metal-semiconductor barriers", *Solid-State Electronics*, vol. 14, no. 7, pp. 541–550, 1971.
- [232] P. P. Altermatt, "Models for numerical device simulations of crystalline silicon solar cells—a review", *Journal of Computational Electronics*, vol. 10, no. 3, pp. 314–330, 2011.
- [233] M. J. Turner, and E. H. Rhoderick, "Metal-silicon Schottky barriers", *Solid-State Electronics*, vol. 11, no. 3, pp. 291–300, 1968.
- [234] R. T. Tung, "Recent advances in Schottky barrier concepts", *Materials Science and Engineering R*, vol. 35, no. 1–3, pp. 1–138, 2001.
- [235] K. T. Butler, and J. H. Harding, "Atomistic simulation of doping effects on growth and charge transport in Si/Ag interfaces in high-performance solar cells", *Physical Review B*, vol. 86, no. 24, pp. 245319-1–245319-7, 2012.
- [236] B. L. Smith, and E. H. Rhoderick, "Schottky barriers on *p*-type silicon", *Solid-State Electronics*, vol. 14, no. 1, pp. 71–75, 1971.
- [237] J. M. Andrews, and M. P. Lepselter, "Reverse current-voltage characteristics of metal-silicide Schottky diodes", *Solid-State Electronics*, vol. 13, no. 7, pp. 1011–1023, 1970.
- [238] K. Varahramyan, and E. J. Verret, "A model for specific contact resistance applicable for titanium silicide-silicon contacts", *Solid-State Electronics*, vol. 39, no. 11, pp. 1601–1607, 1996.

- [239] K. K. Ng, and R. Liu, “On the calculation of specific contact resistivity on <100> Si”, *IEEE Transactions on Electron Devices*, vol. 37, no. 6, pp. 1535–1537, 1990.
- [240] Synopsys TCAD, “Sentaurus Device”, *Release H-2013.03*, Synopsys, <http://www.synopsys.com>.
- [241] N. Wörle, E. Lohmüller, J. Greulich, S. Werner, and S. Mack, “Towards understanding the characteristics of Ag-Al spiking on boron-doped silicon for solar cells”, *Solar Energy Materials and Solar Cells*, vol. 146, pp. 72–79, 2016.
- [242] A. Edler, V. D. Mihailetchi, C. Comparotto, L. J. Koduvelikulathu, R. Kopeczek, R. Harney, T. Böscke, and J. Lossen, “On the metallization losses of bifacial *n*-type silicon solar cells”, in *Proceedings of the 27th European Photovoltaic Solar Energy Conference and Exhibition*, Frankfurt, Germany, 2012, pp. 1429–1431.
- [243] Z. G. Li, L. Liang, A. S. Ionkin, B. M. Fish, M. E. Lewittes, L. K. Cheng, and K. R. Mikeska, “Microstructural comparison of silicon solar cells’ front-side Ag contact and the evolution of current conduction mechanisms”, *Journal of Applied Physics*, vol. 110, no. 7, pp. 074304-1–074304-8, 2011.
- [244] A. Mette, “New concepts for front side metallization of industrial silicon solar cells”, *PhD thesis*, University of Freiburg, Germany, 2007.
- [245] C. Ballif, D. M. Huljic, G. Willeke, and A. Hessler-Wyser, “Silver thick-film contacts on highly doped *n*-type silicon emitters: structural and electronic properties of the interface”, *Applied Physics Letters*, vol. 82, no. 12, pp. 1878–1880, 2003.
- [246] C.-H. Lin, S.-Y. Tsai, S.-P. Hsu, and M.-H. Hsieh, “Investigation of Ag-bulk/glassy-phase/Si heterostructures of printed Ag contacts on crystalline Si solar cells”, *Solar Energy Materials and Solar Cells*, vol. 92, no. 9, pp. 1011–1015, 2008.
- [247] P. N. Vinod, “Specific contact resistance measurements of the screen-printed Ag thick film contacts in the silicon solar cells by three-point probe methodology and TLM method”, *Journal of Materials Science: Materials in Electronics*, vol. 22, no. 9, pp. 1248–1257, 2011.
- [248] R. H. Fowler, and L. Nordheim, “Electron emission in intense electric fields”, in *Proceedings of the Royal Society of London A*, vol. 119, no. 781, pp. 173–181, 1928.
- [249] I. Geisemeyer, F. Fertig, W. Warta, S. Rein, and M. C. Schubert, “Impact of reverse breakdown in shaded silicon solar cells on module level - simulation and experiment”, in *Proceedings of the 27th European Photovoltaic Solar Energy Conference and Exhibition*, Frankfurt, Germany, 2012, pp. 870–874.

- [250] A. Spribile, E. Lohmüller, B. Thaidigsmann, R. Hamid, H. Nussbaumer, F. Clement, and R. Preu, “Wet chemical single-side emitter etch back for MWT solar cells with Al–BSF and challenges for via paste selection”, in *Proceedings of the 28th European Photovoltaic Solar Energy Conference and Exhibition*, Paris, France, 2013, pp. 1080–1084.
- [251] S. Ogawa, and N. Shiono, “Interface-trap generation induced by hot-hole injection at the Si-SiO<sub>2</sub> interface”, *Applied Physics Letters*, vol. 61, no. 7, pp. 807–809, 1992.
- [252] H. Watanabe, K. Fujita, and M. Ichikawa, “Observation and creation of current leakage sites in ultrathin silicon dioxide films using scanning tunneling microscopy”, *Applied Physics Letters*, vol. 72, no. 16, pp. 1987–1989, 1998.
- [253] R. Degraeve, B. Kaczer, and G. Groeseneken, “Degradation and breakdown in thin oxide layers: mechanisms, models and reliability prediction”, *Microelectronics Reliability*, vol. 39, no. 10, pp. 1445–1460, 1999.
- [254] Z. Gingl, C. Pennetta, L. B. Kiss, and L. Reggiani, “Biased percolation and abrupt failure of electronic devices”, *Semiconductor Science and Technology*, vol. 11, no. 12, pp. 1770–1775, 1996.
- [255] C. Pennetta, Z. Gingl, L. B. Kiss, and L. Reggiani, “Biased percolation and electrical breakdown”, *Semiconductor Science and Technology*, vol. 12, no. 9, pp. 1057–1063, 1997.
- [256] N. Guillevin, A. Gutjahr, L. J. Geerligs, J. Anker, E. Bende, I. J. Bennett, M. Koppes, E. Kossen, L. Okel, L. H. Slooff, K. Broek, M. Späth, K. Tool, B. B. van Aken, I. Romijn, J. Wang, Z. Wang, J. Zhai, Z. Wan, S. Tian, Z. Hu, G. Li, B. Yu, and J. Xiong, “High efficiency *n*-type metal-wrap-through cells and modules using industrial processes”, in *Proceedings of the 29th European Photovoltaic Solar Energy Conference and Exhibition*, Amsterdam, Netherlands, 2014, pp. 642–647.
- [257] E. Lohmüller, F. Fertig, S. Werner, I. Geisemeyer, F. Clement, and D. Biro, “Reverse bias behavior of diffused and screen-printed *n*-type Cz-Si solar cells”, *IEEE Journal of Photovoltaics*, vol. 4, no. 6, pp. 1483–1490, 2014.
- [258] O. Breitenstein, W. Warta, and M. Langenkamp, “Lock-in thermography - basics and applications to functional diagnostics of electronic components”, Second Edition, *Springer-Verlag*, Berlin, Germany, 2010.
- [259] Y. Schiele, S. Joos, G. Hahn, and B. Terheiden, “Etch-back of *p*+ structures for selective boron emitters in *n*-type c-Si solar cells”, *Energy Procedia*, vol. 55, pp. 295–301, 2014.

- [260] N. Guillevin, B. Heurtault, L. J. Geerligs, B. B. van Aken, I. J. Bennett, M. J. Jansen, A. W. Weeber, J. H. Bultman, J. Wang, Z. Wang, J. Zhai, Z. Wan, S. Tian, W. Zhao, Z. Hu, G. Li, B. Yu, and J. Xiong, "High power  $n$ -type metal-wrap-through cells and modules using industrial processes", in *Proceedings of the 28th European Photovoltaic Solar Energy Conference and Exhibition*, Paris, France, 2013, pp. 1304–1310.
- [261] F. Dauzou, R. Cabal, and Y. Veschetto, "Electrical behaviour of  $n$ -type silicon solar cells under reverse bias: influence of the manufacturing process", *Solar Energy Materials and Solar Cells*, vol. 104, pp. 175–179, 2012.
- [262] T. Blévin, A. Lanterne, B. Grange, R. Cabal, J. P. Vilcot, and Y. Veschetto, "Development of industrial processes for the fabrication of high efficiency  $n$ -type PERT cells", *Solar Energy Materials and Solar Cells*, vol. 131, pp. 24–29, 2014.
- [263] E. Lohmüller, S. Werner, B. Thaidigsmann, N. Wöhrle, S. Mack, F. Clement, and D. Biro, "The HIP–MWT+ solar cell concept on  $n$ -type silicon and metallization-induced voltage losses", in *Proceedings of the 29th European Photovoltaic Solar Energy Conference and Exhibition*, Amsterdam, Netherlands, 2014, pp. 635–641.
- [264] T. Fellmeth, A. Born, A. Kimmerle, F. Clement, D. Biro, and R. Preu, "Recombination at metal-emitter interfaces of front contact technologies for highly efficient silicon solar cells", *Energy Procedia*, vol. 8, pp. 115–121, 2011.
- [265] T. Fellmeth, F. Clement, and D. Biro, "Analytical modeling of industrial-related silicon solar cells", *IEEE Journal of Photovoltaics*, vol. 4, no. 1, pp. 504–513, 2014.
- [266] V. Reitenbach, M. Spitz, A. Drews, M. Weiß, E. O. Chighali, B. Thaidigsmann, E. Lohmüller, A. Knorz, F. Clement, A. Wolf, D. Biro, and R. Preu, "Process characterisation of MWT solar cells - a new method to analyse via contacts", in *Proceedings of the 27th European Photovoltaic Solar Energy Conference and Exhibition*, Frankfurt, Germany, 2012, pp. 1335–1338.
- [267] N. Mingirulli, D. Biro, R. Preu, S. W. Glunz, and S. Riepe, "Method for determination of recombination activity of cylindric conduction channels for back-contacted solar cells", *Applied Physics Letters*, vol. 91, no. 18, pp. 183512-1–183512-3, 2007.
- [268] B. Thaidigsmann, A. Wolf, and D. Biro, "Accurate determination of the IQE of screen printed silicon solar cells by accounting for the finite reflectance of metal contacts", in *Proceedings of the 24th European Photovoltaic Solar Energy Conference and Exhibition*, Hamburg, Germany, 2009, pp. 2056–2059.

## Bibliography

---

- [269] W. Dunlap, and R. Watters, “Direct measurement of the dielectric constants of silicon and germanium”, *Physical Review*, vol. 92, no. 6, pp. 1396–1397, 1953.
- [270] W. B. Joyce, and R. W. Dixon, “Analytic approximations for the Fermi energy of an ideal Fermi gas”, *Applied Physics Letters*, vol. 31, no. 5, pp. 354–356, 1977.
- [271] K.-H. Oh, J.-H. Chun, K. Banerjee, C. Duvvury, and R. W. Dutton, “Modeling of temperature dependent contact resistance for analysis of ESD reliability”, in *Proceedings of the 41st IEEE Reliability Physics Symposium*, Dallas, USA, 2003, pp. 249–255.
- [272] J. Hohl-Ebinger, and W. Warta, “Bifacial solar cells in STC measurement”, in *Proceedings of the 25th European Photovoltaic Solar Energy Conference and Exhibition*, Valencia, Spain, 2010, pp. 1358–1362.
- [273] M. Glatthaar, J. Hohl-Ebinger, A. Krieg, M. Greif, L. Greco, F. Clement, S. Rein, W. Warta, and R. Preu, “Accurate IV-measurement for back contact solar cells”, in *Proceedings of the 25th European Photovoltaic Solar Energy Conference and Exhibition*, Valencia, Spain, 2010, pp. 2118–2120.
- [274] R. Bock, P. P. Altermatt, and J. Schmidt, “Accurate extraction of doping profiles from electrochemical capacitance voltage measurements”, in *Proceedings of the 23rd European Photovoltaic Solar Energy Conference and Exhibition*, Valencia, Spain, 2008, pp. 1510–1513.
- [275] G. L. Miller, Robinson, D. A. H., and J. D. Wiley, “Contactless measurement of semiconductor conductivity by radio frequency-free-carrier power absorption”, *Review of Scientific Instruments*, vol. 47, no. 7, pp. 799–805, 1976.

# List of Symbols

Symbol	Description	Unit
$A$	Contact area	$\text{mm}^2$
$A^*$	Effective Richardson constant	$\text{A}/(\text{cm}^2 \cdot \text{K}^2)$
$A_0$	Area of etch crater from ECV measurement	$\text{mm}^2$
$A_{\text{cryst}}$	Crystallite coverage fraction	%
$A_{\text{gaps}}$	Total area of gaps without phosphorus BSF	$\text{mm}^2$
$A_{\text{pads}}$	Total area of external contact pads	$\text{mm}^2$
$A_{\text{test}}$	Metallized area on the test structures	$\text{cm}^2$
$A_{\text{vias}}$	Total area inside the vias	$\text{mm}^2$
$A_{\text{wafer}}$	Total wafer surface	$\text{mm}^2$
$C$	Capacitance	F
$C_L$	Contact length	mm
$D$	Diffusion coefficient	$\text{cm}^2/\text{s}$
$D_0$	Maximum diffusion coefficient	$\text{cm}^2/\text{s}$
$D_{\text{amb}}$	Ambipolar diffusion coefficient	$\text{cm}^2/\text{s}$
$D_{\text{B,eff}}$	Effective boron diffusion coefficient	$\text{cm}^2/\text{s}$
$D_p$	Hole diffusion coefficient	$\text{cm}^2/\text{s}$
$E_0$	Characteristic energy	eV
$E_{00}$	Characteristic energy	eV
$E_a$	Activation energy	eV
$E_C$	Energy of the conduction band edge	eV
$E_F$	Fermi energy	eV
$E_g$	Band gap energy	eV
$E_V$	Energy of the valence band edge	eV
$F_M$	Metallization fraction	%

## List of Symbols

---

<b>Symbol</b>	<b>Description</b>	<b>Unit</b>
$F_{M,b}$	Metallization fraction of the base	%
$F_{M,e}$	Metallization fraction of the emitter	%
$FF$	Fill factor	%
$FF_0$	Ideal fill factor	%
$G$	Generation rate	$1/(cm^3 \cdot s)$
$I_{-12V}$	Current at a voltage of -12 V	A
$I_{\text{leak}}$	Leakage current	A
$iV_{OC}$	Implied open-circuit voltage	mV
$iV_{OC,\text{limit}}$	Implied open-circuit voltage limit	mV
$J$	Particel flux	$1/(cm^2 \cdot s)$
$L_{\text{eff}}$	Effective diffusion length	$\mu m$
$L_p$	Bulk diffusion length of holes	$\mu m$
$L_T$	Transfer length	mm
$N$	Charge carrier/Particle concentration	$1/cm^3$
$N(d)$	Depth-dependent dopant concentration	$1/cm^3$
$N_{\text{bulk}}$	Bulk doping concentration	$1/cm^3$
$N_C$	Density of states in the conduction band	$1/cm^3$
$N_{\text{max}}$	Maximum dopant concentration	$1/cm^3$
$N_S$	Surface dopant concentration	$1/cm^3$
$N_V$	Density of states in the valence band	$1/cm^3$
$P_t$	Thermal power dissipation	W
$Q_{\text{tot}}$	Total dopant dose, Total amount of boron atoms	$1/cm^2$
$R$	Reflection, Recombination rate	% , $1/(cm^3 \cdot s)$
$R_C$	Contact resistance	$m\Omega$
$R_{C,\text{cryst}}$	Contact resistance of a single crystallite	$m\Omega$
$R_P$	Area-decoupled shunt resistance	$\Omega cm^2$
$R_S$	Area-decoupled series resistance	$\Omega cm^2$
$R_{S,H-\text{pattern}}$	Area-decoupled series resistance of an H-pattern cell	$\Omega cm^2$
$R_{S,n\text{MWT}+}$	Area-decoupled series resistance of an $n$ MWT+ cell	$\Omega cm^2$
$R_{\text{sh}}$	Sheet resistance	$\Omega /sq$

Symbol	Description	Unit
$R_{\text{sh,4pp}}$	Sheet resistance determined by 4-point-probe measurements	$\Omega/\text{sq}$
$R_{\text{sh,bulk}}$	Bulk sheet resistance	$\Omega/\text{sq}$
$R_{\text{sh,tot}}$	Total sheet resistance	$\Omega/\text{sq}$
$R_{\text{sh,w}}$	Wafer sheet resistance	$\Omega/\text{sq}$
$R_{\text{tot}}$	Total resistance	$\Omega$
$S_{\text{BSF}}$	Surface recombination velocity of the phosphorus-doped BSF	$\text{cm/s}$
$S_{\text{eff}}$	Effective surface recombination velocity	$\text{cm/s}$
$S_{\text{gap}}$	Surface recombination velocity of the BSF gap	$\text{cm/s}$
$S_{\text{met}}$	Surface recombination velocity at the metal-silicon interface	$\text{cm/s}$
$S_{\text{pad}}$	Effective surface recombination velocity underneath the pad	$\text{cm/s}$
$S_{\text{rear}}$	Rear surface recombination velocity	$\text{cm/s}$
$S_{\text{via}}$	Effective surface recombination velocity at the via	$\text{cm/s}$
$T$	Temperature	$^{\circ}\text{C}$ or $\text{K}$
$T_{\text{dep}}$	Deposition temperature	$^{\circ}\text{C}$
$T_{\text{DrIn}}$	Drive-in temperature	$^{\circ}\text{C}$
$T_{\text{DrIn,norm}}$	Normalized drive-in temperature	1
$T_{\text{set}}$	Set peak temperature	$^{\circ}\text{C}$
$V$	Voltage	$\text{mV}$
$V_{\text{bi}}$	Built-in potential	$\text{V}$
$V_{\text{ext}}$	Externally applied potential	$\text{V}$
$V_{\text{MPP}}$	Voltage at the maximum power point	$\text{mV}$
$V_{\text{OC}}$	Open-circuit voltage	$\text{mV}$
$V_{\text{OC,limit}}$	Open-circuit voltage limit	$\text{mV}$
$W$	Wafer thickness	$\mu\text{m}$
$b$	Side length of the crystallite's base area	$\text{nm}$
$a_{\text{cell}}$	Area fraction of the external rear $n$ -type contact pads	%
$a_{\text{gaps}}$	Gap coverage fraction	%
$a_{\text{pads}}$	Pad coverage fraction	%

## List of Symbols

---

<b>Symbol</b>	<b>Description</b>	<b>Unit</b>
$\bar{c}$	Doping-type dependent constant for silicon	1
$c_{\text{FE}}$	Constant for field emission	1
$c_{\text{TFE}}$	Constant for thermionic field emission	1
$d$	Doping profile depth	nm
$d_{\text{cryst}}$	Crystallite penetration depth	nm
$d_f$	Contact distance/Finger distance	nm
$d_{\text{Gen3}}$	Doping profile depth of $\text{BBr}_3$ diffusion process Gen3	nm
$d_{\text{Gen3-DrIn1}}$	Doping profile depth of $\text{BBr}_3$ diffusion process Gen3–DrIn1	nm
$d_{\text{Gen3-DrIn2}}$	Doping profile depth of $\text{BBr}_3$ diffusion process Gen3–DrIn2	nm
$e$	Euler number	1
$f_A$	Area factor	1
$\hbar$	Reduced Plank's constant ( $1.054\ 571\ 726 \cdot 10^{-34}\ \text{Js}$ )	$\text{Js}$
$j$	Current density	$\text{mA}/\text{cm}^2$
$j_0$	Dark saturation current density	$\text{fA}/\text{cm}^2$
$j_{01}$	Dark saturation current density of the first diode in the two-diode model	$\text{mA}/\text{cm}^2$
$j_{02}$	Dark saturation current density of the second diode in the two-diode model	$\text{nA}/\text{cm}^2$
$j_{0b}$	Base dark saturation current density	$\text{fA}/\text{cm}^2$
$j_{0b,\text{BSF}}$	Effective dark saturation current density of the BSF	$\text{fA}/\text{cm}^2$
$j_{0b,\text{eff}}$	Effective dark saturation current density of the base	$\text{fA}/\text{cm}^2$
$j_{0b,\text{gap}}$	Effective dark saturation current density of the BSF gap	$\text{fA}/\text{cm}^2$
$j_{0,\text{met}}$	Dark saturation current density underneath the metal contacts	$\text{fA}/\text{cm}^2$
$j_{0,\text{met,min}}$	Minimal dark saturation current density underneath metal contacts	$\text{fA}/\text{cm}^2$
$j_{0b,\text{met}}$	Dark saturation current density of the metallized base	$\text{fA}/\text{cm}^2$
$j_{0b,\text{pad}}$	Effective dark saturation current density at the pad	$\text{fA}/\text{cm}^2$

<b>Symbol</b>	<b>Description</b>	<b>Unit</b>
$j_{0b,\text{pass}}$	Dark saturation current density of the passivated base	fA/cm <sup>2</sup>
$j_{0\text{BSF}}$	Dark saturation current density of the BSF	fA/cm <sup>2</sup>
$j_{0\text{BSF,met}}$	Dark saturation current density of the metallized BSF	fA/cm <sup>2</sup>
$j_{0e}$	Emitter dark saturation current density	fA/cm <sup>2</sup>
$j_{0e,\text{met}}$	Dark saturation current density of the metallized emitter	fA/cm <sup>2</sup>
$j_{0e,\text{pass}}$	Dark saturation current density of the passivated emitter	fA/cm <sup>2</sup>
$j_{0\text{gap}}$	Dark saturation current density of the BSF gap	fA/cm <sup>2</sup>
$j_{0\text{pad}}$	Dark saturation current density at the pad	fA/cm <sup>2</sup>
$j_{\text{cell}}$	Current density of a reference solar cell	mA/cm <sup>2</sup>
$j_{\text{cell,leak}}$	Current density of the solar cell corrected by leakage current density	mA/cm <sup>2</sup>
$j_{\text{leak}}$	Leakage current density	mA/cm <sup>2</sup>
$j_{\text{MPP}}$	Current density at the maximum power point	mA/cm <sup>2</sup>
$j_{\text{ph}}$	Photo current density	mA/cm <sup>2</sup>
$j_{\text{SC}}$	Short-circuit current density	mA/cm <sup>2</sup>
$k$	Segregation coefficient	1
$k_B$	Boltzmann constant ( $1.380\ 648\ 8 \cdot 10^{-23}\ \text{J/K}$ )	J/K
$m_0$	Electron mass ( $9.109\ 382\ 91 \cdot 10^{-31}\ \text{kg}$ )	kg
$m_t^*$	Effective charge carrier tunneling mass	kg
$n_1$	Diode ideality factor of the first diode in the two-diode model	1
$n_2$	Diode ideality factor of the second diode in the two-diode model	1
$n_{i,\text{eff}}$	Effective intrinsic charge carrier concentration	1/cm <sup>3</sup>
$n_{\text{via}}$	Via density	1/cm <sup>2</sup>
$p$	Measurement points inductive inline measurement	1
$p_{\text{MPP}}$	Power density at the maximum power point	W/cm <sup>2</sup>
$p_{\text{STC}}$	Power density of incident light under standard test conditions	W/m <sup>2</sup>
$pFF$	Pseudo fill factor	%

## List of Symbols

---

<b>Symbol</b>	<b>Description</b>	<b>Unit</b>
$q$	Elementary charge ( $1.602\ 176\ 565 \cdot 10^{-19}\ \text{C}$ )	C
$q\Delta\phi_b'$	Reduction of the Schottky barrier height	eV
$q\phi_b$	Schottky barrier height	eV
$q\phi_b'$	Effective Schottky barrier height	eV
$q\phi_m$	Metal work function	eV
$q\phi_s$	Semiconductor work function	eV
$q\chi_s$	Electron affinity	eV
$r_{\text{via}}$	Via radius	µm
$s$	Number of sensors for inductive inline measurement	1
$s^*$	Slope to determine the dark saturation current density	$1/(\text{cm}^3 \cdot \text{s})$
$t$	Time	s
$t_1$	Drive-in time 1	min
$t_2$	Post-oxidation time 2	min
$t_{\text{DrIn}}$	Drive-in time	min
$t_{\text{PO}}$	Post-oxidation time with constant temperature	min
$v_{\text{OC}}$	Normalized voltage	1
$w$	Wafer designation for inductive inline measurement	1
$w_f$	Contact width/Finger width	µm
$x$	Distance	µm
$\Delta A_i$	Area element i	$\text{nm}^2$
$\Delta FF$	Difference in fill factor	%
$\Delta FF_A$	Difference in fill factor after measurement A	%
$\Delta FF_C$	Difference in fill factor after measurement C	%
$\Delta FF_E$	Difference in fill factor after measurement E	%
$\Delta R_S$	Difference in area-decoupled series resistance	$\Omega \text{cm}^2$
$\Delta Q_{\text{tot}}$	Difference in total amount of boron atoms	$1/\text{cm}^2$
$\Delta V_{\text{OC}}$	Difference in open-circuit voltage	mV
$\Delta V_{\text{OC,limit}}$	Difference in open-circuit voltage limit	mV
$\Delta V_{\text{OC,norm}}$	Normalized difference in open-circuit voltage	mV
$\Delta g_f$	Difference in gas flux	%
$\Delta n$	Excess charge carrier density of electrons	$1/\text{cm}^3$

<b>Symbol</b>	<b>Description</b>	<b>Unit</b>
$\Delta p$	Excess charge carrier density of holes	$1/\text{cm}^3$
$\Delta pFF$	Difference in pseudo fill factor	%
$\Delta\eta$	Difference in energy conversion efficiency	%
$\Delta\sigma$	Time dependent change in conductivity	$1/(\Omega \cdot \text{s})$
$\varepsilon_0$	Permittivity of the vacuum ( $8.854\ 187\ 817 \cdot 10^{-14}$ As/(Vcm))	As/(Vcm)
$\varepsilon_r$	Dielectric constant of the semiconductor	1
$\eta$	Energy conversion efficiency	%
$\lambda$	Wavelength	nm
$\mu_n$	Electron mobility	$\text{cm}^2/(\text{V}\cdot\text{s})$
$\mu_p$	Hole mobility	$\text{cm}^2/(\text{V}\cdot\text{s})$
$\pi$	Circle number (3.141 592 653)	1
$\rho_{\text{bulk}}$	Specific bulk resistance	$\Omega\text{cm}$
$\rho_C$	Specific contact resistance	$\text{m}\Omega\text{cm}^2$
$\rho_{C,\text{cryst}}$	Specific contact resistance of a single crystallite	$\text{m}\Omega\text{cm}^2$
$\sigma$	Standard deviation of the sheet resistance	%
$\sigma_{4\text{pp}}$	Standard deviation of the sheet resistance determined by 4-point-probe measurements	%
$\tau_{\text{bulk}}$	Bulk minority charge carrier lifetime	$\mu\text{s}$
$\tau_{\text{eff}}$	Effective minority charge carrier lifetime	$\mu\text{s}$
$\tau_{\text{intr}}$	Intrinsic minority charge carrier lifetime	$\mu\text{s}$
$\tau_{\text{SRH}}$	Shockley-Read-Hall minority charge carrier lifetime	$\mu\text{s}$
$\tau_{\text{surf}}$	Surface minority charge carrier lifetime	$\mu\text{s}$
$\tau_{\text{via}}$	Via minority charge carrier lifetime	$\mu\text{s}$



## List of Abbreviations

<b>Abbreviation</b>	<b>Meaning</b>
2D	Two-dimensional
3D	Three-dimensional
4pp	4-point-probe
Ag	Silver
Ag1	Silver screen-printing paste 1
Ag2	Silver screen-printing paste 2
Ag3	Silver screen-printing paste 3
Ag-Al	Silver-aluminum
Ag-Al1	Silver-aluminum screen-printing paste 1
Ag-Al2	Silver-aluminum screen-printing paste 2
Al	Aluminum
Al <sub>2</sub> O <sub>3</sub>	Aluminum oxide
Al–BSF	Aluminum back surface field
ALD	Atomic layer deposition
B	Boron
B <sub>2</sub> O <sub>3</sub>	Boric acid
BB	Busbar
BBr <sub>3</sub>	Boron tribromide
BC–BJ	Back-contact back-junction
BCl <sub>3</sub>	Boron trichloride
Br <sub>2</sub>	Bromine
BRL	Boron rich layer
BSF	Back surface field
BSG	Borosilicate glass

## List of Abbreviations

---

<b>Abbreviation</b>	<b>Meaning</b>
CD	Cool-down
Cl <sub>2</sub>	Chlorine
CU	Contact unit
Cz-Si	Czochralski-grown silicon
DB	Diffusion barrier
DLIT	Dark lock-in thermography
ECN	Energy Research Centre of the Netherlands
ECV	Electrochemical capacitance-voltage
FE	Field emission
FSD	Front surface doping
FST	Front surface topography
FZ-Si	Float-zone silicon
Gen1	BBr <sub>3</sub> diffusion process generation 1
Gen2	BBr <sub>3</sub> diffusion process generation 2
Gen3	BBr <sub>3</sub> diffusion process generation 3
Gen3*	BBr <sub>3</sub> diffusion process generation 3 without post-oxidation
Gen3–DrIn1	Gen3-based BBr <sub>3</sub> diffusion process with drive-in time 1
Gen3–DrIn1–PO6, Gen3–B	Gen3-based BBr <sub>3</sub> diffusion process with drive-in time 1 and post-oxidation time 6
Gen3–DrIn2	Gen3-based BBr <sub>3</sub> diffusion process with drive-in time 2
Gen3–PO1	Gen3-based BBr <sub>3</sub> diffusion process with post-oxidation 1
Gen3–PO2	Gen3-based BBr <sub>3</sub> diffusion process with post-oxidation 2
Gen3–PO2–LT, Gen3–A	Gen3-based BBr <sub>3</sub> diffusion process with post-oxidation 2 but lower drive-in temperature
Gen3–PO3	Gen3-based BBr <sub>3</sub> diffusion process with post-oxidation 3
Gen3–PO4	Gen3-based BBr <sub>3</sub> diffusion process with post-oxidation 4
Gen3–PO5, Gen3–C	Gen3-based BBr <sub>3</sub> diffusion process with post-oxidation 5
H <sub>2</sub> O	Water
H <sub>2</sub> O <sub>2</sub>	Hydrogen peroxide
HCl	Hydrochloric acid
HF	Hydrofluoric acid
HIP–MWT	High-performance metal wrap through

<b>Abbreviation</b>	<b>Meaning</b>
HIP–MWT+	Development of the HIP–MWT structure, no emitter within the vias
HNF	Cleaning sequence: HF, HNO <sub>3</sub> , HF
HNO <sub>3</sub>	Nitric acid
IQE	Internal quantum efficiency
ISE	Institute for Solar Energy Systems
KOH	Potassium hydroxide
LEI	Laser edge isolation
LID	Light induced degradation
MPP	Maximum power point
MWT	Metal wrap through
MWT–BSF	Metal wrap through back surface field
MWT–BSF+	Development of the MWT–BSF structure, no emitter is present on the rear side nor within the vias
MWT–PERC	Metal wrap through passivated emitter and rear cell
<i>n</i> MWT	<i>n</i> -type MWT solar cell with full-area phosphorus BSF
<i>n</i> MWT+	<i>n</i> -type MWT solar cell in which the phosphorus BSF is either completely omitted at the external <i>p</i> -type contacts or its maximum surface doping concentration is lowered
N <sub>2</sub>	Nitrogen
<i>I</i> – <i>V</i>	Current–voltage
O <sub>2</sub>	Oxygen
P	Phosphorus
P <sub>4</sub> O <sub>10</sub>	Phosphorus pentoxide
PECVD	Plasma-enhanced chemical vapor deposition
PERC	Passivated emitter and rear cell
PERT	Passivated emitter rear totally diffused
Phos1	POCl <sub>3</sub> diffusion process 1
Phos2	POCl <sub>3</sub> diffusion process 2
Phos3	POCl <sub>3</sub> diffusion process 3
PL	Photoluminescence
PO	Post-oxidation
POCl <sub>3</sub>	Phosphorus oxychloride

## List of Abbreviations

---

<b>Abbreviation</b>	<b>Meaning</b>
PSG	Phosphosilicate glass
PV	Photovoltaics
PV-TEC	Photovoltaic Technology Evaluation Center
QSSPC	Quasi-steady-state photoconductance
R6	Reference paste 6
RBL	Reverse bias load
RefProf	Reference profile
SC1	Standard clean 1
SC2	Standard clean 2
SDE	Alkaline saw-damage etched
SEM	Scanning electron microscopy
Si	Silicon
SiB <sub>4-6</sub>	Silicon boride compounds
SIMS	Secondary ion mass spectroscopy
SiN <sub>x</sub>	Silicon nitride
SiO <sub>2</sub>	Silicon dioxide
SiO <sub>x</sub>	Silicon oxide (applied by PECVD or sputtering)
SiriON	Silicon-rich oxynitride
SP	Screen printing
SRH	Shockley-Read-Hall
STC	Standard test conditions
Std	Standard
TE	Thermionic emission
TFE	Thermionic field emission
TLM	Transmission line model
TXT	Alkaline textured
V1	Via paste 1
V2	Via paste 2
V3	Via paste 3
V4	Via paste 4
V5	Via paste 5
VP	Via paste

# List of Publications

## Publications with peer review

- E. Lohmüller**, B. Thaidigsmann, J. Bartsch, C. Harmel, J. Specht, A. Wolf, F. Clement, M. Hörteis, and D. Biro, “Advanced metallization of rear surface passivated metal wrap through silicon solar cells”, *Energy Procedia*, vol. 8, pp. 546–551, 2011.
- E. Lohmüller**, B. Thaidigsmann, M. Pospischil, U. Jäger, S. Mack, J. Specht, J. Nekarda, M. Retzlaff, A. Krieg, F. Clement, A. Wolf, D. Biro, and R. Preu, “20% efficient passivated large-area metal wrap through solar cells on boron-doped Cz silicon”, *IEEE Electron Device Letters*, vol. 32, no. 12, pp. 1719–1721, 2011.
- E. Lohmüller**, B. Thaidigsmann, F. Clement, A. Wolf, and D. Biro, “Transfer of the HIP–MWT solar cell concept to *n*-type silicon”, *Energy Procedia*, vol. 38, pp. 436–442, 2013.
- E. Lohmüller**, F. Fertig, S. Werner, I. Geisemeyer, F. Clement, and D. Biro, “Reverse bias behavior of diffused and screen-printed *n*-type Cz-Si solar cells”, *IEEE Journal of Photovoltaics*, vol. 4, no. 6, pp. 1483–1490, 2014.
- E. Lohmüller**, M. Thanasa, B. Thaidigsmann, F. Clement, and D. Biro, “Electrical properties of the rear contact structure of MWT silicon solar cells”, *Solar Energy Materials and Solar Cells*, vol. 137, pp. 293–302, 2015.
- E. Lohmüller**, S. Werner, R. Hoenig, J. Greulich, and F. Clement, “Impact of boron doping profiles on the specific contact resistance of screen printed Ag-Al contacts on silicon”, *Solar Energy Materials and Solar Cells*, vol. 142, pp. 2–11, 2015.

- B. Thaidigsmann, F. Clement, A. Wolf, **E. Lohmüller**, F. Fertig, D. Biro, and R. Preu, “HIP–MWT: A simplified structure for metal wrap through solar cells with passivated rear surface”, *Energy Procedia*, vol. 8, pp. 498–502, 2011.
- B. Thaidigsmann, **E. Lohmüller**, U. Jäger, S. Mack, F. Lottspeich, A. Spribble, K. Birmann, D. Erath, A. Wolf, F. Clement, D. Biro, and R. Preu, “Large-area *p*-type HIP–MWT silicon solar cells with screen printed contacts exceeding 20% efficiency”, *Physica Status Solidi RRL*, vol. 5, no. 8, pp. 286–288, 2011.
- B. Thaidigsmann, J. Greulich, **E. Lohmüller**, S. Schmeißer, F. Clement, A. Wolf, D. Biro, and R. Preu, “Loss analysis and efficiency potential of *p*-type MWT–PERC solar cells”, *Solar Energy Materials and Solar Cells*, vol. 106, pp. 89–94, 2012.
- B. Thaidigsmann, **E. Lohmüller**, F. Fertig, F. Clement, and A. Wolf, “Characterization and modeling of screen-printed metal insulator semiconductor tunnel junctions for integrated bypass functionality in crystalline silicon solar cells”, *Journal of Applied Physics*, vol. 113, no. 21, pp. 214502-1–214502-9, 2013.
- M. Hendrichs, B. Thaidigsmann, **E. Lohmüller**, S. Nold, F. Clement, D. Biro, B. Rech, and R. Preu, “Advanced metallization concepts for *p*-type silicon metal-wrap-through (MWT) solar cells”, *Energy Technology*, vol. 2, no. 1, pp. 34–42, 2014.
- N. Wöhrle, **E. Lohmüller**, J. Greulich, S. Werner, and S. Mack, “Towards understanding the characteristics of Ag-Al spiking on boron-doped silicon for solar cells”, *Solar Energy Materials and Solar Cells*, vol. 146, pp. 72–79, 2016.
- F. Fertig, N. Wöhrle, J. Greulich, K. Krauß, **E. Lohmüller**, S. Meier, A. Wolf, and S. Rein, “Bifacial potential of single- and double-sided collecting silicon solar cells”, *Progress in Photovoltaics: Research and Applications*, accepted for publication.

**Oral presentations and posters at international conferences**

"Advanced metallization of rear surface passivated metal wrap through silicon solar cells", <i>1st SiliconPV</i> , Freiburg, Germany, 2011.	Oral presentation
<b>E. Lohmüller</b> , B. Thaidigsmann, S. Werner, F. Clement, A. Wolf, D. Biro, and R. Preu, "Evaluation of via pastes for <i>p</i> - and <i>n</i> -type metal wrap through (MWT) solar cells", in <i>Proceedings of the 27th European Photovoltaic Solar Energy Conference and Exhibition</i> , Frankfurt, Germany, 2012, pp. 590–595.	Oral presentation, Proceedings
"Transfer of the HIP–MWT solar cell concept to <i>n</i> -type silicon", <i>3rd SiliconPV</i> , Hamelin, Germany, 2013.	Poster
<b>E. Lohmüller</b> , S. Werner, J. Schön, M. Thanasa, S. Mack, W. Wolke, A. Wolf, F. Clement, and D. Biro, "Depletion of boron-doped surfaces protected with barrier layers during $\text{POCl}_3$ -diffusion", in <i>Proceedings of the 28th European Photovoltaic Solar Energy Conference and Exhibition</i> , Paris, France, 2013, pp. 1043–1047.	Poster, Proceedings
"Reverse bias behavior of diffused and screen-printed <i>n</i> -type Cz-Si solar cells", <i>40th IEEE Photovoltaic Specialists Conference</i> , Denver, USA, 2014.	Oral presentation
<b>E. Lohmüller</b> , S. Werner, B. Thaidigsmann, N. Wöhrle, S. Mack, F. Clement, and D. Biro, "The HIP–MWT+ solar cell concept on <i>n</i> -type silicon and metallization-induced voltage losses", in <i>Proceedings of the 29th European Photovoltaic Solar Energy Conference and Exhibition</i> , Amsterdam, Netherlands, 2014, pp. 635–641.	Oral presentation, Proceedings
"Impact of boron doping profiles on the specific contact resistance of screen printed Ag-Al contacts on silicon", <i>5th SiliconPV</i> , Constance, Germany, 2015.	Oral presentation

### Co-authorship in conference proceedings

F. Clement, B. Thaidigsmann, R. Hoenig, T. Fellmeth, A. Spribille, **E. Lohmüller**, A. Krieg, M. Glatthaar, H. Wirth, D. Biro, R. Preu, M. Menkoe, K. Meyer, D. Lahmer, H.-J. Krokoszinski, M. Neidert, A. Henning, C. Mohr, and W. Zhang, "Pilot-line processing of highly-efficient MWT silicon solar cells", in *Proceedings of the 25th European Photovoltaic Solar Energy Conference and Exhibition*, Valencia, Spain, 2010, pp. 1097–1101.

D. Biro, B. Thaidigsmann, F. Clement, A. Wolf, **E. Lohmüller**, S. Mack, T. Fellmeth, A. Drews, A. Spribille, E. A. Wotke, F. Lottspeich, M. Hofmann, U. Jäger, and R. Preu, "MWT meets PERC: Towards 20% efficient industrial silicon solar cells", in *Proceedings of the 37th IEEE Photovoltaic Specialists Conference*, Seattle, USA, 2011, pp. 1395–1399.

F. Clement, B. Thaidigsmann, **E. Lohmüller**, J. Specht, U. Jäger, S. Mack, M. Pospischil, A. Spribille, D. Erath, J. Nekarda, M. Hofmann, A. Wolf, D. Biro, and R. Preu, "Paths to achieve efficiencies over 20% with MWT silicon solar cells", in *Proceedings of the 21st International Photovoltaic Science and Engineering Conference*, Fukuoka, Japan, 2011.

A. Spribille, J. Greulich, **E. Lohmüller**, F. Clement, J. Specht, D. Biro, R. Preu, O. Doll, C. Tüshaus, W. Stockum, and I. Köhler, "MWT solar cell processing by use of Isishape® SolarEtch® SiD for rear contact and edge isolation", in *Proceedings of the 27th European Photovoltaic Solar Energy Conference and Exhibition*, Frankfurt, Germany, 2012, pp. 2001–2006.

V. Reitenbach, M. Spitz, A. Drews, M. Weiß, E. O. Chighali, B. Thaidigsmann, **E. Lohmüller**, A. Knorz, F. Clement, A. Wolf, D. Biro, and R. Preu, "Process characterisation of MWT solar cells - a new method to analyse via contacts", in *Proceedings of the 27th European Photovoltaic Solar Energy Conference and Exhibition*, Frankfurt, Germany, 2012, pp. 1335–1338.

A. Spribille, **E. Lohmüller**, B. Thaidigsmann, R. Hamid, H. Nussbaumer, F. Clement, and R. Preu, "Wet chemical single-side emitter etch back for MWT solar cells with Al-BSF and challenges for via paste selection", in *Proceedings of the 28th European Photovoltaic Solar Energy Conference and Exhibition*, Paris, France, 2013, pp. 1080–1084.

S. Fernandez-Robledo, U. Jäger, **E. Lohmüller**, and J. Nekarda, "Laser doping from borosilicate glass for metallization of boron emitters", in *Proceedings of the 28th European Photovoltaic Solar Energy Conference and Exhibition*, Paris, France, 2013, pp. 1126–1130.

B. Thaidigsmann, M. Hendrichs, S. Nold, **E. Lohmüller**, A. Wolf, F. Clement, D. Biro, and R. Preu, “*P*-type MWT solar cells: current status and future expectations”, in *Proceedings of the 28th European Photovoltaic Solar Energy Conference and Exhibition*, Paris, France, 2013, pp. 1099–1104.

S. Mack, A. Wolf, B. Thaidigsmann, **E. Lohmüller**, U. Jäger, M. Pospischil, F. Clement, D. Eberlein, R. Preu, and D. Biro, “Technologies for mass production of >20% efficient *p*-type silicon solar cells”, in *Proceedings of the 28th European Photovoltaic Solar Energy Conference and Exhibition*, Paris, France, 2013, pp. 761–765.

S. Werner, **E. Lohmüller**, S. Maier, A. Kimmerle, A. Spribile, S. Wasmer, F. Clement, and A. Wolf, “Process optimization for the front side of *p*-type silicon solar cells”, in *Proceedings of the 29th European Photovoltaic Solar Energy Conference and Exhibition*, Amsterdam, Netherlands, 2014, pp. 1342–1347.

N. Wöhrle, **E. Lohmüller**, S. Werner, and J. Greulich, “Development, characterization, and modelling of doping profile, contact resistance, and metal spiking in diffused and screen-printed boron emitters”, in *Proceedings of the 31st European Photovoltaic Solar Energy Conference and Exhibition*, Hamburg, Germany, 2015, pp. 495–501.

S. Werner, **E. Lohmüller**, U. Belledin, A. Vlooswijk, R. C. G. Naber, S. Mack, and A. Wolf, “Optimization of BBr<sub>3</sub> diffusion processes for *n*-type silicon solar cells”, in *Proceedings of the 31st European Photovoltaic Solar Energy Conference and Exhibition*, Hamburg, Germany, 2015, pp. 637–641.

## Magazine articles

**E. Lohmüller**, M. Hendrichs, B. Thaidigsmann, U. Eitner, F. Clement, A. Wolf, D. Biro, and R. Preu, “Current status of MWT silicon solar cell and module technology”, *Photovoltaics International*, no. 17, pp. 61–71, 2012.

F. Clement, M. Neidert, A. Henning, C. Mohr, W. Zhang, B. Thaidigsmann, R. Hoenig, T. Fellmeth, A. Spribile, **E. Lohmüller**, A. Krieg, M. Glattahaar, H. Wirth, D. Biro, R. Preu, M. Menkoe, K. Meyer, D. Lahmer, and H.-J. Krokoszinski, “Processing of highly-efficient MWT silicon solar cells”, *Photovoltaics International*, no. 11, pp. 70–75, 2011.

S. Mack, B. Thaidigsmann, **E. Lohmüller**, A. Wolf, F. Clement, M. Hofmann, R. Preu, and D. Biro, “Technologies for mass production of PERC and MWT solar cells”, *Photovoltaics International*, no. 22, pp. 39–46, 2013.

S. Mack, **E. Lohmüller**, P. Rothhardt, S. Meier, S. Werner, A. Wolf, F. Clement, and D. Biro, "Development of bifacial *n*-type solar cells at Fraunhofer ISE: Status and perspectives", *Photovoltaics International*, no. 27, pp. 61–67, 2015.

### **Patent applications**

**E. Lohmüller**, B. Thaidigsmann, J. Bartsch, F. Clement, A. Wolf, and D. Biro, „Verfahren zur Herstellung einer metallischen Kontaktstruktur einer Halbleiterstruktur mit Durchkontaktierung und photovoltaische Solarzelle“, DE 10 2011 018 374, registered on April 20, 2011.

B. Thaidigsmann, **E. Lohmüller**, F. Clement, A. Wolf, D. Biro, and R. Preu, „Photovoltaische Solarzelle und Verfahren zum Herstellen einer photovoltaischen Solarzelle“, DE 10 2012 217 078, registered on September 21, 2012, granted on March 05, 2015.

# Danksagung

Wie sagt man so schön: „*Der Weg ist das Ziel*“. Vielen Dank an alle, die mich die letzten Jahre auf diesem Weg begleitet und unterstützt haben.

Ein herzliches Danke gebührt der Reiner Lemoine Stiftung für die großzügige finanzielle Unterstützung im Rahmen eines Promotionsstipendiums.

Mein besonderer Dank gilt Herrn Prof. Reinecke und Herrn Prof. Willeke für die angenehmen und motivierenden Treffen und Diskussionen, die Neugierde an neuen Ergebnissen und natürlich für die offizielle Betreuung meiner Promotion. Ralf Preu und Daniel Biro gilt mein Dank für die Ermöglichung der zurückliegenden erlebnisreichen Doktorandenzeit, und für die ab und an auch kritisch geführten Diskussionen. Florian Clement, meinem Gruppenleiter und MWT-Pionier, gebührt ebenfalls ein dickes Danke. *Häuptling Dickschicht*, vielen Dank für all deine Unterstützung, dein stets offenes Ohr und das entgegengebrachte Vertrauen, auch abseits der Solarzellenwelt. Danke auch an Andreas Wolf und Sebastian Mack für all die Weichenstellungen und hilfreichen Anregungen.

Absolut unverzichtbar war Sabrina Werner, die mich mit ihrer grandiosen Unterstützung stets auf dem richtigen Weg gehalten hat. *Sabrina*, danke für deine unermüdliche Hilfe nicht nur bei der Bor- und Phosphordiffusion, sondern auch für all die Ideen und Ratschläge und für dein engagiertes und unkompliziertes Mitanpacken. Außerordentlich wertvoll war auch die hervorragende Unterstützung von Benjamin Thaidigsmann, den ich bereits seit Beginn meiner Diplomarbeit bei der Reise durch die Welt der MWT-Solarzellen begleiten durfte. *Benni*, vielen Dank für deine ansteckende Motivation, deine Neugierde und für noch so viele weitere Dinge.

Ohne euch, meine Studenten und Praktikanten, wären viele Untersuchungen gar nicht möglich gewesen. Vielen Dank an Maximilian Weiß, Mikaella

## Danksagung

---

Thanasa, Alexa Langenecker, Benedikt Fischer, Hannah Lea Rößler, Simon Schlipf und Stephan Maus für eure tatkräftige Unterstützung.

Nicht zu vergessen ist die Unterstützung durch das gesamte PV-TEC Team. Ohne euch wären solche Fortschritte und Ergebnisse nicht möglich gewesen. Heike Brinckheger danke ich für die immer zuverlässige und ab und an spontane Nasschemie-Prozessierung, Daniel Trogus und Rupprecht Ackermann für unzählige PECVD-Beschichtungen, Mike Jahn für die Beherrschung des Inkjet-Drucks, Rainer Neubauer für zahlreiche und teilweise recht spontane nasschemische Behandlungen, Philipp Rothhardt und Udo Belledin für ihren Einsatz bei der Inbetriebnahme des  $\text{BBr}_3$ -Diffusionsofens, Udo Belledin und Sabrina Werner für die Unterstützung bei der Entwicklung der  $\text{BBr}_3$ -Diffusionsprozesse und zusammen mit Stefan Maier bei der  $\text{POCl}_3$ -Diffusion, Marc Retzlaff, Vanessa Krumm und Michael Linse für das geschmeidige Aufbringen der Metallkontakte mittels Siebdruck, Ulrich Jäger, Andreas Brandt und Christian Harmel für das Einbringen ihres Knowhows bei Laserprozessen, Achim Kimmerle für die Betreuung der ECV-Messung und für bereits entwickelte  $\text{POCl}_3$ -Prozesse, Alexander Krieg und Friedrich Schwehr für Zelltestermessungen, Fabian Fertig und Ino Geisemeyer für Diskussionen rund um Rückwärtsdurchbrüche und DLIT-Messungen, Bernhard Link und Severin Bang für die Durchführung von DLIT- und IQE-Messungen, Jonas Schön, Nico Wöhrle und Johannes Greulich für wertvolle Diskussionen rund um durchgeführte Simulationen, und Jutta Zielonka für die Anfertigung von REM-Aufnahmen. Auch an die, die hier leider namentlich nicht aufgelistet sind, ist mein herzlichster Dank gerichtet. Ebenso gilt mein Dank auch René Hönig, Max Hendrichs und Karin Krauß für zahlreiche Ideen, die nicht nur während der leckeren und unterhaltungsfrohen Mittagessen entstanden sind.

Meinen ständigen Bürokollegen Max Hendrichs, Nico Wöhrle und Julia Kumm gilt mein Dank für eine angenehme und lockere Atmosphäre.

Verlassen konnte ich mich zu jeder Zeit auch auf die Unterstützung meiner Familie und meiner Freunde. Die liebevolle und motivierende Art von dir, *Sabrina*, ermutigte mich auch in schwierigen Phasen durchzuhalten. *Danke!*

Zu guter Letzt einen *herzlichen Dank* den fleißigen Korrekturlesern Sabrina Werner, Max Hendrichs, Wasan Hasan, Florian Clement, Karin Krauß, Achim Kimmerle und Andreas Wolf. *Damit wärs gschaffd.*

This thesis presents the transfer of the metal wrap through (MWT) solar cell concept from p-type to n-type crystalline Czochralski-grown silicon (Cz-Si) wafers with 156 mm edge length. An industrially-feasible MWT solar cell structure with screen-printed metallization is developed, which combines the advantages of n-doped silicon with those of a rear contact cell structure. The studies focus on reverse bias stability, emitter diffusion, and electrical contacting of highly boron-doped surfaces. The vias and the rear p-type contacts represent the most important MWT specific structures. Detailed investigations result in optimizations and process simplifications with respect to the rear contact configuration. The maximum energy conversion efficiency achieved for large-area n-type Cz-Si MWT solar cells within this work is 20.4%.

New tube furnace diffusion processes are developed to form deep driven-in boron dopings with low surface concentration in a single process step. The emitters formed therewith feature low dark saturation current density of  $(30 \pm 3)$  fA/cm<sup>2</sup> for passivated and textured surface with a sheet resistance of about 120 Ω/sq. Despite low maximum dopant concentration of only  $(1.8 \pm 0.2) \cdot 10^{19}$  cm<sup>-3</sup>, low specific contact resistance of less than 4 mΩcm<sup>2</sup> is obtained for screen-printed and fired metal contacts. It is experimentally shown for the first time that the depth-dependent course of the dopant concentration contributes to a low-ohmic contact formation. This correlation is also demonstrated by means of an analytical model which is based on metal crystallites. Furthermore, it is shown that charge carrier recombination underneath the metal contacts correlates with both the metal crystallites and the junction depths of the boron dopings.

ISBN 978-3-8440-4196-5



9 783844 041965

**SHAKER**  
VERLAG